RECONFIGURABLE PHOTONIC CRYSTAL CAVITIES

A thesis submitted for the degree of
Doctor of Philosophy

Cameron L. C. Smith

ARC Centre of Excellence for
Ultrahigh-bandwidth Devices for Optical Systems

School of Physics, University of Sydney
Sydney, Australia

November 2008

Declaration of originality

This thesis does not contain any material that has been presented for a separate degree at the University of Sydney or any other university. Furthermore, it does not contain any copy or paraphrasing of published work by another person except when explicitly acknowledged throughout the dissertation.

Chapters 3, 4, 5 and 6 of this thesis contain published articles, for which all authors have provided signed statements acknowledging the specified contributions made by the author of this thesis.

I declare this thesis to be wholly my own work, unless stated otherwise.

Signature of Author ....

Acknowledgements

This thesis represents the culmination of almost four years of work and studies towards my Ph.D candidature. In retrospect for that time, certainly a lot has changed: in me as a person; in my knowledge and understanding; indeed, in the world as we know it. Researchers from other regions may not have much sympathy considering their typical Ph.D studies could take up to six, seven or eight years – sometimes even longer – to reach completion. Nevertheless, I still persist that four years is quite a long time to devote to anything during a young adult's life. Four years is almost one-and-a-half terms for an Australian Prime Minister – heck, it's an entire US presidential term. Way back when I signed on to postgraduate work in early 2005, the youth were listening to songs like *The Reason* by Hoobastank and *Boulevard of Broken Dreams* by Green Day, Britney and Kevin hadn't yet borne their first child and Brad had only just separated from Jennifer (you know, covering the important stuff). So yes, four years is a long time.

Before I make a start on the accolades of mentors and colleagues, I would like to first extend my gratitude to family members – in particular, my parents. My *Mother* and *Father* have both been implacable in their support of me, and whether or not I have made it obvious to them, I am deeply thankful. The reassurances they provide, unspoken or otherwise, are something that took me many years to appreciate. I would also like to acknowledge my grandparents for a similar role they have played to this point, both in my personal development and in my education: *Grandpa*, who passed away last year, and *Grandma* on my father's side, and of course, *Oma*, on my mother's side, who has been a true pillar of strength throughout my life.

Professor Benjamin Eggleton has been, without question, the primary influence over my research for the last *five* years, starting initially with my undergraduate thesis and continuing through to the time of this writing. It is difficult exaggerate the impact factor Ben has had, both on me as an individual and on the course of my Ph.D. Ben has been responsible for the tremendous opportunity I have enjoyed, supporting me to participate in research at a world-class facility, meet extraordinary scientists, publish in prestigious journals, receive prizes, launch my career, and certainly not least, *travel the world*. I have been shaped and honed into a much different person to who I was

before meeting Ben, and this will undoubtedly help me in positive ways for years to come.

Doctor Eric Mägi, my co-supervisor, has played a significant role in the practical elements of my research. Eric is highly regarded amongst all the experimentalists at CUDOS, possessing a remarkable ability to unravel highly complex problems with workable solutions. Eric developed and built a vast array of sophisticated equipment, gadgets and machinery that I used extensively throughout my thesis. Furthermore, Eric has been a fount of excellent advice for me over the years and I owe much of the resulting successes to his guidance.

Doctor Christian Grillet became a major mentor of my research in the second year of my doctorate studies. Christian has been instrumental in helping me get started and gather the tools of understanding to keep my research output as strong as it has been. Christian was heavily involved in every paper related to this thesis and it really is difficult to overstate his importance to my work. Together with Christian, I should also tip my hat to *Doctor Christelle Monat*, who contributed significantly to the scientific understanding of the investigations we embarked. For someone to whom English is a second language, Christelle has a profoundly elegant and succinct way with words that engendered enormous respect from me. Both Christian and Christelle have been a massive boon to my Ph.D.

Doctor Snjezana Tomljenovic-Hanic became a prominent figure of my research in the third year of my doctorate studies. The microfluidic work, which formed the central theme of the final two years of my thesis, was based on Snjezana's idea and theoretical expertise. It is somewhat of a shame that it took several years of working in the same corridor before we became well acquainted, since Snjezana is a colleague that I would now also call friend. I will not quickly forget the many hours at tea and coffee time both laughing and commiserating.

Doctor Christian Karnutsch is a character that appeared in more recent times, who became the group leader for optofluidics in the last year of my doctorate studies. Christian (also known as "The Bear") has an experienced and proven-successful understanding of research institute protocols that were highly beneficial to learn from. Moreover, Christian is very generous with his time to sit down and help his students (such as yours truly) that made working with him highly productive and beneficial to the both of us. Christian's sense of humour, although 'quirky' at times, nevertheless helped unwind the stress that inevitably resulted from deadlines and the demands of our enthusiastic arch-supervisor. Cheers, mite!

Uwe Bog was roped into the microfluidic group for six months of his Master's shortly after the arrival of Christian Karnutsch. During that time Uwe and I became fast friends, spending many hours together in the lab, meetings, pubs, clubs and a concert. It was a great privilege to meet Uwe and I intend to catch up with him again soon.

Michael Lee has been a close colleague since my second doctorate year – when he started his Honours. Michael is perhaps the only other person on the entire planet to have endured even more stress and frustration with the fabrication of tapered fibres than myself. Believe me when I say that that is no simple feat, and is definitely something I would not wish on anybody. I will say, however, that it was a small comfort to share that experience with someone else. May the fates smile more favourably on Michael's tapering endeavours in the future.

Darran Wu played a major part in the microfluidic aspects of the thesis. It was his experiments that prompted my own, and I learnt many things about the manipulation of small-scale fluids from his previous work. The latter sections of my thesis work may not have been possible without the insight Darran offered.

At this point I would like to extend many thanks to the groups who fabricated photonic crystal samples, as these samples served as the basis for much of the research contained in the thesis. To *Darren Freeman*, *Steve Madden* and *Barry Luther-Davies* from Australian National University and *Yinlan Ruan* and *Yong-Hee Lee* from Korea Advanced Institute of Science and Technology for the chalcogenide photonic crystal samples. To *Liam O'Faolain*, *Tom White* and *Thomas Krauss* from St. Andrews University of Scotland for the silicon photonic crystal samples. To *Simon Frédérick*, *Dan Dalacu*, *Philip Poole*, *Jean Lapointe*, *Geof Aers*, and *Robin Williams* at the National Research Council, Canada, for both the chance to meet them all *and* the InP photonic crystal samples.

Other significant contributors to the work of my thesis include *Ross McPhedran*, *Harald Giessen*, *David Moss*, *Martjin deSterke* and *Chiara Neto*. Individually, the experience and knowledge in their respective fields is immense. That I was the benefactor of such a collective awareness has truly been an honour.

During the thesis I spent many hours in the confines of my office. As such, I shared much of my time with *Hong*, *Mike*, *Vahid*, and then more recently, *Stephen* and *Parry*. For the most part I got along well with all of them, which is quite an achievement considering the size of the office and the number of conversations ongoing at any one time. It's been a pleasure to know this group of people and I'm sure our paths will cross again throughout the years.

The Optical Society of America (OSA) student chapter was a great privilege to serve as president for my final year. In addition to the OSA itself, I would like to thank *Michaël Roelens* for his help and guidance; *Bill Corcoran* for being an absolutely fantastic and responsible chapter vice president; *Daniel Niell* for his role as treasurer; and *Ian Clarke* for being such a great host at Optium. As a result of OSA activities I was given the opportunity to travel to California to meet other chapter leaders, which I thank *Kiki* for to help make happen. Concluding my remarks about the OSA, I

should note that it was a great honour to welcome *Thomas Baer* and *Elizabeth Rogan* to the School of Physics to give a colloquium.

There are other names that certainly deserve a mention. *Chris Walsh* for his housekeeping and toleration of my protests against office-space adjustments; *Emily Higgins* for organising the great CUDOS holidays – err, workshops; *Ian Littler* for his wisdom and humour who, together with *Alex*, *Joe* and *Martin*, I enjoyed playing tennis with; *Mich* and *Terry* for the help in the Physics Workshop; other students doing Honours or postgraduate research in parallel: *Falk*, *Peter*, *Paul*, *Dane*, *Neil*, *Trina*, *Jamie*, *Sahand*, *Felix*, *Tim*, *Tom Grujic*, *Alessandro*, *Sam*, *Rhys*, *Irena*; and the students I've had under my wing doing special projects over the years: *Ali*, *Tom Lee*, *Tak*, *Anish*, *Patrick*, *Peter* and *Alex*.

I finally conclude with my non-CUDOS friends, all of whom I have accrued many hours of shared pastimes with. *Kelly*, *Lachlan*, *Sarah* and *Ben*: thank you for being who you are ever since high school. *Josh* and *Annie*, *Victor*, *Kristian*, *Stephani*, *Caly*, *Rachel*, *Gerard* and *Briar*, *Lisa* and *Ken*, *Jia*, *Jessica*, *Mark*: you're all awesome. And last, but certainly not least, *Suzi* and *Derek* (and sometimes *Calan*) for the Monday lunches; whilst you three may, on a technicality, be family, I think it's safe to say that you can be considered as friends now, too.

x

Abstract

Photonic crystals are optical structures that contain a periodic modulation of their refractive index, allowing them to control light in recent years of an unprecedented capacity. Photonic crystals may take on a variety of configurations, in particular the photonic crystal cavity, which may "hold" light in small volumes comparable to the light's wavelength. This capability to spatially confine light opens up countless possibilities to explore for research in telecommunications, quantum electrodynamics experiments and high-resolution sensor applications. However, the vast functionality potentially made available by photonic crystal cavities is limited due to the difficulty in redefining photonic crystal components once they are formed in their (typically) solid material. The work presented in this thesis investigates several approaches to overcome this issue by *reconfiguring* photonic crystal cavities.

Initially, a technique to accurately probe photonic crystal waveguides and cavities via evanescent coupling from a silica fibre nanowire is developed. Thus equipped with the capability to monitor such structures, the properties of photonic crystal cavities are adjusted in three separate ways: (i) by tuning with the presence of a nanowire, (ii) by exploiting the photonic crystal's host material photosensitivity, and (iii) by microfluidic infiltration of select holes in a slab photonic crystal.

High insertion efficiency into a photonic crystal waveguide is achieved via the evanescent coupling fibre technique. A silica glass single mode fibre is tapered from its initial dimensions of 125 μm down to an outer diameter of ~1 μm. The "nanowire" acts as the core for light to be guided, with the surrounding air forming its cladding. The nature of this guiding scheme results in a sensitive evanescent field that can strongly interact with its environment. A method to localise coupling to photonic crystal cavities is explored by curving the nanowire into a loop. The curvature offers an additional capability to characterise the dispersion of photonic crystal structures due to its expanding the k-space distribution of the nanowire modes.

Evanescent coupling is utilised to investigate ultra-small (0.5 $(\lambda/n)^3$), InAs/InP quantum dot photonic crystal cavities. The technique enables independent tuning of the Q-factor and wavelength of the cavity mode. This gives rise to the first method to

reconfigure photonic crystal cavities of the thesis. In the context of quantum dot photonic crystal cavities, evanescent coupling allows for optimisation of the extraction efficiency whilst maintaining a high Purcell Factor. It also allows matching of a cavity mode with a spectrally misaligned quantum dot without changing the photonic crystal geometry or degrading the Q-factor. A 3 nm shift is observed.

The photosensitivity of $Ge_{33}As_{12}Se_{55}$ chalcogenide glass is investigated for reconfiguring photonic crystals. A change in refractive index and volume of material in response to exposure to 633 nm light is observed. The resulting shift in wavelength is greater than 5 nm for the resonant coupling wavelength between the evanescent coupling fibre and the modes of the W1 waveguide. This represents the first proof of concept demonstration of the photosensitive post-processing of a planar photonic crystal device.

Post-processed and reconfigurable photonic crystal double heterostructure cavities are achieved via microfluidic infiltration of select holes in a planar structure. A significant number of results are reported. Experimental Fabry-Pérot signatures associated with modes of the induced cavities are in good agreement with numerical simulations. Quality factors of up to $Q = 5.7 \times 10^4$ are observed. The microfluidic cavities are configured spectrally and spatially by adjusting the lengths of the cavities in steps of several microns. The behaviour of Q-factors associated with the microfluidic cavities in terms of both wavelength and cavity length is reported. The cavity writing technique allows for tolerances in the infiltration process. Furthermore, the samples are immersed in toluene, erasing the fluid from the photonic crystal holes and demonstrating the complete reconfigurability that the microfluidic infiltration scheme offers.

Relevant Publications

[1]   C. L. C. Smith, U. Bog, S. Tomljenovic-Hanic, M. W. Lee, D. K. C. Wu, L. O'Faolain, C. Monat, C. Grillet, T. F. Krauss, C. Karnutsch, R. C. McPhedran, B. J. Eggleton "Reconfigurable microfluidic photonic crystal slab cavities," *Opt. Express* **16**, 15887-15896 (2008)

[2]   U. Bog, C. L. C. Smith, M. W. Lee, S. Tomljenovic-Hanic, C. Grillet, C. Monat, L. O'Faolain, C. Karnutsch, T. F. Krauss, R. McPhedran, B. J. Eggleton, "High-*Q* microfluidic cavities in silicon-based 2D photonic crystal structures," *Opt. Lett.* **33** 2206-2208 (2008)

[3]   M. W. Lee, C. Grillet, C. G. Poulton, C. Monat, C. L. C. Smith, E. C. Magi, D. Freeman, S. Madden, B. Luther-Davies, B. J. Eggleton, "Characterizing photonic crystal waveguides with an expanded *k*-space evanescent coupling technique," *Opt. Express* **16**, 13800-13808 (2008)

[4]   C. L. C. Smith, D. K. C. Wu, D. Freeman, Y. Ruan, S. J. Madden, and M. W. Lee, C. Monat, S. Tomljenovic-Hanic, C. Grillet, B. Luther-Davies, H. Giessen, Y.-H. Lee, and B. J. Eggleton, "Microfluidic Photonic Crystal Double Heterostructures," *Appl. Phys. Lett.* **91**, 121103 (2007).

[5]   M. W. Lee, C. Grillet, C. L. C. Smith, D. J. Moss, B. J. Eggleton, D. Freeman, B. Luther-Davies, S. Madden, A. Rode, Y. Ruan, and Y.-H. Lee, "Photosensitive post tuning of chalcogenide photonic crystal waveguides," *Opt. Express* **15**, 1277-1285 (2007).

[6]   C. Grillet, C. Monat, C. L. C. Smith, B. J. Eggleton, D. J. Moss, S. Frederick, D. Dalacu, P. J. Poole, J. Lapointe, G. Aers, and R. L. Williams, "Nanowire coupling to photonic crystal nanocavities for single photon sources," *Opt. Express* **15**, 1267-1276 (2007).

[7]   C. L. C. Smith, C. Grillet, S. Tomljenovic-Hanic, E.C. Mägi, D. Moss, D. Freeman, S. Madden and B. Luther-Davies, B.J. Eggleton, "Characterisation of chalcogenide 2D photonic crystal waveguides and cavities using evanescent coupling," *Physica B- Condensed Matter* **394**, 289-292 (2007).

[8]   C. Grillet, <u>C. L. C. Smith</u>, D. Freeman, S. Madden, B. Luther-Davis, E. C. Mägi, D. J. Moss, and B. J. Eggleton, "Efficient coupling to chalcogenide glass photonic crystal waveguides via silica optical fiber nanowires," *Opt. Express* **14**, 1070-1078 (2006).

Contents

List of Figures

Chapter 1

Introduction

1.1 Breakthroughs in material technology

Breakthroughs in material understanding have revolutionised technology throughout human history. The emergence of our ancestors into the Iron Age from the Stone Age marks a steadily increasing recognition of the utility of naturally occurring materials. Engineers soon discovered that additional advantages could be achieved by meddling with existing materials into more optimised forms, such as bronze alloys and concrete. Today, our society has access to a broad scope of man-made materials with selectable *mechanical* properties thanks to advances made in metallurgy, ceramics and polymers.

The twentieth century saw material advances expand their influence over *electrical* properties. Breakthroughs in semiconductor physics allowed for rapid and dynamic alterations of a material's conductivity, giving rise to the transistor – the fundamental building block of electronics. Societal impact resulting from the electronic revolution is difficult to overstate, with scores of electronic devices pervading many facets of daily living.

The last several decades have seen material influences extend yet further by controlling their *optical* properties. Whilst there were early advances in the form of mirrors, windows and spectacles, it was not until the development of the laser and fibre-optic cable that technological breakthroughs in optics truly began to shine. Recent years have observed the development of *photonic crystals* that can perfectly reflect or direct light. Indeed, a form of photonic crystal structure known as the *photonic crystal cavity* can even *confine* light within a nano-scale volume. A broad scope of applications and research tools are currently being explored with photonic crystal cavities, ranging from chip-based microprocessors to quantum electrodynamics experiments.
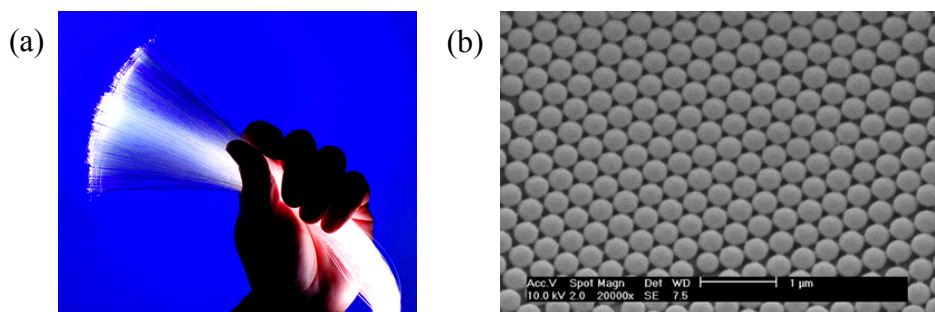
Figure 1.1. Materials to influence optics. (a) Image of a handful of optical fibres. This quaint amount of optical fibre contains enough transmission bandwidth capacity to meet the entire planet's demands for information. (http://www.techeblog.com/index.php/tech-gadget/how-its-made-optical-fiber) (b) Scanning electron microscope (SEM) image of a photonic crystal in polymer. (http://rryoo.kaist.ac.kr/res-3.html)

Increasing research interests in photonic crystal cavities have also given rise to a pursuit for their *reconfigurability*. The nanometer-scale parameters of photonic crystals in general make their fabrication cumbersome and complex, especially so when considering that cavities within photonic crystals are typically formed by extremely subtle variations in the photonic crystal geometry. An appropriate *post-processing* technique to correct for fabrication tolerances or optimise cavity parameters would therefore be greatly beneficial. Unfortunately, the capability to alter the otherwise fixed parameters in photonic crystals is certainly not trivial, as the solid material from which they are made allows for few options to reconfigure them. Despite this, the work contained in this thesis focuses on novel techniques to reconfigure photonic crystal cavities, aiming to promote an additional dimension to their versatility for the suite of applications to which they show remarkable promise.

1.2   Photonic crystals

Photonic crystals are periodic structures that affect the propagation of electromagnetic waves. Their phenomenon manifests naturally – such as in the play of colour on opal gemstones and iridescent butterfly wings. However, it is the artificial form of photonic crystals that receives the greatest research interest. Recent advances in lithographic techniques have enabled the engineering of photonic crystal properties on the nanometre-scale, allowing them to control visible and infrared light. This newfound capability has resulted in photonic crystals emerging as a promising tool for an extensive list of applications, such as ultra-fast information processing, integrated sensing architectures and research into fundamental light-matter interactions.

Figure 1.2. Naturally-occurring photonic crystals. (a) Image of an opal gemstone (http://opaltreasures-rainbowdreams.com/shop/index.php?cPath=22_82). The iridescent play of colour on its surface is a result of the gem's inherent periodic lattice structure. (b) Image of a genus morpho butterfly. (http://technology.newscientist.com/article/dn10006) These butterflies have a periodic cell structure within their wings that give rise to the striking iridescent colouration.

Science has studied the behaviour of photonic crystals for the last 100 years, although the term was first used after Eli Yablonovitch and Sajeev John published two milestone papers in 1987 [2, 3]. Prior to this, photonic crystals in the form of one-dimensional multi-layer dielectric stacks, such as the Bragg mirror, were studied in great detail. Lord Rayleigh showed in 1887 [4] that multi-layer dielectric stacks possess a spectral range of large reflectivity, which today is known as a photonic band-gap. This prevention of photon transmittance through a material is essentially the underlying basis behind the practical applications of photonic crystals.

The photonic crystal operating principle is analogous to the way in which the periodic potential of a semiconductor material affects electron propagation. Forbidden and allowed energy bands are defined in a photonic crystal by periodic modulation of its dielectric constant (i.e. refractive index). Providing sufficient contrast between the refractive indices and the absorption of the materials is minimal, high reflectivity can be obtained.

We are interested in two-dimensional (2D) photonic crystals, where the periodic modulation of refractive index is transposed onto a planar geometry [5, 6]. From this, two-dimensional photonic crystals can be divided into two general categories: low refractive index "holes" in a higher refractive index slab, or high refractive index "rods" in a lower refractive index environment (such as air). The research contained in this thesis predominantly focuses on the "holes in a slab" type of 2D planar photonic crystal, shown in Fig 1.3 (a).
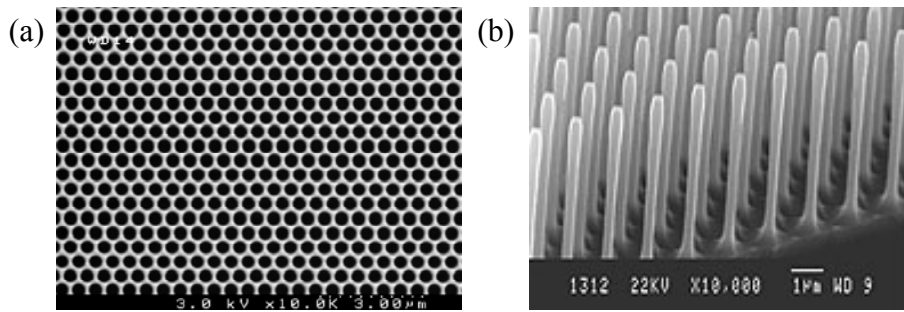
Figure 1.3. Two types of 2D photonic crystal. (a) SEM image of a photonic crystal with "holes in a slab" [7]. (b) SEM image of a photonic crystal with "rods in air" (http://www.electrumlaboratoriet.se/artikel/773/047004/en).

Photonic crystals may reflect the propagation of photons, and whilst this is all well and good, one seeks to go beyond that characteristic towards more sophisticated and meaningful functionalities. To achieve this, the photonic crystal lattice must be locally modified in some way – i.e. the formation of a *defect*. There are a variety of ways to introduce defects into photonic crystals, including changes of holes diameter, changes of holes position or removing holes completely from the lattice.

1.2.1   Photonic crystal waveguides

One of the requirements of a photonic system is for it to have a means of transporting its photons along a waveguide. This is necessary to integrate separate components of a system together and provide information to an end-user. The most common optical waveguide is the optical fibre, which by total internal reflection (TIR) allows highly efficient guidance through its central core. Waveguides can also be formed in photonic crystals via the introduction of a defect, generally exploiting the bandgap mechanism to provide confinement along the guide. Photonic crystal waveguides represent a potential technology to densely integrate photonic components, due to their tailorable dispersion and ability to strongly confine light on micron-scales.

Typically, photonic crystal waveguides are formed by the removal of a row of holes in a planar photonic crystal (Fig. 1.4 (a)), as they were in this work. A line defect from removing one row of holes is termed a "W1" waveguide. Their removal, however, is not always necessary. Waveguides may also be formed by reducing the holes size along the direction of propagation (Fig 1.4 (b)). In both cases, the *in-plane* guidance is caused by the photonic bandgap from the adjacent photonic crystal sections. Propagation is thus allowed along the defect. Careful design of these defects has shown that light can be directionally controlled around very tight, micro-scale bends [8].
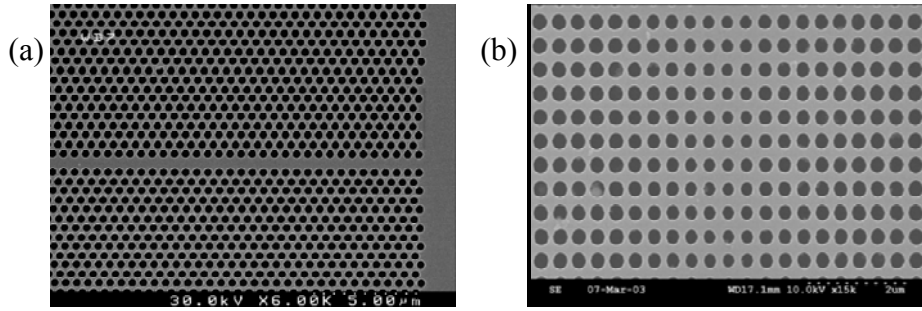
Figure 1.4. (a) W1 waveguide defect introduced into a planar photonic crystal
by removing a row of holes [9]. (b) Waveguide defect formed by reducing the
holes size in middle columns of the image [1].

However, there is then the question of how the *out-of-plane* (i.e. out of page)
confinement is achieved. In the case of 2D planar photonic crystals, this is achieved
by suspending the host material as a membrane within an environment of lower
refractive index. This provides a TIR confinement mechanism to maintain light along
the guide. The thickness of suspended membranes is an important factor, typically
around 150 – 300 nm, and together with the requirement to suspend them, their
fabrication can be considerably complex.

At this point, it is worth mentioning an additional noteworthy characteristic of
photonic crystal waveguides: their ability to dramatically reduce the *group velocity* of
light. The photons themselves are not slowed per se; rather, the photonic crystal
causes them to experience an effectively increased path length. This can be
problematic for the absorptive characteristics of photonic crystal waveguides
(approximately 100dB/cm); however, it can be advantageous for increasing the
interaction between photon and photonic crystal without requiring a proportional
increase in guide length. Importantly, a particular type of photonic crystal waveguide
– the photonic crystal cavity – can "hold" light in a mode that is localised in space for
volumes comparable to the light's wavelength.

1.2.2   Photonic crystal cavities

Optical cavities based on planar photonic crystals have earned much interest in recent
years. This is due to their ability to strongly confine light at a resonant frequency for
scales comparable to the light's wavelength. This trait has promoted their use in
numerous applications, offering the potential to carry out fundamental quantum
electrodynamics experiments [10-12] as well as realise seamless all-optical
functionalities such as channel-drop filters [13, 14], low-threshold lasers [15, 16],
optical switches [17-24], optical buffers [25, 26] and optical sensors [27, 28].

These applications for photonic crystal cavities mentioned above stem from their
ability to enhance the interaction between light and matter. Indeed, this characteristic
of photonic crystal cavities can be quantitatively measured in terms of both their

quality factor, Q, and modal volume, V. Figure 1.5 displays how photonic crystal cavities compare to other optical cavities (as of 2003). Significantly, cavity modal volumes in photonic crystals are much smaller than all other current optical cavity schemes. Whilst their Q-factors are comparably low in the presented table, the current world record of photonic crystal cavity Q-factor is approximately $Q = 2.5 \times 10^6$ [29] and rapidly approaching the values achievable in toroids – without the corresponding increase in modal volume.
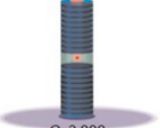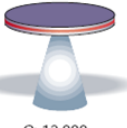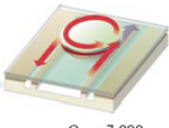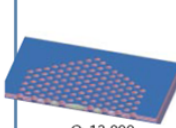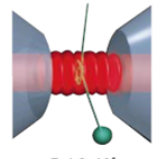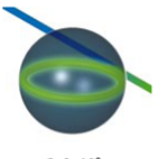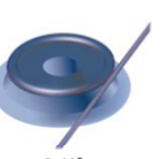
Figure 1.5. Comparison of different optical cavities (2003) for their quality factors and modal volumes [30].

Quality factor is a dimensionless numerical value attached to a resonator's ability to store energy, comparing the frequency for which a system oscillates to the rate at which the energy dissipates. A higher Q corresponds to a lower rate of energy dissipation relative to the oscillation frequency, implying that the oscillations "die out" more slowly. The average lifetime of a resonant photon in an optical cavity is proportional to the cavity's Q.

It is important for device design to make note that the different applications of photonic crystal cavities are interested in varied ratios for Q and V. In general terms (although not always the case), applications seek to maximise Q whilst minimising V. The following list outlines some example applications and their associated ratio of Q to V:

- Spontaneous emission control: Q/V

  - An optical cavity can enhance the rate of spontaneous emission from an embedded quantum dot by increasing its local density of modes. Q/V is proportional to the *Purcell Factor*.

- Nonlinear threshold devices: V/Q^2

  - The power threshold required to exploit nonlinear behaviour of a cavity's material is given by V/Q. The additional factor of $1/Q$ relates to the spectral width of the resonance and therefore the amount of nonlinear refractive index shift required.

- Optical sensing: Q/V

  - Increasing Q decreases the minimum detectable wavelength shift. Decreasing V reduces the amount of analyte necessary to generate a detectable signal.

- Quantum electrodynamics experiments: $Q/V^{1/2}$ [31]

  - For strong matter-photon coupling experiments, $Q/V^{1/2}$ is proportion to g/κ, where g is the atom-field coupling strength and κ is the cavity field decay rate.

The realisation of high Q's is limited by *parasitic* loss mechanisms. These losses can be due to various factors that include poor total internal reflection confinement normal to the plane of the photonic crystal and abrupt perturbations in the cavity mode field. Practical fabrication of photonic crystals may introduce irregularities that contribute to these, thereby resulting in a reduction of Q. As a consequence, fabrication quality of photonic crystals is an imperative for achieving high Q-factors.

1.2.3   Fabrication of planar photonic crystals

Recent advances in fabrication techniques of nanostructures have enabled the realisation of two-dimensional photonic crystal structures. To engineer photonic crystal devices to suit telecommunications wavelengths (1.3 or 1.55 μm) and thereby integrate them into existing technology, a refractive index modulation period in the 300-600 nm range is required. Exact values are dependent on the material refractive index, thickness and shape of the lattice unit cell.

As two-dimensional photonic crystal structures typically guide light in the third dimension by total internal reflection, an appropriate cladding (most commonly air) is chosen with a lower refractive index than the membrane. To make such a device it is

necessary to accurately perforate the photonic crystal slab over tens or hundreds of periods, and additionally produce very smooth wall surfaces. Defect guiding is also highly sensitive to fabrication errors due to the possibility of coupling to out-of-plane radiative modes. This effect can be mitigated by designing the structures to guide modes below the *light-line*, meaning that their effective index is higher than the cladding index so there is no phase-matching to radiative modes. However, practical devices will always involve spatial Fourier components that radiate out of the plane, so fabrication quality is crucial [32].

Photonic crystal slabs must be symmetrical to maintain orthogonality between TE- and TM-like modes. Without this condition when the photonic crystal lattice has only a partial (i.e. TE- or TM-only) bandgap, cross-coupling can transfer power to a lossy mode and thereby compromise device performance [33]. Symmetry in practice requires both vertical sidewalls and identical upper and lower claddings. An air cladding both above and below the photonic crystal structure is favoured to meet the latter symmetry requirement as it also helps to keep the defect modes below the light-line.

The photonic crystal samples in this work were made from chalcogenide, silicon or InP host material. Currently, most 2D photonic crystal structures are fabricated using electron-beam or photolithography combined with dry etching. Indeed, the silicon and InP samples in this work were fabricated by electron-beam lithography. Fabrication capabilities in silicon are well developed due to CMOS technology and research. This is not the case for other high index materials (such as chalcogenide), where novel techniques are being explored. The chalcogenide samples in this work were fabricated by focused ion beam milling.

The silicon photonic crystals in this work were fabricated in a manner similar to that of [34]. A wafer comprising of a 220 nm silicon layer on 2 μm of silica had a pattern exposed on top in an electron beam resist (ZEP520A) using an electron-beam writer (ZEISS GEMINI 1530/RAITH ELPHY) at 30keV. Pattern transfer into the silicon was formed by using reactive ion etching with CHF3 and SF6 gases. The silica beneath the photonic crystal was removed using HF acid while the rest of the pattern was protected with photoresist.

The chalcogenide photonic crystals were formed in 300 nm thick suspended membranes on a silicon wafer, similar to [7]. Suspension of the chalcogenide film was obtained by floating it onto a water surface, which was then captured by a copper mesh transmission electron microscopy grid and dried. The pattern into the chalcogenide was formed by milling the structure with a focused ion beam (FIB) of Ga^+ ions at an energy of 30keV. Redeposition of sputtered material is challenging for FIB milling of narrow and deep holes, which was alleviated in our samples by using a reactive gas.

The InP photonic crystals were fabricated with an InAs quantum dot ensemble embedded in the InP layer. The layers were grown by chemical beam epitaxy on semi-insulating (001) InP substrates with a Riber 32P deposition system. Electron beam lithography was used to write the pattern into a resist material. A series of etching processes translated the pattern into the InP. More details on the fabrication of the InP photonic crystals can be found here [35, 36]. The study of InP as the host material for photonic crystals is separate to the work contained in this thesis. As such, it is not discussed in further detail.

1.3   Chip-based architectures

The silicon microelectronic "chip" is ubiquitous in modern society. Much research has been undertaken to achieve this high technology and continues unabated. The advancement is driven by two major applications: switching technology for computers, and high-speed electronics for wireless telecommunications. Other compound semiconductor materials, such as GaAs, InP or III-V alloys, have played their part in the development of optoelectronic and purely photonic devices. Photonics, associated with signal generation, processing, transmission and detection, is formed by several principal components: lasers, waveguides, modulators, detectors and optical fibres.

Photonic devices rely on the interaction between light and matter, which occurs at much faster rates than typical processes involving electron mobility. However, photonics has a key disadvantage to microelectronics in terms of deployment, due very simply to the fact that chip scale integration of optical components is still in its primitive developmental stages. Neither the standardisation of processes nor the packaging of optical components, both necessary for repeatability and mass production, are available. Nevertheless, roadmaps forecasting the evolution of photonics are being drawn [37-39], where it is a commonly held view that the industrial model of microelectronics, if applied to photonics, will strongly benefit its implementation. Figure 1.6 illustrates recent photonic progress in terms of a 'capacity × distance' indicator. The "Optical Moore's Law" represents a faster growth than the original Moore's Law for integrated circuits.
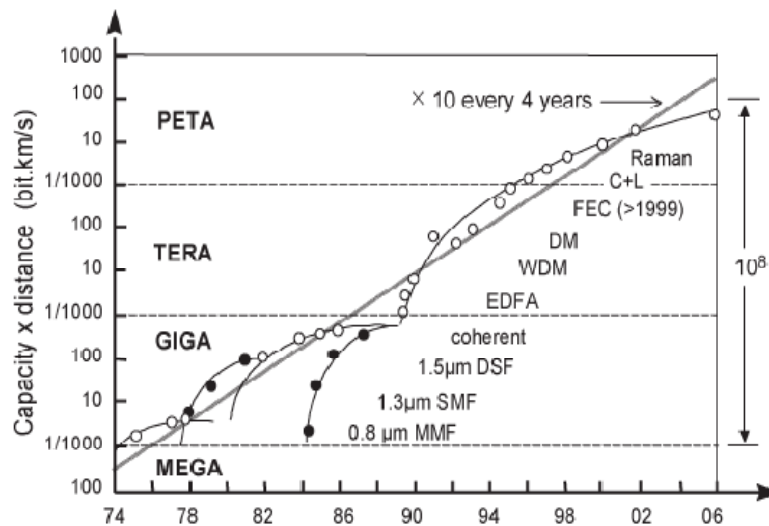
Figure 1.6. Graph depicting the growth of the Capacity × Distance indicator, highlighting an "Optical Moore's Law" corresponding to a factor of ten increase every four years [38].

On top of processing and communication speeds, optical-based devices are receiving much interest in terms of chemical analysis regimes. Optics provides a powerful scheme to monitor analytes due in part to the extensive array of existing photonic detection devices that are adaptive and precise. Employing these devices on a chip-based architecture, one can feasibly develop for portability for rapid and point-of-care medical diagnostics, widespread threat detection and environmental monitoring.

1.3.1 The photonic chip

The evolution of photonics towards extreme miniaturisation strives to integrate many optical components onto the same chip – the "photonic chip" (Fig. 1.7). The goal of such a device is to improve the speeds of both communication and processing. For example, if one were to assume current trends of a 13% per year increase in user demand, as the Atlantic route has recently experienced, an alarming "World Wide Wait" scenario would occur in approximately 2015 [38]. An effective photonic chip may allow for greater capacity and thereby prevent this problem. It could ideally incorporate both processing and transmission/detection on the one single efficient all-optical device.

Already, integrated all-optical signal processing devices are receiving significant research on the computer chip level. The issue of electrical interconnects between processors for intra and inter chip communication is seeking improvement. The reasons for this are due to bandwidth and power consumption. Photonic interconnect solutions are increasingly sought after for the development of 'server farms' and multi-processor CPU applications.
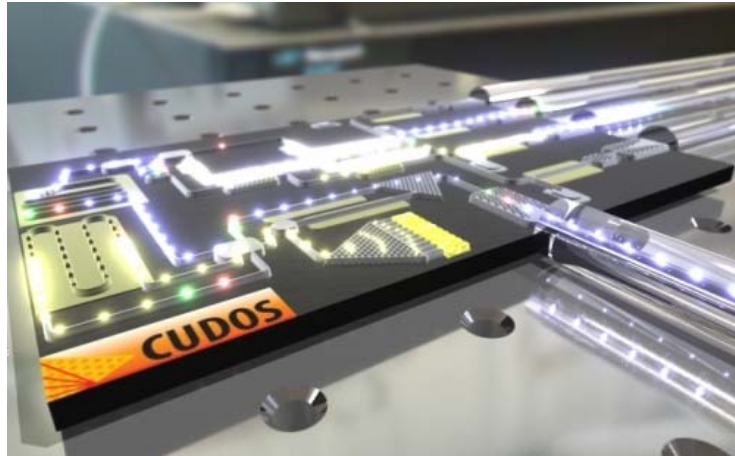
Figure 1.7. Artist's impression of a possible photonic chip. Many optical components are integrated on the one compact device, many of which are envisioned to be realised by photonic crystals.

To realise a photonic chip device, novel tools must be developed that possess the necessary capabilities to form functional components to satisfy the demands for compactness. This poses a significant problem, as the degree of tunability or range of refractive index variation required to create such devices is drastically increased by the corresponding reduction in device dimensions. Photonic crystals have emerged as one of the pre-eminent contenders to overcome these issues due to their nano-sized parameters and the capability to control light on the wavelength scale.

1.3.2 Lab-on-a-chip

Lab-on-a-chip is a particular growing field of research that aims at developing a monolithic device which incorporates one or several laboratory functions on a single chip (such as the example of Fig. 1.8). Lab-on-a-chip devices deal with the handling of extremely small fluid volumes, down to less than picolitres. They are a subset of microelectromechanical systems (MEMS) and are often termed as "Micro Total Analysis Systems" (μTAS). If one defines the lab-on-a-chip to be a device that is capable of performing all its functions and detection on a device that fits in the palm of your hand (or smaller), then existing devices are generally still underdeveloped [40]. Such miniaturisation requires an increased integration of elements to carry out predetermined functions, specifically for improved detection.
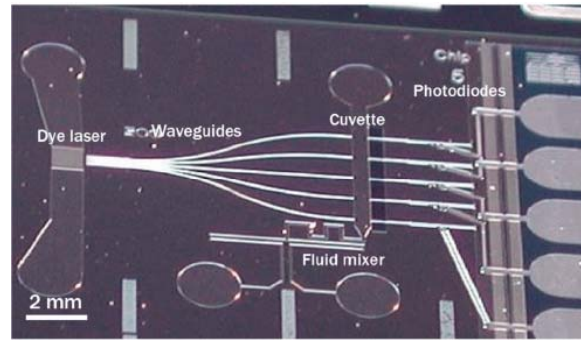
Figure 1.8. Demonstration of an optofluidic lab-on-a-chip that combines various fluidic and photonic elements [41].

The performance of optical detectors is important for the lab-on-a-chip paradigm, especially considering the increasing demands placed on detectors as volumes decrease. Many current analytical instruments have optical detectors made up of components in various materials, mounted in free space on an optical bench or a similar system along an optical axis. Ideally the optical information would be extracted on-chip, reducing complexity and offering device flexibility. The two major problems to overcome for this are sensitivity and scalability. Use of photonic crystals for realising lab-on-a-chip applications are proving to be a promising approach [42], due to their ability to potentially address both these issues. On one hand photonic crystals can be tailored such that they are highly sensitive to subtle changes of refractive index, whilst on the other hand they control light on the wavelength scale; a property which is profoundly scalable.

On top of this, a method to reconfigure a device would create additional versatility, allowing a scheme to optimise a device to suit a particular function, or to change the device configuration completely for an entirely separate function. The integration of photonics with microfluidics (termed optofluidics) is investigating this concept to develop a variety of components for adaptive chemical analysis. The advantage offered by the introduction of fluids to photonics is that fluids are inherently mobile. This provides a means to easily adjust local optical properties in a reconfigurable fashion without degrading the device after use or adjustment. In addition, the fluids (or fluid cocktails) could themselves possess additional functionality, as liquid crystals [43-46], or by containing active or nonlinear components.

1.4   Nonlinear photonic crystals

Numerous studies have been devoted to photonic crystals as controllers of light and the realisation of a variety of useful components. The operating principle is similar to how the periodicity of semiconductor atomic lattices may prevent or allow the flow of electrons. In the case of photonic crystals, the periodicity is formed by a dielectric

modulation. However, the analogy should not be pushed too far. Photons are not subject to Coulomb interactions, like their electron counterparts, and as such are not as easily controlled. Consequently, photonic crystals are not easily tunable. It is therefore natural to consider photonic crystals formed in nonlinear host media, which enables a method to create a functional component.

Several interesting phenomena have been numerically and experimentally demonstrated in nonlinear photonic crystals: gap solitons [47, 48], band-edge bistability [49] and low-threshold lasers [50, 51]. The nonlinear properties of the materials allow for a dynamic change in the system to occur. In particular, intense research has embarked on the pursuit for all-optical switching [17-24] and buffering [25, 26] in photonic crystal cavities, both of which are launched on the trajectory towards photonic circuitry.

1.4.1 All-optical switch

One of the critical components necessary to develop a photonic chip its capability to process high data rate optical signals is the all-optical switch – often termed the "photonic transistor", where light switches light. Early predictions for nonlinear compact photonic crystal cavity switching showed necessary power levels of only several mWs [17, 19]. More recent demonstrations have shown power levels of only µWs [25], with cavity volume absorption energies at several fJs. This contrasts with modern general-purpose electronic CPUs which consume power on the order of 10s of Watts. Developing all-optical logic gates by combination of photonic crystal cavities with highly nonlinear material opens the prospect of integrated photonic devices with design flexibility. This could be useful for novel functionalities, such as all-optical switching arrays in significantly reduced package sizes.

Photonic crystal cavities containing "Kerr" nonlinear material, where the refractive index of the material is intensity dependant, show much promise. Kerr nonlinearity is given by:

$$n_{eff} = n_0 + n_2 \times I, \tag{1.1}$$

where n_{eff} is the effective refractive index of the mode, n_0 is the linear refractive index, n_2 is the nonlinear Kerr coefficient (a third-order term) and I is the electric field intensity in the cavity. By increasing input power, the intensity inside the cavity increases and is magnified by its Q factor. This magnified intensity in turn affects the material's refractive index, thereby shifting the resonance to different wavelengths. A transfer function describing such a system would observe an abrupt change – switching – between two states for a certain power threshold. This threshold can be minimised by using a highly nonlinear material (with a high n_2 coefficient) and a

13

high-Q cavity to enhance the light-matter interaction. Such devices could form all-optical logic gates or photonic transistors.

The underlying principle to realise nonlinear all-optical switches is the concept of bistability [52, 53], illustrated in Fig. 1.9 (a) [20]. For systems that display optical bistability, the outgoing intensity is a strong nonlinear function of the input intensity, possibly even displaying a hysteresis loop. Photonic crystals offer a flexible method to achieve bistability due to their ability to provide controlled directionality and resonant feedback of an optical mode, as illustrated in Fig. 1.9 (b).
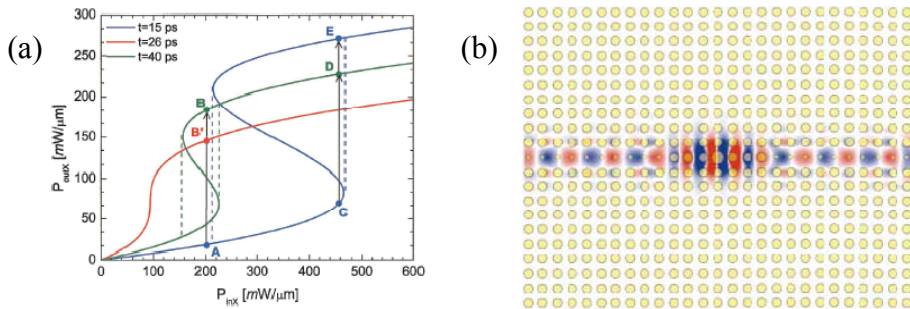
Figure 1.9. (a) Input versus output power for a photonic crystal cavity switch, illustrating bistability. The red, green and blue curves correspond to different control output powers at different times of the switching process [20]. (b) Electric field for a photonic crystal bistable switch at 100% resonant linear transmission. The device illustrated consists of a resonant cavity in photonic crystal coupled to two waveguides serving as input and output ports [19].

A suitable nonlinear material is required to create photonic crystal switch devices. The development of optoelectronic devices often uses III-V semiconductors, such as GaAs and InP, however the work of this thesis concentrates on two promising materials: silicon and chalcogenide. Where chalcogenide is a material receiving renewed interest due to its remarkable optical properties, such as its Kerr nonlinearity, silicon enjoys a well established and mature fabrication industry. In their different ways, both silicon and chalcogenide have much to offer to the frontiers of photonic crystal research.

1.4.2 Silicon & Chalcogenide glass

There are a variety of materials available to create nonlinear photonic crystals. These include III-V semiconductors such as InP and GaAs. The work contained in this thesis is primarily concerned with two materials: silicon (a semiconductor) and chalcogenide (an amorphous glass).

Silicon has received a significant body of photonic research due in no small part to the presence of a fifty-year-old electronic industry that has matured fabrication processes (i.e. CMOS compatible). Functional photonic devices in silicon could be readily

mass-produced and seamlessly integrate with current technologies. Silicon also possesses several key characteristics that make it advantageously suitable for photonic applications.

Silicon, widely used as the basis for electronic applications, has revealed itself as transparent at optical telecommunications wavelengths, clearing the way for its use in photonic applications. Silicon has a high refractive index of $n \approx 3.5$ at 1.55 μm wavelengths, a crucial ingredient for realising ultra-high Q photonic crystal cavity devices [21]. In addition, it is a highly nonlinear material, up to 300 × that of silica, enabling it to be used as a nonlinear component – for example an all-optical switch.

One major hurdle to overcome for silicon photonic applications is the presence of free charge carriers at the atomic level. The nonlinear refractive index modulation used for bistable operation typically occurs by carrier generation resulting from a process termed as two-photon absorption. Free carriers become responsible for a lower bound on switching speeds of ~100's ps, due to a finite time for the charges to diffuse [22, 23]. A technique to overcome the issue of free carriers in silicon has been demonstrated, described as "carrier killing", which doped the nanocavity with Ar^+ ions and reduced switching times to ~70 ps [18]. Comparatively, modern silicon electronic switching speeds clock at approximately 3 GHz (~100's ps), whilst III-V semiconductor based photonic crystal cavity devices have been demonstrated to switch at ~10 ps [24].

Chalcogenide glasses have generated much interest toward the goal of a photonic chip due to a swathe of attractive properties [54]. Chalcogenide glasses are an amorphous transparent material in the infrared containing the chalcogen elements S, Se or Te, combined with network forming elements such as As, Si and Ge. The refractive index of chalcogenide is high (for a glass), typically between 2.4 and 3.0, allowing photonic crystals to be formed. Absorption losses are low over a wide wavelength range (near-to mid-infrared). They possess a relatively high third-order optical nonlinearity (100 – 1000 times that of silica), and low two-photon absorption, which together translate into very low switching power requirements. The nonlinear figure of merit (FOM = $n_2 / \alpha\lambda$, in which α is the two-photon absorption coefficient) is used to classify different nonlinear materials, and for some chalcogenides (such as As_2S_3) it is higher than 12 at telecommunications wavelengths (compared to less than 1 for silicon) [55]. Perhaps most importantly, the pure Kerr-like nonlinearity of chalcogenide glass offers the potential for near instantaneous response times at < 100 fs. The only limitation of these devices would then be the cavity Q factor, since a greater photon lifetime in the cavity would limit response times. Nevertheless, chalcogenide glass photonic crystal cavities could potentially form the basis of ultra-fast and low threshold power all-optical switches.
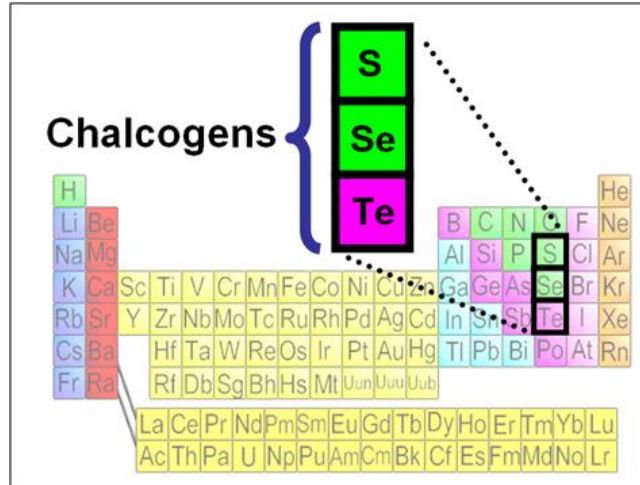
Figure 1.10. Periodic table highlighting the region containing chalcogens.

Chalcogenide glass photonic crystals may be processed by conventional lithographic techniques. Compared to silicon, fabrication technologies for chalcogenide glasses have had much less time to mature. As such, they suffer increased roughness, poorer sidewall profiles and higher optical losses. Nevertheless, high quality chalcogenide glass photonic crystals are being processed with significant quality improvements and are given an optimistic outlook [56].

Single-photon-sources and the Purcell Effect

Single quantum dots – semiconductors whose excitons are confined in all three spatial dimensions – have generated much research interest in recent years due to their atom-like emission. Not only are they capable of emitting triggered single photons [57-60], but they may be embedded within micro-scale cavities [30] that can channel the single photon emission. Such a combined quantum dot / cavity system has the potential to realise efficient single photon sources at telecommunications wavelengths – in other words, a key enabler for quantum key distribution (quantum cryptography) and quantum information processing devices [31, 61]. Such devices would depend highly upon the efficiency to which the photons can be extracted, which can be addressed in two ways: (i) redirection of the quantum dot emission into a single cavity mode and (ii) collection of the photons from the cavity mode to the outside world.

The first point may be addressed by the fact that cavities can funnel a large fraction of the quantum dot emission into an available cavity mode. This emission may then be enhanced by the cavity through the *Purcell Factor* [10], which is given by

$$F_p = \frac{3Q\left(\frac{\lambda}{n}\right)^3}{4\pi^2 V},$$ (1.2)

where F_p is the Purcell Factor, Q is the observed quality factor of the cavity mode, λ is the wavelength of the cavity mode, n is the effective index of the cavity mode and V is the cavity modal volume. One important point to note is that the Purcell Factor is proportional to Q/V. The Purcell Factor represents the maximum possible enhancement of the quantum dot spontaneous emission rate into the cavity mode and requires precise spectral alignment between the quantum dot and cavity resonance.

The second point, relating to coupling from the cavity to the outside world, has two main approaches. The first is collecting part of the intrinsic optical losses of the mode from the cavity using collection optics. The second is introducing an additional channel of escape for the photons. This second approach is investigated in [62], which on top of providing a means to extract light from a cavity mode, enables a subtle way to both probe and tune the cavities without requiring anything to be done to the already processed sample.

1.5   Characterising photonic crystal structures

Characterisation of photonic crystal structures is by no means a trivial task. The micron-scale size of photonic crystal structures represents an immediate difficulty, especially so when considering the nano-scale dimensions of components within the photonic crystal. The most common medium of optical signal transport – the optical fibre – guides its light through a core that is 8 μm in diameter. Coupling light from a standard optical fibre into a sub-micron device is therefore inherently inefficient. This is not only a result of the size mismatch, but also the optical mode profile mismatch and the differences in effective refractive index.

1.5.1   Coupling techniques

Various techniques have been employed in recent years to overcome the difficulty of coupling to micron-scale photonic structures. One method is via the use of a tapered input waveguide [63, 64]. An extended wire from the photonic crystal has its profile tailored to both efficiently collect light from a standard optical fibre and then insert it to within the photonic crystal waveguide (Fig. 1.11). Another method employs perpendicular coupling to either a 1D or 2D photonic crystal by using a grating coupler [65].
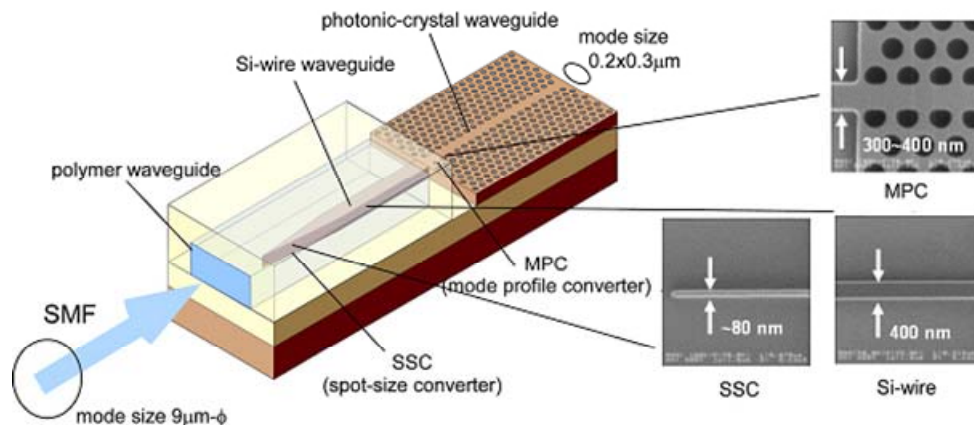
Figure 1.11. Tapered input waveguide to improve insertion efficiency into the photonic crystal [64].

However, both techniques mentioned above have their drawbacks, either by the necessity of creating additional input structures at the fabrication stage – the tapered input waveguide – or a lack of coupling efficiency – the grating coupler. A method to probe photonic crystal structures that overcomes both these difficulties would therefore be highly advantageous.

1.5.2 Evanescent coupling

This thesis utilises evanescent coupling to insert light within micron-scale photonic structures. A silica optical fibre has its dimensions reduced by approximately two orders of magnitude, creating a "nanowire" that allows for significant near-field interaction to occur between the reduced-size fibre and the target device. There are numerous groups interested in nanowire evanescent coupling [1, 9, 66-73]. Knight *et al* [66] describes the first realisation of evanescent coupling to a microcavity, which was a relatively large mode volume glass microsphere cavity. Srinivasan *et al* [67, 68] represents the first realisation of tapered fibre coupling to a wavelength-scale semiconductor cavity, which in these cases were a photonic crystal defect cavity. The differences between [66] and [67, 68] lie in the microcavity material (glass versus silicon), geometry (microsphere versus photonic crystal) and mode volume (hundreds of cubic wavelengths versus less than one cubic wavelength). Hwang *et al* [69] demonstrates evanescent coupling from a nanowire utilised to pump an InP photonic crystal microlaser and to collect its emission. Kuang *et al* [70] theoretically discusses coupling to a photonic crystal waveguide. Barclay *et al* [1] claims the first experimental demonstration of taper-photonic crystal waveguide coupling, with [71] and [72] presenting detailed experimental results on the topic. Coupling to photonic crystal waveguides using the evanescent coupling method has reached efficiencies of over 90% by Barclay *et al* [73]; in more recent work in this thesis, an insertion efficiency of 98% is obtained (albeit 6dB of broadband loss) [9].

1.5.3 Fabricating nanowires

Fabricating the coupling nanowires involves a process that adiabatically reduces the outer diameter of a silica single mode fibre (SMF-28) from 125 µm down to ~1 µm (Fig. 1.12). This is achieved by using a "flame brushing" technique that locally heats a section of the fibre with a butane flame. Whilst the fibre is heated, stages that hold the fibre move outward simultaneously, stretching the silica down to its reduced dimensions. The taper length and profile is tailored by the appropriate choice of flame brushing profile and both elongation rate and elongation length. More details of this are given in Chapter 3.
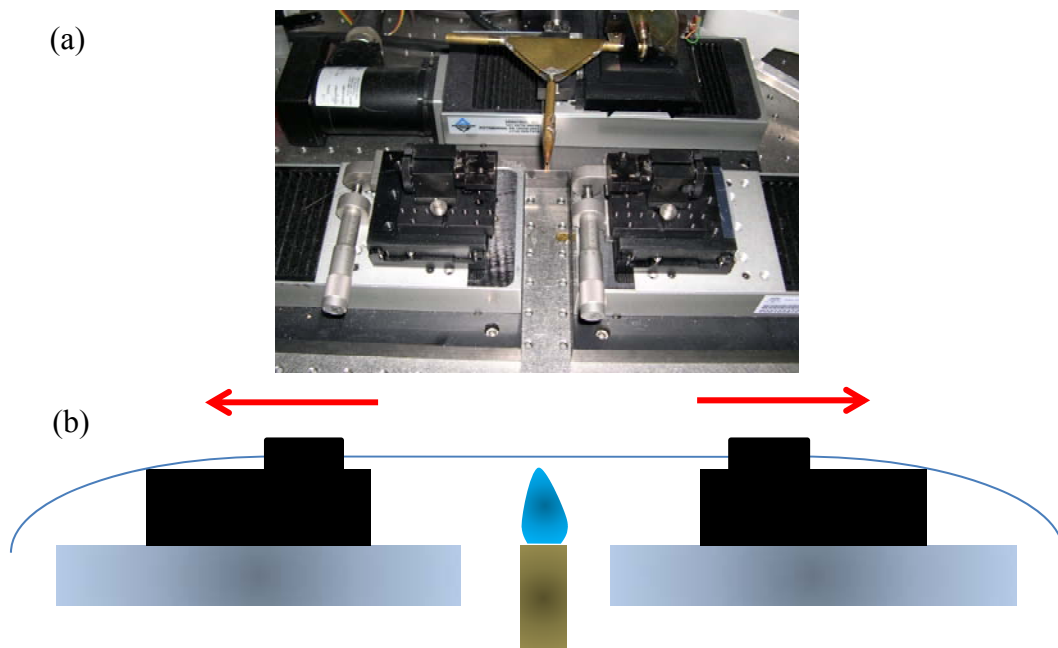
Figure 1.12. (a) Image of the taper station used for work in this thesis. (b) Schematic depicting the tapering process. Two clamps on motorised stages hold and stretch an optical fibre whilst it is heated by a butane flame. In operation, the taper station of (a) is covered by a housing to minimise air flow.

The reduced dimensions of the tapered nanowire cause the fibre to act as the core with the surrounding air becoming the cladding. The air cladding mode of the tapered fibre then exhibits an evanescent tail which expands out of the silica nanowire waveguide and into the surrounding air. Due to the fact that light transport is ensured by the evanescent wave guiding, the ratio of light in the evanescent field becomes high enough to respond to the surrounding environment. This allows tapered nanowires to not only be useful for communicating with micro-scale cavities, but also for miniaturised optical sensors with high sensitivity [74].

1.5.4   Utilising nanowires

How the nanowires are used is depicted in Fig. 1.13 (a). A glass microscope slide with two bolts attached is stationed above the photonic crystal sample. The nanowire is then fixed to the bolts by epoxy resin and allowed to suspend over the device. Select evanescent coupling to photonic crystal waveguides is achieved by inducing a bow shape into the nanowire to prevent unwanted coupling to the wafer substrate. Coupling to a much smaller photonic crystal cavity requires an even more localised coupling. This is achieved by inducing a micro-loop into the nanowire, as shown in Fig. 1.13 (b).
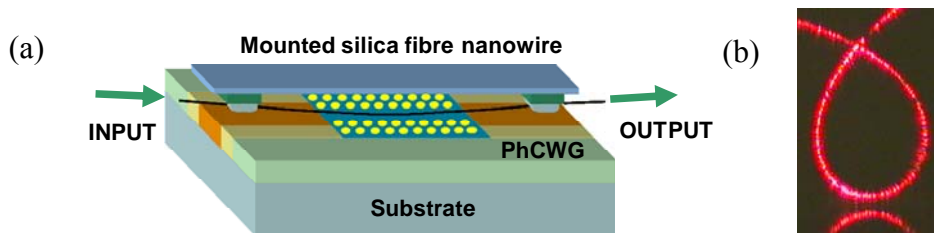
Figure 1.13. (a) Schematic of the evanescent coupling setup. The nanowire is connected to a glass slide via epoxy resin to pre-attached fixed bolts. (b) A tight micro-loop is induced into the nanowires to localise coupling to micron-scale photonic crystal cavities. HeNe (633 nm) laser light is sent through the loop for visibility.

The tightly curved micro-loops may not only selectively couple to photonic crystal cavities but also allow for interesting information to be obtained from the structures. The highly curved tapers result in an expanded distribution of taper modes in k-space. K-space, also known as reciprocal space, has units of inverse length and is the variable axis of a *dispersion relation*. Dispersion relations are a common method to characterise photonic crystals, which portray the frequency dependence (dispersion) of electromagnetic propagation into their structure. Increasing the distribution of a taper mode in k-space allows a greater frequency range of photonic crystal modes within which they may be coupled. Observing a large spectral profile of photonic crystal modes provides information on the dispersive behaviour of the photonic crystal structure, as depicted in Fig. 1.14. This suggests evanescent coupling via tightly curved micro-loops is a promising method for non-invasive characterisation of a photonic crystal device. More details of the above characterisation are given in the following chapter.
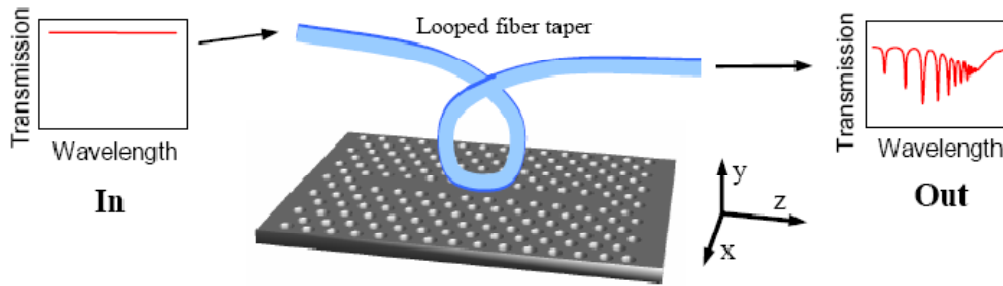
Figure 1.14. A schematic of the setup used to characterise a closed photonic crystal waveguide. A highly curved nanowire is brought into close proximity with the photonic crystal structure and the transmission spectrum through the fibre is monitored. Dips in the spectrum appear where light is coupled from the taper into the waveguide.

1.6   Optofluidics

Optofluidics is an emerging field of research that integrates photonics with fluids [75, 76]. Fluids possess characteristics that cannot be obtained in solids, and by exploring these one can design novel devices. Examples of exploitable fluid characteristics include: the ability to change the optical property of the fluid medium within a device by replacing one fluid with another; the optically smooth interface between two immiscible fluids; and the ability of flowing streams of miscible fluids to create gradients in optical properties by diffusion. Whilst the majority of optical devices and components are currently formed by solid materials, there are cases in which it has been advantageous to use fluids. Liquid crystal displays [77], liquid mirrors in telescopes [78] and electrowetting lenses [79] are prime examples.

Recent methodologies that have been advanced implement optofluidic devices with microfluidic technologies. This allows accurate manipulation of fluids on very small spatial and volume scales, as shown in Fig. 1.15. Integration and reconfigurability are two key advantages for the optofluidic paradigm, since microfluidics has opened up the possibility to incorporate multiple fluidic tasks onto a single chip. Photonic components such as the light source, lenses, waveguides and sensors, which were previously off-chip, can now be realised on the one compact device by building the optics from the microfluidic toolbox: the optofluidic lab-on-a-chip.
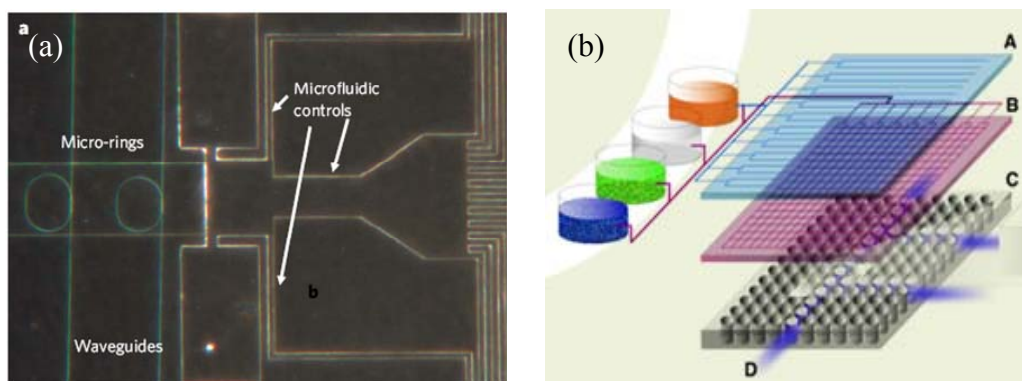
Figure 1.15. (a) Image of a chip-based device with the integration of complex microfluidic components [80]. (b) Generalised layer construction of an optofluidic device. There are typically 3 layers: (i) the microfluidic controls; (ii) the microfluidic channels; and (iii) the optical structure, for example photonic crystals (http://www.optofluidics.caltech.edu/optofluidics/index.html).

1.6.1 Microfluidics for optofluidics

Microfluidics is a field of research with important applications in biotechnology, chemical synthesis and analytical chemistry. There is an extensive body of literature on how the physical properties of fluids on small scales can be used for device functionality [81-83]. Many of these interesting effects can be harnessed to control optical properties, and technological advances in fabrication processes have made it possible to make miniaturised devices capable of integrating complex networks of channels, valves, pumps and other forms of microfluid manipulation. Due to the large range of index modulation achievable through fluid manipulation, which can be induced locally by using microfluidic circuitry, there is a benefit to using fluids. Strong potential is also apparent to develop accurate sensors that can detect subtle changes of fluid index for sub-µL volumes. Indeed, a large market is anticipated for *portable* microfluidic sensor devices in lab-on-a-chip formats for environmental monitoring, medical diagnostics and chemical-weapon detection [76].

Significantly more attention has been given to fluid behaviour on lab-on-a-chip architectures than to the detection aspects [42]. This is because many detection principles are hard to implement and do not scale favourably down to corresponding sizes. As a result, fluorescence detection has been a method of choice for miniaturised systems, despite its requirement of a cumbersome labelling process. More recently, label-free optical resonators have become the preferred approach. These include ring resonators [84, 85] and photonic crystals [86-89]. Nunes *et al* [88] recently investigates a one-dimensional photonic crystal resonator integrated within a microfluidic system, as shown in Fig. 1.16. Here, pillars are used rather than holes in order to allow liquid to be pumped into and through the cavity.
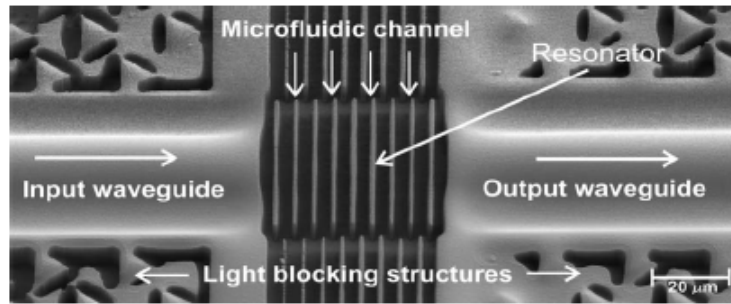
Figure 1.16. Scanning-electron-microscope image of an on-column 1D photonic crystal refractive index chemical sensor [88].

Erickson *et al* [89] combines soft lithography-based nanofluidics with silicon nanophotonics, creating a nanophotonic layer, a nanofluidic delivery structure, and a microfluidic control engine, as shown in Fig. 1.17. This scheme allows selective targeting of a liquid to a row of holes in the photonic crystal, thereby enabling high $\Delta n/n$ (~0.1) refractive index tuning. Variations of such a technique could enable selective introduction of optical nonlinearities or delivery of single molecules into resonant cavities for detection. A foundation for the development of dynamic reconfiguration of photonic circuits is established in this work.
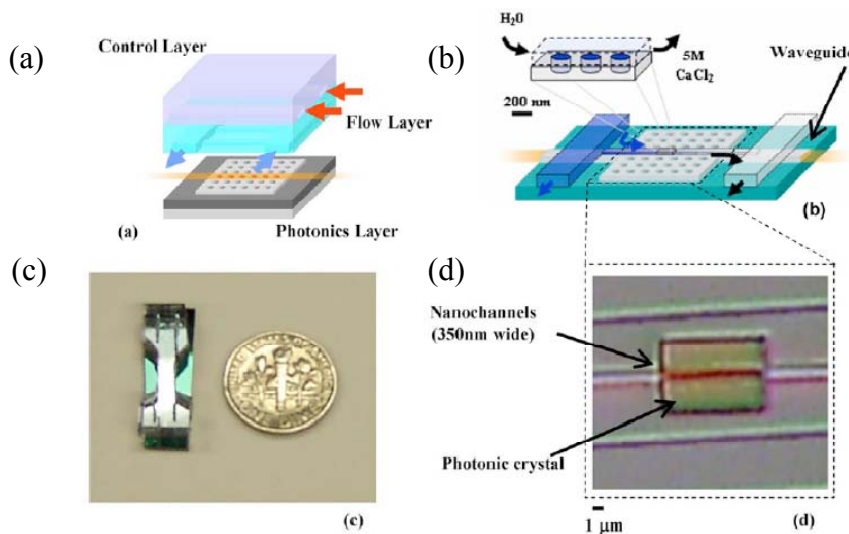
Figure 1.17. Nanofluidically tunable photonic structures [89]. (a) Exploded view of the opto-fluidic assembly showing the lower photonic layer, central fluidic layer and control top layer. (b) Overview of device operation. The microfluidic control engine mixes and dispenses liquid plugs to the nanofluidic array. The nanofluidic structure serves to deliver liquids directly into a targeted row of holes in the photonic crystal, enabling localised, high $\Delta n/n$ refractive index tuning. (c) Photograph of an assembled chip next to a "dime". (d) Optical image showing overlay of nanochannels with photonic crystal.

1.7   Reconfigurable photonic crystal components

A growing body of scientific literature is investigating the possibility of *reconfigurable* photonic crystals [36, 43-46, 89-106]. The pursuit is to increase device functionality by adjusting the photonic crystal properties after fabrication, either to relax fabrication tolerances or allow for optimisation of existing components. On one hand there is the possibility to tune photonic crystals via modulation of the host material refractive index, such as by thermo-optic approaches [90], post-process chemical treatments [36], mechanical deformation [91], mechanical perturbation by atomic force microscopy tip [92], or, as explored in this thesis, exploiting the material's photosensitivity [93]. Similar approaches may also include introducing additional features during the fabrication stage such as fluids in nanochannels (as mentioned in the previous section) [89, 94, 95] and depositing a thin photosensitive chalcogenide strip over the photonic crystal [96]. On the other hand there have been demonstrations showing post-trimming and tuning of photonic crystals by infiltrating the pores with organic materials, such as liquid crystal [43-46] and polymer [97-101], and inorganic materials, such as fluorescent dye [102] and, pertinent to this thesis, microscopy oil [103]. Theoretical studies have suggested that selective infiltration of only a few holes in the photonic crystal can provide an alternative approach for realising compact photonic integrated components, for example single-mode waveguides, broadband low-reflection bends, crossings and splitters [104, 105], and high Q cavities [106].

1.7.1   Photosensitive photonic crystals in chalcogenide glass

One post-process tuning technique to modify the optical properties of a planar photonic crystal device is by the utilisation of photosensitivity within chalcogenide glass [56, 93, 107]. Prior to [93], chalcogenide photosensitivity was successfully demonstrated for the creation of directly written waveguides [108-110], strong Bragg gratings [111], and for the post-tuning of optical components such as distributed feedback lasers [112] and quantum cascade lasers [113].

The photosensitivity of the chalcogenide glass is known to stem from structural rearrangements induced by the absorption of light at frequencies near the absorption band-edge of the material [114]. As a result of the structural rearrangements, changes in the properties of the glass can occur, such as its refractive index and density. The magnitude and sign of the photoinduced changes are often highly dependent on the chemical composition of the glass [115] and on the processing history of the sample [116]. These changes may be reversible or irreversible, with irreversible changes resulting from what is termed "photo annealing" of thin films deposited in a non-equilibrium state [117], and reversible changes resulting from structural rearrangement into a quasi-stable state from exposure [116, 117].
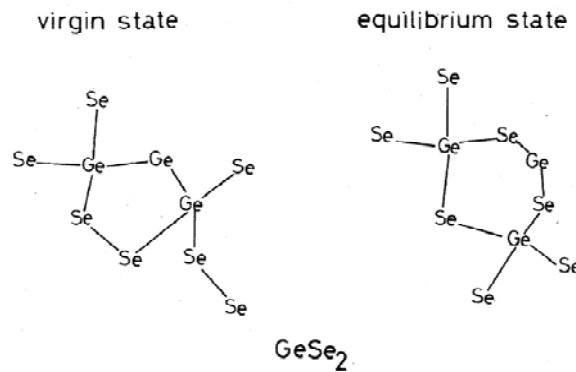
Figure 1.18. Two-dimensional representation of the random-network model appropriate to GeSe$_2$ chalcogenide for the system in virgin state (pre-exposed) and equilibrium state (post-exposed) [115].

Photonic crystal components may be post-processed in chalcogenide glass photonic crystals by exposing the samples to light at frequencies at which the material absorbs. The material's photosensitivity will thereby result in a change in refractive index – as was demonstrated in [93] in chalcogenide glass photonic crystal waveguides. It is possible to translate this to photonic crystal cavities, either by tuning their properties or even potentially *forming* a cavity.

The capability to tune or create a photonic crystal cavity resonance is vital to support numerous applications. For example, the double-heterostructure cavity [21], which shows remarkable promise for achieving ultra-high Q resonances, relies on precise engineering of the lattice constants along a line defect. Local adjustment of the lattice parameters allows for light confinement due to a change in effective refractive index of the defect mode within that region. Similarly, it is feasible to consider forming a double heterostructure cavity by exposing a local region of a photosensitive material photonic crystal waveguide. Modelling suggests that a Q-factor of ~30,000 is achievable in chalcogenide glass by inducing a refractive index shift of 0.01 [118]. A general design rule has been proposed [119] where the form of the cavity electric-field distribution should slowly vary, most ideally by a Gaussian function to suppress out-of-slab photon leakage. Such a profile would be readily possible by laser-spot exposure to the photosensitive material, potentially extending the ~30,000 Q-factor prediction dramatically.

An example where the photosensitivity of chalcogenide glass photonic crystals has served practically is in the demonstration of tuning a cavity resonance for quantum electrodynamics (QED) experiments [96]. Consider single photon source applications, where single quantum dots housed within photonic crystal cavities are to be enhanced via the Purcell Factor of the cavity mode. It is critical that the spectral resonances of the quantum dot and the photonic crystal cavity are precisely aligned, however that is

most often not the case. The photosensitive post-processed technique allows for tuning the cavity to match the resonances, suggesting the potential use for exploiting this effect in QED experiments and other fields of research.

1.7.2 Microfluidic photonic crystal cavities

The introduction of micro- or nano-scale fluids to photonic crystals is a promising way to reconfigure the system. Similar in method to the photosensitive post-processing of photonic crystals, the introduction of a fluid results in a change of effective index for optical modes that overlap it. As a result, one obvious difference between the two techniques is the perturbation of the lattice in the microfluidic regime occurs where the fluid has penetrated the pores, rather than an induced change in the host material. An immediate advantage is that due to the mobility offered by fluids, one can potentially achieve highly versatile and reconfigurable devices that would not degrade after use.
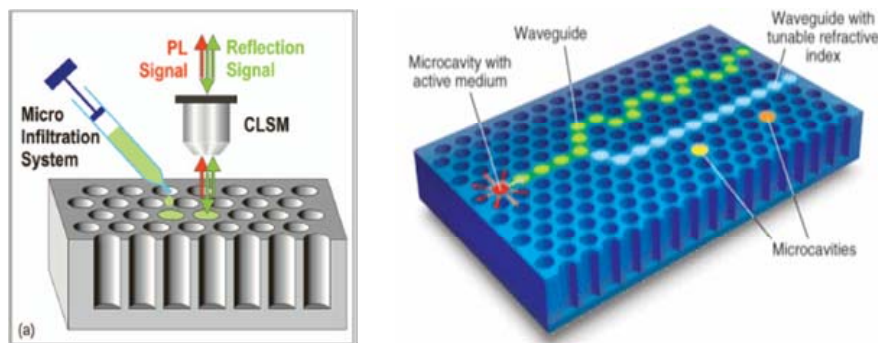
Figure 1.19. Rewritable photonic crystal circuits using fluids to infiltrate the lattice holes "pixel by pixel" [102].

The rewritable / reconfigurability aspect offered by the fusion of microfluidics with photonic devices – optofluidics – has already received a surge of research interest [89, 94, 120-125] in recent years. In addition to this, there is also the potential to develop highly sensitive integrated sensors [27, 41, 126]. In both regards, it has been shown that photonic crystals in general [94, 120, 126] and photonic crystal cavities in particular [27, 28, 86] can be advantageously exploited within optofluidic architectures. The advantage of combining photonic crystal cavities with optofluidics is the potential for high light-liquid interaction to occur when infiltrating the air holes that typically surround and / or form the defect.
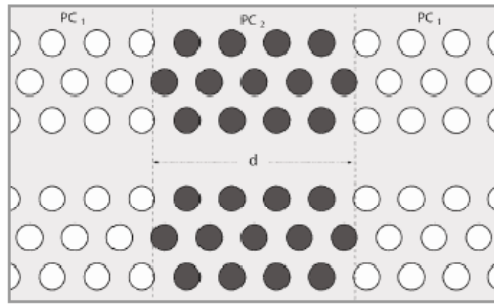
Figure 1.20. Schematic of a photonic crystal double heterostructure formed in a W1 waveguide in the Γ-K direction by air-holes infiltration. Refractive index distribution in the plane of the structures is considered.

Double heterostructure defects can be induced within the photonic crystal lattice by infiltrating a select, local region of holes with a fluid, as shown above in Fig. 1.20. The infiltrated region gives rise to optical modes that have a greater effective index than the surrounding, uninfiltrated photonic crystal optical modes. Similar to forming double heterostructures in photonic crystals via exploiting a photosensitivity processes, this microfluidic approach immediately overcomes one of the major drawbacks from geometry-based double heterostructures, where fabrication precision is critical. This postprocessing technique has the potential to realise arbitrarily-defined photonic crystal components, offering unprecedented flexibility in terms of device geometry and fluids involved, as illustrated below in Fig. 21.
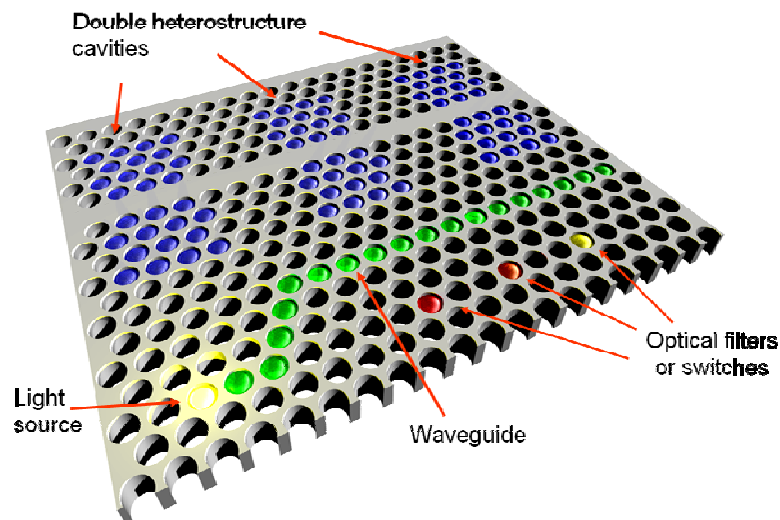
Figure 1.21. Illustration of a sophisticated microfluidic photonic crystal device.

The marriage of photonic crystals with optofluidics also opens the door toward sensing schemes. The fluid infiltration of photonic crystals *forms* a defect, circumventing the difficult requirement of aligning the fluid to a sensing element. Since the holes of the photonic crystal are approximately 0.1fL in volume, incredibly

27

small volumes of analyte are therefore necessary to make a meaningful component. Furthermore, these cavities exhibit high Q-factors despite the presence of a fluid; it has been shown that this microfluidic regime may potentially reach values up to $Q = 1 \times 10^6$ [106]. In summary, the microfluidic photonic crystal cavity regime is not only highly suitable to developing reconfigurable integrated photonic crystal components, but is also primed for accurate, small-volume-analyte sensing devices.

Chapter 2

Theory

The following section aims to provide the mathematical and physical theory required to make sense of the work entailed in this thesis.

First, photonic crystals are explained in terms of the Maxwell's equations, which are then cast as a Hermitian eigenvalue problem. The periodic nature of crystal lattices is described in unique terms which greatly reduce the necessary calculations. The inherent scalability of photonic crystals is described mathematically. The concept of *bandstructure* is introduced, providing a way to make sense of interesting photonic crystal structures and also how to optimise them. Photonic crystal cavities, waveguides and double heterostructures are explained.

Next, evanescent coupling is detailed. The equations describing the coupling and between modes of adjacent waveguides and their associated behaviour are given. A mathematical description of mode distribution in k-space for a curved tapered optical fibre is presented, following with how this promotes the ability to characterise dispersion and propagation loss in a closed photonic crystal waveguide.

Finally, basic descriptions of the qualitative principles underlying microfluidic behaviour are given. In this final section of the chapter, surface tension, contact angle, surface wetting behaviour and capillary action are covered.

2.1 Photonic crystals

Photonic crystals are structures containing a periodic variation of dielectric constant (refractive index), for which the modulation is typically on the scale of nanometres. The periodicity may be in one, two or three dimensions, as depicted below in Fig. 2.1. The work of this thesis is primarily concerned with two-dimensional type photonic crystals.
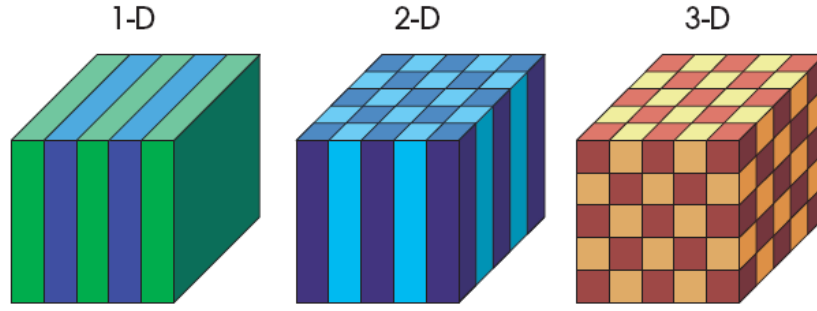
Figure 2.1. Generic examples of one-, two-, and three-dimensional photonic crystals. The different colours represent a periodic modulation of dielectric constant (refractive index) [127].

Photonic crystals offer a method to control the propagation of electromagnetic waves. It is therefore a logical step to study their operating principle by looking to Maxwell's equations[127].

2.1.1 Maxwell's equations

Macroscopic electromagnetism, including the propagation of light in photonic crystals, is governed by the following four Maxwell's equations:

$$\nabla \cdot \mathbf{B} = 0$$

$$\nabla \times \mathbf{E} + \frac{\partial \mathbf{B}}{\partial t} = 0$$

$$\nabla \cdot \mathbf{D} = \rho$$

$$\nabla \times \mathbf{H} - \frac{\partial \mathbf{D}}{\partial t} = \mathbf{J},$$

(2.1)

where $\mathbf{E}$ and $\mathbf{H}$ are the electric and magnetic fields, $\mathbf{D}$ and $\mathbf{B}$ are the displacement and magnetic induction fields, and ρ and $\mathbf{J}$ are the free charge and current densities.

For purposes of this study, a restriction is imposed for macroscopic propagation within a *mixed dielectric medium*; a composite of homogeneous dielectric material that is a function of position vector $\mathbf{r}$ and does not vary with time. It is assumed that there are no free charges or currents, setting $\rho = 0$ and $\mathbf{J} = 0$. One then seeks to relate $\mathbf{D}$ to $\mathbf{E}$ and $\mathbf{B}$ to $\mathbf{H}$. Generally, the components D_i of the displacement field $\mathbf{D}$ are related to the components E_i of the electric field $\mathbf{E}$ via the power series:

$$\frac{D_i}{\varepsilon_0} = \sum_j \varepsilon_{ij} E_j + \sum_{j,k} \chi_{ijk} E_j E_k + O(E^3).$$

(2.2)

It is reasonable to make several additional assumptions for electromagnetic waves in photonic crystals. The first is that the field strengths are small enough so that only the linear regime is considered and χ_{ijk} terms can be neglected. Second, there is no frequency dependence on the dielectric constant (i.e. no material dispersion). Third, only lossless transparent materials are considered, so the dielectric function is real and positive.

With the above assumptions, $\mathbf{D}(\mathbf{r}) = \varepsilon_0\varepsilon(\mathbf{r})\mathbf{E}(\mathbf{r})$ and $\mathbf{B}(\mathbf{r}) = \mu_0\mu(\mathbf{r})\mathbf{H}(\mathbf{r})$ are obtained. Most dielectric materials of interest have a relative magnetic permeability $\mu(\mathbf{r})$ very close to unity, so by argument of simplicity, $\mathbf{B} = \mu_0\mathbf{H}$ is used. Maxwell's equations become:

$$\nabla \cdot \mathbf{H}(\mathbf{r}, t) = 0$$

$$\nabla \times \mathbf{E}(\mathbf{r}, t) + \mu_0 \frac{\partial \mathbf{H}(\mathbf{r}, t)}{\partial t} = 0$$

$$\nabla \cdot [\varepsilon(\mathbf{r})\mathbf{E}(\mathbf{r}, t)] = 0$$

$$\nabla \times \mathbf{H}(\mathbf{r}, t) - \varepsilon_0\varepsilon(\mathbf{r}) \frac{\partial \mathbf{E}(\mathbf{r}, t)}{\partial t} = 0.$$

(2.3)

Generally, $\mathbf{E}$ and $\mathbf{H}$ are complex functions in both time and space, yet the time and spatial dependencies may be separated by expanding the fields into a set of harmonic modes. The harmonic modes can be interpreted as the spatial field patterns (mode profiles) that vary with time. By taking the real part of the complex-valued fields, the physical fields of the harmonic modes can be obtained from

$$\mathbf{H}(\mathbf{r}, t) = \mathbf{H}(\mathbf{r})e^{-i\omega t}$$

$$\mathbf{E}(\mathbf{r}, t) = \mathbf{E}(\mathbf{r})e^{-i\omega t}.$$

(2.4)

The equations governing the mode profiles at a set frequency can be found by inserting the above equations into (2.3). The divergence equations become

$$\nabla \cdot \mathbf{H}(\mathbf{r}) = 0$$

$$\nabla \cdot [\varepsilon(\mathbf{r})\mathbf{E}(\mathbf{r})] = 0,$$

(2.5)

which imply the absence of point sources or sinks for displacement or magnetic fields. The curl equations relate $\mathbf{E}(\mathbf{r})$ to $\mathbf{H}(\mathbf{r})$:

$$\nabla \times \mathbf{E}(\mathbf{r}) - i\omega\mu_0\mathbf{H}(\mathbf{r}) = 0$$
$$\nabla \times \mathbf{H}(\mathbf{r}) + i\omega\varepsilon_0\varepsilon(\mathbf{r})\mathbf{E}(\mathbf{r}) = 0. \tag{2.6}$$

The equations of (2.6) can be decoupled, leading to the time-independent vector Helmholtz equation

$$\nabla \times \left(\frac{1}{\varepsilon(\mathbf{r})}\nabla \times \mathbf{H}(\mathbf{r})\right) = \left(\frac{\omega}{c}\right)^2 \mathbf{H}(\mathbf{r}). \tag{2.7}$$

In photonic crystal literature, this is often described as the "master equation" and is ultimately what gets calculated by the relevant numerical software, such as the *plane wave expansion* method. Equation (2.7) allows the modes $\mathbf{H}(\mathbf{r})$ and their corresponding frequencies to be derived for a given structure $\varepsilon(\mathbf{r})$. $\mathbf{E}(\mathbf{r})$ can be recovered from $\mathbf{H}(\mathbf{r})$ by

$$\mathbf{E}(\mathbf{r}) = \frac{i}{\omega\varepsilon_0\varepsilon(\mathbf{r})}\nabla \times \mathbf{H}(\mathbf{r}). \tag{2.8}$$

The reason why $\mathbf{H}(\mathbf{r})$ is solved first rather than $\mathbf{E}(\mathbf{r})$ is one of mathematical convenience and is detailed here [127].

2.1.2 Electromagnetism as an eigenvalue problem

Solving equation (2.7) for the modes $\mathbf{H}(\mathbf{r})$ of a given system leads to an eigenvalue problem. The eigenvectors $\mathbf{H}(\mathbf{r})$ are the spatial patterns of the harmonic modes. It is common in literature to identify the left hand side of (2.7) by the operator $\widehat{\Theta}$ as:

$$\widehat{\Theta} = \nabla \times \frac{1}{\varepsilon(\mathbf{r})}\nabla \times, \tag{2.9}$$

where $\widehat{\Theta}$ is Hermitian. It is important to note that $\widehat{\Theta}$ is a linear operator, meaning that any linear combination of solutions is itself a solution. For example, given a certain mode profile, another legitimate mode profile can be constructed with the same frequency by doubling field strength everywhere. As such, any two fields that differ by a multiplicative factor are considered the same mode.

The Hermiticity of $\widehat{\Theta}$ forces any two harmonic modes $\mathbf{H}_1(\mathbf{r})$ and $\mathbf{H}_2(\mathbf{r})$ with different frequencies ω_1 and ω_2 to have an inner product of zero. Consider two normalised modes, $\mathbf{H}_1(\mathbf{r})$ and $\mathbf{H}_2(\mathbf{r})$, with frequencies ω_1 and ω_2:

$$\omega_1^2(\mathbf{H}_2, \mathbf{H}_1) = c^2(\mathbf{H}_2, \widehat{\Theta}\mathbf{H}_1) = c^2(\widehat{\Theta}\mathbf{H}_2, \mathbf{H}_1) = \omega_2^2(\mathbf{H}_2, \mathbf{H}_1)$$

(2.10)

$$\Rightarrow (\omega_1^2 - \omega_2^2)(\mathbf{H}_2, \mathbf{H}_1) = 0.$$

For $\omega_1 \neq \omega_2$, then $(\mathbf{H}_1, \mathbf{H}_2) = 0$ and $\mathbf{H}_1$ and $\mathbf{H}_2$ are described as *orthogonal* modes. If two modes have equal frequencies $\omega_1 = \omega_2$, then we say they are degenerate. It is important to note that the eigenvectors for degenerate states are always linearly independent and by a Schmidt orthogonalization procedure may still be made orthogonal to each other. Degenerate modes imply that different field patterns occur with equivalent frequencies. For example, this is possible in a dielectric configuration that is invariant under a 120° rotation, where modes that differ by a corresponding 120° rotation can be expected to have the same frequency.

2.1.3 Periodic geometry and reciprocal space

Photonic crystals are structures composed of a periodic refractive index distribution. It is therefore necessary to apply the Maxwell's equations into a periodic space. The periodicity can be expressed by a function $f(\mathbf{r})$ in terms of a lattice, where $f(\mathbf{r}) = f(\mathbf{r} + \mathbf{R})$ and $\mathbf{R}$ is a lattice vector. Fixed basis vectors $\mathbf{a_1}$, $\mathbf{a_2}$, $\mathbf{a_3}$ are taken such that for all points $\mathbf{R}$ in a three-dimensional lattice, $\mathbf{R} = l\mathbf{a_1} + m\mathbf{a_2} + n\mathbf{a_3}$ for some integers l, m and n. The basis vectors are not unique, as indicated in Fig. 2.2.
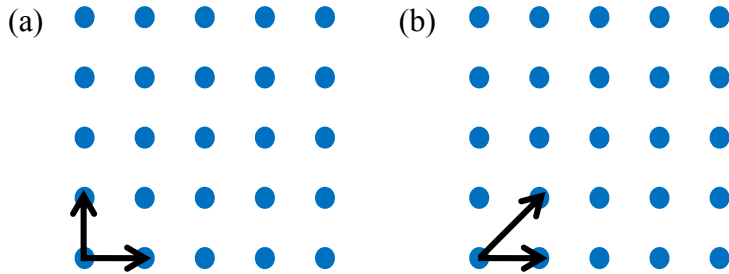
Figure 2.2. Two-dimensional square lattice. The black arrows in (a) and (b) indicate different choices of basis.

The connection between a continuous function $f(\mathbf{R})$ and a discrete lattice is provided by a *unit cell*. A unit cell is a region of space which can be translated by every lattice vector and maps the complete function. A special case, the *primitive unit cell*, is any unit cell that occupies the least possible volume, shown in Fig. 2.3.
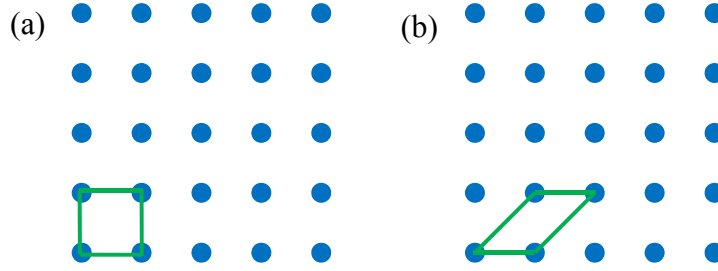
Figure 2.3. Schematic showing two different primitive unit cells in a two-dimensional square lattice.

For every lattice there is an associated *reciprocal lattice*. The vectors of the reciprocal lattice are defined by:

$$\mathbf{b_1} = 2\pi \frac{\mathbf{a_2} \times \mathbf{a_3}}{\mathbf{a_1} \cdot \mathbf{a_2} \times \mathbf{a_3}}$$

$$\mathbf{b_2} = 2\pi \frac{\mathbf{a_3} \times \mathbf{a_1}}{\mathbf{a_2} \cdot \mathbf{a_3} \times \mathbf{a_1}} \tag{2.11}$$

$$\mathbf{b_3} = 2\pi \frac{\mathbf{a_1} \times \mathbf{a_2}}{\mathbf{a_3} \cdot \mathbf{a_1} \times \mathbf{a_2}}$$

Where $\mathbf{a_1}$, $\mathbf{a_2}$, $\mathbf{a_3}$ are the lattice vectors and $\mathbf{b_1}$, $\mathbf{b_2}$, $\mathbf{b_3}$ are the reciprocal lattice vectors. The lattice vectors and the reciprocal lattice vectors are related by the equation

$$\mathbf{a}_i \mathbf{b}_j = 2\pi \delta_{ij}, \tag{2.12}$$

where $\delta_{ij} = 1$ if $i = j$ and 0 otherwise. As a lattice vector is denoted by $\mathbf{R}$, a reciprocal lattice vector is denoted by $\mathbf{G}$. As the lattice vectors have dimensions of length, the reciprocal lattice vectors have dimensions of inverse length, spanning reciprocal space. Figure 2.4 illustrates a conversion from real space to reciprocal space for a triangular lattice.

34

(a)

$\mathbf{a}_1 = a(\mathbf{x}+\mathbf{y}/\sqrt{3})/2$

$\mathbf{a}_2 = a(\mathbf{x}-\mathbf{y}/\sqrt{3})/2$

(b)

$\mathbf{b}_1 = (2\pi/a)(\mathbf{x}+\mathbf{y}/\sqrt{3})$

$\mathbf{b}_2 = (2\pi/a)(\mathbf{x}-\mathbf{y}/\sqrt{3})$

y

x
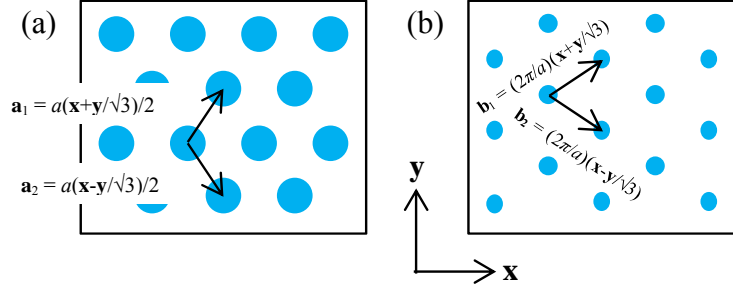
Figure 2.4. A triangular lattice in both (a) real space and (b) reciprocal space. In this case the reciprocal lattice is a rotated version of the original.

2.1.4   First Brillouin Zone

Studies of electromagnetic modes in conventional photonic structures such as optical fibres or other types of waveguides often seek to find the dispersion relation $\mathbf{k} = \mathbf{k}(\omega)$, which gives the wavevector $\mathbf{k}$ for a particular mode with frequency ω. The wavevector determines the phase velocity of the mode in the equation

$$\mathbf{E}(\mathbf{r}, t) = \mathbf{E}(x, y)\exp\left[-i\omega\left(t - \frac{z}{v_p}\right)\right], \qquad (2.13)$$

which describes a mode $\mathbf{E}(x, y)$ propagating along the z axis with phase velocity $v_p = \omega/\mathbf{k}$. The wavevector is closely related to wavelength by the wavenumber: $k = 2\pi/\lambda$.

For the purposes of this work, the dispersion relation is inverted to obtain $\omega = \omega(\mathbf{k})$. This may not be an intuitive approach given that the frequency of an optical source is easily controlled rather than its wavevector. However, the approach here allows the possibility to find different solutions for every value of the wavevector. The optical fibre provides a good way of conveying what happens in this case: as $\mathbf{k}$ increases in the direction of propagation, a greater portion of the mode profile $\mathbf{E}(x, y)$ is bound to the core. Increasing $\mathbf{k}$ without limit therefore causes the effective index of the mode to asymptotically approach the core's refractive index. For sufficiently large $\mathbf{k}$, the system may support multiple modes for which there are several solutions ω_n for each value $\mathbf{k}$. This type of behaviour is shown in Fig. 2.5.

35
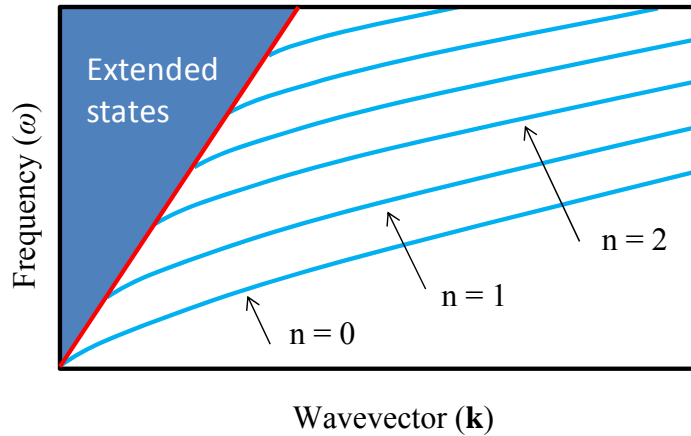
Figure 2.5. Illustration of dispersion curves for modes of a uniform waveguide. The blue lines correspond to modes localised to the waveguide, labelled as band numbers starting with n = 0 being the lowest frequency mode. The shaded region is a continuum of states that extend into the guide and the surrounding medium. The red line is the *light line.*

For periodic systems such as photonic crystals, the dispersion curves are different. It is no longer the case that distinct solutions are found for every value of **k**. Figure 2.6 shows a portion of the dispersion relation – the bandstructure – for a set of modes for a one-dimensional lattice of period *a*. As the wavevector **k** varies, the mode frequencies repeat with period $2\pi/a$.
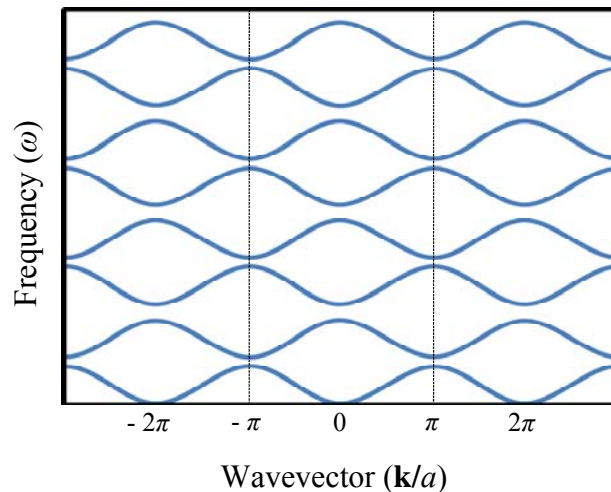
Figure 2.6. Dispersion curves (band structure) for TM/TE modes of a one-dimensional lattice. More bands appear at higher frequencies without limit.

Taking the concept further, any two wavevectors that differ by a reciprocal lattice vector are essentially equivalent, written in equation form as:

36

$$\omega_i(\mathbf{k}) = \omega_i(\mathbf{k} + \mathbf{G}). \tag{2.14}$$

This result simplifies the computational task of calculating modes tremendously, since to find all the modes of the photonic crystal, one only has to solve the problem in the neighbourhood of the origin of wavevector or reciprocal space. This neighbourhood is defined as the part of reciprocal space consisting of all points closer to the origin than to any other reciprocal lattice vector. It is termed the *First Brillouin Zone*.

Figure 2.7 displays the First Brillouin Zone for some commonly encountered photonic crystal types. The points labelled with letters in these diagrams correspond to points of high symmetry within the First Brillouin Zone.
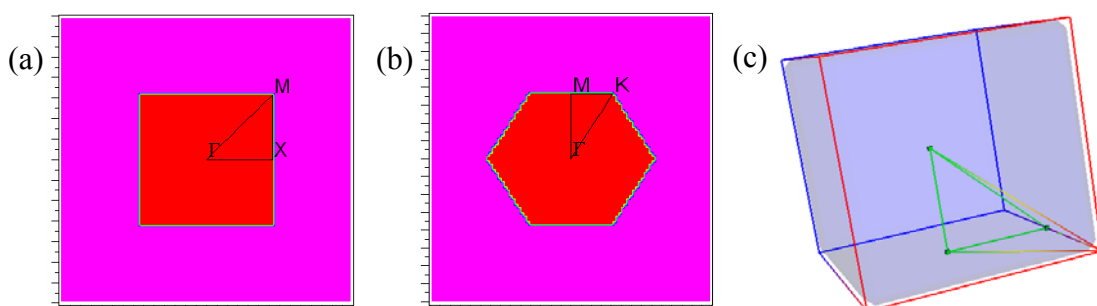
Figure 2.7. First Brillouin Zones for several photonic crystals. (a) 2D square lattice, (b) 2D hexagonal lattice and (c) 3D cubic lattice.

2.1.5   Bloch's Theorem

The modes of a photonic crystal must be solutions to Maxwell's equations. However, their periodic aspect places a restriction on the possible form of the solutions. In particular, the modes must satisfy the appropriate *translation symmetry*. If the refractive index distribution is identical in every unit cell, a mode must be unchanged if it is shifted in space by any lattice vector **R**. At most, the solution may change by a constant phase factor.

Consider a system that is translationally invariant with a translation operator $\hat{T}_d$. When operating on a function $f(\mathbf{r})$ with $\hat{T}_d$, the argument is shifted by **d** and $\hat{T}_d\varepsilon(\mathbf{r}) = \varepsilon(\mathbf{r} - \mathbf{d}) = \varepsilon(\mathbf{r})$. A mode with the form of $e^{i\mathbf{k}\cdot\mathbf{r}}$ is then an eigenfunction of any translation operator over **r**:

$$\hat{T}_{d\mathbf{r}}e^{i\mathbf{k}\cdot\mathbf{r}} = e^{i\mathbf{k}\cdot(\mathbf{r}-d)} = \left(e^{-ikd}\right)e^{i\mathbf{k}\cdot\mathbf{r}}. \tag{2.15}$$

This is a result known as *Bloch's Theorem* and applies to any wave-like phenomenon in a periodic medium. For equation (2.13) the corresponding eigenvalue is e^{-ikd}.

Expanding on this, the converse can be shown where any eigenfunction of $\hat{T}_d$ for all $\mathbf{d} = d\mathbf{r}$ must be proportional to $e^{i\mathbf{k}\cdot\mathbf{r}}$ for some $\mathbf{k}$. The modes of the system can be chosen to be eigenfunctions of all the $\hat{T}_d$'s, so they should have an $\mathbf{r}$ dependence on the form $e^{i\mathbf{k}\cdot\mathbf{r}}$. The modes can then be classified by the particular values for $\mathbf{k}$.

With this in mind, the magnetic field can be expressed as

$$\mathbf{H}(\mathbf{r}) = e^{i\mathbf{k}\cdot\mathbf{r}}\,\mathbf{u}_{\mathbf{k}}(\mathbf{r}), \qquad (2.16)$$

where $\mathbf{u}_{\mathbf{k}}(\mathbf{r}) = \mathbf{u}_{\mathbf{k}}(\mathbf{r} + \mathbf{R})$ for all lattice vectors $\mathbf{R}$. Note that due to *Bloch's Theorem*, only the wavevectors $\mathbf{k}$ inside the First Brillouin Zone need to be considered. For example, consider a wavevector $\mathbf{k}'$ outside the First Brillouin Zone. Then there is a reciprocal lattice vector $\mathbf{G}$ such that $\mathbf{k}' = \mathbf{k} + \mathbf{G}$ and $\mathbf{k}$ is within the First Brillouin Zone. Therefore

$$
\begin{aligned}
\mathbf{H}(\mathbf{r}) &= e^{i\mathbf{k}'\cdot\mathbf{r}}\,\mathbf{u}_{\mathbf{k}'}(\mathbf{r}) \\
&= [e^{i\mathbf{k}\cdot\mathbf{r}}\, e^{i\mathbf{G}\cdot\mathbf{r}}]\,\mathbf{u}_{\mathbf{k}'}(\mathbf{r}) \\
&= e^{i\mathbf{k}\cdot\mathbf{r}}[e^{i\mathbf{G}\cdot\mathbf{r}}\,\mathbf{u}_{\mathbf{k}'}(\mathbf{r})] \\
&= e^{i\mathbf{k}\cdot\mathbf{r}}\,\mathbf{u}_{\mathbf{k}'}(\mathbf{r}),
\end{aligned}
\qquad (2.17)
$$

where we have used the fact that $e^{i\mathbf{G}\cdot\mathbf{r}}$ is a function with the periodicity of the lattice. Implicitly, any solution for a wavevector outside the First Brillouin Zone has a corresponding solution inside the First Brillouin Zone. Armed with the above information, modes take a form like

$$\mathbf{H}_{\mathbf{k}}(\mathbf{r}) = \mathbf{H}_0 e^{i\mathbf{k}\cdot\mathbf{r}}, \qquad (2.18)$$

where $\mathbf{H}_0$ is any constant vector. These are plane waves and are solutions (in this case, the homogenous problem where $\varepsilon = 1$) of the master equation (2.7) with eigenvalues $(\omega/c)^2 = |\mathbf{k}|^2/\varepsilon$. The result is the dispersion relation $\omega = c|\mathbf{k}|/\sqrt{\varepsilon}$. Classifying the plane wave by its wavevector $\mathbf{k}$ specifies how the mode is transformed by a translation operation. In fact there is an infinite number of solutions $\mathbf{k}$ for every ω; however, some are more interesting than others, as depicted in Fig. 2.5 and Fig. 2.6.

2.1.6 Scale invariance of Maxwell's equations

As mentioned in the previous chapter, scalability is an important issue for device miniaturisation, particularly sensing schemes. Photonic crystals are highly suited to these types of application, as they are considered to be completely scalable. This is due to the fact that electromagnetism in dielectric media has no fundamental length

scale other than the assumption that the system is macroscopic. The master equation (2.7) can be described as *scale invariant*, where contraction or expansion of all distances results in the same master equation.

Suppose one is interested in the harmonic modes for a configuration of dielectric $\varepsilon'(\mathbf{r})$ that is a compressed or expanded version of $\varepsilon(\mathbf{r})$: $\varepsilon'(\mathbf{r}) = \varepsilon(\mathbf{r}/\sigma)$ for some scale parameter σ. Using a change of variables in (2.7) where $\mathbf{r}' = \sigma\mathbf{r}$ and $\nabla' = \nabla/\sigma$, we get:

$$\sigma\nabla' \times \left(\frac{1}{\varepsilon(\mathbf{r}'/\sigma)} \sigma\nabla' \times \mathbf{H}(\mathbf{r}'/\sigma) \right) = \left(\frac{\omega}{c}\right)^2 \mathbf{H}(\mathbf{r}'/\sigma). \qquad (2.19)$$

Here, $\varepsilon(\mathbf{r}'/\sigma)$ is the same as $\varepsilon'(\mathbf{r}')$. It follows that

$$\nabla' \times \left(\frac{1}{\varepsilon'(\mathbf{r}')} \nabla' \times \mathbf{H}(\mathbf{r}'/\sigma) \right) = \left(\frac{\omega}{c\sigma}\right)^2 \mathbf{H}(\mathbf{r}'/\sigma). \qquad (2.20)$$

Equation (2.20) is the master equation again with mode profile $\mathbf{H}'(\mathbf{r}') = \mathbf{H}'(\mathbf{r}'/\sigma)$ and frequency $\omega' = \omega/\sigma$. This means the new mode profile and its frequency can be obtained by rescaling the original mode and frequency. The solutions of one length scale determine the solutions for all other length scales.

2.1.7 Polarisation

For transverse electromagnetic waves, polarisation describes the orientation of the electric field oscillations. It is a critical consideration for photonic crystals, as it affects how the propagating wave interacts with the lattice structure. An electric field pointing into the crystal plane is described as TE polarisation; out of plane orientation is TE polarisation.

A note about real systems here: for two dimensional cases one can easily define the two distinct polarisations: TE and TM. However, in the reality of three dimensions where a slab has finite thickness, this no longer holds completely true. At the point where symmetry is maintained for the centre of the slab, $z = 0$, the modes are purely TE or TM polarised. However, deviations from this point will break the symmetry. By continuity of the fields, small changes of location away from the symmetry point will be *mostly* **TE-like** or **TM-like**, as long as the waveguide thickness is less than the wavelength. This is highlighted in Fig. 2.8.
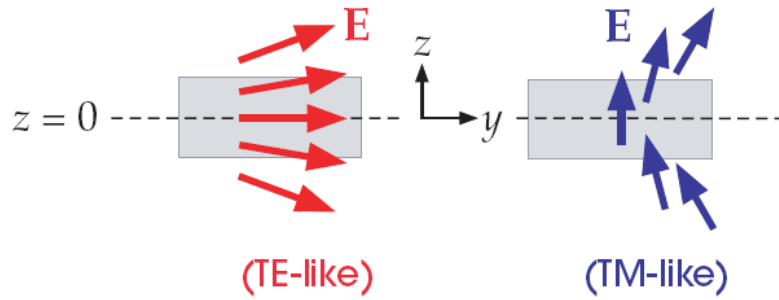
Figure 2.8. Schematic depiction of the electric field lines (**E**) for a thin dielectric structure, where $z = 0$ is the symmetry plane [127]. Deviations from the symmetry plane change the electric field orientation. As a result, modes are described as TE-like or TM-like.

2.1.8   Bandstructures

As stated previously, the master equation results in an infinite number of solutions ω_n for each value of **k**, which are labelled by *band number*, *n*, in order of increasing frequency. Varying **k** over all possible values produces a set of solutions of ω that constitutes a *band*. The bandstructure of the crystal is the collection of all these bands. The values of **k** inside the First Brillouin Zone are the only non-redundant values necessary, so from these the complete bandstructure can be obtained.

Bandstructure problems form curves in one dimension, surfaces in two dimensions and hyper surfaces in three dimensions. Figure 2.9 shows some band surfaces for a two dimensional cubic lattice of rods in air for the two different polarisation cases, TM and TE. The horizontal plane of the figure is the two dimensional reciprocal lattice and the vertical axis represents the mode frequency. Each sheet is a single band.
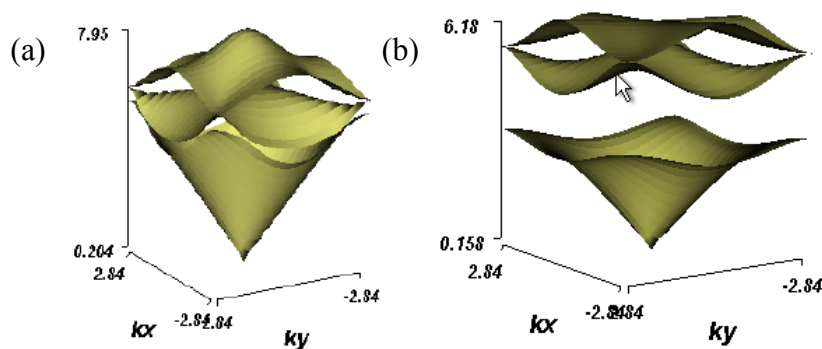
Figure 2.9. Frequency surfaces for a 2D cubic lattice. (a) TM polarisation, (b) TE polarisation. (Obtained from RSoft BandSOLVE).

The bandstructures shown in Fig. 2.9 introduce the concept of *band gap*. If one considers two adjacent bands, say *m* and *m* + 1, then in most cases there will be one or more points in **k**-space where the bands touch. For example, Fig. 2.9 (a) shows

touching of the second and third bands at their corners, together with the first and second bands overlapping where minima of the second sheet are lower than maxima of the first. However, certain index distributions can cause frequency ranges between two bands for which there are no solutions at all. This range is known as a *band gap* and it is impossible for electromagnetic radiation frequencies within that range to propagate in the crystal. Figure 2.9 (b) exhibits a large band gap between the first and second bands.

It is fortunate to note that most common applications of locating and optimising band gaps can be done by using a small subset of points in the First Brillouin Zone. Group theory, which will not be dealt with here, can be used to show that the extremity points of the bands must occur at points of high symmetry. If a band gap is found at the symmetry points, one can be certain that the band gap persists at all points within the First Brillouin Zone.

A *band diagram* can be constructed by identifying the points of symmetry of the First Brillouin Zone and connecting them by straight lines. This connection is known as the **k**-path. Figure 2.7 (a) and (b) illustrate these. Bandstructures can then be calculated and plotted as a single graph, as shown in Fig. 2.10 which correspond to the examples in Fig. 2.9. As expected from the complete surface plots, the bands in the TM band are connected whilst there is a band gap in the TE case.
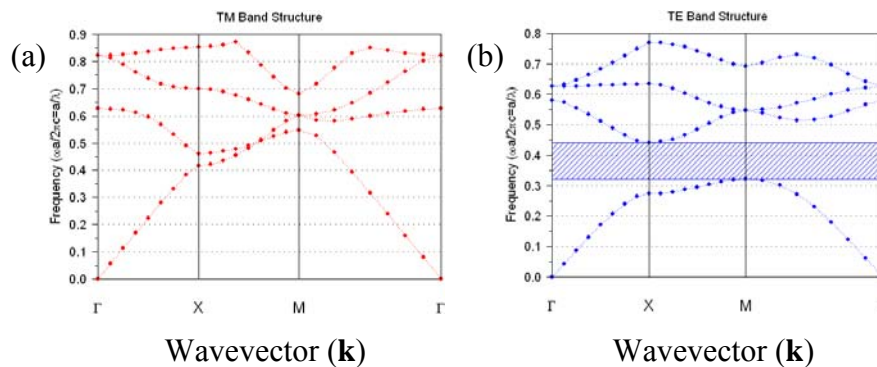
Figure 2.10. TM and TE band diagrams for the cubic lattice of rods in air, corresponding to Fig. 2.9 examples.

An important concept to explain here is the *light line*, which was introduced in Fig. 2.5. The light line essentially describes the crossover point between modes bound to the waveguide (beneath the light line) and the continuum of radiative modes (above the light line). For a given waveguide, the modes that are not confined must extend out to infinity. Far away, the modes will resemble free-space plane waves with a superposition given by

$$\omega = c|\mathbf{k}| = c\sqrt{\left(k_{\parallel}^2 + k_{\perp}^2\right)}, \tag{21}$$

for $k_{\parallel}$ and $k_{\perp}$, which are some parallel and perpendicular real wavevector components with respect to the structure. For a given value of $k_{\parallel}$, there will be modes with every possible frequency greater than $ck_{\perp}$ since $k_{\perp}$ can take any value. As a result, the region above the light line $\omega = ck_{\parallel}$ has a continuous spectrum of states. The region above the light line $\omega > ck_{\parallel}$ is termed the *light cone*.

The region below the light line contains the index-guided modes where the ε is larger. This lowers the frequencies of the modes relative to their corresponding values in free space. The only solutions in air are those with an imaginary perpendicular component:

$$k_{\perp} = \pm i\sqrt{k_{\parallel}^2 - \omega^2/c^2}. \tag{2.22}$$

This corresponds to fields that decay evanescently away from the guide, meaning that the modes confine to the higher index region. For a given $k_{\parallel}$ there are a set of discrete frequencies – bands – due to their being localised in one direction. Increasing $k_{\parallel}$ results in more and more guided bands, eventually approaching the ray-optics limit of total internal reflected rays with a continuum of maintained angles $\theta > \theta_c$.

2.1.9 The physics of band gaps

Harmonic modes in dielectric medium can be quite complicated, although there are some simple ways to understand their qualitative features. In general, a mode tends to concentrate its electric field energy in high-ε regions and remains orthogonal to modes of lower frequency. This can be described by the variational theorem [127], in which the lowest frequency mode corresponds to the field pattern that minimises the electromagnetic energy functional:

$$\begin{aligned} U_f(\mathbf{H}) &= \frac{(\nabla \times \mathbf{E}, \nabla \times \mathbf{E})}{(\mathbf{E}, \varepsilon(\mathbf{r})\mathbf{E})} \\ &= \frac{\int d^3\mathbf{r}|\nabla \times \mathbf{E}(\mathbf{r})|^2}{\int d^3\,\mathbf{r}\varepsilon(\mathbf{r})|\mathbf{E}(\mathbf{r})|^2}. \end{aligned} \tag{2.23}$$

One can observe here that a way to minimise U_f is to maximise the electric field in high-ε regions (denominator) and minimising the amount of spatial oscillations (numerator) – of course, whilst remaining orthogonal to lower frequency modes. This latter point is important, since it distinguishes all modes from each other and results in the higher frequency modes concentrating less of their electric field in the high-ε

region. Consequently, there are differences in electric field profiles of the modes, which cause the existence of the band gap.

Corresponding to the fact that low frequency modes concentrate comparably more of their energy in high-ε regions, it is conventional to refer to the band above a gap as the air band, and the band below as the dielectric band. This is analogous to the electronic band structure of semiconductors where the conduction and valance bands are adjacent above and below the fundamental gap.
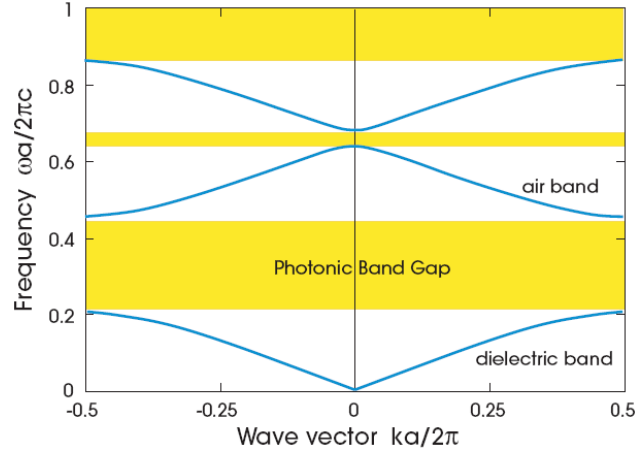
Figure 2.11. A photonic bandstructure for a multilayer film of periodically modulating ε (1D photonic crystal). The band above the photonic band gap is referred to as the air band, and below it is the dielectric band [127].

A band gap will appear in every system possessing a periodic ε modulation where $\varepsilon_1/\varepsilon_2 \neq 1$. The extent of the gap could be characterised by its frequency width, $\Delta\omega$. However, considering the scale invariance of Maxwell's equations, expanding or contracting the crystal by a factor σ will simply scale the gap width as $\Delta\omega/\sigma$. A more appropriate characterisation, independent of the scale of the crystal, is given by the *gap-midgap ratio*. If ω_m is the centre frequency of the gap, the gap-midgap ratio is given by $\Delta\omega/\omega_\mathrm{m}$. For similar reasons, it is common to plot band diagrams in terms of the dimensionless units $\omega a/2\pi c$ and $ka/2\pi$.

If one considers two materials in a multilayer film with dielectric constants ε and $\varepsilon + \Delta\varepsilon$, and thickness $a - d$ and d, then if either the dielectric contrast is weak ($\Delta\varepsilon/\varepsilon \ll 1$) or the thickness d/a is small, the gap-midgap ratio between the first two bands is approximately

$$\frac{\Delta\omega}{\omega_\mathrm{m}} \approx \frac{\Delta\varepsilon}{\varepsilon} \cdot \frac{\sin(\pi d/a)}{\pi}. \tag{2.24}$$

Consequently, this allows one to arrive at a quantified estimation for the extent of a band gap.

2.1.9 Photonic crystal cavities

Two dimensional dielectric functions with band gaps can prevent electromagnetic propagation in the plane of the crystal. Typically within the band gaps, no modes exist. However, one can modify a single lattice site and create a localised mode – or set of closely spaced modes – that are inside the band gap. For photonic crystals, the modification of one or several lattice points forms a *defect*.

There are several options to locally perturb a photonic crystal lattice in a two-dimensional geometry. This includes removing one or several lattice points, changing their size, or adjusting their location. These perturbations ruin the translational symmetry of the lattice, introducing an increased density of states within the band gap. Defect-induced modes extend evanescently since they are prohibited into the rest of the crystal. Providing that the defect has the proper dimensions to support a mode within the band gap, the strong reflection of the photonic crystal surrounding the defect forms a *cavity*.

A defect mode can be described as having its own variation in $\varepsilon(\mathbf{r})$, ε_{defect}, for the mode within the photonic crystal structure. For example, increasing ε_{defect} decreases the defect mode frequency, which pulls a band down from the upper edge of the band gap to a range within the gap. This grants an engineering degree of freedom to design photonic crystal cavity devices. A positive $\Delta\varepsilon$ can be achieved for example by adding dielectric material to holes of a slab photonic crystal profile, as shown below in Fig. 2.12.
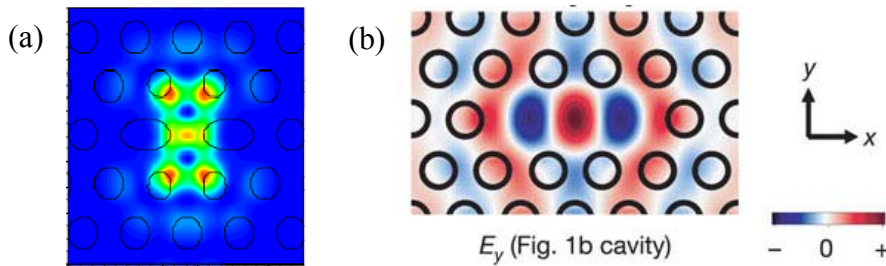
Figure 2.12. (a) Electric field profile of a cavity mode formed by a missing hole and modified adjacent holes [62]. (b) E-field profile of a cavity mode formed by three missing holes [119].

The question of in-plane light confinement is essentially answered by the photonic band gap. What about the direction perpendicular to the plane of periodicity? To understand this, one considers propagation components $\mathbf{k}_z > 0$ (z being out-of-the-

plane) and develops an out-of-plane band structure, shown in Fig. 2.13. Many of the qualitative features of this band structure are common to all two dimensional crystals.
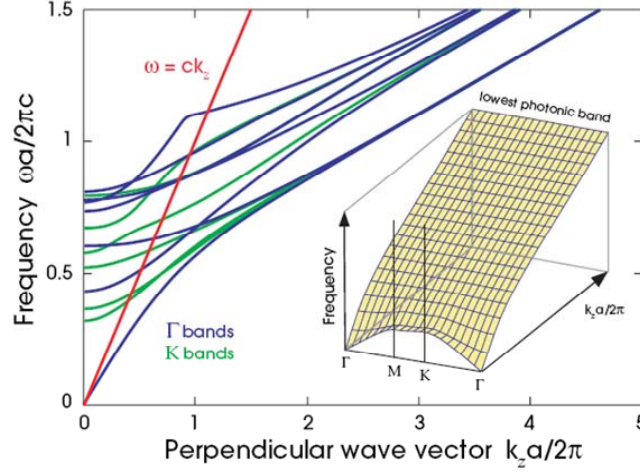
Figure 2.13. Out-of-plane bandstructure of a triangular lattice of air columns. Bands starting at Γ, $\omega(\Gamma, \mathbf{k}_z)$, are plotted with blue lines, and K, $\omega(K, \mathbf{k}_z)$ are plotted with green. The red light line separates the oscillatory modes in the air regions ($\omega \geq c\mathbf{k}_z$) from those that are evanescent in the air regions ($\omega \leq c\mathbf{k}_z$). The inset shows the frequency dependence of the lowest band as $\mathbf{k}_z$ varies [127].

There is no band gap to prevent propagation in the out-of-plane direction. This is a consequence of homogeneity of the crystal in that direction. There is also no distinction between modes which are TE or TM, as the mirror symmetry is broken for $\mathbf{k}_z \neq 0$.

The inset of Fig. 2.13 shows the behaviour of the lowest band for increasing $\mathbf{k}_z$. For the case when $\mathbf{k}_z = 0$, the lowest band spans a broad range of frequencies. As $\mathbf{k}_z$ is increased, the lowest band flattens and the range of allowed frequencies for a given $\mathbf{k}_z$ decreases to zero – i.e. the bandwidth of available frequencies vanishes. This can be explained by the light modes being trapped in neighbouring high-ε regions due to index guiding. Little overlap occurs, decoupling the modes and therefore reducing the bandwidth. This is also displayed by the bands in Fig. 12, where there is large dispersion for $\omega > c\mathbf{k}_z$, and small dispersion for $\omega \ll c\mathbf{k}_z$.

There are two important parameters that describe a photonic crystal cavity: effective modal volume and quality factor. The effective modal volume gives the peak electric field strength in the cavity by the formula [128]:

$$V_{eff} = \frac{\int_V \varepsilon(\mathbf{r})|\mathbf{E}(\mathbf{r})|^2 d^3\mathbf{r}}{\max[\varepsilon(\mathbf{r})|\mathbf{E}(\mathbf{r})|^2]}. \quad (2.25)$$

V_{eff} in photonic crystal cavities is typically defined in terms of some coefficient x times wavelength over effective refractive index: $(x(\lambda/n)^3)$. This takes into account the scale-invariance of Maxwell's equations and also the stronger confinement caused by higher refractive indices.

The quality factor characterises the ability for a cavity to store energy. A mode in a cavity has finite lifetime, acting with a complex frequency $\omega_c = \omega_0 - i\gamma/2$ in which the imaginary part is associated with exponential decay. If the field decays $e^{-\gamma t/2}$, then the energy within the cavity decays as $e^{-\gamma t}$. The loss rate γ is not used conventionally due to the scale-invariance of the Maxwell's equations: instead, the dimensionless quantity, quality factor, is used, given by $Q = \omega_0/\gamma$.

The quality factor can be interpreted in three ways. Firstly, $1/Q$ is a dimensionless decay rate as:

$$\frac{1}{Q} = \frac{P}{\omega_0 \varepsilon}, \qquad (2.26)$$

where P is the dissipated power, U is the electromagnetic energy localised in the cavity and ω_0 is the frequency of the resonance. Secondly, Q is a dimensionless lifetime, referring to the number of optical periods that elapse before the energy decays by a factor of $e^{-2\pi}$. Thirdly, $1/Q$ is the fractional bandwidth of the resonance. This is given by $Q = \omega_0/\Delta\omega$, where $\Delta\omega$ is the full-width half-maximum of the Fourier transformed time-varying field in the cavity.

Where a resonance has more than one decay mechanism, it is common to characterise each of these mechanisms with its own Q, as mentioned in the introductory chapter. These mechanisms may include in-plane losses, out-of-plane losses, surface roughness, crystal irregularities and coupling to escape waveguides. The more a given loss mechanism degrades the overall net Q of the cavity, the lower its own Q is. Introducing the various loss mechanisms is done by adding its inverse to the following equation:

$$\frac{1}{Q_{net}} = \frac{1}{Q_0} + \frac{1}{Q_{first\ decay\ mechanism}} + \frac{1}{Q_{second\ decay\ mechanism}} + \ ... \quad (2.27)$$

where Q_0 is the intrinsic Q of the cavity. Electrical engineers might observe a similarity with the above equation to a system of parallel capacitances. Q_0 is considered an important value, as attempts can be made to minimise other loss mechanisms. In addition to Q_0, the convention used in reference [62] considers two other decay channels: Q_{fibre}, which describes coupling of energy back into the input fibre, and $Q_{parasitic}$, which accounts for any significant perturbation of the mode field inside the cavity. An example of this is broken photonic crystal symmetry, which may

cause the transfer of energy from a TE-like mode to a less well confined TM-like mode.

If one assumes a system where there is only an intrinsic Q_0 and one additional decay mechanism associated with the input scheme, for example Q_{fibre} (all other decay mechanisms approach infinity), then from coupled mode theory in time [129], Q_{net} can be described as

$$Q_{net} = \sqrt{T} \times Q_0, \qquad (2.28)$$

where T is the fraction of transmitted power that does not couple into the cavity. A T of 1 would indicate no power coupling into the cavity; 0.75 would be 25% of transmitted power coupling to the cavity. It is satisfactory to use T for values down to 0.5. The implication of (2.28) is that a cavity which is strongly coupled to will have a reduced net Q.

2.1.10 Photonic crystal waveguides

As mentioned previously, local defects can be used in photonic crystals to trap light. In addition, *linear defects* can also be induced, which guide light in a photonic crystal from one location to another. The principle is similar to the cavity geometry, where a change in $\varepsilon(\mathbf{r})$ can allow for a mode to exist within the photonic band gap. In this case, however, a mode may propagate along the defect, as illustrated in Fig. 2.14. Such a mode is known as a *waveguide mode*.
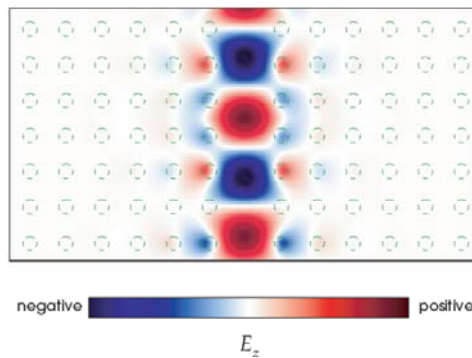
Figure 2.14. The electric field pattern – waveguide mode – associated with a linear defect within a square lattice [127].

A system with a linear defect has one direction within the crystal plane for which the discrete translational symmetry is preserved. In this case it is the direction of the guide. Various techniques have been employed to achieve an appropriate guiding defect, for example removing one or several rows of lattice points, and by changing the parameters of the holes along a row. An important distinction between cavities

47

and waveguides is that a point defect (cavity) mode is *localised* whenever its frequency is in the photonic band gap, whereas for a linear defect (waveguide) mode, its behaviour depends on both its frequency and its wavevector. Therefore a cavity mode considers values of (ω) within a bandgap, and a guided mode considers values of ($\mathbf{k}$, ω) within a bandgap.

The band diagram of Fig. 2.15 shows a guided band lying within the photonic band gap. The gap makes the mode evanescent into the photonic crystal, providing in-plane confinement to the defect. However, the mode is allowed to propagate along the defect, resulting in a guide. Outside the gap, the dark-red region of Fig. 2.15, the modes extend within the photonic crystal and also cover a continuous range of frequencies. The increased ε associated with the removed holes creates an index-guiding effect in all directions, preventing out-of-plane radiation for wavevector components below the light line.
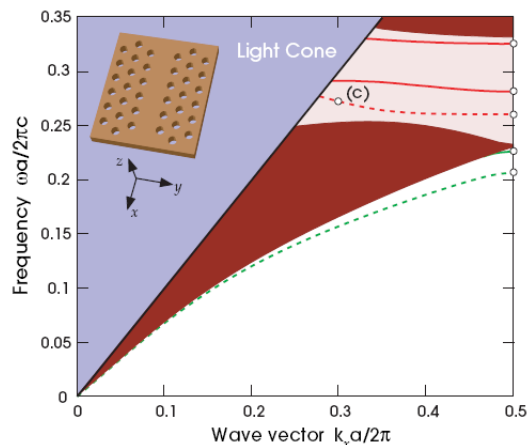
Figure 2.15. The projected band structure of the TE-like states for a "W1" defect along the *x* direction in the hole slab (inset) [127]. Dark-red shaded regions indicate modes that extend into the crystal. Guided modes are introduced in the gap (red bands in pink shaded region).

A crucial aspect of two-dimensional photonic crystal waveguides is therefore its slab thickness. Consider the extreme cases: a slab that is too thin weakly guides (if at all), whilst a slab that is too thick resembles an infinite two-dimensional system and supports higher order modes. Approximately half a wavelength in thickness can be expected for ideal guiding – thick enough for the lowest frequency (fundamental) mode to be well confined, yet thin enough to "cut-off" higher order modes from fitting in the slab. The problem then becomes determining whether the wavelength should be considered as that for either the air or the dielectric. It turns out that the effective ε is mode-dependant by the spatial average of the ε profile weighted by the field profile. The effective vertical wavelengths of TE-like modes are determined mostly by high ε material, whilst for TM-like modes it is mostly the low ε material.

Another important consideration for propagating modes in a photonic crystal is their group velocity. The group velocity is the energy transport velocity when the medium is assumed to be lossless, possesses small material dispersion and the wavevector is real. If one considers the Bloch state $\mathbf{H_k(r)}e^{-i\omega t}$ is a plane wave $e^{i(\mathbf{k \cdot r} - \omega t)}$ multiplied by a periodic function $\mathbf{u_k(r)}$, then it propagates through the crystal and all the scattering events are coherent as a result of $\mathbf{u_k(r)}$. The group velocity is a function of both the band index n and the wavevector $\mathbf{k}$:

$$\mathbf{v}_n(\mathbf{k}) \triangleq \nabla_\mathbf{k}\omega_n \triangleq \frac{\partial \omega_n}{\partial k_x}\hat{\mathbf{x}} + \frac{\partial \omega_n}{\partial k_y}\hat{\mathbf{y}} + \frac{\partial \omega_n}{\partial k_z}\hat{\mathbf{z}}. \qquad (2.29)$$

This information is essentially available from the bandstructure: the group velocity of a mode is the gradient of its band.

2.1.11 Photonic crystal double heterostructures

As mentioned previously, the Q-factor and modal volume, V, of photonic crystal cavities are important parameters for many of their applications. Typically, the ratio Q/V is sought to be maximised. A design rule to increase the Q-factor without much change to modal volume has been proposed for two-dimensional planar geometries [119], describing an avoidance of abrupt cavity edges. The form of the cavity mode electric-field distribution should slowly vary, ideally as a Gaussian profile, to minimise photon leakage out of the slab. However, the exact structure to achieve this has not been established. One successful method, which has realised experimental Q-factors of over 2×10^6, is the *double heterostructure*, as illustrated in Fig. 2.16.

The double heterostructure is formed by combining two different photonic crystal waveguide sections. Figure 2.16 (a) shows a waveguide formed in a photonic crystal by removal of its holes along one direction. Figure 2.16 (b) shows the corresponding calculated bandstructure, which displays a waveguide mode within the photonic bandgap. Figure 2.16 (c) shows the introduction of a section within the photonic crystal waveguide that contains adjusted parameters; the ensemble of which is termed the double heterostructure. The adjustment is achieved by elongating the periodicity of the holes along the direction of the waveguide, increasing the effective refractive index for that section. Figure 2.16 (d) shows the corresponding band diagrams over real space, revealing the formation of a *mode gap*. The mode gap prohibits propagation in the direction along the waveguide. This is combined with the high index slab that provides total internal reflection for out-of-plane confinement and the photonic bandgap for in-plane confinement. A mode excited in the adjusted section is therefore confined in all three dimensions, resulting in a spatially localised cavity.
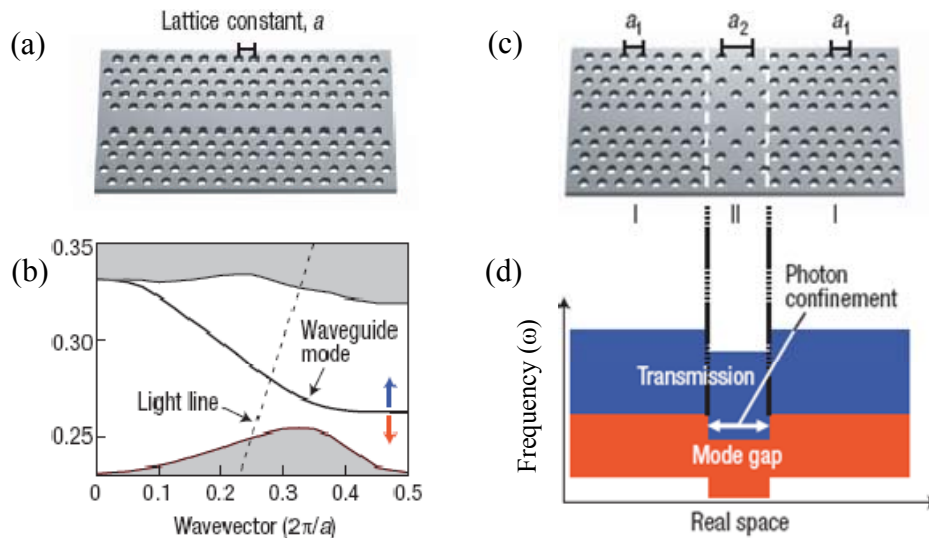
Figure 2.16. Illustration of the operating principle behind the double heterostructure [21]. (a) Planar photonic crystal waveguide. (b) Calculated bandstructure for (a). (c) Photonic crystal double heterostructure, constructed by connecting the waveguide structures I and II. The deformed triangular lattice in II has its periodicity elongated parallel to the waveguide direction. (d) Schematic of the band diagram along the waveguide direction. A mode existing in the waveguide of II will not propagate into section I due to the formation of a mode gap. Instead, the mode of II will decay evanescently outside that region.

A crucial point to the formation of a double heterostructure cavity is the increase in effective refractive index. Typically, this is achieved by local alterations in the periodic geometry of the photonic crystal lattice. One alternative approach to increasing the effective refractive index of a local region is via the infiltration of select holes within the photonic crystal structure by a liquid [106]. In this case, the air holes are replaced with a material of refractive index $n > 1$, as illustrated in Fig. 2.17. Increasing the index of the holes increases the effective index of a mode within that region, consequently lowering its dispersion curve. The difference between infiltrated and uninfiltrated bands is the mode gap, as illustrated in Fig. 2.17 (b). The mode gap is most often measured at the edge of the First Brillouin Zone.
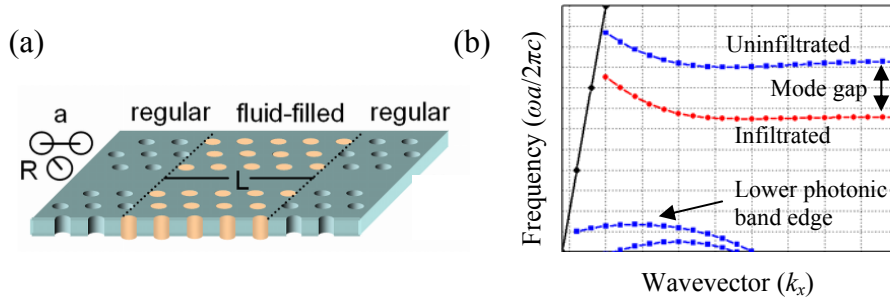
Figure 2.17. (a) Double heterostructure cavity with lattice period *a* and hole radius *R*. The orange indicates a region of fluid-filled holes within the otherwise photonic crystal waveguide structure. (b) Dispersion relation of wavevectors in the direction of the line defect for regular (blue triangles) and fluid-filled (red circles) photonic crystal waveguides (n_{fluid} = 1.51). The difference between the curves is labelled mode gap. Dashed line is the light line. The green line represents a fibre mode, which will be discussed more in the next section.

It has been shown that the size of the mode gap in this regime is comparable to the mode gap of heterostructures formed by different lattice constants photonic crystals [106]. This indicates that the heterostructures formed by air-holes infiltration are indeed capable of the mode gap operation. There are some limiting factors, however. The mode gap must remain within the photonic band gap of both the infiltrated and uninfiltrated cases to prevent it from radiating into the crystal. Therefore it is important that the lowered dispersion curve due to infiltration does not overlap the lower edge of the photonic band gap for the uninfiltrated case. This is achievable if there is a sufficient frequency range between the waveguide mode and the edge of the photonic band gap for the case before infiltration.

Previous numerical studies have been undertaken to investigate the *Q*-factor and mode volume characteristics of air-holes infiltrated photonic crystal double-heterostructures [106]. These parameters are important for numerous photonic crystal applications, as discussed in Chapter 1. Using a finite difference time domain method, a relevant subset of the behaviours of *Q*-factor and modal volume have been obtained and shown in Fig. 2.18 (a). These are plotted as a function of the refractive index infiltrated into the air holes.
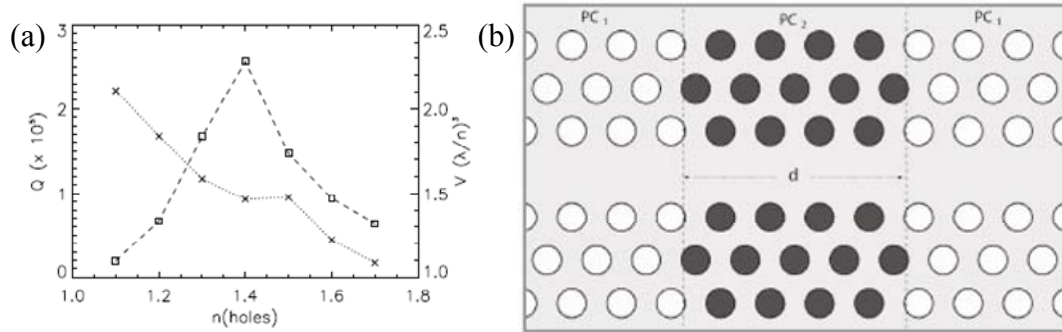
Figure 2.18. (a) Quality factor Q (rectangles) and modal volume V (crosses) as a function of the refractive index of the infiltrated holes. (b) Schematic of the refractive index profile for an air-holes infiltrated photonic crystal double heterostructure [106].

Figure 2.18 (a) shows that as the refractive index of the holes increases, the Q-factor increases initially. This is attributed to the increased average refractive index providing better out of plane confinement and therefore smaller out of plane losses. However, an optimum value is reached before the Q decreases. The decrease is believed to occur because the dispersion curves for the higher refractive indices shift lower whilst the lower band edge for the uninfiltrated photonic crystal section remains fixed (Fig. 2.17 (b)). The resulting minimised separation causes an increased loss to the adjacent photonic crystal. However, it is still worth noting that there is a large range of refractive indices where the quality factor remains of order 10^5.

The results of modal volumes for these resonances, expressed in $(\lambda/n)^3$ with $n = 3.4$ (silicon), are also plotted in Fig. 2.18. As the refractive index of the central holes increases, the modal volume decreases. This is expected behaviour as the resonant mode becomes better confined with the increased difference between the two heterostructures.

2.2 Evanescent coupling

Evanescent coupling is a process by which an electromagnetic wave is transmitted from one waveguide to another by means of an evanescent field. Evanescent coupling may occur when two waveguides are close to one another such that the evanescent field generated by one element does not decay too significantly before reaching the other. Providing the receiving waveguide can support modes of the appropriate frequency, the evanescent field will "connect" the waveguides and coupling between the elements may occur.

Evanescent coupling is essentially identical to the near field interaction involved in electromagnetic field theory. Evanescent waves are not considered in the far field regime, where the components of the wave eventually reach the ratio of the impedance of free space and propagate radiatively. As such, evanescent coupling occurs in close proximity to the waveguide media and is therefore associated with matter. Depending on the impedance of the radiating source, the corresponding near field evanescent wave is predominantly electric (capacitive) or predominantly magnetic (inductive). Evanescent coupling is directly analogous to the coupling between two plates of a capacitor or the primary and secondary coils of a transformer. Mathematically, the process is similar to quantum tunnelling, however using electromagnetic waves rather than quantum-mechanical wave functions.

2.2.1 Coupled mode theory

There are usually two conditions necessary for energy exchange between guided modes. The first is an overlap of the energy profiles between the two modes, which is essentially achieved by the extension of the evanescent fields into the adjacent waveguides. The second is a synchronisation between the two modes, where their propagation constants are equal, $\beta_1 = \beta_2$, and they are *phase matched*.

That being said, if none of the modes of the two waveguides have identical propagation constants, energy exchange is still possible if, for example, a diffraction grating is placed on one or both waveguides. The presence of the grating may even allow modes to couple with propagation constants travelling in opposite directions, $\beta_1 > 0, \beta_2 < 0$.

A general coupled mode theory treats modes in separate waveguides as being mutually orthogonal in the absence of the coupling process. As such, a mathematical description of the coupled modes considers each mode to be otherwise isolated and ideal, requiring a perturbation of some kind to cause the coupling. The perturbation leading to mode coupling may be regarded as the presence of one guide in the vicinity of the other.

The interaction of the waves in a pair of coupled waveguides can be described by the following coupled wave equations [130, 131]:

$$\frac{da_1}{dz} = -i\beta_1 a_1 + i\kappa a_2$$

$$\frac{da_2}{dz} = -i\beta_2 a_2 + ip\kappa a_1.$$

(2.30)

In these equations, z is the direction along the waveguides; a_1 and a_2 are the amplitudes of the two modes which interact via the coupling coefficient, κ; and β_1 and β_2 are their propagation constants. The parameter p assumes the value $p = 1$ for co-propagation coupling and $p = -1$ for contra-directional coupling.

2.2.2 Optical fibre to photonic crystal waveguide coupling

Evanescent coupling from an adiabatically tapered optical fibre to a photonic crystal waveguide is undertaken extensively during the scope of this thesis. This regime allows efficient interfacing between fibre optics and planar photonic crystal devices. One of its distinct advantages is that it circumvents the intrinsic spatial and refractive index mismatch of fibre to photonic crystal waveguide end-fire coupling. The regime experiences coherent interaction over the length of the coupling region between phase-matched modes of each waveguide, allowing for almost unity power transfer between the guides.

In particular, the coupling between the fundamental mode of the tapered fibre and the modes of a W1 photonic crystal waveguide is explored and utilised throughout the thesis. Relative to the taper mode, the photonic crystal waveguide modes have a negative group velocity, resulting in contra-directional coupling as depicted in the schematic of Fig. 2.19. In addition, the ends of the waveguides are abruptly terminated, causing Fresnel reflections at the end facets, indicated by r_1 and r_2. As such, the systems studied in this thesis are similar to that of [73].
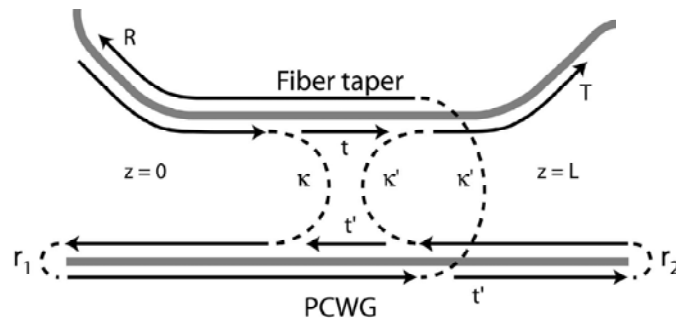
Figure 2.19. Illustration of the contra-directional coupling process and the feedback within the photonic crystal waveguide (PCWG) caused by the reflectivities $r_{1,2}$ of the waveguide terminations [73]. The coupling region extends along the z-axis, with $z = 0$ corresponding to the input, and $z = L$ to the output.

54

In the absence of reflections caused by the photonic crystal waveguide terminations ($r_{1,2} = 0$), the taper-photonic crystal waveguide junction can be characterised as

$$\begin{bmatrix} a_T^+(L) \\ a_{PC}^-(0) \end{bmatrix} = \begin{bmatrix} t & \kappa' \\ \kappa & t' \end{bmatrix} \begin{bmatrix} a_T^+(0) \\ a_{PC}^-(L) \end{bmatrix},$$

(2.31)

where κ and κ' are coupling coefficients; t and t' are transmission coefficients; L is the interaction length; $a_T^+(z)$ and $a_{PC}^-(z)$ are the amplitudes of the forward propagating fundamental fibre taper mode and the backward-propagating photonic crystal waveguide mode, respectively. Non-zero photonic crystal waveguide termination reflections result in feedback for the system. The reflected light may then couple back into the fibre as it re-enters the interaction region. In the presence of feedback, the normalised transmitted and reflected powers in the fibre taper are given by [132]:

$$T = |a_T^+(L)|^2 = \left| t + \frac{\kappa\kappa't'r_1r_2}{1 - r_1t'r_2t'} \right|^2,$$

$$R = |a_T^-(0)|^2 = \left| \frac{\kappa\kappa'r_1}{1 - r_1t'r_2t'} \right|^2,$$

(2.32)

for $a_T^+(0) = 1$ and $a_{PC}^-(L) = 0$. If one measures T and R and considers the equations of (2.32), the efficiency of the fiber-photonic crystal waveguide coupling can be determined, as measured by $|\kappa\kappa'|$.

In general, contra propagating modes have a very large mode number mismatch, so one could expect their inter-coupling to be weak. However, the periodicity of one waveguide offered by the photonic crystal can be considered as an "absorbing" element of this mismatch. It is conventional to write the associated periodicity as

$$\Omega = \frac{2\pi}{\Lambda},$$

(2.33)

where Λ is taken to be the period of the photonic crystal.

A convenient method to apply the equations of (2.30) into the system depicted in Fig. 2.19 is done by converting them into slowly varying mode amplitudes A_1 and A_2, which are introduced via the relations

$$a_j = A_j e^{-i\beta_j z}, \qquad j = 1, 2.$$

(2.34)

Substituting equation (2.34) into equation (2.30) results in exponential functions oscillating with spatial frequencies $|\beta_1 - \beta_2| + \Omega$ and $|\beta_1 - \beta_2| - \Omega$. The high frequency

terms do not contribute substantially to the solutions since rapid oscillations tend to cancel out after integration. Thus, only the low frequency components are kept and the following system of approximate equations is obtained:

$$\frac{dA_1}{dz} = i\kappa A_2 e^{-2i\delta z}$$

$$\frac{dA_2}{dz} = ip\kappa A_1 e^{+2i\delta z}$$

(2.35)

where p is set to -1, and using

$$\delta = \beta - \Omega,$$

(2.36)

which is a detuning parameter. Renaming A_1 as a_T^+ and A_2 as a_{PC}^-, we write the following boundary conditions:

$$a_T^+(0) = 1, \qquad a_{PC}^-(L) = 0.$$

(2.37)

The solutions for this case are found to be

$$a_T^+(z) = \frac{\alpha\cosh\big(\alpha(L-z)\big) - i\delta\sinh\big(\alpha(L-z)\big)}{\alpha\cosh(\alpha L) - i\delta\sinh(\alpha L)}$$

$$a_{PC}^-(z) = i\frac{\kappa\sinh\big(\alpha(L-z)\big)}{\alpha\cosh(\alpha L) - i\delta\sinh(\alpha L)}$$

(2.38)

where

$$\alpha^2 = \kappa^2 - \delta^2.$$

(2.39)

In the limit of perfect tuning ($\delta \to 0$), the reflectivity can be expressed as the squared ratio of the backward propagating mode over the forward:

$$\left|\frac{a_{PC}^-(0)}{a_T^+(0)}\right|^2 = \tanh^2(\kappa L).$$

(2.40)

From this, the reflectivity increases monotonically with increasing coupling length and asymptotically approaches unity for $L \to \infty$.

2.2.3 Coupling bandwidth

As the parameter δ detunes from the limit of the perfect case, the coupling strength decreases. It is conventional to consider the detuning in terms of wavelength, and characterise the *bandwidth* of the system by the full width at half maximum, $\Delta\lambda$. The bandwidth is given by [133]:

$$\Delta\lambda = \frac{G(\kappa L)}{L \left| \frac{d}{d\lambda} (|\beta_1 + \beta_2|) \right|}$$
(2.41)

with

$$G(\kappa L) = 4\sqrt{(\alpha L)^2 + (\kappa L)^2}$$
(2.42)

and α is real. The propagation constants can be written as

$$\beta_1 = n_1 k \qquad \beta_2 = n_2 k,$$
(2.43)

where n_1 and n_2 are the effective refractive indices of the relevant modes of each waveguide and

$$k = \frac{2\pi}{\lambda}.$$
(2.44)

A wavelength dependence on the refractive index is neglected, resulting in the immediate approximation

$$\Delta\lambda = \frac{\lambda^2 G(\kappa L)}{2\pi(n_1 + n_2)L}.$$
(2.45)

In the case where $\kappa L \gg 1$, the function $G(x)$ approaches $G(x) = 4\kappa L$ [133] and the contra-directional bandwidth is approximately

$$\Delta\lambda \approx \frac{2\lambda^2 \kappa}{\pi(n_{PCWG} + n_{taper})},$$
(2.46)

where the refractive indices of the modes relevant to the system under study have been given.

2.2.4 Phase matching

The coupling from one waveguide to another requires the transferring energy to be synchronised between the two guides. This synchronisation requires two conditions to be met. The frequencies must match and the wavevectors must match. This allows the phase angles to coincide during the cycles of oscillation.

Both of the above conditions are quantified in a dispersion relation. Phase matching is given by the intersection of two modes superimposed on a dispersion relation graph, as shown in Fig. 2.20. In the case of an infinitely long tapered fibre with a photonic crystal waveguide, there is only a single point of intersection between the continuous dispersion curves.
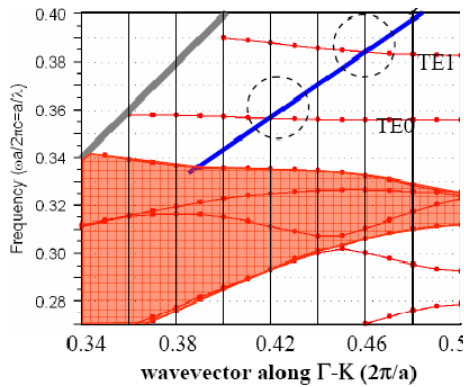
Figure 2.20. Dispersion relation for a photonic crystal waveguide (red lines) and a tapered fibre (blue line). The shaded region represents allowed bands into the photonic crystal. Modes above the light line (grey line) are not included. Dashed circles indicate modes for which phase-matched coupling occurs [9].

A quick note here: as previously mentioned, the slope of dispersion curves gives the group velocity of those modes. At the points of intersection as shown in Fig. 2.20, one can observe that the group velocities between taper mode and photonic crystal waveguide mode have opposite sign. This translates into contra-directional coupling.

2.2.5 Mode spreading in *k*-space

As opposed to straight, unperturbed tapered fibres, highly curved fibre tapers offer an interesting characteristic: their modes undergo an expanded *k*-space distribution. This can occur at the plane of a photonic crystal, which provides access to some interesting information for a given structure. For example, a closed photonic crystal waveguide (terminated by highly reflecting photonic crystal) gives rise to a series of discrete Fabry-Pérot resonances in place of a continuous dispersion curve. Coupling to such a structure with an expanded *k*-space distribution can characterise its dispersive

behaviour by monitoring the profile of spectral positions for the broadband-excited modes.
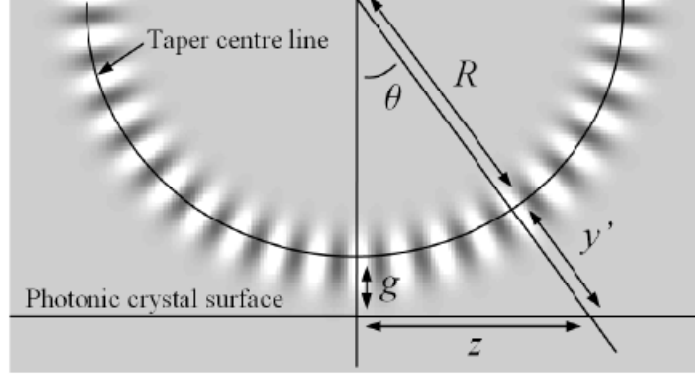
Figure 2.21. The schematic and coordinate system used for mapping the fields of a curved tapered fibre onto a photonic crystal surface. The tapered fibre mode is shown for reference [134].

The bandwidth associated with evanescent coupling in a system as described above depends on both the degree of k-space broadening of the taper mode and the average slope of the waveguide dispersion curve. The k-space extent of the curved taper mode field can be calculated to a good approximation by directly mapping the fields from the coordinate system of the taper to that of a plane parallel to the photonic crystal as depicted in Fig. 2.21. Here, it is assumed that the curvature of the taper is sufficiently small such that the transverse mode profile is not significantly perturbed from the straight waveguide. If a field component of the uncurved taper mode is given in local coordinates by $f(x',y')$, then the Fourier transform of the fields along the z-axis is given by [134]:

$$\tilde{F}(k_z) = \int_{-\infty}^{\infty} f\left(0, \sqrt{z^2 + (R+g)^2} - R\right) e^{i\beta R \arctan\left(\frac{z}{R+g}\right)} e^{-ik_z z} dz, \quad (2.47)$$

where β is the propagation constant of the taper waist and all other variables are shown in Fig. 2.21. Ultimately, equation (47) gives the k-space distribution of the curved taper mode in the z-direction at the photonic crystal surface. These calculations are then summarized in Fig. 2.22 (a), showing that the k-space extent, and hence a greater bandwidth to characterise a photonic crystal waveguide, increases as the taper curvature radius decreases.

59
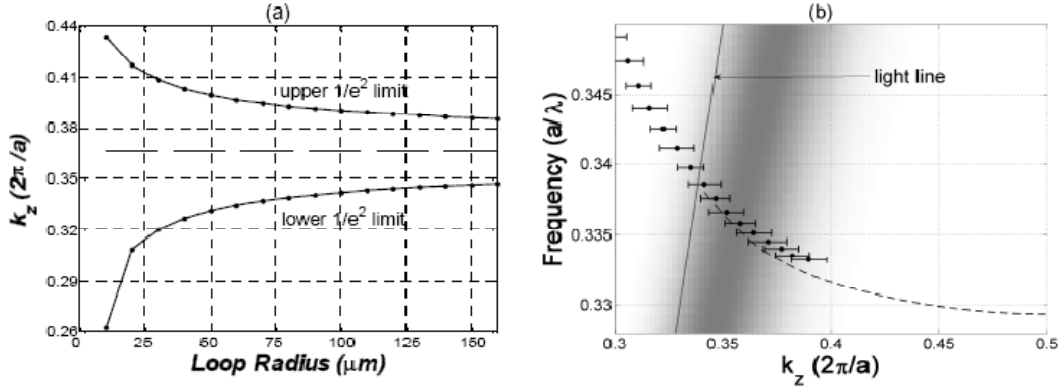
Figure 2.22. (a) The *k*-space interval (to $1/e^2$ of the peak) covered by the curved taper mode as a function of the radius of curvature. (b) Dispersion relation for a highly curved taper and a closed waveguide. The *k*-space distribution of the taper mode is shown by the shaded region and the Fabry-Pérot modes of the closed waveguide are represented by the points. The corresponding horizontal bars show the approximate *k*-space extension of the Fabry-Pérot modes. The dashed line represents a calculated waveguide mode [134].

Figure 2.22 (b) shows the dispersion relation of the expanded *k*-space distribution for the curved tapered fibre and its overlap with the associated Fabry-Pérot resonances for a closed photonic crystal waveguide. The expanded *k*-space distribution allows for a large portion of the closed photonic crystal waveguide to be probed, and its dispersive properties can be obtained by measuring the wavelengths of the resonances.

If it is assumed there is no phase change at the point of reflection from the cavity ends – ignoring the penetration depth into the photonic crystal – then the *k*-space interval between each successive resonance is $\Delta k = 2\pi/2L$, where L is the length of the closed waveguide. The dispersion curve may then be reconstructed by converting the wavelengths to normalised frequency for the dispersion relation, and ordering them by frequency with a spacing of Δk. The absolute wavevector must be estimated with knowledge of the taper *k*-space distribution or comparison with simulation.

The group velocity of a closed photonic crystal waveguide mode in terms of wavelength may be estimated by the formula:

$$\frac{v_g}{c} = \frac{2L\Delta\lambda_{FSR}}{\lambda_0{}^2}, \tag{2.48}$$

where $\Delta\lambda_{FSR}$ is the free spectral range between adjacent resonances and λ_0 is the central wavelength between the resonances. (2.48) is derived from the equation governing the free spectral range of a Fabry-Pérot etalon as $\Delta\lambda = (\lambda_0)^2/(2n_{(g)}l+\lambda_0) \approx (\lambda_0)^2/(2n_{(g)}l)$. This approach is similar what has been used in similar work to

characterise Fabry-Pérot modes of a photonic crystal structure [135, 136], however in those works either an internal light source or free space coupling is required to excite the modes.

2.2.6 Characterising propagation loss

Examination of Q-factor and the coupling strength to a closed waveguide mode can give a direct estimate of the photon lifetime in a cavity and thus an estimate of propagation losses. The intrinsic Q can be related to two sources of losses: the propagation losses, α_{prop}, which include absorption and scattering, and out of plane losses incurred at the cavity terminations. It follows [136]:

$$\frac{2\pi}{\lambda Q} = \frac{\alpha_{prop}}{n_g} + \frac{1-r}{n_g L}, \tag{2.49}$$

where n_g is the group index of the mode as obtained from the dispersion relation, λ is the wavelength of the mode, Q is the inferred intrinsic Q-factor of the mode, r is the reflectivity at the cavity terminations ($r < 1$), and L is the length of the cavity. By comparing the Q obtained from different cavity lengths, one can determine the r at the closed waveguide ends and therefore retrieve the propagation losses as a function of wavelength and group velocity.

2.2.7 The profile of tapered fibres

The successful fabrication of tapered fibre nanowires is crucial to achieve the evanescent coupling. The following provides a mathematical description for the profile of optical fibre tapers [137]. No knowledge of fluid mechanics is required, barring elementary mass conservation, as the tapering is performed sufficiently slow such that there are no strong dynamics and the system is in a quasi-equilibrium. The principle assumes a local section of the fibre cylinder is heated to a uniform temperature, enough to soften the glass for stretching, but not enough to cause it to sag under its own weight. The ends of the taper are steadily pulled apart to create a profile as shown in Fig. 2.23 (a). At the time $t + \delta t$, the hot glass cylinder has stretched to form a narrower cylinder of length $L + \delta x$, where compression is ignored so δx must be positive (Fig. 2.23 (b)). The hot-zone has changed to $L + \delta L$, where δL may be negative due to arbitrary control of the heat source. The instantaneous length l_w of the taper waist at time t is equal to the hot-zone length at that time, implying that the final waist length equals the final hot-zone length.
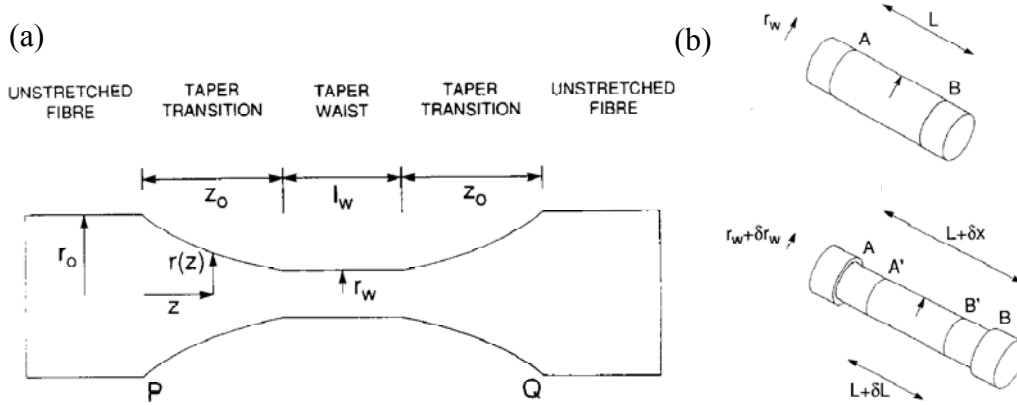
Figure 2.23. (a) The structure of a fibre taper (nanowire), indicating waist, transition and untapered regions. (b) Schematic diagrams of a cylindrical taper waist at time t where AB is uniformly heated, and time $t + \delta t$, where AB has been elongated by δx. The latter forms a narrower cylindrical taper waist, where A′B′ is still heated [137].

The volume of the cylinder at time t must equal its volume at $t + \delta t$, given by

$$\pi(r_w + \delta r_w)^2(L + \delta x) = \pi r_w^2 L, \tag{2.50}$$

where δr_w is the change in the cylinder's radius and is negative. In the limit $\delta t \to 0$, equation (2.50) can be rewritten to give a differential equation

$$\frac{dr_w}{dx} = -\frac{r_w}{2L}, \tag{2.51}$$

which governs the variation of waist radius with extension x. One may then arrive at an expression for $r_w(x)$ by using the initial condition $r_w(0) = r_0$:

$$r_w(x) = r_0 \exp\left[-\frac{1}{2}\int_0^x \frac{dx'}{L(x')}\right]. \tag{2.52}$$

2.2.8 Adiabaticity

Optically, the taper transition regions transform the local fundamental mode from a core mode in the untapered fibre to a cladding mode in the tapered waist. However, if the transformation is to be accompanied by small loss of light from the original fundamental mode, the shape of the taper transitions must be sufficiently gradual to satisfy a criterion for adiabaticity at every point [138, 139]:

$$\left|\frac{dr}{dz}\right| \leq \frac{r(\beta_1 - \beta_2)}{2\pi}, \tag{2.53}$$

where β_1 and β_2 are respectively the local propagation constants in the transition region for the fundamental mode and the mode to which power is most likely to be lost. Of course, it is also desirable for the transition to be as short as possible, allowing the resulting component to be compact and insensitive to environmental degradation. Therefore there is an optimal taper profile that is gradual enough to remain adiabatic yet short as possible to be practically robust.

2.3   Surface Tension

In the work of this thesis we are interested in several relevant microfluidic phenomena. The first of these is *surface tension*. Ultimately, surface tension is responsible for the surface of a liquid behaving like an elastic sheet. It allows insects, such as the pond skater, to stand afloat on water, causes liquids to form droplets and is responsible for capillary action. Surface tension has the dimensions of force per unit length, or equivalently energy per unit area. It is often termed as surface energy.

The physics behind surface tension can be understood qualitatively by considering the interface between a liquid and another medium (for example air). The molecules at the surface of the liquid are attracted by intermolecular forces to other liquid molecules, resulting in a net force of the surface molecules to within liquid (see Fig. 2.24). This net effect ultimately causes the body of fluid to contract such that it occupies a sphere. Quantitatively, the molecules at the surface of the liquid experience an energy deficit $\approx U/2$, where $U = kT$ is the cohesion energy per molecule. If the area per molecule is given by r^2, where r is the radius of the molecule, then the surface tension is given by

$$\gamma = \frac{U}{2r^2},$$
(2.54)

which is given by units of Joules per square metre.

liquid	γ (mJ/m^2)
acetone	24
ethanol	23
cyclohexane	25
ethyl ether	17
glycerol	63
water	73
mercury	485
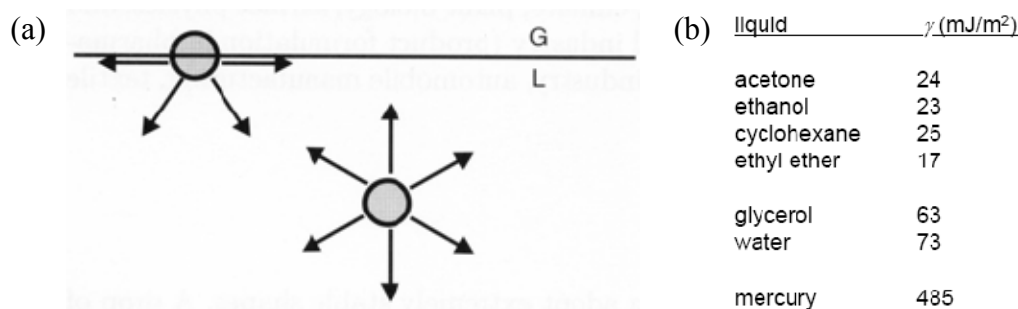
Figure 2.24. (a) Illustration of the interface between a liquid and another medium. The molecules at the surface of the liquid experience a net force attraction into the liquid. (b) Table representing the surface tensions of some common liquids at 20°C.

Another way to understand surface tension is to consider a partially submerged object as shown in Figure 2.25. The total force on the object = weight + buoyancy force + surface tension *force*. By knowing the weight and perimeter of the object, removing the buoyancy force (setting $d = 0$), one can determine the surface tension force = $p\gamma\cos\theta$. Subsequently, its surface tension, γ, and *contact angle, θ,* can be obtained.

This technique is known as the Wilhelmy method. The three-phase line shown in the figure is where the perimeter is taken, which is the point where the three separate substances meet.
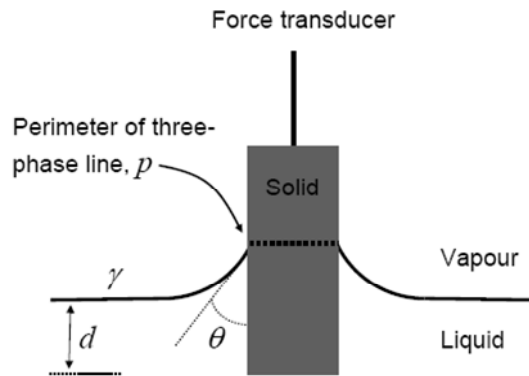
Figure 2.25. Illustration of the Wilhelmy method for how one can measure surface tension force.

This flows on to another concept worth mentioning: contact angle, which is the angle formed where a fluid-fluid (i.e. liquid-gas) interface meets a solid. The contact angle is specific for a given system and is determined by the interactions across the three media. This is most typically illustrated by the meniscus formed from a droplet of liquid resting on a solid surface in air, as for Fig. 2.26. In cases where the contact angle is low (less than 90°) and the droplet spreads across the surface, it is described as *wetting* that surface. If the fluid is water, such a surface is said to be hydrophilic (or hydrophobic when the contact angle is greater than 90°).
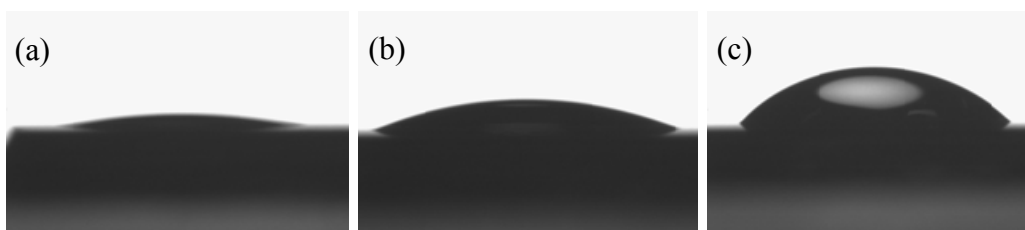
Figure 2.26. Images displaying the contact angle of different fluids on a silicon surface: (a) oil; (b) ultra-violet curable glue; (c) water.

The shape of the droplet can be determined by the Young-Laplace equation, which describes the pressure difference sustained across the interface of two static fluids due to surface tension. It is a statement of normal stress for the fluids, where the interface is treated as a zero-thickness surface:

$$\Delta p = \gamma \nabla \cdot \hat{u}$$
$$= 2\gamma H$$
$$= \gamma \left(\frac{1}{R_1} + \frac{1}{R_2} \right), \qquad (2.55)$$

where Δp is the capillary pressure difference across the fluid interface, γ is the surface tension, $\hat{u}$ is the unit normal to the surface, H is the mean curvature, and R_1 and R_2 are the principle radii of curvature. Only a normal interface is considered, as a static interface is not possible under tangential stress.

A phenomenon as a result of contact angle is *capillary action*, which causes a fluid to propagate through thin tubing. It can occur upward against gravity when the adhesive intermolecular forces between the liquid and tubing are greater than the cohesive intermolecular forces inside the liquid – i.e. when the liquid has a low contact angle with the tubing, thus forming a concave meniscus. The reverse will happen when a convex meniscus is formed (weak wetting) between the liquid and tubing surface, such as with mercury and glass, as depicted in Fig. 2.27.
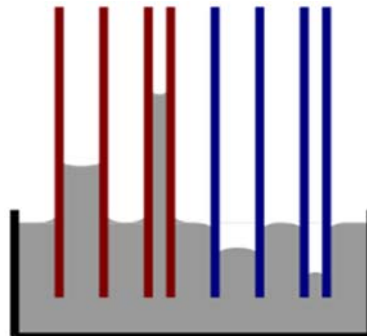
Figure 2.27. Illustration of capillary action. Red tubes represent contact angles less than 90°, blue for greater than 90°.

Capillary action occurs often in everyday life and nature. Sponges are able to soak water into them via their pores which behave like capillaries. It allows trees to soak water from the ground to its leaves. It is essential for draining the constantly-produced tear-fluid from our eyes. Its effects are studied on the International Space Station to investigate appropriate ways for propagating fluids in situations of very low gravity. More relevant to this work, capillary action is interesting to the optofluidic community for lab-on-a-chip concepts, where fluids can be transported to and from a localised region for dynamic device reconfigurability. In particular to this work, it is relevant to the infiltration of a fluid into the nanometre-scale holes of a photonic crystal.

Chapter 3

Evanescent coupling into photonic crystals

This chapter presents three articles relating to the development of nanowire evanescent coupling into modes in photonic crystals. As mentioned in section 1.2, two-dimensional photonic crystal structures have become a promising class of dielectric structure for micro- and nano-photonics. A major challenge, however, is efficiently inserting light into modes suspended by their geometry. The first two articles describe evanescent coupling as both an efficient and non-invasive approach to achieving this end. The third article presents the ability of the nanowire evanescent coupling scheme to characterise the dispersive properties of photonic crystal waveguides in a single measurement.

3.1.1 Bow- and loop-shaped nanowires

The photonic crystal structures used in the following articles are formed into the surface of chalcogenide wafers. Surrounding the photonic crystal is unpatterned material. When using the tapered silica nanowires to couple to modes of the photonic crystal structures, it is necessary to localise the coupling to the particular waveguide or cavity of interest. Without meeting this criterion, the evanescent field from the nanowire interacts with either undesired sections of the photonic crystal or bulk substrate. Both of these situations result in unwanted loss and adversely affect the quality of the measurements.

The coupling localisation is achieved by inducing a shape into the nanowire. The first article introduces a bow-shape into the nanowire, formed by moving the two ends of the fibre closer together and allowing gravity to give rise to a curved profile. This enables local coupling along the length of a waveguide defect in a photonic crystal. The second article introduces a loop-shape into the nanowire. The loop is formed by first moving the two ends of the fibre together to create slack, and then rotating one end until there is enough torsion to cause the loop. The loop dimensions may then be

reduced by moving the ends apart, thereby shortening the coupling length to the order of a micron. It is shown that this is sufficient to exclusively couple to a point defect in a photonic crystal structure. More details on the fabrication of silica nanowires can be found in section 1.5.3.

3.1.2   Characterising dispersion of photonic crystal waveguides

The evanescent coupling looped nanowires are utilised to experimentally characterise the dispersive properties of closed photonic crystal waveguides. This is achieved by monitoring Fabry-Pérot resonances generated by the closed waveguide and, noting that the resonances occur at equal spacing in reciprocal space (k-space), retrieving the dispersion of the structure from the spectral profile of the free spectral ranges between the resonances. The small radius of curvature in the loop leads to an increased coupling range in k-space, representing a crucial element for the technique.

The nanowires in the following articles and through the thesis are comprised of ~10 mm transition regions to either side of a 3 mm taper waist. The radii of the induced loops are ~50 μm.

Contributors

In the first of the following three articles, reproduced from *Optics Express* Vol. 14, pp. 1070–1078, 2006, Dr. Christian Grillet wrote the majority of the manuscript and performed FDTD analyses. This thesis author's contributions were as follows:

- Performed many of the experimental measurements and tapered fibre fabrication

- Provided some of the figures presented

- Contributed to the writing of the manuscript

The second article, reproduced from *Physica B-Condensed Matter* Vol. 394, pp. 289-292, 2007, was written by this thesis' author. The contributions were as follows:

- Performed the presented experimental measurements and tapered fibre fabrication

- Provided all of the figures presented

- Contributed significantly to the writing of the manuscript

The third article, reproduced from *Optics Express* Vol. 16, pp. 13800-13808, 2008, was first-authored by Michael W. Lee, who also performed the experiments. This thesis author's contributions were as follows:

- Provided expertise for characterisation and tapered fibre fabrication

- Contributed to the writing of the manuscript

The photonic crystal samples used in these articles were fabricated by Darren Freeman at the Australian National University.

Formal acknowledgement of the contributions of the author of this thesis is included in Appendix A.

Efficient coupling to chalcogenide glass photonic crystal waveguides via silica optical fiber nanowires

Christian Grillet[1], Cameron Smith[1], Darren Freeman[2], Steve Madden[2], Barry Luther-Davies[2], Eric C. Magi[1], David J. Moss[1] and Benjamin J.Eggleton[1]

[1]*Centre for Ultrahigh-bandwidth Devices for Optical Systems (CUDOS), School of Physics, University of Sydney, NSW 2006, Australia*
[2]*Centre for Ultrahigh-bandwidth Devices for Optical Systems (CUDOS), Laser Physics Centre, The Australian National University, Canberra, ACT 0200, Australia*
grillet@physics.usyd.edu.au

Abstract: We demonstrate highly efficient evanescent coupling between a highly nonlinear chalcogenide glass two dimensional photonic crystal waveguide and a silica fiber nanowire. We achieve 98% insertion efficiency to the fundamental photonic crystal waveguide mode with a 3dB coupling bandwidth of 12nm, in good agreement with theory. This scheme provides a promising platform to realize low power nanocavity based all-optical switching and logic functions.

© 2006 Optical Society of America

OCIS codes: (060.1810) Couplers, switches, and multiplexers; (130.2790) Guided waves

References and links

1. E. Yablonovitch, "Inhibited spontaneous emission in solid-state physics and electronics," Phys. Rev. Lett. **58**, 2059-2062 (1987).
2. S. John, "Strong localization of photons in certain disordered dielectric superlattices," Phys. Rev. Lett. **58**, 2486 (1987).
3. S. Noda, T. Baba, Roadmap on photonic crystals (Springer, 2003).
4. C. Monat, C. Seassal, X. Letartre, P. Viktorovitch, P. Regreny, M. Gendry, P. Rojo-Romeo, G. Hollinger, E. Jalaguier, S. Pocas, and B. Aspar, "InP 2D photonic crystal microlasers on silicon wafer: room temperature operation at 1.55 μm," Electron. Lett. **37**, 764 (2001).
5. S. J. McNab, N. Moll, and Y. A. Vlasov, "Ultra-low loss photonic integrated circuit with membrane-type photonic crystal waveguides," Opt. Express **11**, 2927-2939 (2003), http://www.opticsexpress.org/abstract.cfm?URI=OPEX-11-22-2927.
6. X. Letartre, C. Seassal, C. Grillet, P. Rojo-Romeo, P. Viktorovitch, M. Le Vassor d'Yerville, D. Cassagne, and C. Jouanin, "Group velocity and propagation losses measurement in a single-line photonic-crystal waveguide on InP membranes" Appl. Phys. Lett. **79**, 2312 (2001).
7. E. Centeno and D. Felbacq, "Optical bistability in finite-size nonlinear bidimensional photonic crystals doped by a microcavity," Phys. Rev. B **62**, 7683-7686(R) (2000).
8. M. Soljacic, M. Ibanescu, S. G. Johnson, Y. Fink, and J. D. Joannopoulos, "Optimal bistable switching in nonlinear photonic crystals," Phys. Rev. E **66**, 055601(R) (2002).
9. M. F. Yanik, S. Fan, and M. Soljacic, "High-contrast all-optical bistable switching in photonic crystal microcavities," Appl. Phys. Lett. **83**, 2739-2741 (2003).
10. M. Notomi, A. Shinya, S. Mitsugi, G. Kira, E. Kuramochi, and T. Tanabe, "Optical bistable switching action of Si high-Q photonic-crystal nanocavities," Opt. Express **13**, 2678-2687 (2005) http://www.opticsexpress.org/abstract.cfm?URI=OPEX-13-7-2678
11. T. Tanabe, M. Notomi, S. Mitsugi, A. Shinya, E. Kurarmochi, "Fast bistable all-optical switch and memory on a silicon photonic crystal on-chip," Opt. Lett. **30**, 19 (2005).
12. R. E. Slusher, B. J. Eggleton, Nonlinear photonic crystals (Springer, Berlin, 2003).
13. M. Soljacic, and J. D. Joannopoulos, "Enhancement of nonlinear effects using photonic crystals," Nature Materials **3**, 211-219 (2004).
14. Y. Ruan, W. Li, R. Jarvis, N. Madsen, A. Rode, and B. Luther-Davies, "Fabrication and characterization of low loss rib chalcogenide waveguides made by dry etching," Opt. Express **12**, 5140-5145 (2004), http://www.opticsexpress.org/abstract.cfm?URI=OPEX-12-21-5140
15. V. G. Ta'eed, M. Shokook-Saremi, L. B. Fu, D. J. Moss, M. Rochette, I. C. M. Littler, B. J. Eggleton, Y. Ruan, B. Luther-Davies, "Integrated all-optical pulse regenerator in chalcogenide waveguides," Opt. Lett. **30**, 2900-2902 (2005).

16. P. E. Barclay, K. Srinivasan, and O. Painter, "Nonlinear response of silicon photonic crystal microresonators excited via an integrated waveguide and fiber taper," Opt. Express 13, 801-820 (2005), http://www.opticsexpress.org/abstract.cfm?URI=OPEX-13-3-801

17. F. Raineri, Crina Cojocaru, P. Monnier, A. Levenson, R. Raj, C. Seassal, X. Letartre, and P. Viktorovitch, "Ultrafast dynamics of the third-order nonlinear response in a two-dimensional InP-based photonic crystal" Appl. Phys. Lett. 85, 1880 (2004).

18. F. Raineri, C. Cojocaru, R. Raj, P. Monnier, A. Levenson, C. Seassal, X. Letartre, and P. Viktorovitch, "Tuning a two-dimensional photonic crystal resonance via optical carrier injection," Opt. Lett. 30, 010064 (2005).

19. D. Freeman, S. Madden, and B. Luther-Davies, "Fabrication of planar photonic crystals in a chalcogenide glass using a focused ion beam," Opt. Express 13, 3079-3086 (2005), http://www.opticsexpress.org/abstract.cfm?URI=OPEX-13-8-3079

20. C. Grillet, D. Freeman, B. Luther-Davies, S. Madden, R. McPhedran, D. J. Moss, M. J. Steel, and B. J. Eggleton, "Characterization and modeling of Fano resonances in chalcogenide photonic crystal membranes," Opt. Express 14, 369-376 (2006), http://www.opticsexpress.org/abstract.cfm?URI=OPEX-14-1-369

21. P. E. Barclay, K. Srinivasan, M. Borselli, and O. Painter, "Probing the dispersive and spatial properties of photonic crystal waveguides via highly efficient coupling from fiber tapers," Appl. Phys. Lett. 85, 4 (2004).

22. J. Knight, G. Cheung, F. Jacques, and T. Birks, "Phase-matched excitation of whispering-gallery-mode resonances by a fiber taper," Opt. Lett. 22, 1129-1131 (1997).

23. K. Srinivasan, P. E. Barclay, M. Borselli, and O. Painter, "Optical-fiber based measurement of an ultra-small volume high-Q photonic crystal microcavity," Phys. Rev. B 70, 081306(R) (2004).

24. K. Srinivasan, P. E. Barclay, M. Borselli, and O. Painter, "An optical-fiber based probe for photonic crystal microcavities," IEEE J. Sel. Areas Commun. 23, 1321–1329 (2005).

25. I. Hwang, S. Kim, J. Yang, S. Kim, S. Lee, and Y. Lee, "Curved-microfiber photon coupling for photonic crystal light emitter," Appl. Phys. Lett. 87, 131107 (2005).

26. W. Kuang, C. Kim, A. Stapleton, and J. D. O'Brien, "Grating-assisted coupling of optical fibers and photonic crystal waveguides," Opt. Lett. 27, 1604–1607 (2002).

27. P. E. Barclay, K. Srinivasan, M. Borselli, and O. Painter, "Experimental demonstration of evanescent coupling from optical fiber tapers to photonic crystal waveguides," Electron. Lett. 39, 842 (2003).

28. P. E. Barclay, K. Srinivasan, M. Borselli, and O. Painter, "Efficient input and output optical fiber coupling to a photonic crystal waveguide," Opt. Lett. 29, 697–699 (2004).

29. P. E. Barclay, K. Srinivasan, and O. Painter, "Design of photonic crystal waveguides for evanescent coupling to optical fiber tapers and integration with high-Q cavities," J. Opt. Soc. Am. B 20, 2274–2284 (2003).

30. Y. K. Lizé, E. C. Mägi, V. G. Ta'eed, J. A. Bolger, P. Steinvurzel, and B. J. Eggleton, "Microstructured optical fiber photonic wires with subwavelength core diameter," Opt. Express 12, 3209-3217 (2004), http://www.opticsexpress.org/abstract.cfm?URI=OPEX-12-14-3209

31. D. Marcuse, "Bandwith of forward and backward coupling directional couplers," J. Lightwave Technol. 5 1773-1777 (1987).

32. M. Qiu, M. Swillo, "Contra-directional coupling between two-dimensional photonic crystal waveguides," Phot. and Nanostructures (2003).

1. Introduction

Two-dimensional (2D) photonic crystal (PhC) slabs have become a promising class of dielectric structure for micro- and nano-photonics. Their ability to control light at the wavelength scale [1-2] has already led to impressive demonstrations of various passive devices [3] and micro-lasers [4]. These achievements have been enabled by advanced technologies for patterning and etching materials such as silicon [5] or III-V semiconductors [6]. One of the promises of photonic crystals has been the realization of ultra-low power all-optical switches and logic via nonlinear high-Q nanocavities [7-9]. This has been highlighted by the recent demonstration in silicon photonic crystals of all-optical switching with <10 fJ pulse energies, and response times of <100 ps [10-11]. It is hoped that 2D PhC membranes will find utility in all-optical processors for ultra-fast and low power switching, optical logic gates, pulse regeneration, wavelength conversion, dispersion management and a variety of other applications [12-13].

Chalcogenide glasses are promising alternative nonlinear materials to silicon with which to realize all-optical photonic crystal devices. Whilst not possessing the mature fabrication techniques of silicon, chalcogenide glasses possess a number of significant advantages, such as high nonlinearity (n_2 as high as 100-1000× that of silica), low linear absorption, low two-photon absorption [14-15] and the absence of the free-carrier effects that have posed a

challenge to realizing ultrafast all-optical devices in silicon. In particular, the large refractive index of chalcogenide glasses (compared to other glasses) of 2.4 to 3.0 opens up the possibility of achieving compact nonlinear devices. In addition to reducing the switching power requirements, the pure Kerr-like nonlinearities offer the potential for near instantaneous response times (<100 fs) and are only limited by the resonator Q-factor. This compares favorably to carrier-based nonlinear effects, as exploited in silicon [10-11, 16] or III-V-based devices [17-18], which rely on dissipation to occur after switching, limiting the response time to tens of picoseconds.

We recently demonstrated chalcogenide glass photonic crystals fabricated by focused ion beam (FIB) milling [19-20]. In this paper we demonstrate more than 98% coupling efficiency to a two-dimensional photonic crystal waveguide (PCWG) in a chalcogenide membrane through the use of evanescent coupling via tapered optical fibre nanowires (Fig. 1). We observe coupling to both the fundamental and first higher order modes of the PCWG. The 3dB bandwidth of the coupling resonance to the fundamental mode is 12nm and the absolute coupling wavelength of 1550nm is in good agreement with theoretical results. This work is the result of recent advances in chalcogenide glass photonic crystal membrane fabrication by FIB milling [19-20], and the development of silica nanowire evanescent probing techniques [21], and represents an important step in the route to realizing low power nanocavity based all-optical switching in chalcogenide glass photonic crystals.
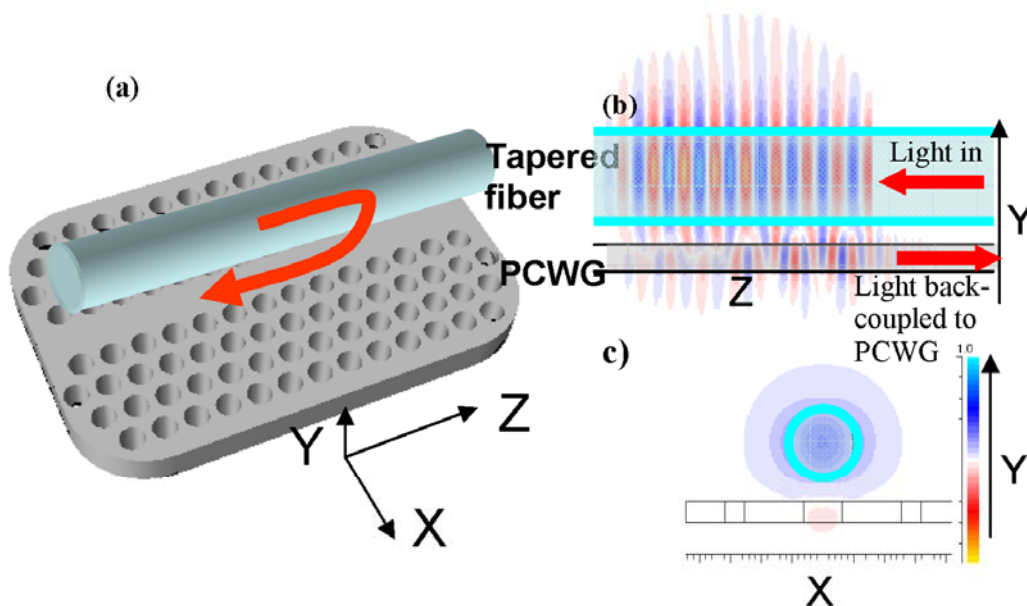
Fig. 1. (a) Schematic showing the coupling scheme of a PCWG and a tapered fiber, in this case backward coupling as explained in section 4. (b) Cross sectional view along YZ axis of the coupling mechanism between the taper and the PCWG. c) Cross sectional view normal to the direction of propagation.

2. Device Fabrication

Full details of the fabrication process are briefly reviewed here and will be published elsewhere, see [19] for an earlier approach. A chalcogenide film of thickness 300nm, composed of AMTIR-1 glass ($Ge_{33}As_{12}Se_{55}$ - refractive index ~2.7 @ 1.55 µm) was deposited by ultrafast pulsed laser deposition on a 50nm thick silicon nitride (Si_3N_4) membrane supported on a silicon substrate. The Si_3N_4 membrane was fabricated by wet etching the backside of a nitrided Si wafer. The Si_3N_4 initially 100nm thick was then accurately thinned to 50nm using Reactive Ion Etching. This resulted in a free-standing chalcogenide film on a thin (50nm) silicon nitride support film with an open aperture of approximately 130µm.

72

Subsequently a thin Au coating was applied to both sides and a Ga$^+$ FIB was used to mill cylindrical holes into the film from the back side (through the nitride). Consequently the beam first had to penetrate the relatively robust nitride layer before milling the softer glass, which greatly reduced the sculpting of the upper glass surface by the low intensity beam pedestal and resulted in nearly vertical sidewalls. The triangular lattice consisted of 550nm spaced holes of radius ~200nm (0.36×period). High-resolution scanned electron micrographs of a typical structure are shown in Fig. 2, taken at normal incidence imaged from the glass side. The final device under test was not imaged in this way because we have observed electron-induced refractive index changes in the past. Finally, the Au was wet etched and stripped for testing. The sidewall roughness can be very low in these structures, estimated to be <3 nm in our previous work [19]. The nearly cylindrical holes had sharp edges where they met the surface of the membrane. Figure 2 shows a PhC membrane waveguide consisting of a "W1" defect comprising a missing row of holes along the Γ-K direction. The waveguide under test consists of an open W1 with 160 holes removed (~ 90 μm). Since previous work we have added a drift correction scheme to greatly improve lattice periodicity in the device under test, to be published elsewhere.
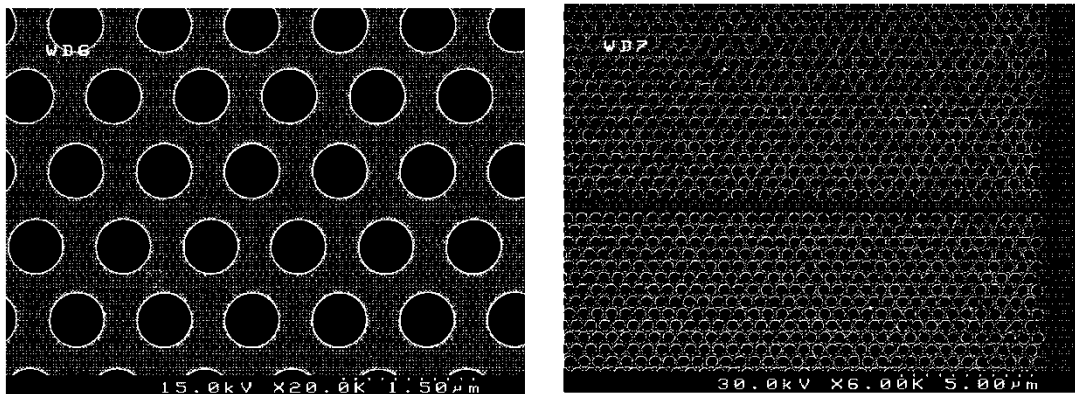
Fig. 2. Scanned electron micrographs of a chalcogenide glass photonic crystal membrane fabricated by focused ion beam (FIB) milling of an AMTIR-1 chalcogenide glass film. left: film imaged at 0°. Right: picture of "W1" defect waveguide.

3. Experiment

Coupling to waveguides and cavities with very small mode field dimensions is a challenge that has attracted significant attention. One approach to coupling is evanescent coupling via silica nanowires [21-28]. Reference [22] describes the first realization of evanescent coupling to a microcavity, which in this case was a relatively large mode volume glass microsphere cavity. Reference [23] represents the first realization of tapered fiber coupling to a wavelength-scale semiconductor microcavity, in this case, a photonic crystal defect microcavity. The distinction between references [22] and [23] are in the microcavity material (glass vs. silicon), geometry (microsphere vs. photonic crystal), and mode volumes (hundreds of cubic wavelengths vs. less than one cubic wavelength). Reference [25] is a recent demonstration of evanescent coupling from a taper utilized to pump an InP photonic crystal microlaser and to collect its light emission. Reference [26] theoretically discusses coupling to a photonic crystal waveguide, while reference [27] can be considered as the first experimental demonstration of taper-PCWG coupling and [21] and [29] present detailed experimental results on this topic. Coupling efficiencies of over 90% have been demonstrated in silicon based photonic crystal waveguides [28]. Here, we use this approach to demonstrate efficient coupling to chalcogenide glass based photonic crystal waveguides.

Figures 3 and 4 illustrate the principle of operation of this coupling scheme [26, 29]. Figure 3 shows the experimental configuration for coupling. Figure 4 shows both the photonic

crystal waveguide dispersion relations calculated using a plane wave method (RSoft BandSolve) as well as that for the silica nanowire. Only TE-like modes (E field lying mainly in the slab) are included. The fiber taper is brought into close proximity with the photonic crystal waveguide, as illustrated in Fig. 3, such that the evanescent field overlaps with the waveguide mode field (see Fig. 1). Efficient coupling can occur in cases where phase matching between two modes that have appropriate transverse spatial overlap is accomplished. This occurs where the nanowire dispersion curve crosses the waveguide mode dispersion curve, as indicated by the dashed circles in Fig. 4, given by

$$\beta_{taper} = \beta_{PCWG} \, ,$$
(1)

where β_{taper}, β_{PCWG} are the propagation constants of the taper mode and the photonic crystal waveguide mode respectively. Note that in this case the mode is coupled in to a waveguide mode with group velocity in the negative direction, i.e. undergoes a contra-directional coupling.
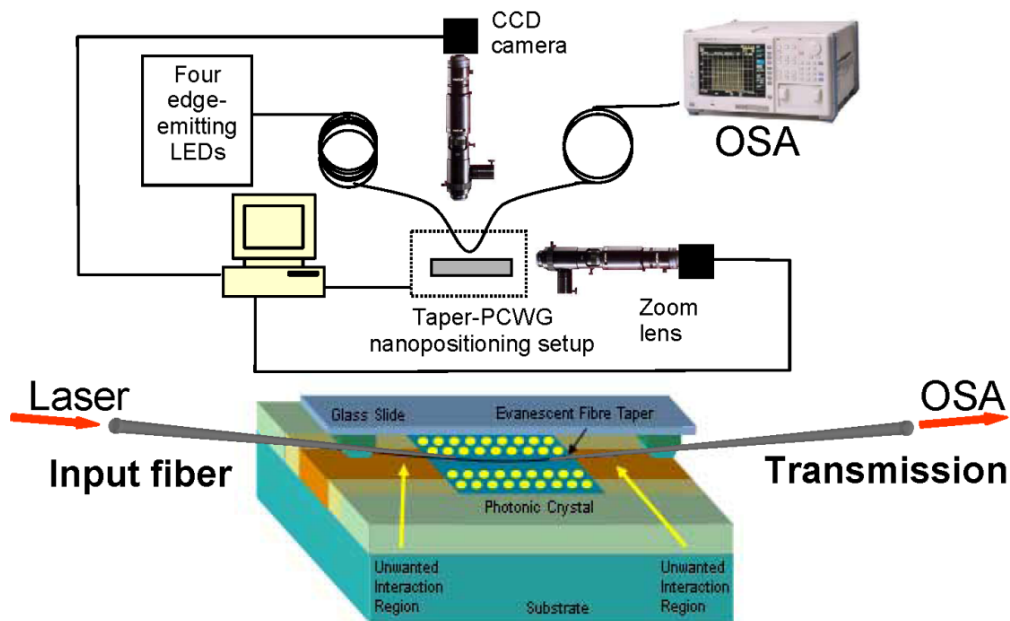
Fig. 3. (Top) Expimental measurement setup for evanescent coupling from silica nanowire to photonic crystal waveguide. (Bottom) Close up on the taper-PCWG alignment set up.

Since the nanowire mode field must extend evanescently for some length outside the silica core, typical nanowire diameters need to be sub-micron. The fiber tapers are manufactured using a procedure developed previously [30] and applied to both standard SMF and microstructured optical fibre (MOF). In this work, the fiber taper is manufactured using a computer controlled taper rig whilst butane flame brushing the fiber (SMF-28) under controlled tension. The taper profiles are tailored by the appropriate choice of flame brushing profile, elongation and rate of elongation. Taper waist lengths are typically a few mm, with outside diameters down to 800nm being achieved. The fiber taper is then glued onto a glass slide. The mounted fiber is spliced to two SMF-28 fibers allowing the in-situ measurements. Tapers manufactured in this way present virtually no insertion loss. The finished fiber taper is aligned above and parallel to the photonic crystal waveguide using an automated nanopositioning facility. Both vertical and lateral positioning is imaged with two microscopes

onto CCD cameras. Light is launched into the single mode fiber using a source consisting of four edge-emitting LEDs (Agilent EELED 83437A) covering the 1250-1700 nm bandwidth. In the taper region, light is adiabatically converted into the fundamental air-guided mode, allowing its evanescent tail to interact with the PCWG. The output end of the fiber is connected to an optical spectrum analyser (Agilent 86140B) where the transmission spectrum through the nanotaper is measured.
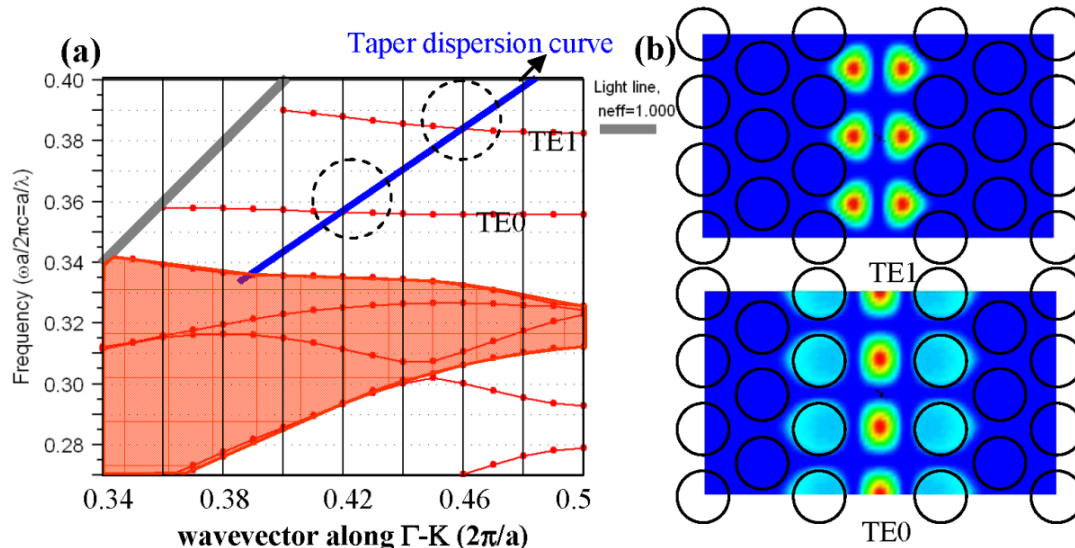
Fig. 4 (a) Dispersion diagram for the photonic crystal waveguides (red line) and the nanowire (blue line). Allowed bands of the surrounding photonic crystal are indicated by the shaded red region. Modes above the light line (grey line) that can couple to the continuum of radiative modes are not included. Dashed circle indicates modes for which phasematched coupling occurs. (b) Magnetic field profiles of the fundamental and first higher order PCWG modes.

Since typical taper waist lengths are at least a few mm (limited on the short side by the requirement of having adiabatic transition regions) whereas photonic crystal membrane lengths are at most a few hundred microns, there is the possibility of evanescent coupling to the surrounding substrate region. For this reason we introduced a curvature in the taper waist, limiting the interaction region to the photonic crystal itself. Once the fiber is tapered, a bowing is induced by releasing the tension in the fiber (the movable clamps holding the taper are driven towards each other about 0.1 mm). The taper is then mounted onto a glass slide (Fig. 3) and embedded in epoxy resin. A curved shape is then induced by applying a small pressure on the taper while the resin is still curing. The curved tapers manufactured in this way do not suffer extra losses compared to straight tapers. The main limitation of testing with curved tapers, compared to straight tapers [21], is that the diameter of the taper at the interaction region, (controlling the propagation constant of the taper mode interacting with the PCWG mode) could not be tuned, preventing the experimental mapping of the PCWG band structure using a single taper. Figure 5 shows pictures of a typical nanowire taper loop with a loop diameter of 500µm.
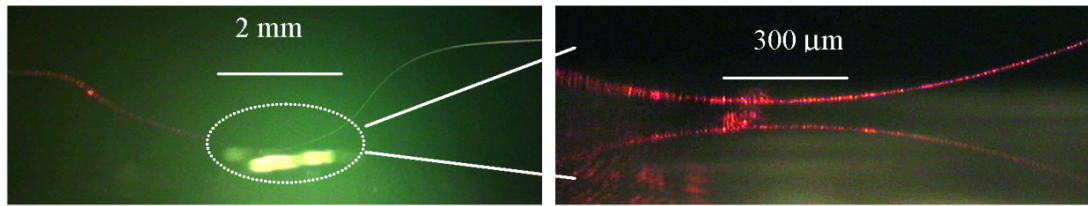
Fig. 5. Picture of the curved microfiber used in the experiment. The reflection of the taper on the sample is clearly visible in the close up.

4. Results and discussion

Figure 6 shows the transmission spectrum through the nanowire, with the nanowire placed at different separations from the PC waveguide, from >1.5μm (red curve) to direct contact (black curve). The spectra have been normalized to transmission through the taper in the absence of the PCWG. Clearly, the coupling efficiency is extremely sensitive to the nanowire – waveguide separation. First, it is evident that off-resonance loss increases when the taper aproaches the PCWG, and increases with increasing wavelength. One source of this is related to scattering that occurs at the taper-PCWG interface which is expected to be both broadband and higher at longer wavelengths where the evanescent field expands. A second contribution to the broadband loss occurs because the input source is unpolarized. The taper mode can couple to TM-like modes. In this frequency range, the TM dispersion curve closely resembles the taper dispersion curve, which results in a broadband codirectional coupling. Since the TM-like modes of the PCWG are very lossy, this manifests as an overall 3dB broadband loss. We estimate the overall off resonance loss at around 6 dB in line with observations.

From Figure 6, resonances corresponding to coupling to both the fundamental W1 guided mode (TE0) and the first W1 higher order mode (TE1) can be identified. We found that the strength of the coupling to these modes was highly dependent on precise lateral positioning of the taper. When the taper is displaced away from the PCWG, these two resonances disappear confirming the coupling to localized modes (i.e to PCWG modes). Because TE0 is even and TE1 is odd in the in-plane direction (Fig. 4(b)), we should expect that only TE0 can couple to the taper mode when the taper is placed at the center of the PCWG. However, unless the taper is accurately placed at the center of the PCWG along the overall interaction length, the antisymmetric nature of the TE1 mode is difficult to confirm, especially when one considers the lateral extension of this mode (~ 800nm). Nevertheless, we found that the strength of the coupling to the TE1 mode was highly dependent on precise lateral positioning of the taper.

#10099 - $15.00 USD   Received 22 December 2005; revised 23 January 2006; accepted 26 January 2006
(C) 2006 OSA   6 February 2006 / Vol. 14, No. 3 / OPTICS EXPRESS 1076

76
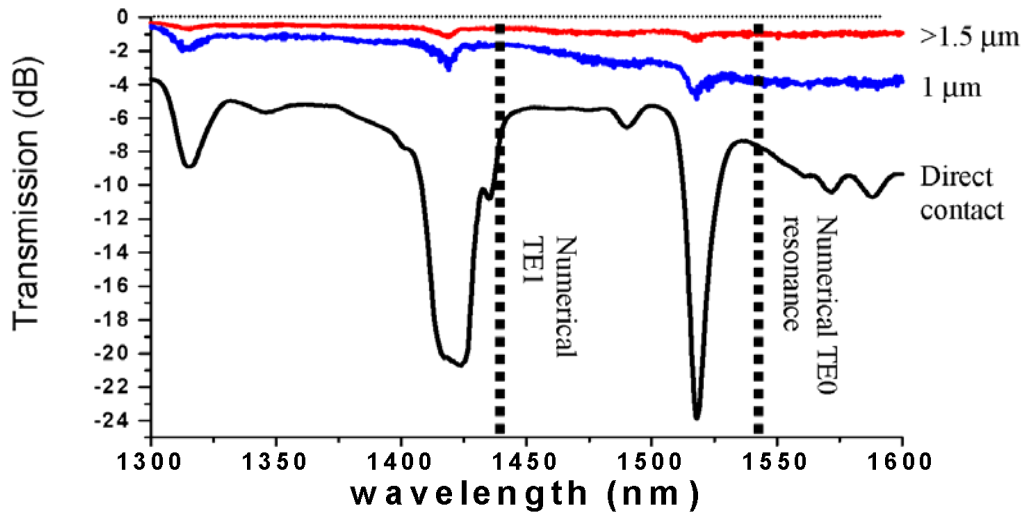
Fig. 6. Transmission spectrum of tapered nanowire, in close proximity to chalcogenide glass photonic crystal waveguide, showing resonant coupling. Red curve is for large (>1.5 μm) fibre-waveguide separation. Blue curve for a 1 μm separation. Black curve is for direct contact. Transmission spectra have been normalized to the transmission through the taper in absence of the PCWG.

The dotted lines in Fig. 6 indicate the resonant coupling wavelengths determined from mode dispersion relations calculated using a plane-wave method (Fig. 4). The strong narrow resonance near 1520nm is > 18 dB in depth, and reflects the resonant coupling to the fundamental TE0 mode of the PCWG, in relatively good agreement with the dispersion diagram prediction for the absolute wavelength. The residual difference of ~ 20nm arises from measurement uncertainty in the PC air hole radius as well as effects due to the thin silicon nitride layer and chalcogenide material dispersion, neither of which are taken into account in the modeling. The resonance depth of 18dB corresponds to more than 98% coupling efficiency, which is comparable to the best coupling efficiencies reported to date [28].

The 3dB width of this resonance is ~ 12nm. It is known [31] that the 3 dB bandwidth for a contradirectional coupler is approximately

$$\Delta\lambda = \frac{2\lambda_{res}^2\kappa}{\pi(n_{PCWG} + n_{taper})},$$ (2)

where λ_{res} is the resonant wavelength, κ the coupling coefficient and n_{PCWG} and n_{taper} are the group index values respectively of the PCWG and the taper. From Fig. 4, we estimate n_{PCWG} and n_{taper} to 30 and 1.3 respectively, yielding a coupling coefficient $\kappa \sim 0.24 \ \mu m^{-1}$. Contradirectional coupling is also characterized [21,31-32] by a transmission function of the form:

$$T = 1 - \tanh^2(\kappa L_c),$$ (3)

where L_c is the length of the taper/PCWG coupler. Given a transmission of 2% and a coupling coefficient $\kappa \sim 0.24 \ \mu m^{-1}$, the deduced coupling length is ~ 10 μm. The large broad resonance (~25nm) near 1420nm results from coupling to the first higher order mode (TE1) of the W-1 waveguide which is antisymmetric in the in-plane direction and is in good agreement with theory. Table 1 summarizes the experimental results.

77

Table 1. Experimental evanescent coupling results

	n_{PCWG}	λ_{res} (nm)	$\Delta\lambda$ (nm)	κ inferred (μm^{-1})	Insertion efficiency $(1\text{-}T)$
TE0	30	1520	12	0.24	> 98%
TE1	14	1425	25	0.3	~ 97%

5. Conclusions

In conclusion, we have demonstrated 98% coupling efficiency to a chalcogenide glass planar photonic crystal defect waveguide, fabricated by focused ion beam milling. We achieve good agreement with theoretical calculations of the coupling resonant wavelength and observe coupling to higher order photonic crystal modes. These results are on par with the best reported results in silicon photonic crystals and represent the first demonstration of coupling to PhCs made from highly nonlinear glass. This work represents a significant step in the drive towards Kerr nonlinearity based all-optical switching in photonic crystal nanocavities.

Acknowledgments

ELSEVIER

Characterisation of chalcogenide 2D photonic crystal waveguides and nanocavities using silica fibre nanowires

C. Smith[a],[*], C. Grillet[a], S. Tomljenovic-Hanic[a], E.C. Mägi[a], D. Moss[a], B.J. Eggleton[a], D. Freeman[b], S. Madden[b], B. Luther-Davies[b]

[a]Centre for Ultrahigh-Bandwidth Devices for Optical Systems (CUDOS)—A28, School of Physics, University of Sydney, Sydney, NSW 2006, Australia
[b]Centre for Ultrahigh-Bandwidth Devices for Optical Systems (CUDOS), The Australian Nation University, Canberra, ACT 0200, Australia

Abstract

We describe the fabrication of low-loss, highly flexible silica fibre nanowires which are used to characterise chalcogenide two-dimensional photonic crystal waveguide circuits and nanocavities. Localised coupling is achieved in good agreement with theory.
Crown Copyright © 2007 Published by Elsevier B.V. All rights reserved.

Keywords: Nanowires; Nonlinear; Evanescent; Nanocavities; Waveguides; Chalcogenide

1. Introduction

Photonic crystals (PhCs) are a class of optical structure, where the propagation of light is controlled by using a strong periodic modulation of the refractive index [1,2]. Large index contrast in a PhC gives rise to a photonic band-gap, within which light cannot propagate, providing a possible mechanism to trap and manipulate light for photonic circuitry.

Using the PhC mechanism, different types of optical circuitry components in these structures have been realised, including *waveguides* [3,4]: a defect row of holes that act as a conduit for light (see Fig. 1(b)), and *nanocavities:* compact (wavelength-scale) optical structures with high *Q*-factors and small mode volumes [5,6] (see Fig. 1(a)). PhC waveguides (PhCWGs) and PhC nanocavities (PhCNCs) have captivated much research interest for the pursuit of all-optical signal processing [7,8].

For the purpose of all-optical signal processing, an interesting glass type to fabricate PhC structures from is chalcogenide. Chalcogenide glasses are transparent in the infrared and posses a high refractive index sufficient for PhC devices (typically 2.4–2.7); they have high third-order nonlinearity (100–$1000 \times$ that of silica) and exhibit low two-photon absorption, making these materials promising for achieving low-power ultra-fast optical switching and optical logic [9]; and they can be processed using conventional lithographic techniques.

Recently, we reported initial results demonstrating highly efficient coupling to chalcogenide PhCWGs [10] (Fig. 2). This was accomplished via the use of evanescent coupling from silica fibre nanowires, made by extreme tapering of a standard single-mode fibre.

In this paper we describe the fabrication of highly flexible, low-loss silica nanowires that are used to achieve localised coupling to chalcogenide PhCWGs and PhCNCs. We demonstrate silica nanowires with sub-micron dimensions and virtually zero bend loss. We present detailed measurements of chalcogenide PhCWGs and PhCNCs, including coupling dependence upon polarisation and return-reflection differences between waveguides and cavities. We also observe a tuning effect on shifting the adjacent holes of a PhCNC. All together, these results promote understanding of the fundamental properties of the PhCWG and PhCNC structures, as well as the system's evanescent coupling behaviour.

2. Principle

The principle of evanescent coupling to PhCWG and PhCNC modes is illustrated in Fig. 2 [11]. The silica

---
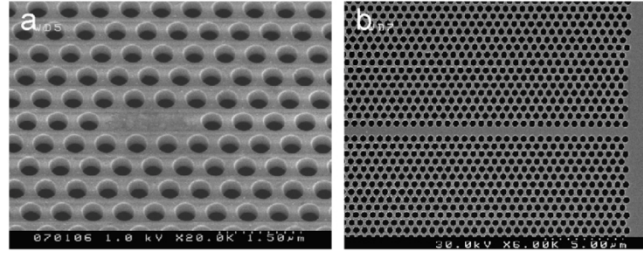
Fig. 1. Electron micrographs of: (a) PhCNC and (b) PhCWG.
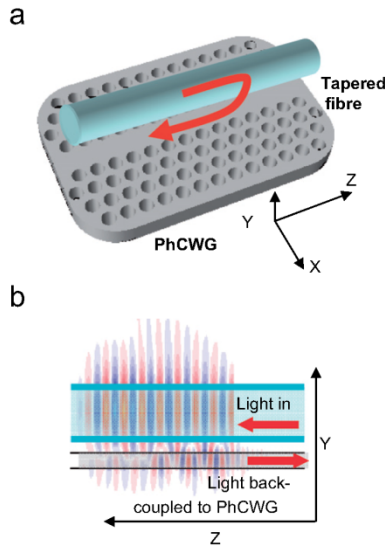
Fig. 2. Coupling scheme used: (a) schematic showing the coupling from a tapered fibre to PhCWG, (b) cross-sectional view along *YZ* axis of coupling mechanism between tapered fibre and PhCWG.

Fig. 3. Dispersion diagram for the PhC structure (red line) and the nanowire (blue line). Dashed circle indicates modes for which phase-matched coupling occurs.

single-mode fibre taper is brought into close proximity with a PhC structure. Coupling light from the taper to a PhC structure requires two necessary conditions: (i) phase matching between the fibre mode and the PhC mode, where the dispersion curve of the PhC structure crosses the dispersion curve of the fibre, given by

$$\beta_{\text{taper}} = \beta_{\text{PhC}}, \tag{1}$$

where β_{taper} and β_{PhC} are the propagation constants of the taper mode and the PhC structure mode, respectively (Fig. 3); and (ii) spatial overlap of the fibre mode and PhC structure modes such that they interact and phase matching may occur. In this geometry, we achieve contra-directional phase matching, where the signal is coupled into the PhC structure mode in the opposite direction of propagation [10].

Silica fibre nanowires offer an efficient scheme for achieving both conditions. Provided the dimensions are small enough (~1 μm), the mode field of the nanowire extends evanescently and interacts with the PhC structure (Fig. 2(b)).

It is important to note that the evanescent field must interact for coupling *locally* to the waveguide or cavity region of the PhC. Interaction outside the structure region will result in unwanted effects, in particular coupling to the substrate which manifests as loss. However, by exploiting the viscous nature of molten silica, we can shape the nanowire in various ways and overcome this problem, achieving highly localised coupling with minimal loss.

3. Fabrication

The silica fibre must be reduced in size to a 1 μm diameter in order to obtain an evanescently extended mode field, sufficient to couple into PhCWG and PhCNC. This was achieved by using a fibre tapering process to scale the outer diameter of a standard single-moded fibre down by 2 orders of magnitude. The tapering process uses a flame to soften the silica glass while it is simultaneously "stretched" to the desired size.

Two shapes of nanowires were used in the experiments to interact with the PhC structures; one with an induced "bow shape" (Fig. 4(a)) and another with an induced "loop" (Fig. 4(b)). Both of these shapes avoided unwanted

Fig. 4. Pictures of nanowire: (a) "bow-shaped" nanowire, (b) "looped" nanowire and (c) top view of looped nanowire above PhCWG.

Fig. 5. Experimental setup used: (a) entire rig from source to detector and (b) zoom-in illustration of aforementioned experiment.

then milled into the film with a Ga^+ FIB system. The triangular lattice consisted of 550 nm spaced holes of radius $\sim$200 nm ($0.36 \times$ Period); for further information on their fabrication, see Ref. [12].

4. Experiment and characterisation

The experimental setup used an edge-emitting LED source which fed through the system illustrated in Fig. 5(a). An adjustable polariser was put in place for the polarisation-dependent measurements. A circulator allowed the capability to obtain return-reflection measurements.

We investigated the polarisation dependence of the fundamental PhCWG mode. For the polarisation-dependant measurements, a transverse magnetic (TM) polarisation state was first obtained by placing the nanowire on a smooth metal surface (Au layer) and honing the adjustable polariser such that the transmission reached the point of maximum loss. This arises from a surface plasmonic effect [13]. Since only transverse electric (TE)-like (E field lying mainly in the slab) modes possess a band-gap in the wavelength range of interest, it is preferable to begin the experiment starting at a TE polarisation state. As such, the polariser was initially rotated 90° from TM to TE polarisation.

Polarisation dependence measurements as a function of wavelength can be viewed in Fig. 6. The nanowire was aligned parallel and in direct contact with the PhCWG. The polarisation was adjusted from a TE state to a TM state in increments of 15°. One can observe the change in transmission at the TE_0 mode resonance, almost completely disappearing for TM polarisation. This is in good agreement with $\cos\theta$ extinction between the two polarisation states and clearly confirms the TE polarisation state of the fundamental PhCWG mode.

For the following experiments, the polariser was set to select only TE-like modes. Return-reflection measurements were taken, comparing the effect of open and closed PhCWGs. Closed PhCWGs act as a linear defect with highly reflective mirrors at both terminations [14]. Fig. 7

interaction with the surrounding substrate while still achieving strong coupling to the PhC structures.

The bow-shaped nanowires were created by moving the ends of the tapered fibre closer together by 0.18 mm and then levering the fibre slightly to form the curve. Obtaining the looped nanowires involved a process of moving the tapered fibre ends closer together by 3 mm and subsequently twisting one end to induce a loop. The loop nominally formed at the taper waist where the fibre diameter is smallest. The distance the fibres were pushed together formed an approximate circumference length. Once the loop was formed, the ends were then moved back, tightening the loop to an approximate circumference of 0.4 mm. Both forms of nanowire were each mounted onto a microscope slide (Fig. 5(b)) and prepared for experimental use.

The sample PhC devices used for our characterisation experiments consisted of a chalcogenide film of thickness 300 nm, composed of AMTIR-1 glass ($Ge_{33}As_{12}Se_{55}$—refractive index $\sim$2.7@1.55 μm). The PhC structures were

Fig. 6. Graph displaying the dependence of polarisation on coupling to the PhCWG. Maximum depth at TE, minimum at TM.
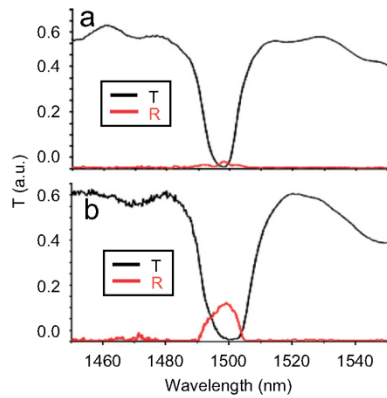
Fig. 7. Linear transmission (black) and reflection (red) spectra at the TE_0 mode for: (a) closed PhCWG structure (b) open PhCWG structure.

shows both normalised and transmission measurements as a function of wavelength when the nanowire is aligned, parallel and in close contact with the PhCWG. In the absence of mirrors (open PhCWG), the normalised reflected power at the resonance is negligible (Fig. 7(a)). In the presence of the mirrors, a reflected power of $\sim20\%$ is measured back into the nanowire (Fig. 7(b)). This confirms the contra-directional nature of the coupling scheme: light back-couples to the TE_0 mode of the PhCWG, gets reflected by the end mirror and finally couples to the backward-propagating mode of the nano-wire. The coupling efficiency and the mirror reflectivity will be detailed elsewhere.

Coupling to PhCNCs was achieved by using the looped nanowires to couple locally to the very small, several-microns in size, structure. The PhCNCs investigated had the structure type that consisted of three missing holes in a triangular lattice with period $a = 540$ nm and a slight lateral displacement of the adjacent holes to the cavity (see Fig. 8(a)) in order to increase the intrinsic Q-factor [5,15]. The measurements were taken with the nanowire in direct contact and parallel to the main cavity direction. Resonances were observed in the transmission spectrum around 1640 nm. We observed an expected drift of the resonances corresponding to a shift d of the adjacent holes, which alters the effective length of the cavity [15] (see Fig. 8(b)). These resonances display experimental Q ranging from 500 ($d/a = 0.18a$) to 800 ($d/a = 0.2a$) with transmission drop ranging from 1.7 to 2.2 dB. These results represent the first demonstration of direct coupling to wavelength-scale nanocavities made in Chalcogenide.

5. Conclusion

In conclusion, we have demonstrated the fabrication of highly flexible, low-loss silica nanowires that are used to achieve localised coupling to chalcogenide PhCWGs and
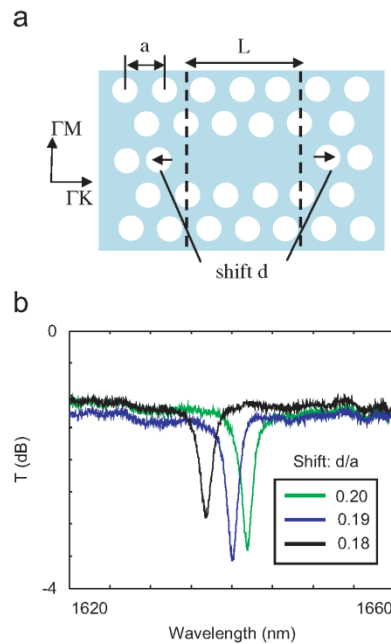
Fig. 8. (a) layout of the nanocavity structure, and (b) transmission spectra for coupling to three different PhCNC, each trace corresponding to a varying displacement of adjacent holes to the cavity.

PhCNCs. We have presented detailed measurements of chalcogenide PhCWGs and PhCNCs, including coupling dependence upon polarisation as well as return-reflection differences between waveguides and cavities. We were able to couple to small modal volume 2D PhCNCs made in Chalcogenide and to observe the tuning effect on the resonant wavelength due to a shift in the PhCNC adjacent hole position. Combined, the results provide a strong basis in the understanding of these structures and represent a significant step in the drive towards Kerr nonlinearity-based all-optical switching cavities.

References

[1] E. Yablonovitch, Phys. Rev. Lett. 58 (1987) 2059.
[2] S. John, Phys. Rev. Lett. 58 (1987) 2486.
[3] M. Loncar, et al., J. Lightwave Technol. 18 (2000) 1402.
[4] Y. Desieres, et al., J. Appl. Phys. 92 (2002) 2227.
[5] Y. Akahane, et al., Nature 425 (2003) 944.
[6] K. Srinivasan, et al., Phys. Rev. B 70 (2004) 081306.
[7] T. Tanabe, et al., Appl. Phys. Lett. 87 (2005) 151112.
[8] P.E. Barclay, et al., Opt. Express 13 (2005) 801.
[9] A. Zakery, et al., J. Opt. Soc. Am. B 22 (2005) 591.
[10] C. Grillet, et al., Opt. Express 14 (2006) 1070.
[11] P.E. Barclay, et al., Opt. Lett. 29 (2004) 697.
[12] D. Freeman, et al., Opt. Express 13 (2005) 3079.
[13] R. Willsch, Electron. Lett. 26 (1990) 1113.
[14] X. Letartre, et al., Appl. Phys. Lett. 79 (2001) 2312.
[15] C. Sauvan, P. Lalanne, J.P. Hugonin, Phys. Rev. B 71 (2005) 165118.

Characterizing photonic crystal waveguides with an expanded k-space evanescent coupling technique

Michael W. Lee[1*], Christian Grillet[1], Christopher G. Poulton[2], Christelle Monat[1],
Cameron L. C. Smith[1], Eric Mägi[1], Darren Freeman[3], Steve Madden[3],
Barry Luther-Davies[3], and Benjamin J. Eggleton[1]

[1]*Centre for Ultrahigh-bandwidth Devices for Optical Systems (CUDOS), School of Physics,
University of Sydney, Sydney, NSW 2006, Australia*
[2]*Centre for Ultrahigh-bandwidth Devices for Optical Systems (CUDOS), and Department of Mathematical Sciences,
University of Technology, Sydney, P.O. Box 123, Broadway NSW 2007, Australia*
[3]*Centre for Ultrahigh-bandwidth Devices for Optical Systems (CUDOS), Laser Physics Centre,
Australian National University, Canberra, ACT 0200, Australia*
Corresponding author: mlee@physics.usyd.edu.au

Abstract: We demonstrate a direct, single measurement technique for characterizing the dispersion of a photonic crystal waveguide (PCWG) using a tapered fiber evanescent coupling method. A highly curved fiber taper is used to probe the Fabry-Pérot spectrum of a closed PCWG over a broad k-space range, and from this measurement the dispersive properties of the waveguide can be found. Waveguide propagation losses can also be estimated from measurements of closed waveguides with different lengths. The validity of this method is demonstrated by comparing the results obtained on a 'W1' PCWG in chalcogenide glass with numerical simulation.

©2008 Optical Society of America

OCIS codes: (130.5296) Photonic crystal waveguides; (130.2790) Guided waves; (060.2300) Fiber measurements

References and links

1. J.-M. Lourtioz, H. Benisty, V. Berger, J.-M. Gerard, D. Maystre, and A. Tchelnokov, *Photonic Crystals: Towards Nanoscale Photonic Devices* (Springer, 2005).
2. S. McNab, N. Moll, and Y. Vlasov, "Ultra-low loss photonic integrated circuit with membrane-type photonic crystal waveguides," Opt. Express **11**, 2927-2939 (2003).
3. T. F. Krauss, "Planar photonic crystal waveguide devices for integrated optics," Phys. Status Solidi (a) **197**, 688-702, (2003).
4. T. J. Karle, Y. J. Chai, C. N. Morgan, I. H. White, and T. F. Krauss, "Observation of pulse compression in photonic crystal coupled cavity waveguides," J. Lightwave Technol. **22**, 514-519 (2004).
5. A. Martinez, F. Cuesta, and J. Martí, "Ultrashort 2-D photonic crystal directional couplers," IEEE Photon. Technol. Lett. **15**, 694-696 (2003).
6. M. Soljačić, S. G. Johnson, S. Fan, M. Ibanescu, E. Ippen, and J. D. Joannopoulos, "Photonic-crystal slow-light enhancement of nonlinear phase sensitivity," J. Opt. Soc. Am. B **19**, 2052-2059 (2002).
7. M. Notomi, K. Yamada, A. Shinya, J. Takahashi, C. Takahashi, and I. Yokohama, "Extremely large group velocity dispersion of line-defect waveguides in photonic crystal slabs," Phys. Rev. Lett. **87**, 253902 (2001).
8. A. Gomez-Iglesias, D. O'Brien, L. O'Faolain, A. Miller, and T. F. Krauss, "Direct measurement of the group index of photonic crystal waveguides via Fourier transform spectral interferometry," Appl. Phys. Lett. **90**, 261107 (2007).
9. R. J. P. Engelen, T. Karle, H. Gersen, J. Korterik, T. Krauss, L. Kuipers, and N. van Hulst, "Local probing of Bloch mode dispersion in a photonic crystal waveguide," Opt. Express **13**, 4457-4464 (2005).
10. N. Le Thomas, R. Houdré, M. V. Kotlyar, D. O'Brien, and T. F. Krauss, "Exploring light propagating in photonic crystals with Fourier optics," J. Opt. Soc. Am. B **24**, 2964-2971 (2007).
11. M. Notomi, A. Shinya, K. Yamada, J. Takahashi, C. Takahashi, and I. Yokohama, "Structural tuning of guiding modes of line-defect waveguides of SOI photonic crystal slabs," IEEE J. Quantum Electron. **38**, 736-742 (2002).

12. X. Letartre, C. Seassal, C. Grillet, P. Rojo-Romeo, P. Viktorovitch, M. Le Vassor d'Yerville, D. Cassagne, and C. Jouanin, "Group velocity and propagation losses measurement in a single-line photonic-crystal waveguide on InP membranes," Appl. Phys. Lett. **79**, 2312 (2001).

13. J. C. Knight, G. Cheung, F. Jacques, and T. A. Birks, "Phase-matched excitation of whispering-gallery-mode resonances by a fiber taper," Opt. Lett. **22**, 1129-1131 (1997).

14. P. E. Barclay, K. Srinivasan, M. Borselli, and O. Painter, "Efficient input and output fiber coupling to a photonic crystal waveguide," Opt. Lett. **29**, 697-699 (2004).

15. P.E. Barclay, K. Srinivasan, M. Borselli, and O. Painter, "Probing the dispersive and spatial properties of photonic crystal waveguides via highly efficient coupling from fiber tapers," Appl. Phys. Lett. **85**, 4-6 (2004).

16. K. Srinivasan, P. E. Barclay, M. Borselli, and O. Painter, "Optical-fiber based measurement of an ultra-small volume high-Q photonic crystal microcavity," Phys. Rev. B **70**, 081306(R) (2004).

17. M. Fujii, C. Koos, C. Poulton, I. Sakagami, J. Leuthold and W. Freude, "A simple and rigorous verification technique for nonlinear FDTD algorithms by optical parametric four-wave mixing," Microwave Opt. Technol. Lett. **48**, 88-91 (2005).

18. C. Koos, M. Fujii, C. G. Poulton, R. Steingrueber, J. Leuthold, and W. Freude, "FDTD modelling of dispersive nonlinear ring resonators: accuracy studies and experiments," IEEE J. Quantum Electron. **42**, 1215-1223 (2006).

19. G. J. Pearce, T. D. Hedley, and D. M. Bird, "Adaptive curvilinear coordinates in a plane-wave solution of Maxwell's equations in photonic crystals," Phys. Rev. B, **71**, 195108 (2005).

20. C. Grillet, C. Monat, C. L. Smith, B. J. Eggleton, D. J. Moss, S. Frédérick, D. Dalacu, P. J. Poole, J. Lapointe, G. Aers, and R. L. Williams, "Nanowire coupling to photonic crystal nanocavities for single photon sources," Opt. Express **15**, 1267-1276 (2007).

21. D. Freeman, C. Grillet, M. W. Lee, C. L. C. Smith, Y. Ruan, A. Rode, M. Krolikowska, S. Tomljenovic-Hanic, C. M. De Sterke, M. J. Steel, B. Luther-Davies, S. Madden, D. J. Moss, Y. H. Lee, and B. J. Eggleton, "Chalcogenide glass photonic crystals," Photonics Nanostruct. Fundam. Appl. **6**, 3-11 (2008).

22. M. W. Lee, C. Grillet, C. L. C. Smith, D. J. Moss, B. J. Eggleton, D. Freeman, B. Luther-Davies, S. Madden, A. Rode, Y. Ruan, and Y. Lee, "Photosensitive post tuning of chalcogenide photonic crystal waveguides," Opt. Express **15**, 1277-1285 (2007).

23. E. Kuramochi, M. Notomi, S. Hughes, A. Shinya, T. Watanabe and L. Ramunno, "Disorder-induced scattering loss of line-defect waveguides in photonic crystal slabs," Phys Rev B. **72**, 161318 (2005).

24. S. Combrié, E. Weidner, A. DeRossi, S. Bansropun, S. Cassette, A. Talneau, and H. Benisty, "Detailed analysis by Fabry-Pérot method of slab photonic crystal line-defect waveguides and cavities in aluminium-free material system," Opt. Express **14**, 7353-7361 (2006).

25. D. Y. Choi, S. Madden, A. Rode, R. Wang, and B. Luther-Davies, "Fabrication of low loss $Ge_{33}As_{12}Se_{55}$ (AMTIR-1) planar waveguides," Appl. Phys. Lett. **91**, 011115 (2007).

26. J. Schrauwen, D. Van Thourhout, and R. Baets, "Focused-ion-beam fabricated vertical fiber couplers on silicon-on-insulator waveguides," Appl. Phys. Lett. **89**, 141102 (2006).

27. L. O'Faolain, T. P. White, D. O'Brien, X. Yuan, M. D. Settle, and T. F. Krauss, "Dependence of extrinsic loss on group velocity in photonic crystal waveguides," Opt. Express **15**, 13129-13138 (2007).

28. J. Li, T. P. White, L. O'Faolain, A. Gomez-Iglesias, and T. F. Krauss, "Systematic design of flat band slow light in photonic crystal waveguides," Opt. Express **16**, 6227-6232 (2008).

1. Introduction

Planar photonic crystals, which are formed by creating a periodic array of air holes in a thin dielectric slab, present an attractive platform for the development of compact optical devices. This is due to the ability to control light on the wavelength scale within defects in the lattice [1]. Waveguide defects are of interest both as interconnects for optical integrated circuits [2] and also as functional devices in their own right [3]. The broad ability to engineer the dispersion of these waveguides, due to the many degrees of freedom in their design, has led to applications in pulse compression [4], compact couplers [5] and broadband slow light waveguides for optical buffers and enhanced light/matter interaction [6].

Experimentally characterizing the dispersive properties of novel waveguide designs is an important step in realizing some of the potential applications of photonic crystal waveguides. Previously, several techniques have been employed including observation of Fabry-Pérot (FP) resonances in the transmission spectrum from photonic crystal/ ridge waveguide interfaces [7], analysis of fringes from an external Mach-Zehnder interferometer [8], phase sensitive near field microscopy [9] and Fourier optics techniques [10]; although those techniques have proven their ability to retrieve the dispersion curve, they require the presence of conventional index guiding access waveguides that 1) can limit the insertion efficiency unless an elaborate and multistep manufacturing process (such as inverse tapers [3, 11]) is employed, 2) can hinder the measurements due to coupling issues in the slow light regime between the photonic

crystal waveguide (PCWG) and the ridge waveguide. Another technique, based on observing FP resonances in the photoluminescence spectra of closed PCWGs has also been demonstrated [12]. This technique does not require access waveguides but relies on the use of internal emitters such as quantum wells or quantum dots, making it incompatible with passive structures. Evanescent coupling using a tapered fiber, which has been used to efficiently probe a variety of microphotonic devices [13], including PCWGs [14], has also been used to extract the dispersion properties without the need of integrated access waveguides [15]. However, this technique requires multiple measurements, while probing the structure with a variable taper diameter.

In this work we demonstrate a simple technique for characterizing the dispersion and group velocity of a photonic crystal waveguide that is based on tapered fiber evanescent coupling and that requires only a single spectral measurement. We measure the FP spectrum of a closed PCWG using a tapered fiber and, noting that the resonances are approximately equally spaced in reciprocal-space (*k*-space), we retrieve the dispersion of the waveguide, whose shape is in good agreement with simulation. This method crucially employs a taper with a small radius of curvature which leads to an increased coupling range in *k*-space. We also show that our approach can be used to estimate the waveguide propagation losses. Because it provides a quick and simple characterization of the waveguide spectral properties, our technique can assist the development of novel waveguide designs for dispersion engineering in photonic crystals without the need of integrated access waveguides or internal light sources.
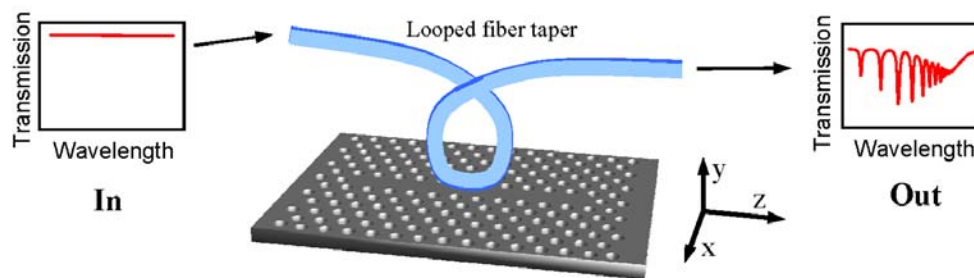
Fig. 1. A schematic of the setup used to characterize the photonic crystal waveguide. A highly curved taper is brought into close proximity with a closed photonic crystal waveguide and the transmission spectrum through the taper is monitored. Dips in the spectrum appear where light is coupled from the taper and into the waveguide.

2. Principle

Figure 1 summarizes the method that we propose for characterizing the dispersion and propagation loss of a PCWG. The figure depicts a highly curved fiber taper (~25μm radius of curvature) in close proximity to a closed PCWG. A closed waveguide, with photonic crystal mirrors at each end, forms a long linear cavity which supports Fabry-Pérot (FP) resonances based on the guided modes of the waveguide. Fiber tapers have been used to probe a range of microcavities including whispering gallery mode resonators [13] and photonic crystal resonators [16]. Here, the taper is used to excite the FP modes, which are observed as dips in the transmission spectrum of the taper since this is where optical power is coupled out of the taper and into the closed waveguide. The taper transmission spectrum allows us to measure the wavelengths and quality factors (Q) of the FP resonances.

2.1 Broadband evanescent coupling

Evanescent coupling between two modes can occur when they have the same frequency and are phase matched, i.e. when there is some overlap of their *k*-space distribution. This

85

translates into an overlap between the two modes on a band diagram. In the case of an infinitely long taper and waveguide there is only a single point of intersection between the two continuous dispersion curves. In contrast, using a highly curved taper results in an expanded *k*-space distribution of the taper mode at the plane of the sample, and a closed waveguide gives rise to a series of discrete FP resonances in place of the continuous waveguide dispersion curve. The bandwidth of coupling achieved depends on both the degree of *k*-space broadening of the taper mode and the average slope of the waveguide dispersion curve.
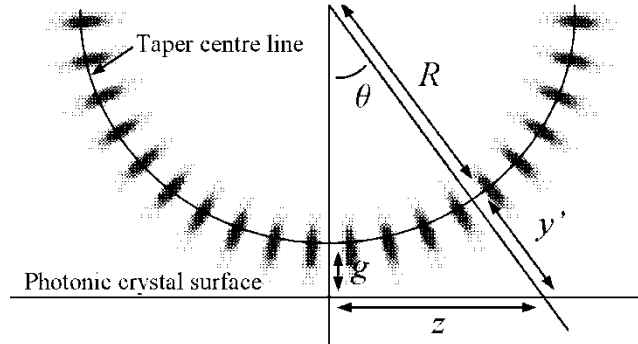
Fig. 2. The coordinate system used for mapping the fields of the curved taper onto the photonic crystal surface. The taper mode is shown for reference.

To illllustrate the underlying principle, we numerically examine the *k*-space extent of the curved taper mode and its overlap with the FP resonances of a closed W1 waveguide (a single row of holes removed in a triangular lattice). The extent of the curved-taper mode fields in the k_z direction can be calculated to a good approximation by directly mapping the fields from the coordinate system of the taper to that of a plane parallel to the photonic crystal. In doing so we assume that the curvature remains sufficiently small that the transverse mode profile is not significantly perturbed from that of a straight waveguide. If a field component of the uncurved taper mode is represented in local coordinates by $f(x',y')$, then the Fourier transform of the fields along the *z*-axis is given by:

$$\tilde{F}(k_z) = \int_{-\infty}^{\infty} f(0,\sqrt{z^2 + (R+g)^2} - R)\exp(i\beta R \arctan\frac{z}{R+g})e^{-ik_z z}dz \qquad (1),$$

where β is the propagation constant of the taper at the waist, and the other variables are as shown in Fig. 2. This gives the *k*-space distribution of the curved taper mode in the *z*-direction at the photonic crystal surface. These calculations are summarized in Fig. 3(a), which plots the approximate size (to $1/e^2$) of the taper mode *k*-space distribution as a function of the radius of curvature. The taper waist was 0.8μm and the wavelength considered was 1550nm. The *k*-space extent, and hence the ability to characterize the PCWG, clearly increases as the curvature radius is reduced.

The resonances of the closed waveguide were computed using a finite-difference time domain (FDTD) algorithm [17], implemented on a large parallel cluster. The frequencies of the resonances for an 80 period W1 type closed waveguide were found by examining the spectral response of the structure to a broadband excitation. The mode fields were then computed at the resonant peaks and the spatial frequencies of the modes along the waveguide axis were evaluated numerically. The computational demands of simulating such a large structure meant that the modes in the slow group velocity band edge (beyond $k_z \sim 0.4$) could not be accurately calculated. Thus we used plane wave expansion calculations for comparison with our experimental results. The result of these calculations is summarized in Fig. 3(b), which shows the expanded *k*-space distribution of the curved taper mode and its overlap with the discrete FP resonances. On the same graph we show the dispersion curve of the fundamental waveguide mode, as calculated using the plane-wave method. The discrepancy

between the two curves is due to the limitations in discretization of the two methods [18, 19]; we can nevertheless see from this graph that the resonances of the complete structure lie to a good approximation on the dispersion curve of the infinite waveguide. We also observe that using a highly-curved taper allows a large portion of the PCWG dispersion curve to be probed in a single measurement (>50% of the k-space below the light line at telecommunications wavelengths).
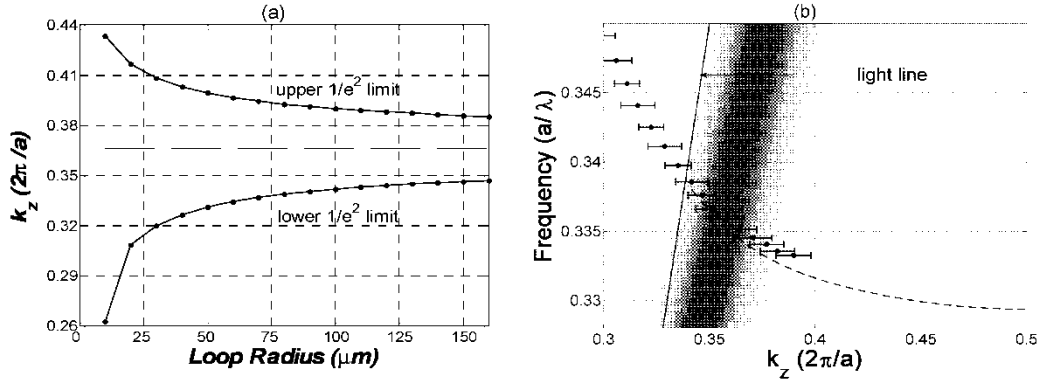
Fig. 3. (a). The k-space interval (to $1/e^2$ of the peak) covered by the curved taper mode as a function of the radius of curvature. Here, the taper waist diameter is 0.8μm and the wavelength is 1550nm. (b). The case of a tightly looped taper (47μm loop diameter) and closed waveguide. The k-space distribution of the taper mode is shown by the shaded region and the FP modes of the closed waveguide are represented by the points and horizontal bars, which show the approximate k-space extension of the modes. The dashed line is a plane wave calculation of the waveguide mode.

2.2 Characterizing the dispersive properties

The dispersive properties of the PCWG can be obtained by measuring the wavelengths of the FP resonances in the closed waveguide. If we assume that there is no phase change upon reflection from the cavity ends (effectively ignoring the penetration depth into the bulk photonic crystal region), then the k-space interval between each successive resonance is $\Delta k = 2\pi/2l$, where l is the length of the closed waveguide. The dispersion curve of the waveguide mode may be reconstructed with the following procedure: the wavelengths of the resonances are converted to reduced frequency, $f = a/\lambda$, where a is the lattice constant of the photonic crystal, then these frequencies are plotted in order with a spacing of Δk. This provides a reconstruction of the waveguide dispersion curve, however the absolute wavevector must be estimated by knowledge of the taper k-space distribution or by comparison with simulation.

The group velocity of the PCWG mode as a function of wavelength may be estimated by measuring the free spectral range (FSR) between the FP resonances and applying the formula;

$$\frac{v_g}{c} = \frac{2l\Delta\lambda_{FSR}}{\lambda_0^2} \tag{2},$$

where $\Delta\lambda_{FSR}$ is the free spectral range between two adjacent resonances and λ_0 is the central wavelength between the resonances. This method is similar to those presented in Refs. [7, 12], however, in those works either an internal light source, or free space coupling is required to excite the FP modes.

2.3 Characterizing propagation loss

Examination of the Q-factors and coupling strengths of the FP resonances can give us a direct estimate of the photon lifetime in the closed waveguide and thus an estimate of the propagation losses. In our particular case, and for moderately slow group velocities, the derived intrinsic Q can be related to two sources of losses: the propagation losses (including

both absorption and scattering loss) and out of plane radiation losses incurred at the cavity terminations (R<1, where R is the intensity reflectivity). It follows [12]:

$$\frac{2\pi}{\lambda Q} = \frac{\alpha_{prop}}{n_g} + \frac{1-R}{n_g L}$$

(3)

By comparing the Q obtained from different cavity lengths, one can determine the reflection at the closed waveguide ends and therefore extract the propagation losses as a function of wavelength and group velocity.

3. Experimental setup

The experimental setup used in this work consisted of a nanopositioning stage, a looped fiber taper and a spectral measurement system, made up of a broadband light source (Erbium ASE) and an optical spectrum analyzer (Agilent 86140B set to 60pm resolution bandwidth). The nanopositioning stage could be used to control the position of the taper in increments of ~100nm and we were able to align the taper with the waveguide leaving a small air gap between them. Due to some mechanical flexibility in the taper and the presence of attractive forces between the taper and the sample, estimating the size of the gap was difficult. All measurements, unless otherwise noted, were made with the taper out of contact with the sample. A linear polarizer was set so that the light in the taper was TE polarized at the sample.

The tapers used in this work were created by flame brushing and elongating a standard single mode (at 1550nm) fiber using the technique described in [20]. The loop was formed by introducing some slack into the taper and applying a twist to form the loop. The loop was then tightened by removing most of the slack from the taper. The resultant tapers have waist diameters ~0.8μm with a typical loop radius of ~25μm.

The test photonic crystal sample was fabricated in AMTIR-1 ($Ge_{33}As_{12}Se_{55}$) glass by focused ion beam (FIB) milling using the method described in [21]. The target parameters for the lattice were a period of 520nm, a hole radius of 0.3 times the period and a slab thickness of 300nm. In addition to the AMTIR-1 membrane there was also a 30nm thick Si_3N_4 layer on the side of the membrane closest to the taper. The nominal refractive index for the thin film, ultrafast pulsed laser deposited, AMTIR-1 layer was 2.68. Waveguides were formed in the lattice by removing a single row of holes and closed waveguides were available with 80, 120 and 160 holes removed (cavity lengths of 41.6μm, 62.4μm and 83.2μm respectively). There were 21 rows of holes on each side of the waveguides and 20 at each of the ends.

88

4. Results and discussion
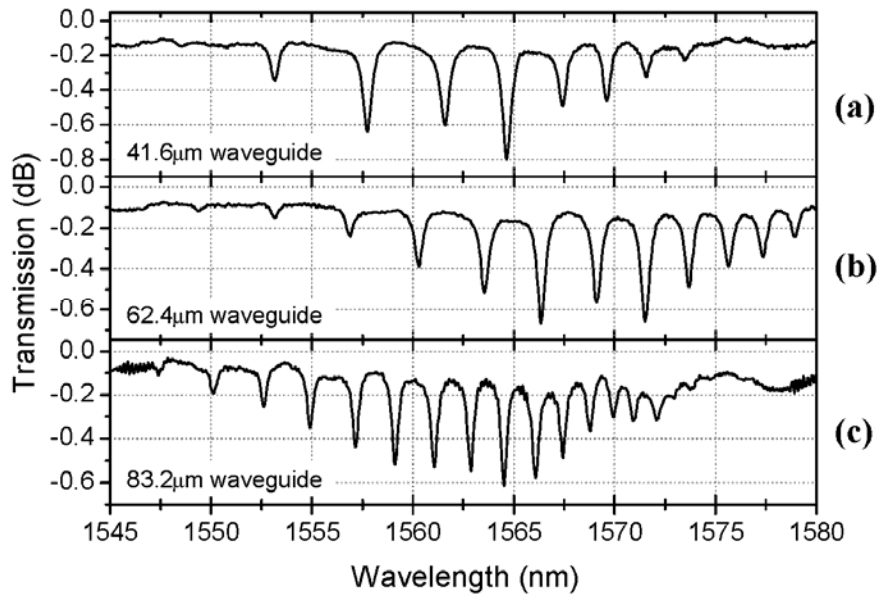
Fig. 4. The coupling spectra obtained for each of the three lengths of closed waveguide. Dips represent coupling to the FP modes of the closed waveguide.

The evanescent coupling spectrum for each of the three waveguide lengths is shown in Fig. 4. Each spectrum exhibits a series of dips which correspond to the FP resonances of the closed waveguides. The taper loop radius was ~40μm and the waist diameter was ~0.8μm for these measurements. As expected, the average FSR decreased for longer closed waveguides. To confirm that the resonances we observe are related to the closed waveguide, and not to the taper, we measured the coupling spectra of the 160 hole closed waveguide using two different looped tapers. Figure 5 shows the spectra obtained with the two tapers, taper 1 corresponds to the taper used above, while taper 2 had a loop radius of ~24μm and a waist diameter of ~0.8μm. In both traces the FP resonances occur at the same wavelengths, although the smaller loop diameter of taper 2 allowed it to couple over a larger wavelength range, as predicted in section 2.1. In this case the measurement with taper 2 was taken with the taper in contact with the sample, however, no difference in the coupling range was observed with the taper in or out of contact.
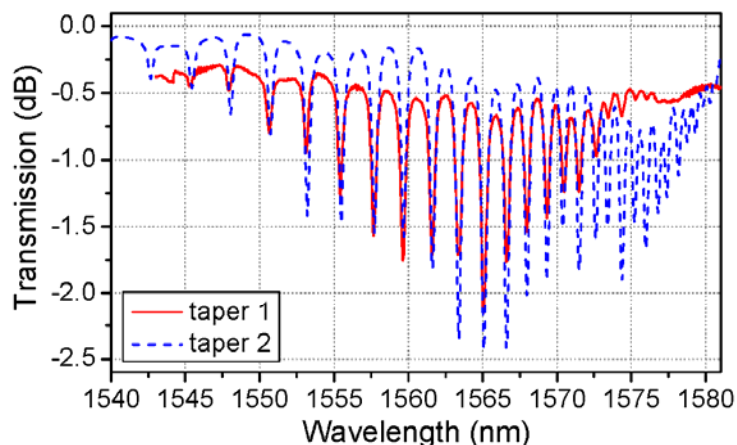
Fig. 5. The coupling spectra obtained for the 160 hole closed waveguide using two different looped tapers. The FP resonances appear at the same wavelengths in each case.

89

To demonstrate the reconstruction of the PCWG dispersion curve, we take the data from taper 2 in Fig. 5 and apply the method described in section 2.2. The resulting dispersion curve is shown in Fig. 6(a). The shape of the experimentally retrieved curve shows a good match with the simulated curve. The simulation parameters were the same as the sample target parameters, except the radius of the holes was reduced to 0.28a. We believe that this lies within the uncertainty for the real fabricated samples. The simulation was performed using the RSoft bandSOLVE program, which uses the plane wave expansion method.
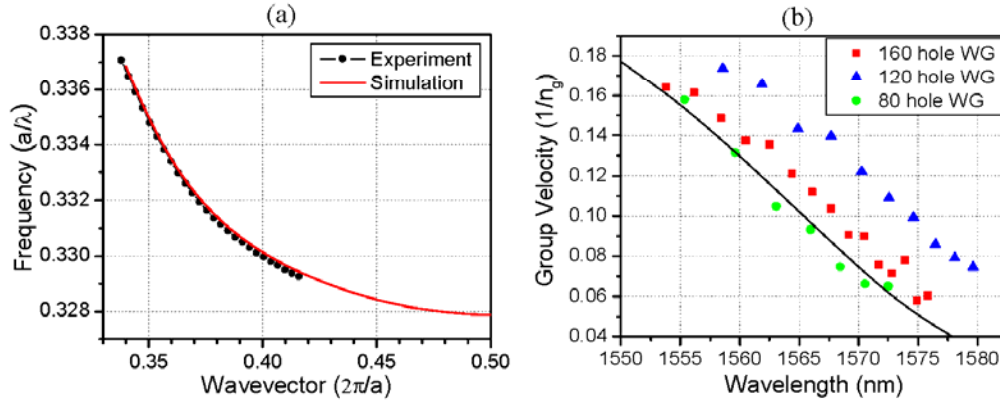
Fig. 6. (a). Comparison between the experimentally reconstructed dispersion curve of the W1 waveguide, and a plane wave simulation for that system. The absolute wavevectors for the experimental curve were determined by matching the small k values with simulation. (b) Comparison of the experimentally obtained group velocity for each of the three lengths of waveguide with a plane wave simulation (continuous line).

The group velocity of the waveguide mode as a function of wavelength was evaluated for each of the three waveguide lengths using Eq. (2). The wavelengths of the FP resonances were taken from Fig. 4 and the results for the group velocities are plotted in Fig. 6(b). The obtained group velocities show good agreement with the simulated curve, where the slope of each data set matches the simulation well. The measured group velocity varied in an approximately linear fashion with wavelength from approximately c/5 to c/20. The offset between the different waveguide lengths may be explained by small variations between the parameters of each sample, e.g. refractive index due to photosensitive processes [22]. The simulation data is the same as for the dispersion curve in Fig. 6(a).

Figure 7(a) shows the intrinsic Q [20] obtained for the closed waveguide samples with respectively 80 and 160 holes removed. By using Eq. (3) and comparing the two lengths of closed waveguide, the propagation loss was estimated as shown in Fig. 7(b). Propagation losses ranging from about 130dB/cm for a n_g of 8 till 370 dB/cm for a n_g of 20 can be estimated. Those values are far from state of the art values obtained in Si [23] or GaAs [24] PCWGs. The lower refractive index of the AMTIR-1 compared to Si or GaAs can not explain this discrepancy on its own. Measurements on bulk glasses indicate that the intrinsic loss of AMTIR-1 at 1550nm is around 0.1 dB/cm and low propagation losses down to 0.3 dB/cm were obtained in rib AMTIR-1 waveguides fabricated using a photolithography and plasma etching process [25] ruling out the AMTIR-1 as responsible for these large propagation losses. Extrinsic scattering losses (due to surface irregularities and non homogeneity) are believed to play a negligible role in those losses, especially considering the high degree of quality of these structures (smooth sidewalls, uniform lattice [21]). We are still investigating the cause of these enhanced losses but a possible explanation may be increased absorption resulting from incomplete removal of the carbon layer used to prevent charge build up during FIB milling, or alternatively undesired Ga implantation resulting from FIB milling [26]. Note that in Ref. [26], large optical losses on the order of 1dB/μm have been reported in 220 nm thick Si

waveguide gratings milled with a FIB (resulting in Ga ion implantation), about four orders of magnitude larger than that for non-implanted waveguides. The losses measured in our sample, however, should not be considered as an intrinsic limitation of PCWGs in chalcogenide glasses. Despite the high propagation losses, believed to be dominated by absorption, one can notice the expected increase of the propagation losses with n_g. Interestingly the loss trend seems to follow an n_g^b dependence with $1<b<2$ in line with previous recent reports [27].
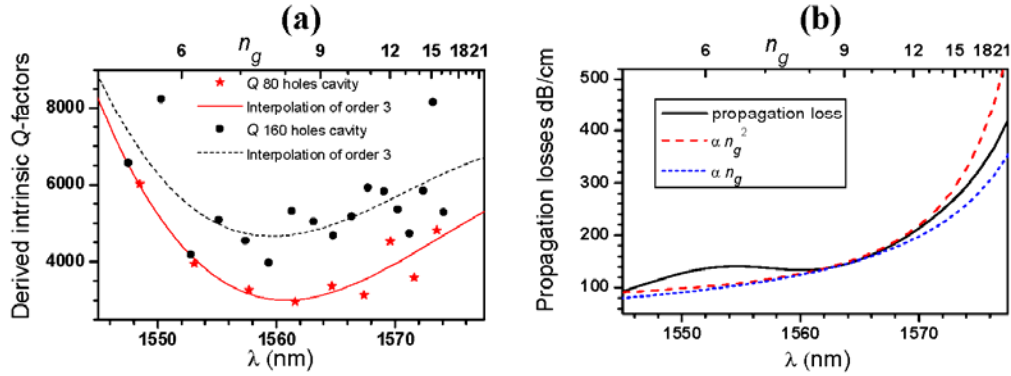
Fig. 7. (a). Comparison between the intrinsic Q-factor obtained with an 80 holes removed closed waveguide and a 160 holes removed closed waveguide as a function of wavelength and group index. (b). Propagation losses obtained using Eq. (3). The blue curves correspond to hypothetical losses that would respectively be characterized by a n_g and n_g^2 dependence.

For both the reconstruction of the dispersion curve and the determination of the group velocity we observed a good agreement between the experimental data and simulation; however we were not able to access the very low group velocity region of the dispersion curve near the mode cutoff. We do not believe this to be a fundamental limitation of the technique; rather it was a limitation for the particular tapers used in this experiment. A taper with a smaller bending radius and appropriate waist dimension should be able to probe further towards the cut-off. In addition, the sample we used had a large loss, which resulted in relatively wide resonances, so closely spaced peaks near the cut-off region were difficult to resolve.

5. Conclusion

In conclusion, we have demonstrated a fast, single measurement technique that allows for measuring the dispersion and group velocity of a photonic crystal waveguide. The method is based on evanescent coupling via a highly curved fiber taper which provides the basis for a broadband characterization of the waveguide. Both the dispersion and group velocity curves are in good agreement with numerical simulations. Although this technique requires dedicated test structures (closed waveguides), the requirement for only a single spectral measurement per waveguide makes it attractive for systematically and directly characterizing the full properties (dispersion and losses) of the PCWG without the use of integrated access waveguides or internal light sources which may affect the PCWG signature. This technique could be advantageous for rapidly probing novel waveguide designs that are developed, for instance, in the context of slow light dispersion engineering (such as in Ref. [28]) without the need for enhancing the coupling into the slow light regime.

Acknowledgments

91

3.2   Epilogue

The effects of propagating light along a looped, self-touching tapered optical fibre have been previously investigated [140-142]. It has been shown that self-coupling occurs near the contact point which gives rise to interference oscillations in the transmission spectrum. As illustrated in Fig. 3.1, the cause of the oscillation can be described by the interference of two coherent beams as:

$$P(\lambda_0) = |a_1(\lambda_0)\exp(i\beta(\lambda_0)S) + a_2(\lambda_0)|^2. \tag{3.1}$$

In this case, beam 1 propagates through the loop with an amplitude of $a_1(\lambda_0)\exp(i\beta(\lambda_0)S)$, where S is the loop length and $\beta(\lambda_0)$ is the wavelength-dependant propagation constant. Beam 2 propagates directly through the crossover point with an amplitude of $a_2(\lambda_0)$, circumventing the rest of the loop.
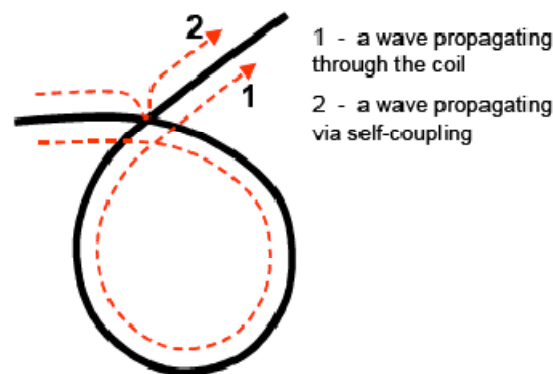
Figure 3.1. Illustration of two interfering waves (dashed) contributing to the transmission spectrum of the self-coupling microloop. 1 – a wave propagating through the loop; 2 – a wave propagating through the self-coupling region [142].

The interference is particularly noticeable in the second article presented above, where the oscillations cause a "ripple" to superimpose over the transmission spectra. Ideally this can be ignored by cancelling the ripple out with a reference trace. However, the effect is dynamic due to the entire loop "breathing" on scales of nanometres over periods of seconds. The breathing becomes especially significant when intermolecular forces have non-trivial influence on the nanowire as it comes into close proximity with the photonic crystal surface. This causes a change in the loop's length and therefore the phase of beam 1 at the point of interference.

3.2.1 Helical nanowire

Figure 3.2 below is an image of a helical evanescent coupling nanowire. The helical characteristic overcomes the issue of self-coupling caused at the touching crossover points. The ability to localise coupling to photonic crystal cavities is not adversely affected as the radius of curvature remains ~50 μm.

Figure 3.2. Top view image of a helical-shaped nanowire. The focal plane is at the lowest point of the helical nanowire, with the side "wings" approaching the viewer and shifting out of focus.

The helical nanowire is formed by annealing the silica glass nanowire with a flame after it has been looped. By careful manipulation, the loop may be pried open without it necessarily returning to contact. This not only removes self-coupling but improves the stability for taking time-consuming measurements. The only drawback is an observed 2 dB of added scattering loss through the nanowire, which for the work of this thesis did not present a significant problem.

Summary

This work forms the foundation for the remaining work of the thesis, enabling the ability to characterise the properties of a photonic crystal structure.

The paper reproduced from *Optics Express* Vol. 14, pp. 1070–1078, 2006 made the following advancements:

- Efficient (98%) coupling between highly nonlinear chalcogenide planar photonic crystal waveguide and silica fibre nanowire.

- A 3dB coupling bandwidth of 12 nm was in good agreement with theory.

The paper reproduced from *Physica B-Condensed Matter* Vol. 394, pp. 289-292, 2007, made the following advancements:

- Coupling between a photonic crystal cavity and silica fibre nanowire

The paper reproduced from *Optics Express* Vol. 16, pp. 13800-13808, 2008, made the following advancements:

- Utilising the evanescent coupling scheme to monitor the dispersion in a single measurement of a closed photonic crystal waveguide without access waveguides.

- Propagation losses may also be inferred from the measurements.

Chapter 4

Adjusting photonic crystal cavity resonances

This chapter presents an article exploring nanowire evanescent coupling into photonic crystal cavities designed as single photon sources. Two important concepts are highlighted in this work. On one hand, the coupling technique enables the characterisation of ultra-small $(0.5(\lambda/n)^3)$ and high-Q cavities. On the other, it is shown that the nanowire can itself perturb the modes within a microcavity, for which a shift in resonance of up to 3 nm is reported. This latter point is particularly relevant to the spectral alignment of quantum dots to their host microcavities, which is a crucial problem to overcome to efficiently extract single emitted photons.

The underlying goal of this work is to develop quantum cryptography with single photon sources, which would utilise quantum mechanics to guarantee completely secure communication. Embedding a quantum dot (or quantum dots layer, as shown in Fig. 1) within a photonic crystal cavity provides a potential means toward this end with two key aspects. Firstly, the presence of the cavity enables controlled direction of the quantum dot emission, therefore improving device efficiency. Secondly, the exciton density of states may be manipulated by through the Purcell effect, which is related to the properties of the cavity and allows optimisation of the emission rate of the quantum dots.
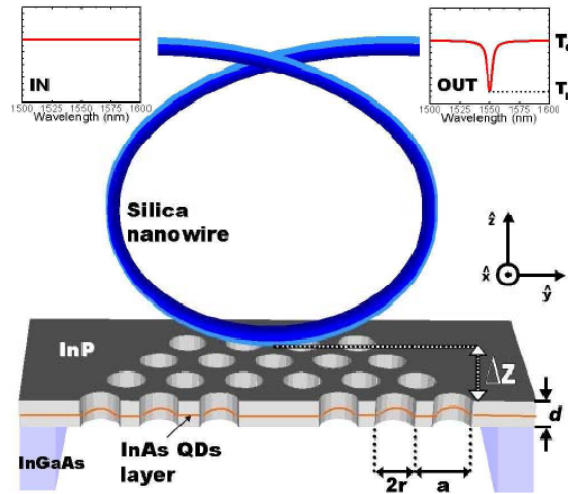
Figure 4.1. The looped silica nanowire is brought in to close proximity with the InP photonic crystal microcavity. The structures are designed with an InAs quantum dots layer through the centre of the suspended membrane.

Figure 4.1 illustrates the experiments of this work. A looped nanowire evanescently couples to a photonic crystal cavity, probing its properties. Adjustment of the nanowire's orientation with respect to the cavity geometry, as well as its proximity to the cavity, results in a shift of the cavity resonance. This is due to the nanowire's perturbing effect on the resonant mode's effective refractive index.
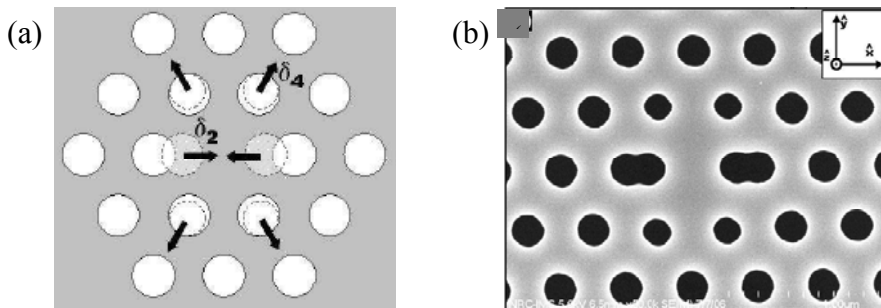
Figure 4.2. (a) Schematic of the photonic crystal cavity design. (b) Scanning electron microscope image of a typical microcavity used in the following article.

The effect of quantum dots in the system is not explored specifically in this work, instead providing a backdrop to motivate the cavity investigation with nanowires. Figure 4.2 illustrates the design of the cavities to provide small modal volumes and high Q-factors. The fabrication details of these cavities is mentioned in reference [143].

Contributors

In the following article reproduced from *Optics Express* Vol. 15, pp. 1267–1276, 2007, Dr. Christian Grillet wrote the majority of the manuscript. This thesis author's contributions were as follows:

- Performed the presented experimental measurements

- Fabricated tapered fibre for experiment

- Contributed to the writing of the manuscript

The InP samples were fabricated by the Institute for Microstructural Sciences at NRC, Canada, which is also where the photoluminescence spectra were obtained.

Formal acknowledgement of the contributions of the author of this thesis is included in Appendix A.

Nanowire coupling to photonic crystal nanocavities for single photon sources

Christian Grillet, Christelle Monat, Cameron L. C. Smith, Benjamin J. Eggleton

Centre for Ultrahigh-bandwidth Devices for Optical Systems (CUDOS)
School of Physics, University of Sydney, Sydney, NSW, 2006, Australia
grillet@physics.usyd.edu.au

David J. Moss

Institut national de la recherche scientifique (INRS)
Énergie, Matériaux et Télécommunications, Université du Québec
1650 boulevard Lionel-Boulet, Varennes, Québec, Canada, J3X-1S2
moss@emt.inrs.ca

Simon Frédérick*, Dan Dalacu, Philip J. Poole, Jean Lapointe, Geof Aers and Robin L. Williams*

Institute for Microstructural Sciences, National Research Council, Ottawa, Canada, K1A 0R6
*Also at Physics Department, University of Ottawa, Ottawa, Canada, K1N0R6
Robin.Williams@nrc-cnrc.gc.ca

Abstract: We demonstrate highly efficient evanescent coupling via a silica loop-nanowire, to ultra-small (0.5 $(\lambda/n)^3$), InAs/InP quantum dot photonic crystal cavities, specifically designed for single photon source applications. This coupling technique enables the tuning of both the Q-factor and the wavelength of the cavity mode independently, which is highly relevant for single photon source applications. First, this allows for the optimization of the extraction efficiency while maintaining a high Purcell factor. Second, the cavity mode can be matched with a spectrally misaligned quantum dot without changing the structure or degrading the Q-factor: a 3 nm resonance shift is reported.

© 2007 Optical society of America

References and links

1. C. Santori, M. Pelton, G. Solomon, Y. Dale, and Y. Yamamoto, "Triggered Single Photons from a Quantum Dot," Phys. Rev. Lett. **86**, 1502-1505 (2001).
2. V. Zwiller, H. Blom, P. Jonsson, N. Panev, S. Jeppesen, T. Tsegaye, E. Goobar, M. E. Pistol, and L. Samuelson, and G. Bjork, "Single quantum dots emit single photons at a time: Antibunching experiments," Appl. Phys. Lett. **78**, 2476-2478 (2001).
3. M. B. Ward, O. Z. Karimov, D. C. Unitt, Z. L. Yuan, P. See, D. G. Gevaux, A. J. Shields, P. Atkinson and D. A. Ritchie, "On-demand single-photon source for 1.3 µm telecom fiber," Appl. Phys. Lett. **86**, 201111 (2005).
4. C. Zinoni, B. Alloing, C. Monat, V. Zwiller, L. H. Li, A. Fiore, L. Lunghi, A. Gerardino, H. de Riedmatten, H. Zbinden, and N. Gisin, "Time-resolved and anti-bunching experiments on single quantum dots at 1300nm," Appl. Phys. Lett. **88**, 131102 (2006).
5. K. J. Vahala "Optical microcavities," Nature **424**, 839-846 (2003).
6. E. Knill, R. Laflamme, and G. J. Milburn, "A scheme for efficient quantum computation with linear optics," Nature **409**, 46-52 (2001).
7. A. Imamoglu, "Are quatum dots useful for quantum computation?," Physica E **16**, 47-50 (2003).
8. J. Vuckovic, D. Englund, D. Fattal, E. Waks, and Y. Yamamoto, "Generation and manipulation of nonclassical light using photonic crystals," Physica E **32**, 466-470 (2006).

9. J. M. Gerard and B. Gayral, "Toward high-efficiency quantum-dot single photon sources," in *Quantum Dots, Nanoparticles, and Nanoclusters*, D. L. Huffaker and P. Bhattacharya, eds, Proc. SPIE **5361**, 88-95 (2004).

10. D. Englund, D. Fattal, E. Waks, G. Solomon, B. Zhang, T. Nakaoka, Y. Arakawa, Y. Yamamoto, and J. Vuckovic, "Controlling the spontaneous emission rate of single quantum dots in a two-dimensional photonic crystal," Phys. Rev. Lett. **95**, 013904 (2005).

11. J. M. Gérard, B. Sermage, B. Gayral, B. Legrand, E. Costard, and V. Thierry-Mieg, "Enhanced Spontaneous Emission by Quantum Boxes in a Monolithic Optical Microcavity," Phys. Rev. Lett. **81**, 1110-1113 (1998).

12. G. S. Solomon, M. Pelton, and Y. Yamamoto, "Single-mode Spontaneous Emission from a Single Quantum Dot in a Three-Dimensional Microcavity," Phys. Rev. Lett. **86**, 3903-3906 (2001).

13. A. Badolato, K. Hennessy, M. Atature, J. Dreiser, E. Hu, P. M. Petroff, A. Imamoglu, "Deterministic coupling of single quantum dots to single nanocavity modes," Science **308**, 1158-1161 (2005).

14. D. Dalacu, S. Frédérick, P. J. Poole, G. C. Aers, and R. L. Williams, "Postfabrication fine-tuning of photonic crystal microcavities in InAs/InP quantum dot membranes," Appl. Phys. Lett. **87**, 151107 (2005).

15. D. Chitrani, R. L. Williams, J. Lefebvre, P. J. Poole, and G. C. Aers, "Optical spectroscopy of single, site-selected, InAs/InP self-assembled quantum dots," Appl. Phys. Lett. **84**, 978-980 (2004).

16. W.L. Barnes, G. Bjork, J.M. Gerard, P. Jonsson, J.A.E. Wasey, P.T. Worthing, and V. Zwiller, "Solid-state single photon sources: light collection strategies," Eur. Phys. J. D **18**, 197–210 (2002).

17. E. Moreau, I. Robert, J. M. Gerard, I. Abram, L. Manin, and V. Thierry-Mieg "Single-mode solid-state single photon source based on isolated quantum dots in pillar microcavities," Appl. Phys. Lett. **79**. 2865-2967 (2001).

18. M. Pelton, C. Santori, J. Vuckovic, B. Zhang, G. S. Solomon, J. Plant, and Y. Yamamoto, "Efficient Source of Single Photons: A Single Quantum Dot in a Micropost Microcavity," Phys. Rev. Lett. **89**, 233602 (2002).

19. Y. Akahane, T. Asano, B. S. Song, and S. Noda, "High-Q photonic nanocavity in a two-dimensional photonic crystal," Nature **425**, 944-947 (2003).

20. K. Srinivasan, P. E. Barclay, M. Borselli, and O. Painter, "Optical-fiber-based measurement of an ultrasmall volume high-Q photonic crystal microcavity," Phys. Rev. B **70**, 081306 (2004).

21. B.-S. Song, S. Noda, T. Asano, and Y. Akahane, "Ultra-high-Q photonic double heterostructure nanocavity," Nature Mat. 4, 207-210 (2005).

22. E. Kuramochi, M. Notomi, S. Mitsugi, A. Shinya, T. Tanabe, and T. Watanabe "Ultrahigh-Q photonic crystal nanocavities realized by the local width modulation of a line defect," Appl. Phys. Lett. 88, 041112 (2006).

23. J. C. Knight, G. Cheung, F. Jacques, and T. A. Birks, "Phase-matched excitation of whispering-gallery-mode resonances by a fiber taper," Opt. Lett. **22**, 1129-1131 (1997).

24. M. Cai, O. Painter, and K. J. Vahala, "Observation of critical coupling in a fiber taper to a silica-microsphere whispering-gallery mode system," Phys. Rev. Lett. **85**, 74-77 (2000).

25. I. Hwang, S. K. Kim, J. Yang, S. H Kim, S. Lee, and Y. Lee, "Curved-microfiber photon coupling for photonic crystal light emitter," Appl. Phys. Lett. **87**, 131107 (2005).

26. J. Vuckovic, and Y. Yamamoto, "Photonic crystal microcavities for cavity quantum electrodynamics with a single quantum dot," Appl. Phys. Lett. **82**, 2374-2376 (2003).

27. D. Dalacu, S. Frédérick, A. Bogdanov, P. J. Poole, G. C. Aers, and R. L. Williams, "Fabrication and optical characterization of hexagonal photonic crystal microcavities in InP-based membranes containing InAs/InP quantum dots," J. Appl. Phys. **98**, 023101 (2005).

28. T. Yoshie, A. Scherer, J. Hendrickson, G. Khitrova, H. M. Gibbs, G. Rupper, C. Ell, O. B. Shchekin & D. G. Deppe, "Vacuum Rabi splitting with a single quantum dot in a photonic crystal nanocavity," Nature 432, 200-203 (2004).

29. K. Hennessy, C. Högerle, E. Hu, A. Badolato and A. Imamoğlu, "Tuning photonic nanocavities by atomic force microscope nano-oxidation," Appl. Phys. Lett. 89, 041118 (2006).

30. D. Englund, J. Vuckovic, "A direct analysis of photonic nanostructures," Opt. Express **14**, 3472-3483 (2006).

31. S. Frédérick, D. Dalacu, J. Lapointe, P.J. Poole, G.C. Aers and R.L. Williams, "Experimental demonstration of high quality factor, x-dipole modes in InAs/InP quantum dot photonic crystal microcavity membranes," Appl. Phys. Lett. **89**, 091115 (2006).

32. C. Grillet, C. Smith, D. Freeman, S. Madden, B. Luther-Davies, E. Magi, D. Moss, and B. Eggleton, "Efficient coupling to chalcogenide glass photonic crystal waveguides via silica optical fiber nanowires," Opt. Express **14**, 1070-1078 (2006).

33. C. Manolatou, M. J. Khan, S. Fan, P. R. Villeneuve, H. A. Haus, and J. D. Joannopoulos, "Coupling of modes analysis of resonant channel add-drop filters," IEEE J. Quantum Electron. **35**, 1322-1331 (1999).

34. I. Marki, M. Salt, and H. P. Herzig, "Tuning the resonance of a photonic crystal microcavity with an AFM probe," Opt. Express **14**, 2969-2978 (2006).

35. C. Santori, D. Fattal, J. Vuckovic, G. S. Solomon, and Y. Yamamoto, "Indistinguishable photons from a single-photon device," Nature **419**, 594-597 (2002).

36. H. M. H. Chong, and R. Delarue, "Tuning of photonic crystal waveguide microcavity by thermooptic effect," IEEE Photon. Technol. Lett. **16**, 1528-1530 (2004).

37. D. Erickson, T. Rockwood, T. Emery, A. Scherer, and D. Psaltis, "Nanofluidic tuning of photonic crystal circuits," Opt. Lett. **31**, 59-61 (2006).

1. Introduction

Single semiconductor quantum dots (QDs) have attracted much attention this last decade because of their atom-like emission at telecom wavelengths. Not only do they have the potential to emit triggered single photons one at a time [1-4], but they can be embedded into solid-state, three-dimensional microcavities [5] that are capable of channelling the single photon emission. The resulting QD-microcavity combination promises to provide efficient single photon sources (SPS) at telecom wavelengths; a key enabler for optical fiber-based quantum key distribution (quantum cryptography) and quantum information processing [6-8]. The practicality of such sources depends crucially on the degree to which the photons can be efficiently extracted, a process which, as pointed out by Gerard et al [9], can be addressed by (a) redirection of the QD emission into a single cavity mode and (b) efficient extraction of the photons that are in the cavity mode to the outside world.

In addressing point (a), one notes that microcavities can funnel a large fraction (β) of the spontaneous emission (SE) of an emitter into the available cavity mode, potentially enhanced [10-12] by the well-known Purcell factor F_p, which is proportional to the ratio Q/V for the mode, where Q and V are the quality factor and the effective mode volume respectively. The Purcell factor actually represents the maximum possible enhancement of the QD SE rate into the cavity mode. Achieving this maximum requires precise matching of the QD emission characteristics and its spatial location relative to the cavity mode. Many efforts are currently devoted to the realization of QD-microcavity systems that fill those conditions through sophisticated fabrication process [10, 13-15]. For coupling the cavity mode to the outside world, point (b) above, there are two main strategies: one can either collect part of the intrinsic optical losses of the mode using collection optics with limited numerical aperture, or alternatively introduce an additional channel of escape to the photons. The appropriate coupling strategy to maximize the collection efficiency is highly dependent on the characteristics of the cavity mode that the emitter is coupled to [16]. SPS based on micropillar or VCSEL-type cavities [17, 18, 3] offer a natural direct "end-fire" coupling along the cavity axis because of their highly directive emission radiation. On the other hand, two dimensional (2D) photonic crystal (PhC) membrane based cavities can provide modes with far more attractive Purcell factors by introducing a carefully designed defect into the PhC [19-22]. However, achieving a higher Q/V is generally accomplished to the detriment of the directionality of the emission, making the intrinsic optical losses of these modes much more difficult to collect.

By introducing an additional output channel close to the cavity, evanescent coupling via silica nanowires provides an alternative fiber-based technique to end-fire coupling. Because this approach usually requires precise matching of the nanowire mode to the probed optical modes, it has initially been used to probe "whispering-gallery-mode"-type cavities [23, 24]. PhC cavities that have been interrogated so far with this method have been largely restricted. The first realization of tapered fiber nanowire coupling to a wavelength-scale PhC microcavity was recently reported [20]. However, the graded square lattice design involved in those experiments would not allow efficient coupling with a single quantum emitter. More recently [25], evanescent coupling via a nanowire taper to simultaneously pump a PhC microlaser and to collect its light emission has been reported. This demonstration used an "elongated" cavity, specifically tailored to optimize the phase matching between the nanowire taper and the microcavity.

In this work, we demonstrate efficient evanescent coupling to ultra-small (0.5 $(\lambda/n)^3$) high Q PhC cavities, via a tapered silica fiber nanowire. The cavity has been specifically designed and realized for SPS applications and exhibits modes with a high Purcell factor. We show that the cavity-nanowire system displays unique properties that are especially relevant to SPS applications. This system provides a flexible and non-invasive approach to tune both the Q and the resonance wavelength of the cavity mode. Firstly, this approach allows one to adjust the coupling strength in order to achieve an optimized extraction efficiency while maintaining a high Purcell factor. Secondly, the coupling technique can also tune the cavity wavelength in

100

order to match it to the QD emitter wavelength, enabling an actual SE rate enhancement via the Purcell effect. In section 2, we first present the design, fabrication and characteristics of the ultra-small, 0.5 $(\lambda/n)^3$, single-defect, InAs/InP QD photonic crystal cavities emitting around 1.55 μm. In section 3, we describe the realization of tapered silica nanowires specifically fabricated into a tight loop and the principle of the evanescent coupling technique. Section 4 highlights the experimental transmission results that have been obtained with the cavity-nanowire coupled system and includes a demonstration of the tuning of the cavity wavelength (>3 nm) with this method. Finally, in section 5, we discuss the potential of this technique for SPS applications, focusing mainly on the analysis of the extraction efficiency.

2. Cavity design and device fabrication

The set of cavities investigated is a modified missing-hole defect in a hexagonal lattice [26]. A typical scanning electron microscope (SEM) image of the defect microcavity studied is shown in Fig. 1(a): it consists of one hole removed that is successively surrounded by one ring of modified holes, followed by 19 rings of holes.

The basic heterostructure used in this study was grown by chemical beam epitaxy (CBE) on a semi insulating InP(001) substrate. It is comprised of one self-assembled InAs QD layer in the middle of a 293 nm thick InP cladding layer that is grown on top of an InGaAs sacrificial layer. The QD growth conditions have been optimized to ensure that the generated photoluminescence (PL) displays an emission peak around 1.55 μm at room temperature. The PhC structure is then realized by a combination of electron beam lithography and inductively coupled plasma (ICP) etching. The final wet-etching of the InGaAs layer releases the InP membrane around the PhC structure, to create a PhC suspended microcavity. Full details of the fabrication process and cavity design can be found in [27].

For this 293 nm thick InP membrane, with a refractive index n of 3.17, a period a of 440 nm and a hole radius r of 130 nm have been chosen as the PhC parameters in order to open up a photonic band gap around 1550 nm. Such cavities give rise to donor-type defect modes with optical field antinodes in the high index material, as displayed on Fig. 1(b), suitable for coupling to the embedded QD active medium.
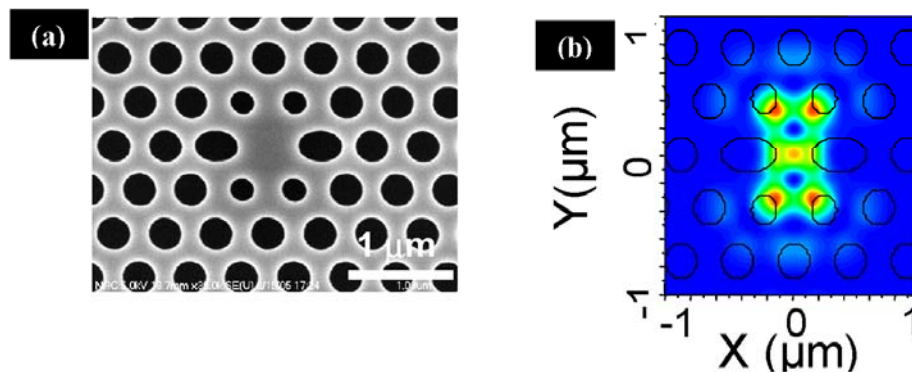
Fig. 1. (a) SEM image of a modified single missing hole defect. (b) 3D FDTD electric field intensity of the fundamental cavity mode

Room-temperature PL measurements were made with HeNe excitation at 632.8 nm in order to extract the intrinsic Q-factor of the cavities. Excitation and collection were performed through the same large numerical aperture objective (NA=0.55) with a spot size of 2 μm. In-plane optical modes generated in the PhC microcavity undergo out of plane losses at the cavity boundaries: those losses are collected in the direction normal to the surface and spectrally analyzed. We focused on a particular set of cavities for which the fundamental mode appears within the range of interest for fiber-based SPS applications (around 1550 nm). Figure 2 shows PL spectra for a set of 3 cavity structures with nominally identical parameters. The curves are offset for clarity. Each spectrum displays several peaks corresponding to resonant

modes in the cavity. The Q-factors of the primary cavity mode [see Fig. 2(b)], as determined from the linewidth of the PL peaks, range from 2000 to 2900. Theoretically, Q-factors above 40000 are possible in these cavities [26], together with modal volumes V of ~ 0.5 $(\lambda/n)^3$, where

$$V = \int \varepsilon(r)\left|E(r)\right|^2 dr^3 / \max\left[\varepsilon(r)\left|E(r)\right|^2\right] \qquad (1)$$

The corresponding Q/V-ratios of the probed cavities range between 4000 and 5800 $[(\lambda/n)^3]^{-1}$, which is around twice [10] and four times [28, 29] lower than the best Q/V ratios demonstrated with photonic crystal structures including QDs. Actually, the variation in Q-factor and resonant frequency, together with the overall, relatively low size of the Q-factors, demonstrate the extreme sensitivity of these modes to fabrication inaccuracies [30]. We have recently fabricated cavities of this type displaying Q-factors as high as 28000 [31] and associated Q/V ratios twice higher than [28, 29].
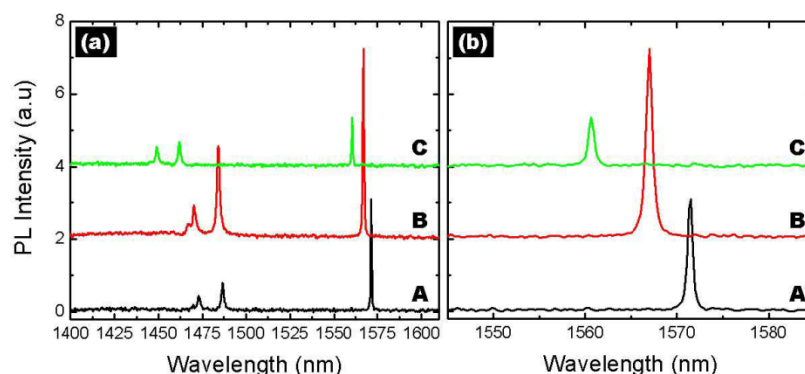
Fig. 2. (a) PL spectra for 3 cavity structures with nominally identical parameters: $r{\sim}0.3a$. Each spectrum displays several peaks corresponding to cavity modes. (b) Close-up of the spectral region of interest

3. Tapered nanowire coupling experiment

Figure 3 illustrates the principle of operation of evanescent coupling between a tapered fiber and a PhC microcavity. The silica fiber diameter must be reduced to the micrometer-scale in order to obtain an evanescently extended mode field [32] that can efficiently interact with the nanocavity. The fiber taper is manufactured using a flame brushing tapering process that heats and stretches conventional SMF fiber. Taper waist lengths are typically a few millimetres, with outside diameters down to 800 nm being achieved. In order to spatially localize the interaction to the PhC cavity itself, we introduce a curvature in the taper waist by inducing a loop shape in the taper [Fig. 3(b)].

(a)   (b)
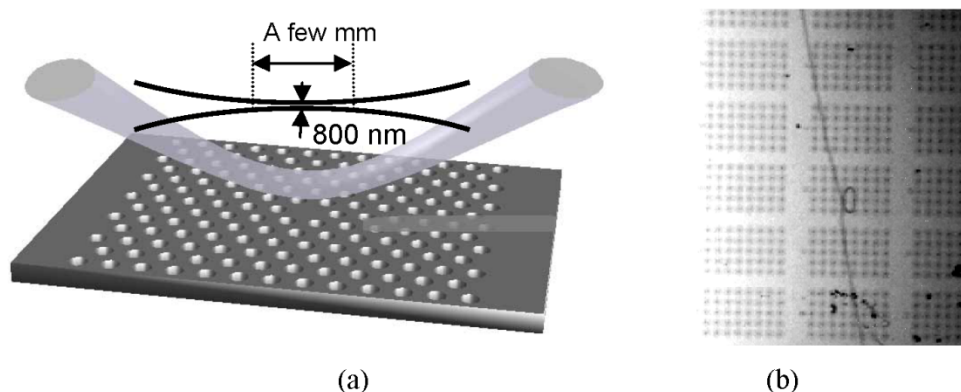
Fig. 3. (a) Schematic showing the coupling from a tapered fibre to PhC cavity; (b) Top-view of the final tapered fibre loop above PhC cavities.

102

By doing so, we not only limit the interaction region to the area of interest (namely the PhC cavity defect), minimizing scattering losses, but we also reinforce the mechanical stability of the taper. Obtaining the looped nanowires involves a process of moving the tapered fiber ends closer together by 3 mm and subsequently twisting one end to induce a loop. The loop nominally forms at the taper waist where the fiber diameter is the smallest. Once the loop is formed, the ends are then moved back, tightening the loop to achieve a circumference of approximately 0.4 mm.

In this experiment, the looped taper is brought into direct contact with the PhC cavity. Light is launched into the SMF fiber using a broadband erbium source at 1550nm (Fig. 4). Before reaching the taper region the light passes through a polariser to select TE-like polarisation (E mainly lying in the plane of the PhC structure). In the taper region, light is adiabatically converted into the fundamental evanescent taper mode. The output of the fiber is connected to an optical spectrum analyser where the transmission through the nanotaper is measured (Fig. 4). The procedure has been repeated on three distinct but nominally identical cavities. All the measurements are performed at room temperature.
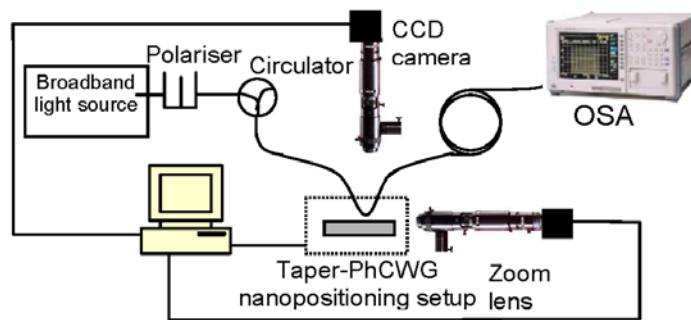
Fig. 4. Experimental measurement setup for evanescent coupling from silica nanowire to photonic crystal waveguide.

4. Results and discussion

Figure 5 shows the transmission spectra in dB for the three cavities, normalized with respect to the transmission through the taper in the absence of the PhC. The vertical lines indicate the wavelengths of the optical modes from the PL measurements. As can be seen, the transmittance drops dramatically at the resonant wavelengths of the cavities. The relatively good agreement of the resonance wavelengths between the PL measurements and the evanescent coupling measurements confirm our ability to excite the ultra-small cavity modes using this technique. The slight red shift observed for each resonance is expected and is a direct consequence of bringing the taper into close proximity to the cavity, inducing an increase in the effective index of the mode. Off-resonance losses are related to scattering at the taper-PhC interface and direct coupling to TM PhC Bloch modes due to the broken symmetry [25].

The net quality factor of the coupled system measured experimentally, Q_T, encompasses the different decay channels available to the photons.

$$\frac{1}{Q_T} = \frac{1}{Q_0} + \frac{1}{Q_{fiber}} + \frac{1}{Q_{parasitic}} \tag{2}$$

where Q_0 is the intrinsic Q-factor of the cavity, Q_{fiber} the Q-factor associated with the coupling between the cavity and the taper and $Q_{parasitic}$ is related to the parasitic losses induced by any significant perturbation of the mode field inside the cavity (for instance TE to TM mode conversion occurring because of the broken symmetry induced by the presence of the taper). In an ideal system, the taper-cavity coupling should not induce losses other than the desirable funnelling of photons into the nanowire, meaning that $Q_{parasitic}$ should be infinity. From coupled mode theory in time [33], and under the condition that the junction behaves ideally

103

(i.e. $Q_{parasitic}$ tends to infinity), the transmittance is given in terms of the intrinsic Q_0 and loaded Q_T-factors of the cavity as

$$Q_T = \sqrt{T} \times Q_0 \qquad (3)$$

From Fig. 5, a transmittance T of 0.5 and an experimental value of $Q_T \sim 2000$ can be determined for cavity A. Note that according to Eq. (2) this value of Q_T yields a lower bound for the intrinsic Q_0-factor due to the taper's loading effect on the cavity. From Eq. (3), we infer an intrinsic Q_0-factor of ~ 2830, in good agreement with the intrinsic Q_0-factor determined from the PL line width of the resonance peak, which yields 2900.
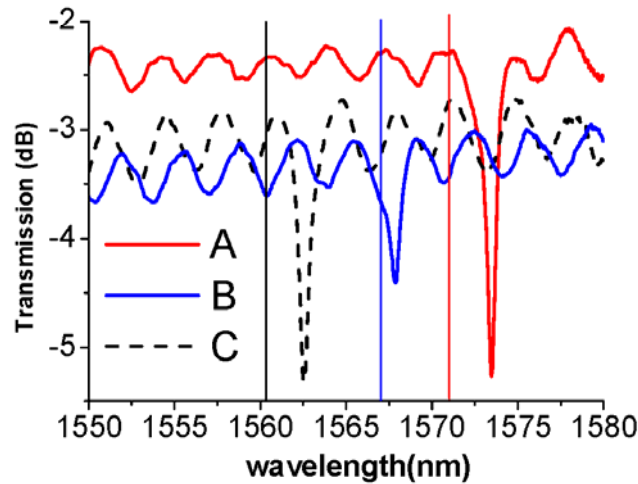
Fig. 5. Transmission spectra of tapered nanowire, in close contact to 3 distinct PhC cavities showing resonant coupling. Transmission spectra have been normalized to the transmission through the taper in the absence of the PhC.

Surprisingly, considering the taper is in contact with the cavity, this result suggests that the system is actually behaving almost as an ideal junction, with $Q_{parasitic} \sim 80000$ –far greater than any other contributing Q-factors. For cavities B and C, respectively, we obtain a transmittance T of 0.75, 0.57 and experimental Q_T-factors of 1650 and 1850. Using the same approach, we infer intrinsic Q_0-factors of 1900 and 2380, in line with the intrinsic Q_0-factors evaluated from PL measurements, which confirms the degree of ideality of these junctions.

Figure 6 displays the normalized experimental transmission spectra in linear scale, showing a resonance shift with coupling conditions for cavity A. Note that the looped taper is in direct contact with the PhC cavity for each of the four spectra. As stated above, the highly localised mode is very sensitive to perturbations. In our configuration, the silica nanowire perturbs the field of the microcavity in a controlled way. Curve 1) corresponds to the case where the nanowire is positioned slightly out of the cavity field maximum [see Fig. 1(b)]. This is sufficient to induce an increase in the effective index of the cavity mode causing a slight red shift of the resonance compared to the wavelength (1571 nm) determined from the PL measurement.

By subsequently displacing the nanowire slightly, we observe a shift of the resonance towards longer wavelengths (curves 2 to 4). This can be attributed to a stronger perturbation of the cavity field by the presence of the taper, resulting in a significant tuning of the resonance of >3 nm (curve 4) without degrading the Q-factor of the resonance. This mechanism can be compared to an AFM tip probing the cavity mode [34].

104
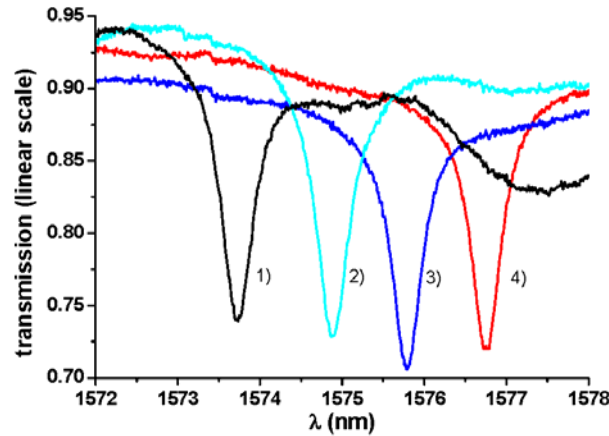
Fig. 6. Nano-mechanical tuning. From 1) to 4), experimental shift of the resonant wavelength obtained when "perturbing" the cavity with the taper.

5. Prospects of a coupled taper 2D PhC single photon source system

The results reported above quantify the loading of light from the nanowire to the optical mode of PhC microcavities. Similar out-coupling efficiencies from the cavity to the nanowire can be inferred, since the two (in- and out-) coupling processes are fundamentally equivalent. As compared to other approaches, evanescent coupling through the use of nanowires presents some unique advantages. It offers an efficient scheme for pumping/ loading a PhC nanocavity [20] and collecting light through the same fiber-based communication channel [25]. In addition, as discussed below, it provides an adjustable extraction channel as well as a flexible means to tune the cavity (Q, λ) properties.

As stated in the introduction, SPS out-coupling methods involve either the collection of a fraction of the photons that are "naturally" lost outside the cavity, or the introduction of a dedicated optical decay channel for photon extraction. For both approaches, efficient extraction of single photons implies maximizing the decay rate associated with the collected photons of the QD-cavity system, relative to any other photon loss contributions. However, this must be achieved without degrading too strongly the total Q_T-factor of the mode that the emitter is coupled to. Those ideas are more quantitatively described in the following analysis.

The extraction efficiency (ε) is equal to the product of the SE coupling factor β and the collection efficiency (η) of the photons that have been emitted into the cavity mode.

$$\varepsilon = \beta \times \eta \qquad (4)$$

with

$$\beta = \frac{F_p}{F_p + 1} \qquad (5)$$

where the Purcell Factor is

$$F_P = \frac{3Q_T (\lambda/n)^3}{4\pi^2 V} \qquad (6)$$

and

$$\eta = \frac{1/Q_c}{1/Q_c + 1/Q_0} = 1 - \frac{Q_T}{Q_0} \qquad (7)$$

In the expression (7), the total Q_T-factor has been explicitly divided into two terms that correspond to the optical losses either collected (Q_c) or not collected (Q_0). Depending on the coupling strategy, these two terms must be interpreted slightly differently. If using an

additional coupling channel, Q_0 is the intrinsic Q-factor of the cavity (as defined in Section 4) and Q_c is associated with the optical losses induced by the coupling process (denoted as Q_{fiber} for the nanowire coupling). Note that (6) is then valid under the assumption that no other parasitic losses are added by the additional channel ($Q_{parasitic} \rightarrow \infty$). On the other hand, in the case where no additional optical decay channels are offered to the cavity, Q_c (Q_0) must be interpreted as the intrinsic cavity optical losses that do (do not) fall into the numerical aperture of the collection optics. Whilst the discussion below does not rely on this, for simplicity, we assume that the coupling strategy involves an additional coupling channel, as is the case for the evanescent coupled nanowire.

The relations (5) and (7) highlight two counter trends as the coupling strength ($\propto 1/Q_c$) is increased. Whereas F_p and β both increase ($F_p \gg 1$ and $\beta \rightarrow 1$) as the coupling strength is decreased ($Q_c \rightarrow 0$ or $Q_T \rightarrow Q_0$), the efficiency η of coupling to the outside world decreases ($\eta \rightarrow 0$). These two competing trends yield a maximum in the extraction efficiency ε as a function of the net Q_T-factor, as displayed in Fig. 7(a). The corresponding Purcell factor, F_p, (obtained from Eq. (6) with $V=0.5\times(\lambda/n)^3$) is superimposed on the same plot; indeed, the Purcell factor is important in itself, independently of the extraction efficiency, from the viewpoint of enhancing the possible repetition rate of the SPS by speeding up the the QD SE process. In addition, the Purcell effect also contributes to make the photons indistinguishable by reducing the QD radiative lifetime below the dephasing time [35, 8]. Indistinguishability proves to be important for quantum information schemes that rely on multiphoton interference. Therefore, for some applications, an overall figure of merit should be defined by the product of ε and F_p [see Fig. 7(b)]. It is clear that the optimum coupling occurs for a relatively narrow range of net Q_T-factors (or Q_c), the width of this range being highly dependent on the volume V and intrinsic Q_0 of the cavity mode.
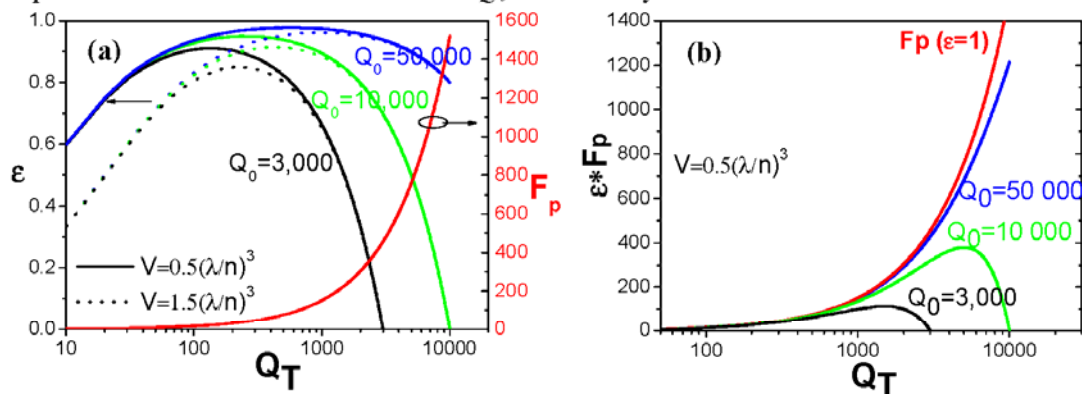
Fig. 7. (a) Extraction efficiency (left axis) and Purcell factor (right axis) as a function of the net Q_T-factor of the cavity. The extraction efficiency has been plotted for three different values of Q_0, respectively of 3000 (black), 10000 (green) and 50000 (blue) as well as two different mode volumes V of $0.5\times(\lambda/n)^3$ (solid line) and $1.5\times(\lambda/n)^3$ (dotted line). (b) Figure of merit defined by the product of the Purcell factor with the extraction efficiency ε as a function of Q_T, for a mode volume V of $0.5\times(\lambda/n)^3$ and three different values of Q_0. The case $\varepsilon=1$ is also represented.

Two points can be highlighted from this analysis. The optimal net Q_T –factor, that maximises ε, as well as the maximum attainable efficiency ε_{max}, both increase with the intrinsic Q_0/V factor of the cavity. Higher Q_0/V factors also enlarge the range of net Q_T-values that enable extraction efficiencies above a benchmark value of 90%. This behavior reinforces the strong interest in high Q_0/V PhC microcavities to achieve both high Purcell factors and SPS extraction efficiencies and highlights the interest in having a coupling channel whose strength is *a posteriori* tunable. Tuning enables one to achieve the "well balanced" coupling efficiency Q_c: it allows one to take full advantage of the Q_0/V cavity produced by the fabrication process regarding ε and it can be adapted to the targeted application, which in practice may require optimizing either ε or F_p.

Traditional PhC cavity out-coupling methods include vertical coupling into an objective or lateral coupling to a PhC waveguide that is integrated onto the same structure as the cavity [8]. For the former approach, the cavity design must be optimized so that the mode displays both a high Q_T/V and a highly directive radiation pattern that overlaps well with the numerical aperture of the collection optics [31]. For the second approach, a balanced and well controlled PhC cavity to waveguide coupling structure must be realized to get a net Q_T-value close to the optimum value [see Fig. 7(b)]. Both approaches rely on the accurate fabrication of precise designs. However, nanocavities with ultra low volumes are particularly sensitive to fabrication inaccuracies that tend to compromise the Q-factor or mode directivity designed theoretically.

In contrast, evanescent coupling to nanowires allows tuning of the coupling strength Q_c by modifying the overlap of the cavity-nanowire system [20, 25]. This, in turn, enables the tuning of Q_T which determines both the Purcell factor and the extraction efficiency, ε. Coupling can thus be adjusted to compensate for inevitable deviations from the ideal design of the fabricated cavity characteristics (such as Q_0), and according to the requirements of the particular application. Additional "parasitic" losses induced by the evanescent coupling are limited, as demonstrated above, making this approach viable. The preliminary measurements of section 4 for cavity A (Q_T=2000 and Q_0=2830) yield a collection efficiency η of ~ 30% according to Eq. (7), while the associated cavity Purcell factor F_p is close to 300. This indicates that the extraction efficiency ε for such a system, if used as a SPS, could be as high as 30%, while maintaining a high Purcell factor. Note that even though this value of 30 % is smaller than the theoretical maximum for ε of > 90%, [from Fig. 7(a)], it is nonetheless higher than what has been achieved for PhC SPSs to date [8, 10].

Finally, our observation of a shift of cavity resonant wavelength with coupling conditions (Fig. 6) offers a way to address the extremely important issue of aligning the cavity resonant wavelength with the QD emission wavelength. Enhancing the QD SE rate via the Purcell factor offered by the cavity mode requires critical spectral matching between the single QD and the cavity mode. Whilst PhC cavities enable the achievement of both high Q_0-modes and potentially high Purcell factors, they also reduce the probability of obtaining accurate spectral matching of the spectrally narrow cavity mode and the QD emission. Whilst optical tuning of PhC modes has been achieved through thermo-optic approaches [36], liquid infiltration of PhC [37] or post-process chemical treatments [27,29], evanescent coupling offers a simple and flexible method to couple a spectrally misaligned QD with the cavity mode without changing the device structure. This reversible, post-fabrication tuning approach can correct spectral mismatches as wide as 3 nm with a high degree of control.

6. Conclusions

In conclusion we have demonstrated efficient coupling to the smallest volume microcavity to date, via a tapered silica nanowire micro-loop. These PhC based nanocavities, containing QDs, are specifically designed for SPS applications. We have demonstrated that this probing technique enables us to gain accurate knowledge of the intrinsic Q-factor of the cavity mode. In addition, it offers numerous advantages for coupling to SPS, such as the ability to couple without inducing significant parasitic losses, the ability to adjust the cavity coupling strength to optimize the extraction efficiency while maintaining high Purcell factors, the ability to tune the cavity resonant wavelength in order to match it to the QD emission and finally, the ability to both deliver pump light and extract photon emission through the same fiber-based channel. These advantages demonstrate that this coupling approach is highly relevant to SPS applications.

Acknowledgment

4.1   Epilogue

Figure 4.3 presents some results that were not published, using samples fabricated by the same group as the collaborators of the article above. The results below highlight the ability of the evanescent coupling technique to observe high Q-factors ($> 30{,}000$) and reinforce the perturbing effect the nanowire can have on the system. As the results portray, decreasing the distance between nanowire and photonic crystal cavity has several noticeable effects to the cavity's resonant mode. The Q-factor decreases since there is a greater channel for the photons to escape the system. This coincides with a greater coupling strength to the modes. The resonance also shifts to longer wavelengths as the effective refractive index is increased due to the closer presence of the nanowire.
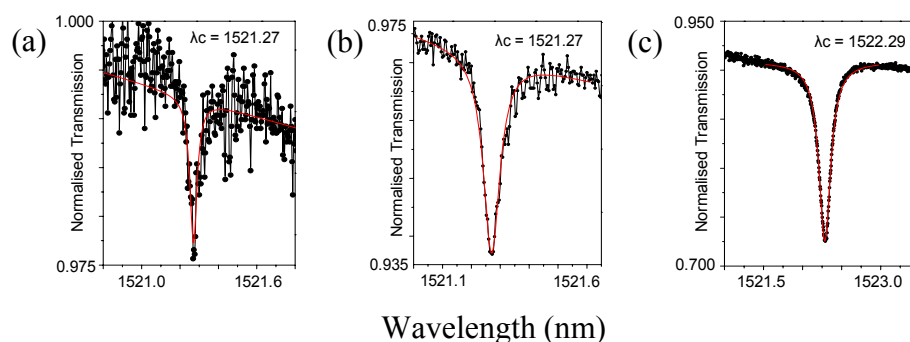
Figure 4.3. From left to right, the distance between nanowire and cavity surface is decreased. The nanowire is in contact with the photonic crystal in (c). (a) $Q = 33{,}600$; (b) $Q = 21{,}800$; (c) $Q = 8{,}300$.

The distance between nanowire and photonic crystal surface is not specified in this work. Obtaining such information accurately is experimentally difficult due to both the changing position of the nanowire over time as well as the attraction between the nanowire and the wafer surface. Precise knowledge of this would enable detailed consideration of the effects related to coupling to TM slab modes and vertical confinement asymmetry.

Summary

This work represents the first demonstration of tuning the resonance of a photonic crystal cavity for the thesis.

The paper reproduced from *Optics Express* Vol. 15, pp. 1267–1276, 2007, made the following advancements:

- Demonstration of coupling to the smallest photonic crystal cavity at the date of publication $(0.5(\lambda/n)^3)$.

- Tuning the Q-factor and wavelength of the cavities were shown to be tuned independently.

Chapter 5

Photosensitive post tuning of photonic crystals

This chapter presents an article investigating the photosensitive aspect of chalcogenide glass to post-tune the properties of a photonic crystal structure. A technique is proposed that exposes a photonic crystal formed in chalcogenide glass to laser light at frequencies for which the material absorbs. The result is a change in the material's refractive index as well as an expansion of its volume, thereby altering the properties of the photonic crystal. Such a scheme may be employed at any time after the initial device is made, either to potentially account for fabrication tolerances or to arbitrarily optimise a structure for flexible functionality.

The photonic crystal structures in the article are all W1 waveguides formed in $Ge_{22}As_{12}Se_{55}$ chalcogenide glass. For the experiments, the entire waveguide and photonic crystal section is exposed to HeNe laser light (633 nm). The glass absorbs at this wavelength and undergoes structural change, resulting in a 5 nm shift in the waveguide mode resonance. This demonstration paves the way toward realising more sophisticated geometries by selectively post-tuning a local region of a photonic crystal structure.

Contributors

In the following article reproduced from *Optics Express* Vol. 15, pp. 1277–1285, 2007, Michael W. Lee wrote the majority of the manuscript and performed the bulk of experiments. This thesis author's contributions were as follows:

- Provided expertise for characterisation and tapered fibre fabrication

- Contributed to the writing of the manuscript

Formal acknowledgement of the contributions of the author of this thesis is included in Appendix A.

Photosensitive post tuning of chalcogenide photonic crystal waveguides

Michael W. Lee, Christian Grillet, Cameron L.C. Smith, David J. Moss*, Benjamin J. Eggleton

Centre for Ultrahigh-bandwidth Devices for Optical Systems (CUDOS)
School of Physics, University of Sydney, Sydney, NSW, 2006, Australia
grillet@physics.usyd.edu.au
* Now with Institut national de la recherche scientifique (INRS)
Énergie, Matériaux et Télécommunications, Université du Québec
1650 boulevard Lionel-Boulet, Varennes, Québec, Canada, J3X-1S2

Darren Freeman, Barry Luther-Davies, Steve Madden, Andrei Rode

Centre for Ultrahigh bandwidth Devices for Optical Systems, Laser Physics Centre, Australian National University, Canberra, Australia

Yinlan Ruan

Center of Expertise in Photonics, School of Chemistry and Physics, University of Adelaide, Adelaide, Australia

Yong-hee Lee

Nanolaser Laboratory, Department of Physics, Korea Advanced Institute of Science and Technology, Daejeon 305-701, Korea

Abstract: We present experimental results on post-tuning the dispersion of a two-dimensional photonic crystal waveguide made from $Ge_{33}As_{12}Se_{55}$ chalcogenide glass by exploiting the material photosensitivity to near-bandgap light. The change in the refractive index and volume of the material in response to exposure to 633nm light resulted in a shift of more than 5nm in the resonant coupling wavelength between a tapered optical fiber and the modes of a W1 waveguide. This represents a first proof of principle demonstration of the photosensitive post-tuning of a planar photonic crystal device.

References and links

1. J-M. Lourtioz, H. Benisty, V. Berger, J-M. Gerard, D. Maystre, and A. Tchelnokov, Photonic Crystals: Towards Nanoscale Photonic Devices (Springer, 2005).
2. H. M. H. Chong, and R. Delarue, "Tuning of photonic crystal waveguide microcavity by thermooptic effect," IEEE Phot. Tech. Lett. **16**, 1528-1530 (2004).
3. R. Ferrini, J. Martz, L. Zuppiroli, B. Wild, V. Zabelin, L. A. Dunbar, R. Houdré, M. Mulot, and S. Anand, "Planar photonic crystals infiltrated with liquid crystals: optical characterization of molecule orientation," Opt. Lett. **31**, 1238-1240 (2006).
4. D. Erickson, T. Rockwood, T. Emery, A. Sherer, and D. Psaltis, "Nanofluidic tuning of photonic crystal circuits," Opt. Lett. **31**, 59-61 (2006).
5. D. Dalacu, S. Frédérick, P. J. Poole, G. C. Aers, and R. L. Williams, "Postfabrication fine-tuning of photonic crystal microcavities in InAs/InP quantum dot membranes," Appl. Phys. Lett. **87**, 151107 (2005).
6. W. Park, J-B. Lee, "Mechanically tunable photonic crystal structure," Appl. Phys. Lett. **85**, 4845-4847 (2004).
7. I. Marki, M. Salt, and H. P. Herzig, "Tuning the resonance of a photonic crystal microcavity with an AFM probe," Opt. Express **14**, 2969-2978 (2006).

---

8. J. M. Gerard and B. Gayral, "Toward high-efficiency quantum-dot single photon sources," in Quantum Dots, Nanoparticles, and Nanoclusters, D. L. Huffaker and P. Bhattacharya, eds, Proc. SPIE 5361, 88-95 (2004).

9. D. Englund, D. Fattal, E. Waks, G. Solomon, B. Zhang, T. Nakaoka, Y. Arakawa, Y. Yamamoto, and J. Vuckovic, "Controlling the spontaneous emission rate of single quantum dots in a two-dimensional photonic crystal," Phys. Rev. Lett. 95, 013904 (2005).

10. A. Zakery, S. R. Elliot, "Optical properties and applications of chalcogenide glasses: a review," J. Non-Cryst. Solids 330, 1-12 (2003).

11. C. Grillet, C. Smith, D. Freeman, S. Madden, B. Luther-Davies, E. Magi, D. Moss, and B. Eggleton, "Efficient coupling to chalcogenide glass photonic crystal waveguides via silica optical fiber nanowires," Opt. Express 14, 1070-1078 (2006).

12. S. Ramachandran, and S. Bishop, "Photoinduced integrated-optics in rapid thermally annealed chalcogenide glasses," IEEE J. Sel. Top. Quantum Electron. 11, 260-270 (2005).

13. R. Decorby, N. Ponnampalam, M. Pai, H. Nguyen, P. Dwivedi, T. Clement, C. Haugen, J. McMullin, and S. Kasap, " High index contrast waveguides in Chalcogenide glass and polymer," IEEE J. Sel. Top. Quantum Electron. 11, 539-546 (2005).

14. V. Lyubin, M. Klebanov, A. Feigel, and B. Sfez,, "Films of chalcogenide glassy semiconductors: New phenomena and new applications," Thin Solid Films 459, 183-186 (2004).

15. M. Shokooh-Saremi, V. Taeed, I. Littler, D. Moss, B. Eggleton, Y. Ruan, and B. Luther-Davies, "Ultra-strong, well-apodised Bragg gratings in Chalcogenide rib waveguides," Electron. Lett. 41, 13-14 (2005).

16. T. Sudoh, Y. Nakano, and K. Tada, "Wavelength trimming technology for multiple-wavelength distributed feedback laser array by photo-induced refractive index change," Electron. Lett. 33, 216-217 (1997).

17. S. Song, S. Howard, Z. Liu, A. Dirisu, C. Gmachl, and C. Arnold, "Mode tuning of quantum cascade lasers through optical processing of Chalcogenide glass claddings," Appl. Phys. Lett. 89, 041115 (2006).

18. A. Zakery, Y. Ruan, A. V. Rode, M. Samoc, and B. Luther-Davies, "Low-loss waveguides in ultrafast laser-deposited As_2S_3 chalcogenide films ," J. Opt. Soc. Am. B 20, 1844-1852 (2003).

19. T. T. Nang, M. Okuda and T. Matsushita, "Photo-induced absorption change in some Se-based glass alloy systems," Phys. Rev. B 19, 947-955 (1979).

20. K. Tanaka, "Reversible photostructural change: Mechanisms, properties and applications," J. Non-Cryst. Solids 35-36, 1023-1034 (1980)

21. S. R. Elliott, "A unified model for reversible photostructural effects in chalcogenide glasses," J. Non-Cryst. Solids 81, 71-98 (1986)

22. Y. Ruan, M. Kim, Y. Lee, B. Luther-Davies, and A. Rode, "Fabrication of high-Q chalcogenide photonic crystal resonators by e-beam lithography," submitted to Applied Physics Letters.

23. D. Freeman, S. Madden, and B. Luther-Davies,"Fabrication of planar photonic crystals in a chalcogenide glass using a focused ion beam," Opt. Express 13, 3079-3086 (2005).

24. C. Grillet, D. Freeman, B. Luther-Davies, S. Madden, R. McPhedran, D. J. Moss, M. J. Steel, and B. J. Eggleton, "Characterization and modeling of Fano resonances in chalcogenide photonic crystal membranes," Opt. Express 14, 369-376 (2006).

25. Y. K. Lizé, E. C. Mägi, V. G. Ta'eed, J. A. Bolger, P. Steinvurzel, and B. J. Eggleton, "Microstructured optical fiber photonic wires with subwavelength core diameter," Opt. Express 12, 3209-3217 (2004).

26. S. Madden, "Investigation into the photosensitivity of AMTIR-1 films," Laser Physics Centre, Australian National University (personal communication, 2006).

27. A. Zakery and M. Hatami, "Nonlinear optical properties of pulsed-laser-deposited GeAsSe films and simulation of a nonlinear directional coupler switch ," J. Opt. Soc. Am. B 22, 591-597 (2005)

28. T. Igo, Y. Noguchi and H. Nagai, "Photoexpansion and 'thermal contraction' of amorphous chalcogenide glasses," Appl. Phys. Lett. 25, 193-194 (1974)

29. B. Song, S. Noda, T. Asano, and Y. Akahane, "Ultra-high-Q photonic double heterostructure nanocavity," Nature Mater. 4, 207-210 (2005).

30. S. Tomljenovic-Hanic, M. Steel, C. de Sterke, and D. Moss, "High-Q cavities in photosensitive photonic crystals," Opt. Lett. Accepted in press.

1. Introduction

Planar Photonic Crystals (PhC), which consist of a thin high index dielectric slab patterned with a 2D periodic array of air holes, are now recognized as a promising platform for achieving light control in a planar integrated circuit. Their ability to confine light at the wavelength scale has led to the demonstration of unprecedented compact photonic devices for integrated optical circuits [1]. However, in order to achieve desirable functionalities careful engineering and high accuracy fabrication is required. Although advances both in numerical

112

designs and nanofabrication techniques have enabled the development of more intricate photonic crystal systems, the required level of fabrication accuracy remains a limiting factor.

Post trimming of the properties of individual components is thus highly attractive, not only to relax the fabrication tolerances but also to allow individual components to be optimized for different environments or applications. Tuning of photonic crystal properties has previously been achieved through thermo-optic approaches [2], liquid crystal infusion [3], integration of nanofluidic circuitry [4], post-process chemical treatments [5], mechanical deformation [6] or mechanical perturbation of the electro-magnetic environment with an Atomic Force Microscopy (AFM) tip [7]. Although these approaches can provide enough tuning to modify the optical properties of very compact devices, they generally lack the highly desirable ability to induce changes locally. In particular, single Quantum Dot (QD) devices based on cavity QED require fine tuning of the photonic crystal cavity resonance in relation to the emission wavelength of the QD [8,9].

In this paper we demonstrate a novel post-process tuning technique which utilizes the photosensitivity of chalcogenide glass [10] to modify the optical properties of a planar photonic crystal device. A W1 PhC waveguide was exposed to 633nm light at an intensity of 1.3W/cm^2. The resulting change in the dispersion of the modes of the waveguide was detected *in situ* using an evanescent probing technique [11], and a shift of 5 nm in the resonant coupling wavelength was observed. We show that the photoinduced change in the photonic crystal grows as a saturating exponential with increasing exposure.

Previously, the chalcogenide photosensitivity has been successfully utilized for the creation of directly written waveguides [12, 13, 14], strong Bragg gratings [15] and for post-tuning of optical components such as distributed feedback lasers [16] and quantum cascade lasers [17]. The photosensitivity of the chalcogenides is known to arise from structural rearrangements induced by the absorption of light at frequencies near the absorption band-edge of the material [18]. These structural rearrangements lead to changes in the properties of the glass such as the refractive index and density. Some of the various photoinduced phenomena are reviewed in [10]. The magnitude and sign of these photoinduced changes can be highly dependant on the chemical composition of the glass [19] and on the processing history of the sample [20]. Furthermore, these changes may be either reversible or irreversible, with irreversible changes resulting from "photo-annealing" of thin films deposited in a non-equilibrium state [21], and reversible changes resulting from structural rearrangement into a quasi-stable state upon exposure [20, 21].
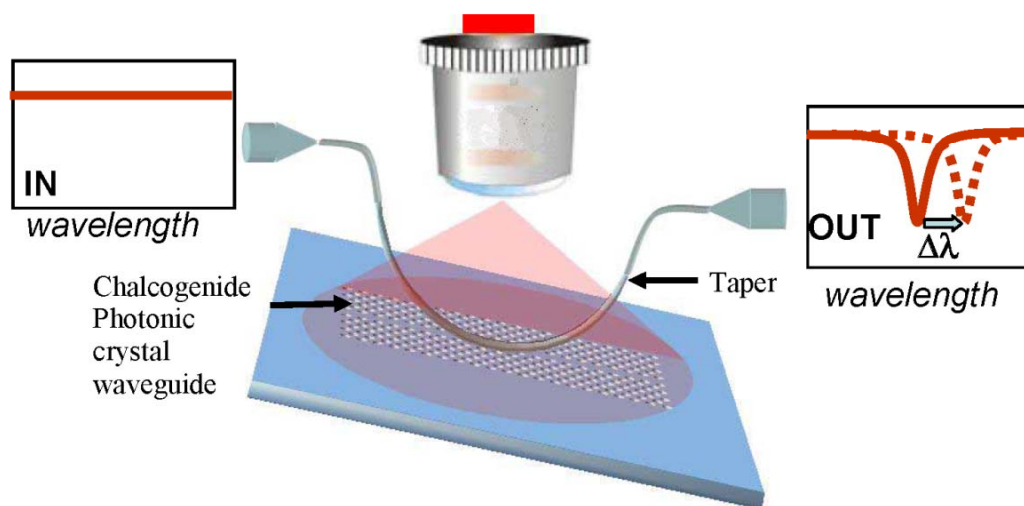

Fig. 1. A schematic diagram showing the principle of the photosensitive post tuning of a chalcogenide photonic crystal waveguide.

113

2. Principle

Figure 1 shows the principle of the photosensitive post-tuning experiment. The resonant coupling wavelength from the fiber taper to the modes of the chalcogenide glass PhC waveguide was monitored by measuring the transmission spectrum through the taper with an Optical Spectrum Analyzer (OSA). The dips in the transmission spectrum are associated with coupling to the modes of the PhC waveguide. The photoinduced change in the PhC was observed by monitoring the shift in wavelength of these dips during the exposure of the PhC sample to 633nm light.

3. Photonic crystal waveguide design and device fabrication

Figure 2 shows an optical microscope image and a Scanning Electron Microscope (SEM) image of the photonic crystal structure used in this experiment. The structure under test consists of a ~ 70 μm "W1" waveguide, i.e. a missing row of holes along the Γ-K direction of a triangular lattice of air holes in a chalcogenide membrane.

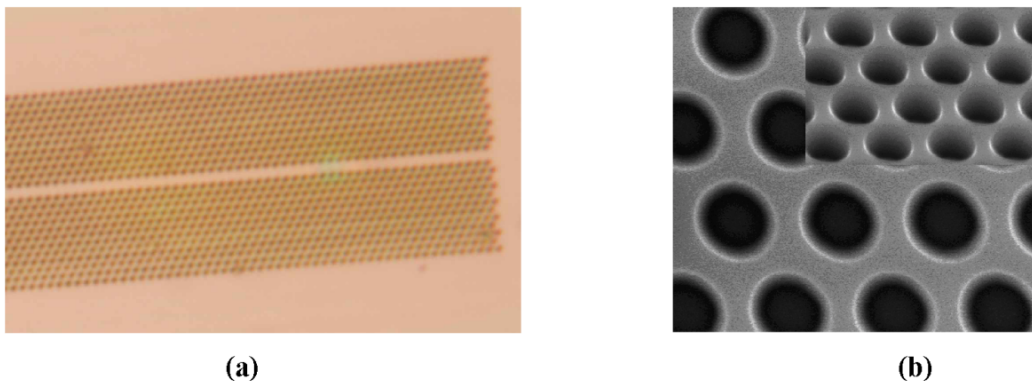**(a)**   **(b)**

Fig. 2. (a) Optical microscope image of the W1 PhC waveguide used in this experiment. (b) Scanning electron microscope image. Hole pitch is 550nm.

Details of the fabrication process are presented elsewhere [22] and are summarized briefly here. First, a 300nm thick film of $Ge_{33}As_{12}Se_{55}$ (AMTIR-1) chalcogenide glass [23, 24] was deposited by Ultrafast Pulsed Laser Deposition (UPLD) onto an oxidised silicon wafer. The sample was then coated with a thin layer of polymer photoresist (PMMA). The PhC structure was written into the photoresist by electron beam lithography and transferred into the chalcogenide layer using Chemically Assisted Ion Beam Etching (CAIBE). Finally, a free standing suspended PhC structure was formed by wet etching the oxidised silicon layer beneath the chalcogenide film. The resulting 300nm thick suspended membrane had a nominal refractive index of 2.7 and hence corresponded to a thickness of $\lambda/2n$ close to λ=1.55 μm, ensuring that only the fundamental mode is vertically confined in this structure. A lattice parameter of 550nm and hole radius of 165nm were chosen in order to open up a photonic band gap for the TE-like modes (E field mainly lying in the plane of the slab) near 1550nm. The chalcogenide PhC membrane was kept in its as deposited state (not thermally annealed) and was protected from ambient light prior to the experiment.

4. Post-trimming photosensitive experiment

A schematic diagram of the "post-trimming" experiment is shown in Fig. 3. It consists of; (i) the evanescent coupling setup which was used to probe the modes of the PhC waveguide, allowing the photoinduced change to be monitored and; (ii) the "writing" system, which consisted of a 633nm linearly polarized 0.8mW CW Helium Neon laser source, a lens and a beamsplitter.
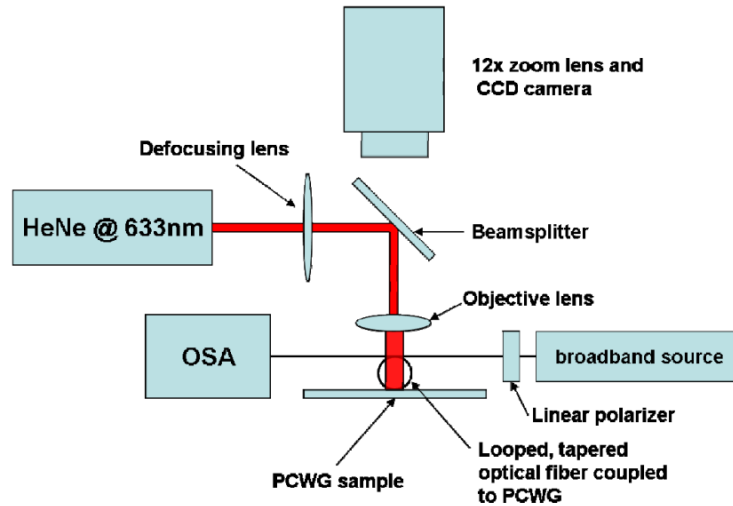
Fig. 3. A schematic diagram of the experimental setup for both coupling into the Photonic Crystal Waveguide (PCWG) using evanescent coupling and photosensitive post-processing the PhC sample.

It consists of; (i) the evanescent coupling setup which was used to probe the modes of the PhC waveguide, allowing the photoinduced change to be monitored and; (ii) the "writing" system, which consisted of a 633nm linearly polarized 0.8 mW CW Helium Neon laser source, a lens and a beam splitter.

The evanescent coupling system is described in detail in [11]. Evanescent coupling is a phase-matched technique where, in this case, the evanescent field of a tapered optical fiber is used to couple light into the PhC waveguide brought into close proximity with the tapered fiber (Fig. 4. a and b). The condition for coupling to occur is that the taper mode and PhC waveguide mode must possess some spatial overlap, as well as sharing the same momentum. This occurs where the taper dispersion curve intersects the dispersion curve of the waveguide mode. Figure 4b shows the calculated band structure of a W1 waveguide with the same parameters as the sample used in this work. Overlaid on this is the dispersion curve corresponding to the mode of a 1.3 μm diameter fiber taper. The band structures were calculated with the RSoft bandSOLVE program which uses the method of plane wave expansion to calculate the bands.
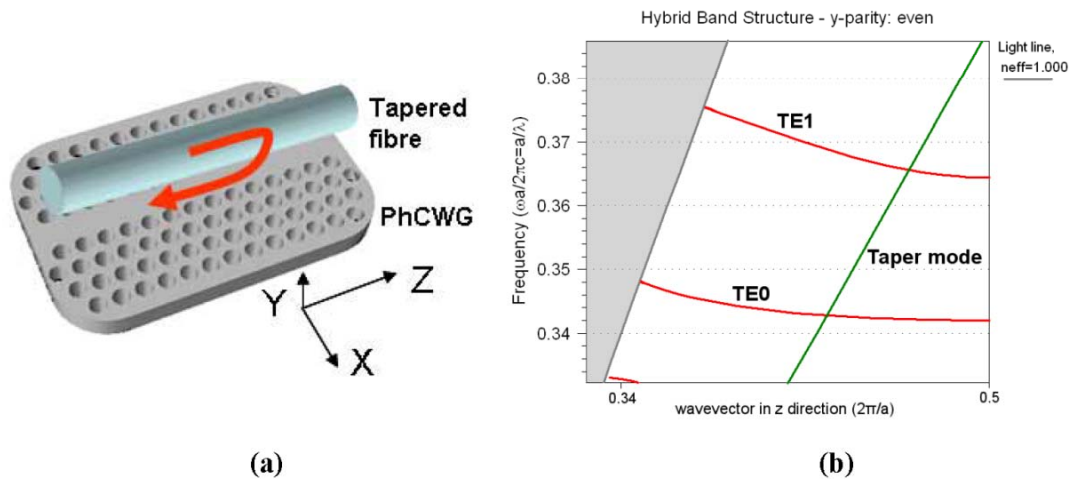

(a)   (b)

Fig. 4. a) Schematic showing the coupling from a tapered fibre to PhC waveguide, b) Band structure of the W1 waveguide used in this work (red) overlaid with the dispersion curve of the tapered fiber in green.

115

The tapered fibers were fabricated using a procedure reported previously [25], and for this work the fiber taper was made from standard single mode fiber. After tapering, the fibre was formed into a loop in the waist region in order to localize the interaction region between the taper and the photonic crystal waveguide. The taper used in this work was estimated to have a waist diameter of ~ 1.3 µm and a loop diameter of ~ 200µm. The loss through the taper was ~1dB in the wavelength range of 1550nm-1620nm. To achieve evanescent coupling, the taper was aligned above and parallel to the photonic crystal and then moved into direct contact so that the relative alignment of the taper with the waveguide, and hence the coupling, remained fixed throughout the experiment. A broadband light source (Hewlet Packard 83437A, a four ELED light source) was launched into the taper through a polarizer to select TE polarization and the output end of the fiber was connected to an OSA (Agilent 86140B) where the transmission spectrum through the taper was measured. The polarization was adjusted by placing the taper onto the bulk PhC region and then adjusting the polarizer to minimize the loss in the transmission of the taper. Since the PhC has a bandgap in the TE modes at the frequencies of interest, loss is associated with coupling to TM modes of the bulk PhC and hence minimizing the loss results in the TE polarization at the taper waist.

Figure 5 shows a typical transmission spectrum through the fiber taper when aligned and in contact with the PhC waveguide. Resonances corresponding to coupling to both the fundamental W1 guided mode (TE_0) and the first higher order mode (TE_1) can be identified. The coupling wavelengths are in good agreement with the predicted values based on band structure calculations. The small difference between the predicted coupling wavelengths, shown by the dashed line, and the experimentally measured values is due to the uncertainty in the PhC air hole spacing and radius, slab thickness and refractive index as well as the dispersion of the chalcogenide which is not taken into account in the modeling. The transmission dip associated with coupling to the fundamental TE_0 mode was ~6dB, which equates to ~ 75% of the light being coupled from the taper into the waveguide. This lower coupling efficiency compared to [11] is expected because of the looped taper shape used in this experiment which results in a substantially smaller coupling length.
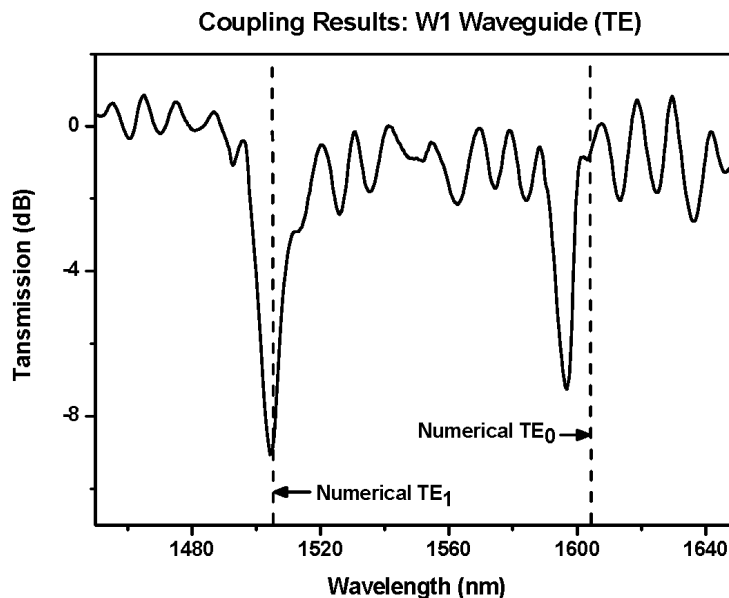
Fig.5. Transmission spectrum through the tapered fiber for coupling to the W1 waveguide, with the fiber in direct contact with the waveguide. Dashed lines represent numerically predicted values for the TE_0 and TE_1 coupling resonances.

In order to expose the sample to actinic light, the laser source was focused on the sample via a lens and beam splitter (see Fig. 3). A wavelength of 633 nm was chosen because the photon energy is close to but slightly below the electronic band edge for AMTIR-1, where

these glasses are generally photosensitive [14]. The beamsplitter was used to direct the beam towards the sample at normal incidence, while allowing in-situ imaging of the sample. A defocusing lens was introduced in order to control the laser spot size at the sample. The defocusing lens was positioned to give a spot diameter of ~ 280 μm ($1/e^2$ Gaussian spot). Given that the photonic crystal waveguide is ~70μm long, this means that the incident intensity varied by less than 10% across the sample. The power measured at the sample was 400μW corresponding to a peak intensity of 1.3W/cm^2 for the Gaussian laser spot. After obtaining an optimal coupling into the PhC waveguide, the HeNe laser was turned on and the position of the laser spot adjusted so that it was centered on the PhC structure. During alignment the laser was strongly attenuated (40 dB). The sample was exposed for a period of ~5 hours and the transmission spectrum through the taper was recorded at one minute intervals during this time. Further, the sample was monitored for a period of ~5 days following the exposure to determine whether the observed change was stable. The experiment was conducted at room temperature with the ambient room light switched off.

5. Results and discussion

Figure 6 shows the transmission spectrum of the fiber-taper due to coupling to the fundamental PhC waveguide mode for different exposure times. The resonance associated with coupling to the TE_0 mode was observed to shift to longer wavelengths with increasing exposure. The same trend was observed for the higher order TE_1 PhC waveguide mode. In addition, we observed an increase in the coupling strength with exposure.
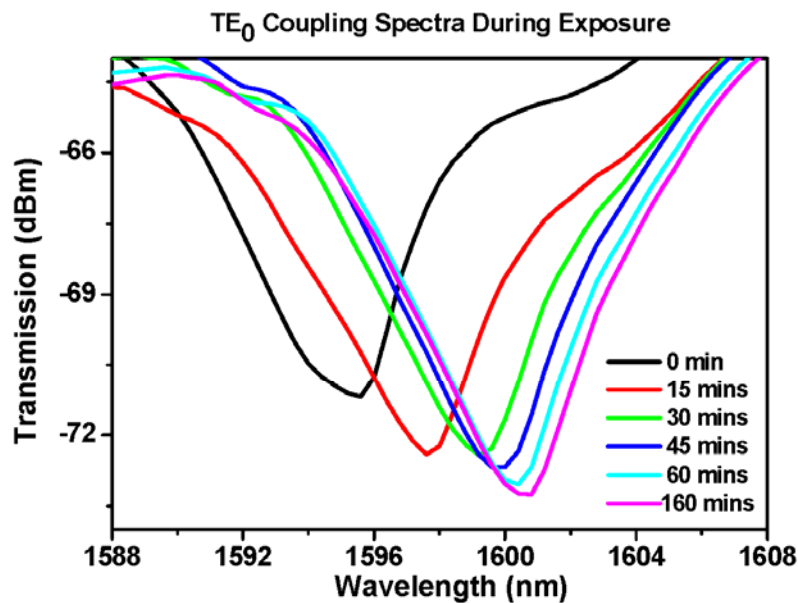
Fig. 6. Photosensitive tuning of the TE_0 mode during the exposure. The resonance dip is plotted for a range of times during the exposure.

Figure 7 shows a plot of the resonant wavelength versus exposure fluence, which clearly displays saturation behaviour at higher fluences. The circles in the graph are experimental data points whilst the curve is an empirical fit to an exponential curve. The maximum wavelength shift was 5.2nm ±0.4nm whilst the maximum increase in the resonance depth was ~ 2dB.

117

Shift of TE_0 Coupling Wavelength During Exposure
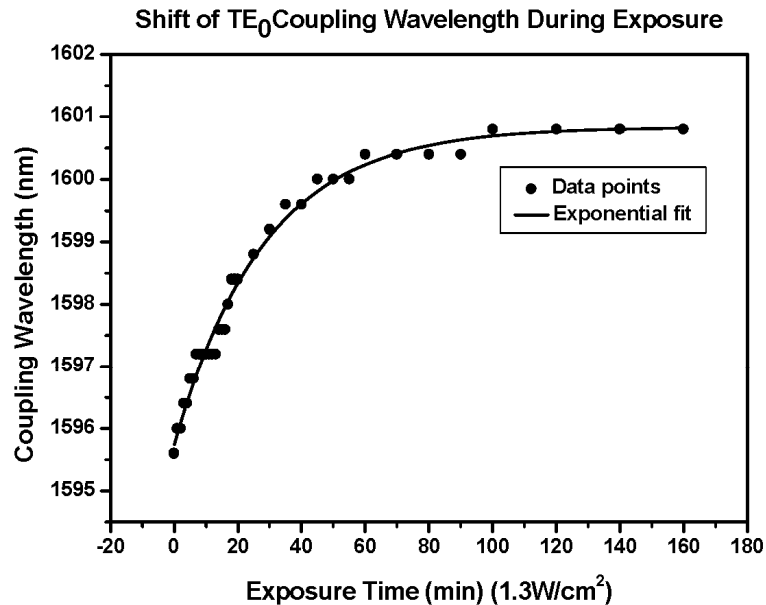
Fig. 7. Shift in coupling wavelength versus exposure fluence at 633nm of the PhC TE_0 waveguide mode.

The exact cause of the observed increase in coupling strength is still under investigation but it is likely to be related to a modification of the waveguide mode field profile resulting from changes in the waveguide dispersion curve. In principle, one would expect that in modifying the group index of the PhC waveguide mode, the overlap with the taper mode, and hence the coupling strength, could change. The shift in the coupling wavelength of the higher order waveguide mode follows the same trend as for the fundamental mode and during the exposure there was no relative shift between the two modes, i.e. the wavelength difference remained constant to within the resolution of the OSA.

Preliminary investigations into the photosensitivity of unpatterened AMTIR-1 films [26] at 633nm have shown a decrease in the material refractive index and a volume expansion. These results are consistent with previous work by Zakery *et al.* [27], who reported a refractive index decrease in AMTIR-1 due to exposure, and Igo *et al.* [28], who reported photoexpansion in a range of As-Se-Ge glasses. For the PhC waveguide, a refractive index decrease results in a shift of the waveguide modes to shorter wavelengths. Our calculations indicate that a wavelength shift of ~5nm is obtained with an index change of 0.01, and that this change occurs linearly in the region of interest. Conversely, expansion of the PhC causes a shift towards longer wavelengths, a ~5nm wavelength shift of the TE_0 mode is obtained for 0.31% material expansion. Thus we attribute the observed wavelength shift to a combination of these two competing effects. However, the material expansion has the bigger effect in this case leading to the observed resonance shift to longer wavelengths. Work is in progress to resolve the magnitude of each contribution to the resonance shift.

For many potential applications, the ability to tune the resonance towards longer wavelengths in a controlled manner is particularly relevant. For instance, the double heterostructure cavity suggested by Noda *et al.* [29] relies on precise engineering of the lattice constants along a line defect. Light is confined to the central region (larger lattice constant) due to the differences between the mode-gap frequencies along this line defect. In the same way, it should be possible to create a double heterostructure cavity by exposing a small region of a W1 in chalcogenide photonic crystal. Based on band structure calculations, a 5nm shift is equivalent to the band shift that would be induced by an increase in the refractive index of ~ 0.01. Results reported in [30] show that this should lead to a cavity Q ~30000. In order to reach the maximum Q predicted theoretically, a ~ 20nm shift would be required. Future

studies into different techniques or different chalcogenide glass compositions may increase the tuning range.

Another area where the photosensitivity of chalcogenide glass could prove to be highly practical is single quantum dot devices based on cavity QED, such as a single photon source. This technique offers a way to align the cavity resonant wavelength with the QD emission wavelength – an important challenge since enhancing the QD SE rate via the Purcell factor of the cavity mode requires critical spectral matching between the single QD and the cavity mode. The ability to tune the cavity resonant wavelength, via a photosensitive chalcogenide cladding applied on top of the PhC device for instance, in order to match it to the QD emission appears highly promising.

6. Conclusions

We present the first experimental demonstration of photosensitive post-tuning of a planar photonic crystal device. We use the material photosensitivity of $Ge_{33}As_{12}Se_{55}$ (AMTIR-1) chalcogenide glass to 633nm light in order to modify the resonant coupling wavelength of a W1 photonic crystal waveguide by up to ~ 5nm towards longer wavelengths. The wavelength shift showed a saturating exponential growth trend with increasing exposure, and this suggests that a high degree of control over the photosensitive tuning process should be possible. This work demonstrates that this post-processing technique is highly promising for applications where fine post-tuning of existing structures is required, such as for single photon source applications or for directly photo-writing resonant cavity structures.

Acknowledgments

5.1   Epilogue

Following the work detailed in the article above, initial work has begun to investigate inducing cavities into photonic crystals by means of exploiting photosensitive effects. Here, the samples (still $Ge_{22}As_{12}Se_{55}$) undergo a negative Δn refractive index change. Therefore, to induce a high-Q cavity with greater refractive index than its surrounds, a shadow mask is required as illustrated in Fig. 5.1.
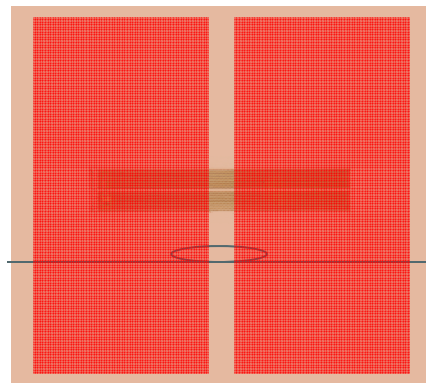
Figure 5.1. Top view illustration of the exposure experiment to induce a cavity. A shadow mask is used to maintain a local region of higher refractive index whilst the surrounding sections have theirs exposed and thus lowered.

Figure 5.2 displays initial results of an experiment performed as per Fig. 5.1. During exposure, a cavity resonance steadily becomes more pronounced. After 20 minutes of exposure, the cavity resonance is clearly observed, possessing a Q-factor of $Q \approx 2,000$. However, this is not an especially high value, despite the experiment being a first-attempt. One possible reason for this is that the Δn is less than expected, which could be due to the particular batch of chalcogenide material. Other possible explanations for the low Q include the presence of the nanowire affecting the results and other parasitic losses caused during exposure.
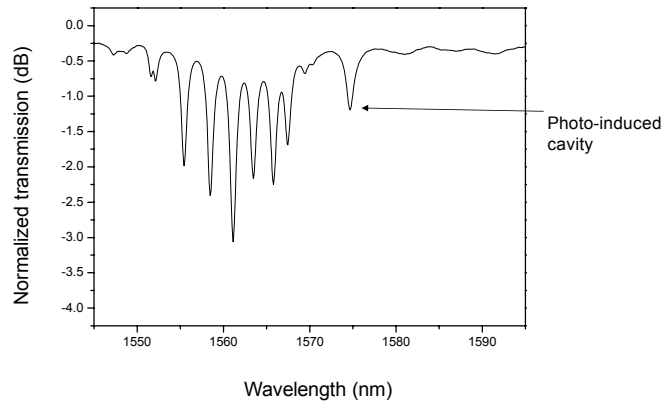
Figure 5.2. Trace of a photosensitive induced cavity after 20 minutes of exposure. The cavity resonance is steadily more pronounced throughout the exposure.

Figure 5.3 shows an image of the photonic crystal waveguide structure after the exposure experiment. An observable line representing the formation of a double-heterostructure is clearly evident.
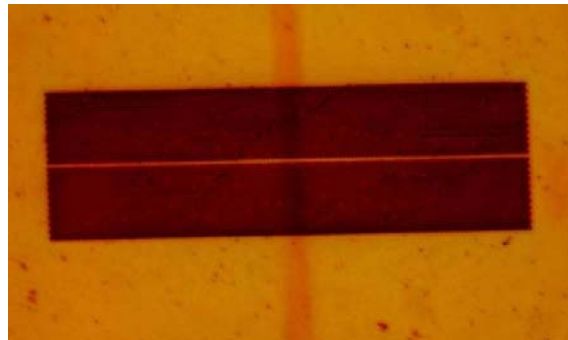
Figure 5.3. Image of the photonic crystal waveguide after the shadow mask exposure experiment.

Improving on these results may utilise a chalcogenide glass that possesses a positive Δn change. This would then allow a single laser spot to induce a cavity rather than requiring a shadow mask. This has the advantage of a gentle refractive index profile – a Gaussian – to more strongly confine photons for high-Q resonances, as shown in Fig. 5.4.

121
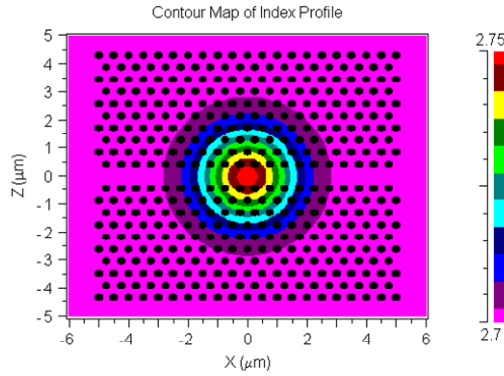
Figure 5.4. Using a material with a positive Δn allows one to simply write a laser spot onto the structure. This would enjoy a Gaussian profile – ideal for high-*Q* cavities.

More sophisticated photonic crystal functionalities may be demonstrated as a follow-up to this work. Examples include the introduction of access channels between fabricated waveguides, or even coupled resonator optical waveguides (CROWs) which could be formed by parallel double-heterostructures.

Summary

This work represents the first demonstration for photosensitive post-tuning of a photonic crystal waveguide structure.

The paper reproduced from *Optics Express* Vol. 15, pp. 1277–1285, 2007, made the following advancements:

- First experimental results for photosensitive post-tuning of a photonic crystal waveguide, made from chalcogenide glass.

Chapter 6

Microfluidic photonic crystal cavities

This chapter presents three articles relating to a microfluidic approach to post-tune photonic crystal cavities. As noted in the Chapter 2, the formation of a cavity within a photonic crystal requires modification of the lattice in some way. In this work that modification is achieved by infiltrating the holes of a photonic crystal with a fluid. The infiltration of holes with a fluid increases their refractive index and therefore changes the device's optical properties. The liquid infiltration scheme offers two promising methods to postprocess photonic crystal cavities. Firstly, the inherent mobility of fluids enables significant refractive index change to occur in the holes. Secondly, the fluids themselves can easily be doped with functional components.

The first article presents a proof-of-concept demonstration for infiltrating a region of holes in a planar photonic crystal that forms a double-heterostructure cavity. The dispersive effects of the photonic crystal are shown to manifest in the free-spectral-range of the Fabry-Pérot resonances. The second article presents high Q-factors in the microfluidic cavities of silicon-based photonic crystals, with values reaching $Q = 57,000$. These results are discussed in terms of sensing potential. The third article presents a complete reconfigurability of this technique, demonstrating accurate changes in cavity length and then erasing the penetrated fluid entirely. As the cavity lengths are changed, the trends of Q-factor, resonance frequencies and tolerance of Q-factor are investigated.

Infiltration technique

The infiltration of liquid into the air holes of a planar photonic crystal involves the use of a tapered glass microtip, whose apex diameter is reduced to $\varnothing = 220$ nm, and piezo-electric manipulation stages to make use of the microtip. The glass microtip is first moved by the manipulation stages into a fluid reservoir, gathering a small volume that remains attached due to adhesive forces. The gathered fluid forms into droplets along the length of the microtip, which may then be deposited in proximity to the

photonic crystal to be infiltrated. The array of droplets offers a range of choice in volume. The microtip may then be used to select a droplet of appropriate volume and draw it across the photonic crystal. Providing the wetting properties of the fluid and photonic crystal material are both amenable to the process, the fluid will penetrate the pores via capillary action and remain suspended there. It is advisable to use a fluid that is non-volatile (such as oil) and also optically lossless at wavelengths of interest.
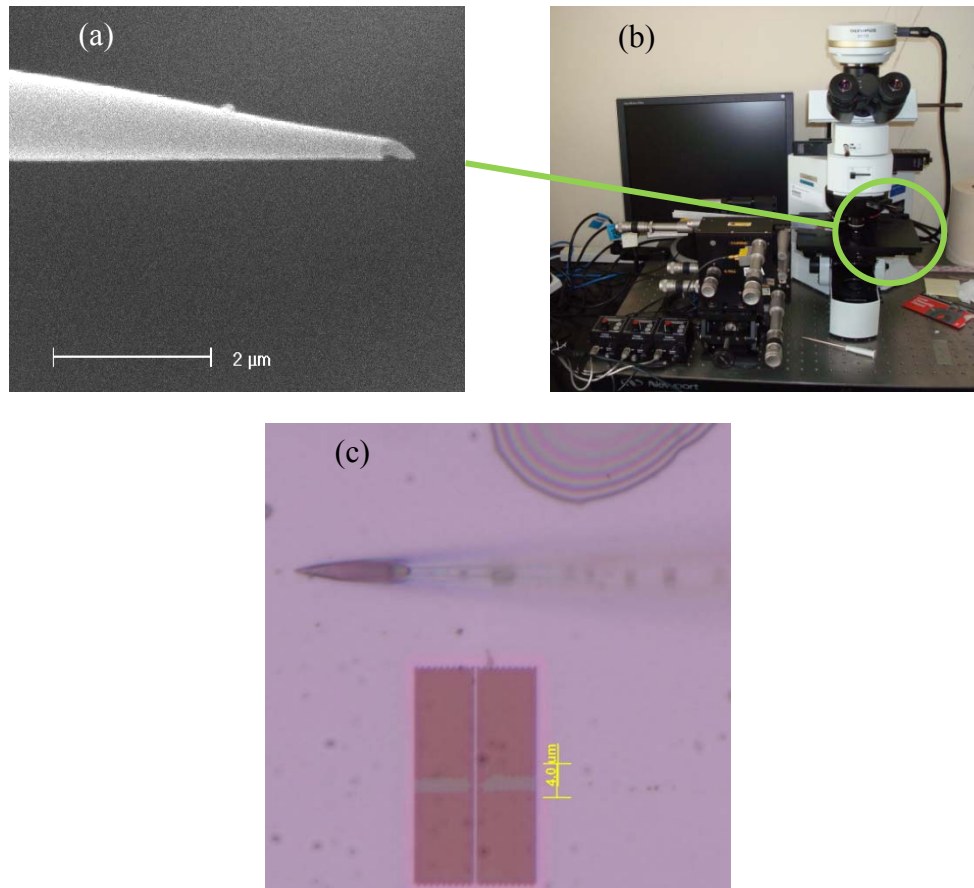
Figure 6.1: The liquid infiltration apparatus. (a) SEM image of a tapered glass microtip with apex diameter $\varnothing = 220$ nm. (b) Infiltration setup, consisting of $150\times$ microscope and piezo-electric stages to manipulate the tapered microtip. (c) Microscope image of the infiltration technique showing fluid reservoir, photonic crystal section and the glass microtip manipulating a small volume of fluid.

Contributors

In the first of the following three articles, reproduced from *Applied Physics Letters* Vol. 91, 121103, 2007, the author of the thesis wrote the article. This thesis author's contributions were as follows:

- Performed the microfluidic infiltration and characterisation measurements

- Performed calculations and provided the figures presented

- Contributed the majority of writing of the manuscript

In the second of the following three articles, *Optics Letters* Vol. 33, 2008, Uwe Bog shared an equal part in the undertaking of experiments and primarily wrote the manuscript. This thesis author's contributions were as follows:

- Performed the presented experimental measurements

- Fabricated tapered fibre for experiment

- Contributed to the writing of the manuscript

In the third of the following three articles, *Optics Express* Vol. 16, pp. 15887-15896, 2008, Uwe Bog shared an equal part in the undertaking of experiments while the author of this thesis primarily wrote the manuscript. This thesis author's contributions were as follows:

- Performed the presented experimental measurements

- Fabricated tapered fibre for experiment

- Contributed the majority of writing for the manuscript

Formal acknowledgement of the contributions of the author of this thesis is included in Appendix A.

Microfluidic photonic crystal double heterostructures

Cameron L. C. Smith,[a] Darran K. C. Wu, Michael W. Lee, Christelle Monat, Snjezana Tomljenovic-Hanic, Christian Grillet, and Benjamin J. Eggleton
Centre for Ultrahigh-Bandwidth Devices for Optical Systems (CUDOS), School of Physics, University of Sydney, Sydney, New South Wales 2006, Australia

Darren Freeman, Yinlan Ruan,[b] Steve Madden, and Barry Luther-Davies
Centre for Ultrahigh-Bandwidth Devices for Optical Systems (CUDOS), Laser Physics Centre, Australian National University, Canberra, Australian Capital Territory 0200, Australia

Harald Giessen
4th Physics Institute, University of Stuttgart, D-70569 Stuttgart, Germany

Yong-Hee Lee
Nanolaser Laboratory, Department of Physics, Korea Advanced Institute of Science and Technology (KAIST), Daejon 305-701, Korea

We demonstrate postprocessed and reconfigurable photonic crystal double-heterostructure cavities via selective fluid infiltration. We experimentally investigate the microfluidic cavities via evanescent probing from a tapered fiber at telecommunication wavelengths. Fabry-Pérot fringes associated with modes of the induced cavity are in good agreement with the theory. We also demonstrate a cavity with quality factor $Q=4300$. Our defect-writing technique does not require nanometer-scale alterations in lattice geometry and may be undertaken at any time after photonic crystal waveguide fabrication. © 2007 American Institute of Physics. [DOI: 10.1063/1.2785988]

Research into optical microcavities based on photonic crystal slabs (PCSs) has attracted significant attention in the past several years. There are numerous applications for compact and low-loss microcavities, such as channel drop filters,[1] low-threshold lasers,[2] cavity quantum electrodynamics experiments,[3] optical switching,[4] and optical sensing.[5] The cavity design goals for these applications are high Q factors and small mode volumes.[6] Indeed, these two conditions can potentially give rise to a dramatic enhancement of light-matter interaction over a compact space, which is of particular relevance for optical switching and sensing.

The use of photonic crystal microcavities has widely exploited local alterations in the periodic geometry of PCS lattices. These structural modifications, referred to as "defects," are performed during the fabrication step and typically result in the appearance of one or several cavity modes that are spatially confined within the defect. The defect is made, for instance, by omitting, shrinking, or enlarging one or more holes in the PCS.[7] More recently, "double heterostructures" have been achieved from a slight change of the PCS period over a finite area of the nominal PCS lattice.[8] However, the nanometer-scale precision required to realize sophisticated and optimized geometries eventually becomes a limiting factor in achieving high-Q cavities, as pointed out by Asano *et al.*[9]

Recently, several groups have reported demonstrations of postprocessed PCS structures, granting them the flexibility to tune or reconfigure device properties to suit various applications at any time after the PCS is fabricated.[10–13] In particular, Intonti *et al.* introduced a "pixel by pixel" approach for writing and rewriting PCS defect structures via fluid

infiltration.[12] Theoretical results of Tomljenovic-Hanic *et al.* showed that high Q-factor cavities could be achieved in PCSs from fluid infiltration[14] by forming double-heterostructured geometries, providing an integrated optofluidic sensing architecture.

In this letter, we present experimental demonstrations of double heterostructure type microcavities formed within PCSs after their fabrication. Instead of exploiting a change of the PCS period, the double heterostructures are created by selectively fluid-filling a restricted region of the PCS using a micropipette. This approach offers a flexible way to write microcavities by choosing (i) the index of the infused liquid and (ii) the length and pattern of the infiltrated PCS area. In addition, the reversible nature enabled by fluid mobility offers a "rewrite" potential, paving the way for reconfigurable microphotonic devices[15] and sensing architectures.

Figure 1(a) illustrates the microfluidic-filled double-heterostructure waveguide cavity of the present study. The initial PCS structure is a W1 waveguide that results from the omission of a single row of air holes along the Γ-K direction of a triangular photonic crystal lattice. The central section of the waveguide, denoted by the lighter circles, is filled with a liquid across its length. The fluid-filled holes present a dif-
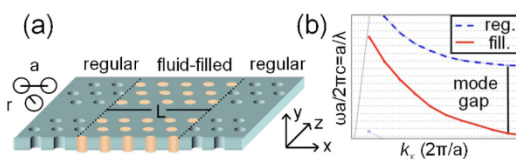

FIG. 1. (Color online) (a) Double-heterostructure microcavity with lattice period a and hole radius r. Fluid-filled holes have a refractive index $n=1.4$; the rest are $n=1.0$. Refractive index of the slab is $n=2.68$. (b) Dispersion relation for regular (dashed) and fluid-filled (solid) photonic crystal waveguides. The difference between the curves is labeled mode gap.

91, 121103-1

ferent refractive index n_{holes} than those enclosed in the surrounding nominal PC lattice, with the different PCS sections forming a double heterostructure.

Figure 1(b) summarizes the mechanism of the double-heterostructure cavity, which can be understood qualitatively by comparison of the dispersion curves of two W1 waveguides with different n_{holes}.[8] As a result of the n_{holes} increase (here from 1 to 1.4), the fundamental guided mode of the waveguide is shifted towards lower frequencies. This creates a "mode gap" between the fundamental mode of the filled and unfilled waveguides. Consequently, a waveguide mode that is excited in the fluid-filled section with a frequency lying in this mode-gap window cannot propagate any further in the surrounding unfilled waveguide area. Instead, it remains localized within the fluid-filled section, decaying evanescently in the surrounding unfilled region.[14]

The experimental PCS structure is made from chalcogenide glass ("AMTIR-1" $Ge_{33}As_{12}Se_{55}$), having a refractive index $n_{slab}=2.68$. The lattice constant is $a=550$ nm, slab thickness $T=300$ nm, and hole radius $r=190$ nm. The photonic bandgap of this structure spans optical telecommunication frequencies. The entire PCS structure is 40 periods in the x direction and 19 periods in the z direction. To create the cavity, we introduce an index-matching fluid of refractive index $n=1.4$ selectively into some air holes of the PCS. We use a tapered glass micropipette with 2 μm tip diameter, which is mounted onto a micromechanical stage. The tip is inserted within a large meniscus of the filling fluid. As the tip is withdrawn from the meniscus, droplets of the fluid remain along its length due to surface tension and the hydrophilic nature of the glass. These droplets are then deposited in close proximity to the PCS structure under a high magnification (100×) microscope. Finally, by careful manipulation of the micropipette, a droplet of choice is drawn along the photonic crystal to create the double heterostructure.

We investigate the fluid-filled double heterostructures via evanescent probing.[16] A silica fiber with its diameter reduced to 0.8 μm for a 2 mm length is brought into close proximity with the cavity. Due to the reduction in size, the evanescent field extends significantly beyond the tapered fiber boundary, allowing it to interact with the waveguide.

Evanescent probing provides a method to check that the fluid penetrates the pores of the photonic crystal and does not form an excess fluid "layer." This is evident when an overabundance of fluid is drawn along the waveguide and unwanted meniscus forms; the tapered fiber suffers significant broadband losses. Typically the fluid infiltration experiments described further below did not result in observable loss.

The first investigated PCS double heterostructure has a fluid-filled section of 9.8 μm length, as shown in Fig. 2(a). Figures 2(b) and 2(c) show the experimental transmission through the tapered fiber as it is evanescently coupled to the waveguide, before and after the liquid infiltration. For both measurements, the tapered optical fiber is in contact with the structure, over a length estimated to be 15 μm. Without the liquid, a single dip is obtained at 1570 nm, which corresponds to the coupling into the fundamental mode of the waveguide.[17] After the liquid infiltration, the spectrum displays additional features at slightly longer wavelengths to the reference fundamental. We attribute these dips to Fabry-Pérot (FP) resonances as the fundamental mode of the fluid-filled waveguide [solid curve of Fig. 1(b)] undergoes multiple reflections at the discontinuities between the different
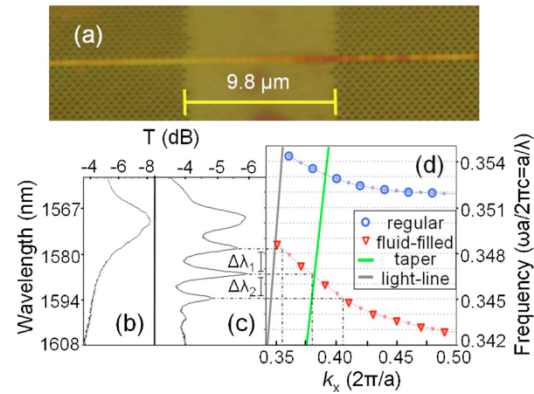

FIG. 2. (Color online) (a) Microscope image of W1 PCS structure with a 9.8 μm fluid-filled section. [(b) and (c)] Experimental transmission from the taper when it is coupled to the W1 PCS, (b) before and (c) after the fluid filling. (d) Dispersion curves of the silica taper and the W1 PCS, both fluid filled (triangles) and unfilled with fluid (circles), as calculated separately using a 3D plane-wave method. Used wavevector k_x is taken along the waveguide direction. Where the taper curve intersects with W1 PCS curves, phase matching (coupling) occurs. Trace (c) displays additional FP resonances, which can be related to the calculated dispersion curve of the fluid-filled W1 PCS.

PCS sections, which act as effective mirrors in the mode-gap window.

The number of FP peaks that are observed experimentally is limited to 3–4 over the predicted mode-gap window. Note that the coupling strength of the FP peaks with the taper is at a maximum for the 1586.5 nm feature and decreases for the other peaks on both sides of this wavelength due to an increased phase mismatch between the fiber and the cavity modes.[16] Also, one can notice a larger linewidth of the shorter wavelength dip at 1570 nm, which corresponds with coupling to the fundamental mode of the regular waveguide where the tapered fiber interacts with it outside the fluid-filled section. The wavelength of the FP resonances should roughly meet the following condition:

$$2k_xL = 2\pi p, \qquad (1)$$

which relates the wavevectors k_x of the FP resonances to the fluid-filled cavity length L through an integer p.[18,19]

The wavelengths of the experimental dips have been superimposed onto the dispersion curve of the infiltrated waveguide mode of Fig. 2(d), calculated using a three-dimensional (3D) plane-wave method with a supercell approach (RSoft's BANDSOLVE) using the PCS parameters mentioned earlier. Their corresponding wavevectors, as extracted from the dispersion curve, display a nearly equal separation that is roughly π/L, in close agreement with Eq. (1). At the same time, the experimental free spectral range between the resonances becomes smaller as λ becomes longer ($\Delta\lambda_1=7.65$ nm and $\Delta\lambda_2=7.45$ nm). This is consistent with the dispersive behavior of the infiltrated waveguide mode that presents a decrease in group velocity at lower energy. Indeed, the group velocity can be related to the wavelength separation $\Delta\lambda$ between the FP peaks, according to $V_g=2\,Lc\Delta\lambda/\lambda^2$. This relation produces an estimate of the group velocity ranging between $c/16.8$ and $c/17.2$, in close agreement with the dispersion displayed in Fig. 2(d). The slight discrepancy between experimental and theoretical data
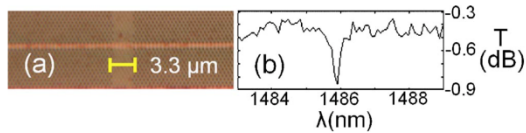
127

FIG. 3. (Color online) (a) Image of W1 PCS structure with a 3.3 μm fluid-filled section. (b) Corresponding experimental transmission when probed by evanescent coupling displaying high-Q ($Q=4300$) resonance.

(especially for the fundamental mode resonance frequency) is attributed to the simplification of our modeling, which is based on the assumption that coupling between the cavity and the taper is weak. This is not the case due to the direct contact between the taper and the waveguide.

Second, we investigate a fluid-filled cavity with length $L=3.3$ μm, as shown in Fig. 3(a). Evanescent probing of this structure provides a transmission spectrum with a distinct and narrow feature, as displayed in Fig. 3(b). The corresponding net Q-factor Q_T of the dip measured experimentally encompasses all the different decay channels available to the photons in the system, given by

$$\frac{1}{Q_T} = \frac{1}{Q_0} + \frac{1}{Q_{fiber}} + \frac{1}{Q_{parasitic}}, \qquad (2)$$

where Q_0 is the intrinsic Q-factor of the cavity, Q_{fiber} is the coupling between the cavity and the taper, and $Q_{parasitic}$ is the parasitic losses associated with any significant perturbation of the cavity mode field.[10] Our measured quality factor is $Q_T=4300$, with a transmittance of 90%.

Apart from the reconfigurable photonic device application offered by this approach, potential can be found for optical sensors.[5,15] The sensor based PCS designs that have been proposed thus far typically require an alignment between the defect and infiltrated area. In addition, high Q-factors of the optical modes involved in the sensing scheme are typically degraded by the fluid infiltration step. Here, these problems are solved because the initial structure presents no cavity mode in the absence of fluid while the fluid itself potentially generates the high-Q resonances. This architecture could be readily exploited to create a series of multiple and parallel integrated sensors, each of them having, for instance, a different infiltrated width and addressing a different substance.

In conclusion, we demonstrate a postprocessing capability to form photonic crystal double heterostructures at telecommunication wavelengths. These are introduced within a PCS by selectively filling a small region of air holes using a micropipette, whose size can be readily rewritten. Initial experiments observed cavity characteristics with a measured Q-factor of $Q=4300$.

[1] B. S. Song, S. Noda, and T. Asano, Science **300**, 1537 (2003).
[2] H. G. Park, J. K. Hwang, J. Huh, H. Y. Ryu, Y. H. Lee, and J. S. Kim, Appl. Phys. Lett. **79**, 3032 (2001).
[3] D. Englund, D. Fattal, E. Waks, G. Solomon, B. Zhang, T. Nakaoka, Y. Arakawa, Y. Yamamoto, and J. Vučković, Phys. Rev. Lett. **95**, 013904 (2005).
[4] T. Tanabe, M. Notomi, S. Mitsugi, A. Shinya, and E. Kuramochi, Opt. Lett. **30**, 2575 (2005).
[5] M. Loncar, A. Scherer, and Y. M. Qiu, Appl. Phys. Lett. **82**, 4648 (2003).
[6] K. J. Vahala, Nature (London) **424**, 839 (2003).
[7] Y. Akahane, T. Asano, B. S. Song, and S. Noda, Nature (London) **425**, 944 (2003).
[8] B. S. Song, S. Noda, T. Asano, and Y. Akahane, Nat. Mater. **4**, 207 (2005).
[9] T. Asano, B. S. Song, and S. Noda, Opt. Express **14**, 1996 (2006).
[10] C. Grillet, C. Monat, C. L. C. Smith, B. J. Eggleton, D. J. Moss, S. Frederick, D. Dalacu, P. J. Poole, J. Lapointe, G. Aers, and R. L. Williams, Opt. Express **15**, 1267 (2007).
[11] M. W. Lee, C. Grillet, C. L. C. Smith, D. J. Moss, B. J. Eggleton, D. Freeman, B. Luther-Davies, S. Madden, A. Rode, Y. Ruan, and Y.-H. Lee, Opt. Express **15**, 1277 (2007).
[12] F. Intonti, S. Vignolini, V. Turck, M. Colocci, P. Bettotti, L. Pavesi, S. L. Schweizer, R. Wehrspohn, and D. Wiersma, Appl. Phys. Lett. **89**, 211117 (2006).
[13] D. Erickson, T. Rockwood, T. Emery, A. Scherer, and D. Psaltis, Opt. Lett. **31**, 59 (2006).
[14] S. Tomljenovic-Hanic, C. M. de Sterke, and M. J. Steel, Opt. Express **14**, 12451 (2006).
[15] C. Monat, P. Domachuk, and B. J. Eggleton, Nat. Photonics **1**, 106 (2007).
[16] P. E. Barclay, K. Srinivasan, M. Borselli, and O. Painter, Electron. Lett. **39**, 842 (2003).
[17] C. Grillet, C. Smith, D. Freeman, S. Madden, B. Luther-Davies, E. C. Mägi, D. J. Moss, and B. J. Eggleton, Opt. Express **14**, 1070 (2006).
[18] X. Letartre, C. Seassal, C. Grillet, P. Rojo-Romeo, P. Viktorovitch, M. L. d'Yerville, D. Cassagne, and C. Jouanin, Appl. Phys. Lett. **79**, 2312 (2001).
[19] M. Notomi, K. Yamada, A. Shinya, J. Takahashi, C. Takahashi, and I. Yokohama, Phys. Rev. Lett. **87**, 253902 (2001).

128

High-Q microfluidic cavities in silicon-based two-dimensional photonic crystal structures

Uwe Bog,[1] Cameron L. C. Smith,[1] Michael W. Lee,[1] Snjezana Tomljenovic-Hanic,[1] Christian Grillet,[1] Christelle Monat,[1] Liam O'Faolain,[2] Christian Karnutsch,[1,*] Thomas F. Krauss,[2] Ross C. McPhedran,[1] and Benjamin J. Eggleton[1]

[1]*Centre for Ultrahigh Bandwidth Devices for Optical Systems (CUDOS), School of Physics, University of Sydney, Sydney, NSW 2006, Australia*
[2]*School of Physics and Astronomy, University of St. Andrews, St. Andrews, Fife KY16 9SS, Scotland*
Corresponding author: c.karnutsch@physics.usyd.edu.au

We demonstrate postprocessed microfluidic double-heterostructure cavities in silicon-based photonic crystal slab waveguides. The cavity structure is realized by selective fluid infiltration of air holes using a glass microtip, resulting in a local change of the average refractive index of the photonic crystal. The microcavities are probed by evanescent coupling from a silica nanowire. An intrinsic quality factor of 57,000 has been derived from our measurements, representing what we believe to be the largest value observed in microfluidic photonic crystal cavities to date. © 2008 Optical Society of America

OCIS codes: 130.5296, 130.6010, 230.5298, 230.5750, 260.5740, 350.4238.

Optical microcavities in general, and two-dimensional photonic crystal (PhC) resonators in particular, represent a versatile platform for realizing various small-scale optical functionalities, such as lasers, optical switches, or sensors [1]. Design rules usually aim at generating high Q-factors and small modal volumes to trap light for a long time in a tiny fraction of space, which is crucial for high device performance and compactness. PhC microresonators are usually created by introducing a local inhomogeneity in the periodic lattice of air pores [1,2]. Such a "defect" typically consists of a permanent alteration of one or several hole dimensions and/or position. Achieving high-Q resonators through this approach however requires nanometer-scale fabrication accuracy [3], while the resulting resonator somewhat lacks tunability.

The infiltration of PhCs with fluids or polymers for realizing tunable optical devices or sensors was first suggested a decade ago [4] and experimentally demonstrated in both three-dimensional [5] and 2D [6–8] geometries. Later on, this idea was expanded through the concept of selective filling of individual air pores in a 2D PhC for creating various integrated functions and tunable photonic elements [9–11]. The actual breakthrough was achieved with recent advances in the development of microinfiltration techniques [12,13] and optofluidic integration [14] for locally infiltrating selected air pores. Whereas most of these demonstrations rely on the challenging infiltration of preexisting PhC cavities [6,8] or waveguide defects [14], we have shown that a PhC resonator could be directly created by infusing a fluid into any section of a uniform PhC waveguide [11,13]. This approach, which exploits the microfluidic equivalent of the double-heterostructure (DH) concept [15], relaxes the constraint on both the fabrication and infiltration accuracies for creating infused PhC microresonators. However, the first PhC cavities based on this concept exhibited Q-factors of only a few thousands [13],

which may preclude their use for sensing applications and lies well below the theoretical predictions [11].

In this Letter we demonstrate high-Q microfluidic DH cavities in silicon-based PhC slab waveguides. We present what we believe to be the highest Q-factor ever reported in the context of microfluidic cavity geometries in 2D PhC structures, 12 times higher than in our previous work [13], which was undertaken on chalcogenide waveguides. In addition to the different wetting properties of silicon and chalcogenide, the reduction of the hole diameter in the present study ($\varnothing = 265$ nm instead of $\varnothing = 380$ nm in chalcogenide) has implied successful improvement of our microtip-based infiltration technique. Besides the larger refractive index of silicon, the demonstration of higher Q-values is mainly attributed to the mature silicon PhC fabrication technology, resulting in reduced waveguide propagation losses. This allows us to show and discuss the high potential of this approach for resonance-based optofluidic sensing.

In this Letter a W0.9 PhC slab waveguide with a triangular lattice of air holes is investigated. The W0.9 configuration is a W1 waveguide—a PhC defect waveguide formed by omitting a row of holes in the $\Gamma - K$ direction—where the PhC structure has been shifted inward such that the guide width is 0.9 times that of a W1. The PhC lattice exhibits a nominal periodicity of $a = 410$ nm and a hole diameter of 265 nm ($0.646a$). It is fabricated into a 220-nm ($0.537a$)-thick suspended silicon membrane ($n_{Si} = 3.52$). The dimensions of the PhC structure are 25 μm $\times$ 14 μm. The PhC waveguides are tailored to exhibit a photonic bandgap around 1400 nm for TE-like polarization. Their fabrication process is described in detail in [16].

The fluid infiltration (Fig. 1) starts with a glass microtip—tapered down to a diameter of 220 nm—being immersed into a fluid reservoir. When the tip is pulled out, fluid droplets remain attached
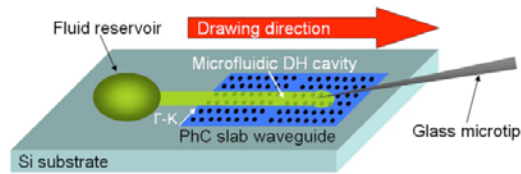
129

Fig. 1. (Color online) Schematic showing the fluid infiltration process. A glass microtip that has been immersed into a fluid is drawn across a PhC waveguide, creating a microfluidic DH cavity.

due to adhesive forces and the hydrophilic nature of the glass. These residues form a smaller reservoir as the tip is brought into contact with the sample surface close to the waveguide structure. By drawing a selected reservoir in a line across the PhC waveguide, the fluid enters the holes under the influence of capillary forces, leading to the formation of a microfluidic DH cavity. Different cavity widths can be realized by successively repeating this drawing process. To achieve accurate control the tip is mounted onto a piezoactuated three-axis translation stage (Thorlabs NanoMax). The infiltration process is monitored by using a high-magnification (150×) optical microscope (Olympus BX61). The infiltrated liquid (Cargille immersion oil, type B) has a refractive index of n_{liquid}=1.50 at 1400 nm. Cavity widths of 3.3 [Fig. 2(a)] and 16 μm are investigated as typical representatives for a narrow and wide cavity.

The infiltration causes the original dispersion curve of the fundamental PhC waveguide mode to shift to lower frequencies while still remaining in the photonic bandgap of the surrounding uninfiltrated PhC [Fig. 2(b)]. This newly generated band structure exhibits modes that can propagate only inside the infiltrated area. This is due to the light now being confined in all spatial directions by either total internal reflection (orthogonal to the PhC plane), the photonic bandgap (in-plane perpendicular to the $\Gamma-K$ direction), and the mode-gap (along the $\Gamma-K$ direction) [15]. In comparison to the W1 configuration, the fundamental waveguide mode of the W0.9 structure is
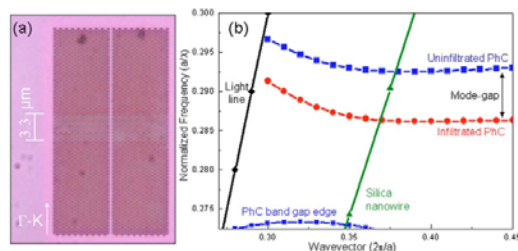
localized at higher frequencies and is further apart from the lower bandgap edge of the PhC [17]. The resulting mode-gap offered by the W0.9 makes it more promising for generating DH cavities, enabling a broader range of liquid refractive indices to be used, until the Q-factor becomes degraded by shifting the waveguide mode too close to the lower PhC bandgap edge [11].

The infiltrated DH cavities were investigated by evanescent coupling, bringing a silica nanowire into close proximity above the PhC waveguide [13]. The optical signal that is launched into the nanowire is TE polarized and delivered by a near-IR (NIR) supercontinuum source (Fianium Femtopower 1060 SC450). The evanescent interaction between the PhC structure and the nanowire affects the spectral characteristics of the transmitted light, which is monitored using a high-resolution optical spectrum analyzer (Ando AQ6317B). The nanowire presents a waist diameter of 1.3 μm and is shaped into an unclosed loop. The loop allows us to restrict the evanescent interaction to a localized area. All measurements are taken while the nanowire is not in contact with the PhC structure.

Figure 3 shows the transmission spectrum associated with the 3.3 μm wide microfluidic DH cavity. Pronounced local minima are observed, attributed to Fabry–Perot (FP) modes of the microfluidic cavity, as the mode-gap effect causes the interfaces between the infiltrated and the uninfiltrated waveguides to act as highly reflective mirrors. The measured group velocities derived from the free spectral range between the FP modes are in good agreement with simulations (details will be published elsewhere [17]). The resonances exhibit measured Q-factors ranging between Q_M=19,300 [for resonance (1), transmission T=0.88] and Q_M=36,300 [resonance (4), T=0.91]. Taking the transmission T into account, the intrinsic Q-factor Q_{intr} is calculated by the first approximation coupled mode theory in the time domain to be $Q_{\text{intr}}=Q_M/T^{1/2}$. Hence, for resonances (1) and (4) intrinsic Q-factors of Q_{intr}=20,810 and Q_{intr}=38.050 are derived. This 3.3 μm wide PhC cavity corre-

Fig. 2. (Color online) (a) Microscope picture (150× magnification) showing a microfluidic DH cavity of 3.3 μm in width. The infiltration area appears as the region where the contrast between the holes and the PhC matrix is reduced. (b) Calculated dispersion relation of the fundamental mode of a W0.9 PhC waveguide, which is either uninfiltrated (rectangles) or infiltrated with a liquid of n_{liquid} =1.5 (filled circles). The line represents the dispersion curve of the silica nanowire used for evanescent coupling.
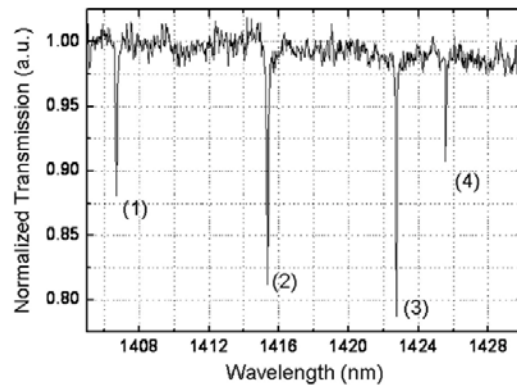

Fig. 3. Transmission spectrum while probing a microfluidic DH cavity of 3.3 μm in width. The rightmost cavity mode (4) exhibits a measured Q-factor of Q_M=36,300.

sponds to a modal volume of $\sim 1.5\ (\lambda/n)^3$ [11], showing the potential of generating high quality factors in very compact microfluidic devices.

Figure 4 shows the transmission spectrum when probing a 16 μm cavity. More spectral dips are observed, as expected in longer cavities that typically sustain an increased number of modes. The associated Q-factors are higher than for the shorter cavity, showing that the loss must be dominated by the reflection losses at the infiltrated–uninfiltrated interfaces. As an example, resonances (5) and (6) exhibit measured Q-factors of Q_M=45,740 and Q_M=52,050. The derived intrinsic Q-factors for these resonances are Q_{intr}=50,430 and Q_{intr}=57,080, respectively.

In contrast with early demonstrations of infused PhC cavities, where the Q-factor was typically degraded after the infiltration step [8], the high Q-factors presented here demonstrate that the DH cavity can be applied as a highly sensitive microfluidic sensor. PhC cavity band sensors typically exploit the resonance shift $\Delta\lambda$ that occurs when the refractive index of the analyte in the PhC holes changes by a value Δn. The shift of the waveguide band structure induced by the fluid infiltration, as calculated by plane-wave expansion, allows us to estimate a potential sensitivity $\Delta\lambda/\Delta n$ of 60 nm/RIU (refractive index unit). Considering the FWHM of the cavity resonance as the resolution limit, a minimum refractive index change of δn_{fluid}=4.5×10^{-4} could be detected by exploiting resonance (6) in Fig. 4. This value compares favorably with the values (δn_{fluid}=0.002) demonstrated in a previous work on PhC based sensors [6], although the ratio of the electromagnetic energy overlapping with the PhC holes appears to be limited to $\sim$6% in our case, as estimated from the first-order approximation electromagnetic perturbation theory [18]. This overlap could be improved by engineering the cavity geometry.

In summary, we have demonstrated high Q-factors in postprocessed microfluidic photonic crystal double-heterostructure cavities. These cavities were created
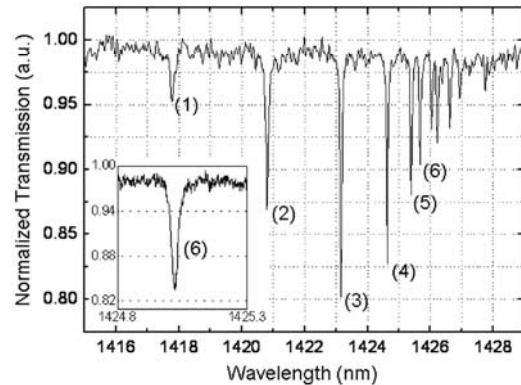

Fig. 4. Transmission spectrum while probing a 16 μm cavity. The measured Q-factors for the cavity modes (5) and (6) are Q_M=45,740 and Q_M=52,050. Inset, close-up view of resonance (6).

by infiltrating silicon-based photonic crystal slab waveguides, showing the possibility for realizing complex microfluidic structures in standard silicon chip technology. The high Q-factors measured show the potential for creating high-performance microfluidic devices on a wavelength-scale. An intrinsic Q-factor of 57,000 has been derived, sufficient for a wide range of applications in high-discrimination sensing, low-threshold microlasers, and quantum-electrodynamic studies.

References

1. K. Busch, S. Lölkes, R. B. Wehrspohn, and H. Föll, *Photonic Crystals-Advances in Design, Fabrication, and Characterization* (Wiley-VCH, 2004).
2. S. John, Phys. Rev. Lett. **58**, 2486 (1987).
3. T. Asano, B. S. Song, and S. Noda, Opt. Express **14**, 1996 (2006).
4. K. Busch and S. John, Phys. Rev. Lett. **83**, 967 (1999).
5. K. Yoshino, Y. Shimoda, Y. Kawagishi, K. Nakayama, and M. Ozaki, Appl. Phys. Lett. **75**, 932 (1999).
6. E. Chow, A. Grot, L. W. Mirkarimi, M. Sigalas, and G. Girolami, Opt. Lett. **29**, 1093 (2004).
7. S. W. Leonard, J. P. Mondia, H. M. van Driel, O. Toader, S. John, K. Busch, A. Birner, U. Gösele, and V. Lehmann, Phys. Rev. B **61**, R2389 (2000).
8. M. Loncar, A. Scherer, and Y. M. Qiu, Appl. Phys. Lett. **82**, 4648 (2003).
9. S. F. Mingaleev, M. Schillinger, D. Hermann, and K. Busch, Opt. Lett. **29**, 2858 (2004).
10. H. Takeda and K. Yoshino, Phys. Rev. B **67**, 073106 (2003).
11. S. Tomljenovic-Hanic, C. M. de Sterke, and M. J. Steel, Opt. Express **14**, 12451 (2006).
12. F. Intonti, S. Vignolini, V. Turck, M. Colocci, P. Bettotti, L. Pavesi, S. L. Schweizer, R. Wehrspohn, and D. Wiersma, Appl. Phys. Lett. **89**, 211117 (2006).
13. C. L. C. Smith, D. K. C. Wu, M. W. Lee, C. Monat, S. Tomljenovic-Hanic, C. Grillet, B. J. Eggleton, D. Freeman, Y. Ruan, S. Madden, B. Luther-Davies, H. Giessen, and Y.-H. Lee, Appl. Phys. Lett. **91**, 121103 (2007).
14. D. Erickson, T. Rockwood, T. Emery, A. Scherer, and D. Psaltis, Opt. Lett. **31**, 59 (2006).
15. B. S. Song, S. Noda, T. Asano, and Y. Akahane, Nat. Mater. **4**, 207 (2005).
16. J. Li, T. P. White, L. O'Faolain, A. Gomez-Iglesias, and T. F. Krauss, Opt. Express **16**, 6227 (2008).
17. C. L. C. Smith, U. Bog, S. Tomljenovic-Hanic, M. W. Lee, D. K. C. Wu, L. O'Faolain, C. Monat, C. Grillet, T. F. Krauss, C. Karnutsch, R. C. McPhedran, and B. J. Eggleton, Opt. Express **16**, 15887 (2008).
18. N. Mortensen, S. Xiao, and J. Pedersen, Microfluid. Nanofluid. **4**, 117 (2008).

131

Reconfigurable microfluidic photonic crystal slab cavities

Cameron L. C. Smith,[1,*] Uwe Bog,[1] Snjezana Tomljenovic-Hanic,[1] Michael W. Lee,[1] Darran K. C. Wu,[1] Liam O'Faolain,[2] Christelle Monat,[1] Christian Grillet,[1] Thomas. F. Krauss,[2] Christian Karnutsch,[1] Ross C. McPhedran,[1] Benjamin J. Eggleton[1]

[1]*Centre for Ultrahigh-bandwidth Devices for Optical Systems (CUDOS), School of Physics University of Sydney, Sydney, NSW 2006, Australia*
[2]*School of Physics and Astronomy, University of St. Andrews, St. Andrews, Fife KY16 9SS, Scotland*
[*]*Corresponding author: c.smith@physics.usyd.edu.au*

Abstract: We demonstrate the spectral and spatial reconfigurability of photonic crystal double-heterostructure cavities in silicon by microfluidic infiltration of selected air holes. The lengths of the microfluidic cavities are changed by adjusting the region of infiltrated holes in steps of several microns. We systematically investigate the spectral signature of these cavities, showing high Q-factor resonances for a broad range of cavity lengths. The fluid can be removed by immersing the device in toluene, offering complete reconfigurability. Our cavity writing technique allows for tolerances in the infiltration process and provides flexibility as it can be employed at any time after photonic crystal fabrication.

©2008 Optical Society of America

OCIS codes: (230.5298) Photonic crystals; (280.4788) Optical sensing and sensors.

References and links

1. D. Psaltis, S. R. Quake, and C. H. Yang, "Developing optofluidic technology through the fusion of microfluidics and optics," Nature **442**, 381-386 (2006).
2. C. Monat, P. Domachuk, and B. J. Eggleton, "Integrated optofluidics: A new river of light," Nat. Photon. **1**, 106-114 (2007).
3. M. Loncar, A. Scherer, and Y. M. Qiu, "Photonic crystal laser sources for chemical detection," Appl. Phys. Lett. **82**, 4648-4650 (2003).
4. M. L. Adams, M. Loncar, A. Scherer, and Y. M. Qiu, "Microfluidic integration of porous photonic crystal nanolasers for chemical sensing," IEEE J. Sel. Areas Commun. **23**, 1348-1354 (2005).
5. S. Balslev, A. M. Jorgensen, B. Bilenberg, K. B. Mogensen, D. Snakenborg, O. Geschke, J. P. Kutter, and A. Kristensen, "Lab-on-a-chip with integrated optical transducers," Lab on a Chip **6**, 213-217 (2006).
6. S. S. Xiao, and N. A. Mortensen, "Proposal of highly sensitive optofluidic sensors based on dispersive photonic crystal waveguides," J. Opt. A: Pure Appl. Opt. **9**, S463-S467 (2007).
7. S. H. Kim, J. H. Choi, S. K. Lee, S. H. Kim, S. M. Yang, Y. H. Lee, C. Seassal, P. Regrency, and P. Viktorovitch, "Optofluidic integration of a photonic crystal nanolaser," Opt. Express **16**, 6515-6527 (2008).
8. K. Busch and S. John, "Liquid-crystal photonic-band-gap materials: The tunable electromagnetic vacuum," Phys. Rev. Lett. **83**, 967-970 (1999).
9. P. Mach, M. Dolinski, K. W. Baldwin, J. A. Rogers, C. Kerbage, R. S. Windeler, and B. J. Eggleton, "Tunable microfluidic optical fiber," Appl. Phys. Lett. **80**, 4294-4296 (2002).
10. B. Maune, M. Loncar, J. Witzens, M. Hochberg, T. Baehr-Jones, D. Psaltis, A. Scherer, and Y. M. Qiu, "Liquid-crystal electric tuning of a photonic crystal laser," Appl. Phys. Lett. **85**, 360-362 (2004).
11. J. C. Galas, J. Torres, M. Belotti, Q. Kou, and Y. Chen, "Microfluidic tunable dye laser with integrated mixer and ring resonator," Appl. Phys. Lett. **86**, 264101 (2005).
12. D. Erickson, T. Rockwood, T. Emery, A. Scherer, and D. Psaltis, "Nanofluidic tuning of photonic crystal circuits," Opt. Lett. **31**, 59-61 (2006).
13. F. B. Arango, M. B. Christiansen, M. Gersborg-Hansen, and A. Kristensen, "Optofluidic tuning of photonic crystal band edge lasers," Appl. Phys. Lett. **91**, 223503 (2007).
14. A. Groisman, S. Zamek, K. Campbell, L. Pang, U. Levy, and Y. Fainman, "Optofluidic 1x4 switch," Opt. Express **16**, 13499-13508 (2008).
15. P. El-Kallassi, S. Balog, R. Houdre, L. Balet, L. Li, M. Francardi, A. Gerardino, A. Fiore, R. Ferrini, and L. Zuppiroli, "Local infiltration of planar photonic crystals with UV-curable polymers," J. Opt. Soc. Am. B **25**, 1562-1567 (2008).

16. E. Chow, A. Grot, L. W. Mirkarimi, M. Sigalas, and G. Girolami, "Ultracompact biochemical sensor built with two-dimensional photonic crystal microcavity," Opt. Lett. **29**, 1093-1095 (2004).
17. S. Kita, K. Nozaki, and T. Baba, "Refractive index sensing utilizing a cw photonic crystal nanolaser and its array configuration," Opt. Express **16**, 8174-8180 (2008).
18. T. F. Krauss, "Photonic crystals - Cavities without leaks," Nat. Mater. **2**, 777-778 (2003).
19. K. J. Vahala, "Optical microcavities," Nature **424**, 839-846 (2003).
20. B. S. Song, S. Noda, and T. Asano, "Photonic devices based on in-plane hetero photonic crystals," Science **300**, 1537-1537 (2003).
21. E. Centeno, and D. Felbacq, "Optical bistability in finite-size nonlinear bidimensional photonic crystals doped by a microcavity," Phys. Rev. B **62**, R7683-R7686 (2000).
22. B. S. Song, S. Noda, T. Asano, and Y. Akahane, "Ultra-high-Q photonic double-heterostructure nanocavity," Nat. Mater. **4**, 207-210 (2005).
23. C. L. C. Smith, D. K. C. Wu, M. W. Lee, C. Monat, S. Tomljenovic-Hanic, C. Grillet, B. J. Eggleton, D. Freeman, Y. Ruan, S. Madden, B. Luther-Davies, H. Giessen, and Y. H. Lee, "Microfluidic photonic crystal double heterostructures," Appl. Phys. Lett. **91**, 121103 (2007).
24. F. Intonti, S. Vignolini, V. Turck, M. Colocci, P. Bettotti, L. Pavesi, S. L. Schweizer, R. Wehrspohn, and D. Wiersma, "Rewritable photonic circuits," Appl. Phys. Lett. **89**, 211117 (2006).
25. S. Tomljenovic-Hanic, C. M. de Sterke, and M. J. Steel, "Design of high-Q cavities in photonic crystal slab heterostructures by air-holes infiltration," Opt. Express **14**, 12451-12456 (2006).
26. J. Li, T. P. White, L. O'Faolain, A. Gomez-Iglesias, and T. F. Krauss, "Systematic design of flat band slow light in photonic crystal waveguides," Opt. Express **16**, 6227-6232 (2008).
27. "Datasheet TYPIOB, Immersion Oil Type B," (Cargille Laboratories, 2002).
28. J. C. Knight, G. Cheung, F. Jacques, and T. A. Birks, "Phase-matched excitation of whispering-gallery-mode resonances by a fiber taper," Opt. Lett. **22**, 1129-1131 (1997).
29. P. E. Barclay, K. Srinivasan, M. Borselli, and O. Painter, "Probing the dispersive and spatial properties of photonic crystal waveguides via highly efficient coupling from fiber tapers," Appl. Phys. Lett. **85**, 4-6 (2004).
30. C. Grillet, C. Smith, D. Freeman, S. Madden, B. Luther-Davis, E. C. Mägi, D. J. Moss, and B. J. Eggleton, "Efficient coupling to chalcogenide glass photonic crystal waveguides via silica optical fiber nanowires," Opt. Express **14**, 1070-1078 (2006).
31. I. K. Hwang, S. K. Kim, J. K. Yang, S. H. Kim, S. H. Lee, and Y. H. Lee, "Curved-microfiber photon coupling for photonic crystal light emitter," Appl. Phys. Lett. **87**, 131107 (2005).
32. X. Letartre, C. Seassal, C. Grillet, P. Rojo-Romeo, P. Viktorovitch, M. L. d'Yerville, D. Cassagne, and C. Jouanin, "Group velocity and propagation losses measurement in a single-line photonic-crystal waveguide on InP membranes," Appl. Phys. Lett. **79**, 2312-2314 (2001).
33. M. Notomi, K. Yamada, A. Shinya, J. Takahashi, C. Takahashi, and I. Yokohama, "Extremely large group-velocity dispersion of line-defect waveguides in photonic crystal slabs," Phys. Rev. Lett. **87**, 253902 (2001).
34. K. Srinivasan and O. Painter, "Fourier space design of high-Q cavities in standard and compressed hexagonal lattice photonic crystals," Opt. Express **11**, 579-593 (2003).
35. U. Bog, C. L. C. Smith, M. W. Lee, S. Tomljenovic-Hanic, C. Grillet, C. Monat, L. O'Faolain, C. Karnutsch, T. F. Krauss, R. McPhedran, and B. J. Eggleton, "High-Q microfluidic cavities in silicon-based 2D photonic crystal structures," Opt. Lett. **33** (2008).
36. C. Schuller, F. Klopf, J. P. Reithmaier, M. Kamp, and A. Forchel, "Tunable photonic crystals fabricated in III-V semiconductor slab waveguides using infiltrated liquid crystals," Appl. Phys. Lett. **82**, 2767-2769 (2003).

1. Introduction

Optofluidics is an emerging field of research that integrates microfluidics with nano-photonics. Demonstrations of optofluidic devices exploit the characteristics of fluids to achieve dynamic manipulation of optical properties and reveal the promise for their widespread use [1, 2]. There is, on the one hand, a potential to realize highly sensitive integrated sensors [3-7], while on the other, a flexible means to write, tune or reconfigure photonic devices for a swathe of applications [8-15]. Recently there have been advances in the development of fully integrated microfluidic and photonic platforms [11-13]. In this regard, it has been shown that photonic crystals (PhCs) in general [6, 9, 12, 13] and PhC cavities in particular [3, 7, 10, 15-17] can be advantageously exploited within optofluidic architectures. The latter is due to the potentially high light-liquid interaction that occurs when infiltrating the air holes that typically surround and/or form the PhC cavity.

PhC cavities have received much interest in recent years due to their ability to strongly confine light on the wavelength scale [18, 19]. This capability promotes their use in numerous applications, including channel-drop filters [20] and optical switching [21]. PhC cavities are

created by altering the periodicity of the PhC through the introduction of a defect (such as removal or positional shift of air holes). Song *et al.* demonstrated more recently "double-heterostructure" (DH) PhC cavities [22], where two PhC geometries containing slightly different lattice parameters are combined. This is done in such a way that light is spatially confined within the central section of the PhC where the effective refractive index is larger. However, all these approaches present certain drawbacks when combining the generated PhC cavity with microfluids. First, this requires precise alignment between the micro-scale defect forming the PhC cavity and the liquid to be infiltrated; or alternatively demands a large amount of liquid which is not practical in many sensing applications. Second, the properties of PhC cavities are static when geometry-based, lacking flexibility. Lastly, the Q-factor of the geometry-based PhC cavity is typically degraded after the infiltration step [3], which is detrimental to the performance in both the sensing and optical device regimes.

By contrast, we demonstrate an approach for realizing optofluidic PhC cavities, based on a principle similar to the DH but able to overcome most of the difficulties mentioned above. The technique relies on the selective infiltration of a section of an otherwise cavity-free PhC structure [23, 24]. First, the optofluidic PhC cavities are created during the infiltration step, relaxing the constraint on alignment between the fluid and a pre-existing micro-scale cavity. Second, these cavities can be configured in a flexible manner by altering the size or geometry of the infiltrated region as well as the refractive index of the liquid. The optofluidic structures may then be reconfigured by removing the fluid and returning the PhC to its original state. Third, these cavities exhibit high Q-factors despite the presence of a fluid: it has been shown that this microfluidic regime may potentially reach Q-factors of $Q = 1 \times 10^6$ [25].

In this paper we demonstrate the spectral and spatial reconfigurability of such optofluidic PhC DH cavities made in silicon by controlling the size of the selectively infiltrated region of air holes with fluid using a glass micro-tip. The microfluidic PhC cavity dimensions are altered by infiltrating a greater region of the holes to micrometer accuracies. The spectral signature measured from the generated microfluidic cavities is in good agreement with numerical simulations. Furthermore, we show that the Q-factor remains relatively high over a wide range of the cavity length, allowing for tolerances in the infiltration process. Eventually, the fluid is removable by immersing the infiltrated PhC in a bath of toluene, showing that this approach is a versatile method to create postprocessed and reconfigurable microcavities. Reconfigurable microfluidic PhC devices may be optimized for a broad scope of micron-scale all-optical applications integrated on a single chip, including sensing architectures and arbitrarily defined post-processed PhC structures.

2. Device and experiment

Figure 1(a) summarizes the principle of the microfluidic DH geometry. The adjacent regions (regular PhC) contain a regular triangular PhC lattice of air holes $n_{holes} = 1$, while the central region (infiltrated PhC) contains the same triangular PhC lattice yet with holes possessing an increased refractive index $n_{holes} = 1.5$ due to the presence of a fluid. A waveguide across the DH gives different dispersion curves associated with the different PhC sections. This results in the waveguide modes within the two sections existing at different frequencies. As illustrated in Fig. 1(b), this causes a "mode gap", where light coupled to the waveguide mode of the infiltrated PhC section with a frequency lying in this gap does not propagate in the surrounding unchanged regular PhC section. Instead, the light remains localized, decaying evanescently in the adjacent regions.

The PhC structures are made from silicon, having a refractive index $n_{Si} = 3.52$ at 1.4 μm wavelength. We use a triangular lattice which nominally consists of a period $a = 410$ nm, suspended slab of thickness $T = 220$ nm ($0.537a$), and hole radius $r = 140$ nm ($0.341a$). A defect waveguide is introduced into these structures by removing one row of holes along the Γ-K direction of the lattice as shown in Fig. 1(a). The structures are 34 periods (14 μm) across by 61 periods (25 μm) along. The fabrication steps are identical to those used to create the devices of [26].

The two PhC sections to either side of the defect waveguide are shifted closer together by 35 nm each to reduce the guide width to 0.9 times the width of a W1 waveguide, creating a so-called W0.9. This modification is done to increase the frequency range between the fundamental waveguide mode and the low-frequency edge of the PhC photonic bandgap (PBG) (Fig. 1(b) and (c)). The mode gap corresponding to the infiltrated W0.9 therefore does not overlap the PBG edge and allows for a broad selection of fluid indices to configure our devices, where an increase in refractive index of the fluid extends the mode-gap. It is noticed that evanescent coupling to the structure is improved by using W0.9 waveguides rather than W1.
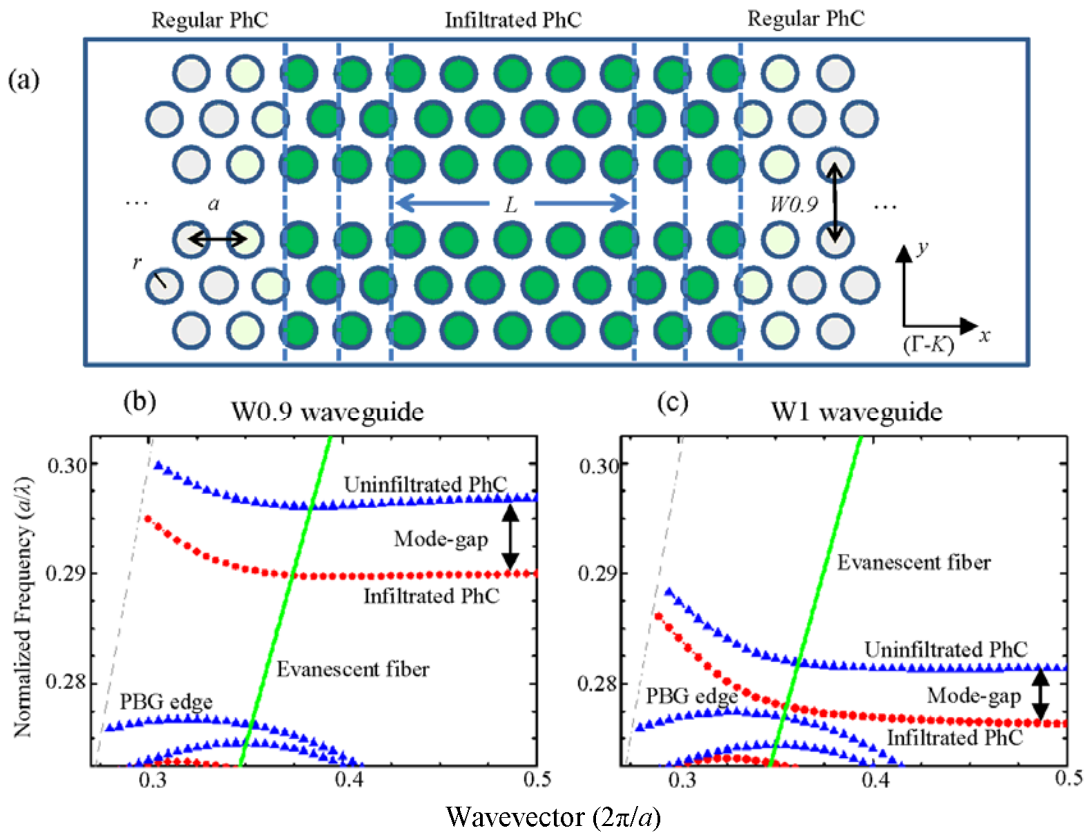
Fig. 1. (a) Schematic of fluid-filled PhC. (b) Calculated dispersion relation of the W0.9 PhC: blue triangles represent the PhC with air holes and red circles represent the PhC with fluid-filled holes. The green (solid) curve represents the evanescent coupling taper. The gray (dashed) curve represents the light-line. (c) Dispersion relation of a regular W1 waveguide with otherwise the same parameters as (b).

The fluid infiltration, illustrated in Fig. 2, is achieved by using a tapered glass micro-tip with apex diameter $\varnothing$ = 220 nm. The micro-tip is controlled by a 3-axis piezo-electric stage (Thorlabs NanoMax) and is initially inserted within a meniscus of the filling fluid. We use a Cargille microscopy immersion oil type B of index n_{fluid} = 1.50 and absorption loss of 0.45 dB/cm at 1400 nm [27]. As the tip is withdrawn from the meniscus, droplets remain attached along its length due to adhesive forces between the glass and the fluid. These droplets are then deposited on the device chip beside the PhC structure under a microscope objective (Olympus BX61, LMPlanFl, 100×, 0.8 NA). This objective compromises between a large magnification to resolve properly the PhC waveguide and a sufficient working distance to allow for the micro-tip during infiltration. Lastly, the tapered glass micro-tip is used to draw a chosen droplet along the photonic crystal, perpendicular to the waveguide, to create the DH cavity.

135

The surface of the PhC and the particular fluid used each determine the penetration of the fluid into the pores of the PhC. If the fluid is phobic to the surface of the PhC, it forms a large meniscus and does not penetrate the air holes, instead remaining above. The selected immersion oil used in the experiments is philic to the surface. In this case, the fluid infiltrates the PhC holes via capillary action and remains suspended within them due to the fluid's surface tension. The selected fluid is also non-volatile and therefore does not evaporate out of the PhC pores.
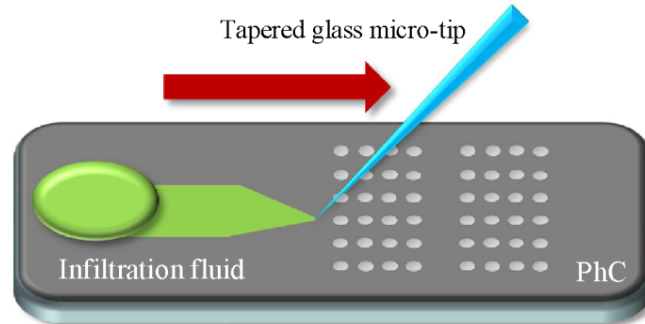
Fig. 2. Infiltration schematic: a glass micro-tip is used to draw the infiltration fluid across the PhC section, forming the DH stripe.

We investigate the fluid-filled DH cavities via evanescent coupling [28-30]. We use a standard single-mode fiber, reducing its diameter down from 125 μm to 1.3 μm over a length of 2 mm. Due to the reduction in diameter, the evanescent field of the propagating mode extends significantly beyond the tapered fiber's boundary, allowing it to interact with the PhC structure. Coupling can occur when there is a phase match between the fiber and PhC modes. Numerically, this is when dispersion curves of the taper and the PhC structure respectively intersect.

The tapered fibers have an intentionally induced shape to localize coupling to the micro-scale fluid-filled section of the DH. This is achieved by closing the fiber ends together after it had been tapered, twisting one end and then stretching the fiber ends apart. This forms a "loop" shape with a radius of approximately 30 μm. The looped nanowire is then annealed with a flame to "set" the silica glass and the induced shape. The loop is then pried open, leaving a "U" profile similar to [31].
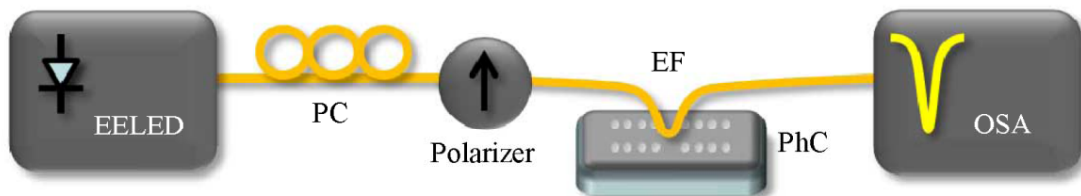

Fig. 3. Evanescent coupling schematic: polarization controller (PC) and polarizer select TE-like light from the edge-emitting light-emitting diode (EELED) source. The evanescent fiber (EF) couples light to the PhC sample and is connected to an optical spectrum analyzer (OSA) for monitoring.

The characterization setup is illustrated in Fig. 3. A broadband edge-emitting light-emitting diode source (HP 83437A) is connected to a polarization controller and polarizer that selects TE-like polarization (electric field lying in the plane of the PhC). The polarized light propagates through the nanowire, evanescently coupling to the PhC sample section and eventually monitored by an optical spectrum analyzer (OSA). Light coupled to the sample is not received at the OSA, resulting as a dip in the measured spectrum. A 6-axis nano-alignment system is utilized to position the nanowire and PhC sample. This process is imaged from above using a CCD camera and zooming lens.
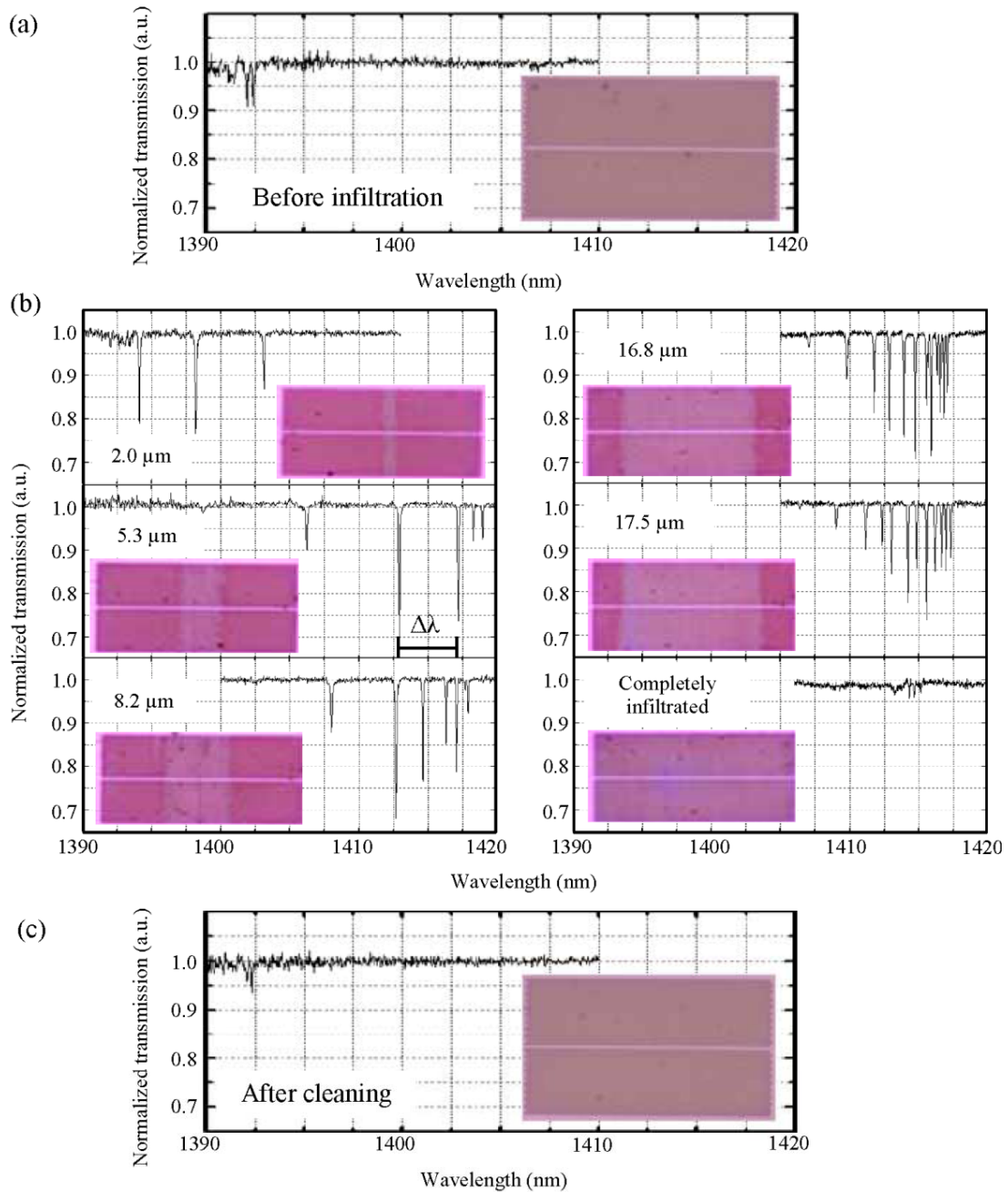
3. Results

(a)

(b)

(c)

Fig. 4. (a) Spectrum of the case before infiltration. (b) Spectrum for varying infiltrated cavity lengths. (c) Spectrum of the case after cleaning. Insets are 150× microscope images of the corresponding waveguide/cavities.

The experiment starts with infiltrating a DH stripe (initially 2 μm) and incrementally increasing the infiltrated region on the same PhC structure in steps of ≈ 2 μm. Figure 4 shows the measurement spectra from the infiltration experiments. These correspond to the case before infiltration (Fig. 4(a)), the 2 μm, 5.3 μm, 8.2 μm, 16.8 μm and 17.5 μm length cavities plus completely infiltrated case (Fig. 4(b)) and the case after cleaning (Fig. 4(c)). Cleaning of the infiltrated PhC is achieved by immersing the sample in a bath of toluene for several minutes. We also write and characterize cavities of length 10.3 μm, 11.5 μm, 13.9 μm,

137

20.1 µm and 21.3 µm, but for brevity are omitted. Each measured spectrum is obtained via evanescent coupling where the nanowire is out of contact with the structure. The cavities are imaged with a 150×, NA 0.9 microscope objective using a blue color filter to improve resolution. The resulting images are displayed in the insets of Fig 4. For each, the contrast between the infiltrated and uninfiltrated PhC clearly attests the presence of the liquid into the middle of the structure, allowing us to estimate the respective width of the produced cavities.

The spectral signature of the initial PhC waveguide is measured before the infiltration process and shown in Fig. 4(a). The spectral dip at 1392 nm is associated with coupling to the fundamental TE-like waveguide mode. The discrete features are attributed to Fresnel reflections at the open ends of the PhC waveguide. After infiltration, (Fig. 4(b)), features appear at longer wavelengths. This is due to the increased effective refractive index of the modes from the presence of the fluid, as explained in Fig. 1. The observed fringe spectra are attributed to Fabry-Pérot (FP) modes sustained by the microfluidic cavity. The coupling strengths of the FP fringes with the taper are at a maximum where the phase-matching is strongest. It can be seen that as the cavity length increases, the fringe spacing becomes smaller, which is consistent with an increased density of modes for larger cavities. The wavelengths of the FP resonances should indeed closely meet the following condition:

$$2k_xL = 2\pi p, \tag{1}$$

which relates the wavevectors k_x of the FP resonances to the fluid-filled cavity length L through an integer p [32, 33]. When the PhC region is completely filled, the majority of these fringes disappear as the mode-gap effect no longer exists. In this case there is only coupling to the fluid-filled PhC fundamental waveguide mode, containing features that again occur due to Fresnel reflections at the open ends of the PhC structure. After fluid removal (Fig. 4(c)), the spectral signature is very similar to the case before infiltration.
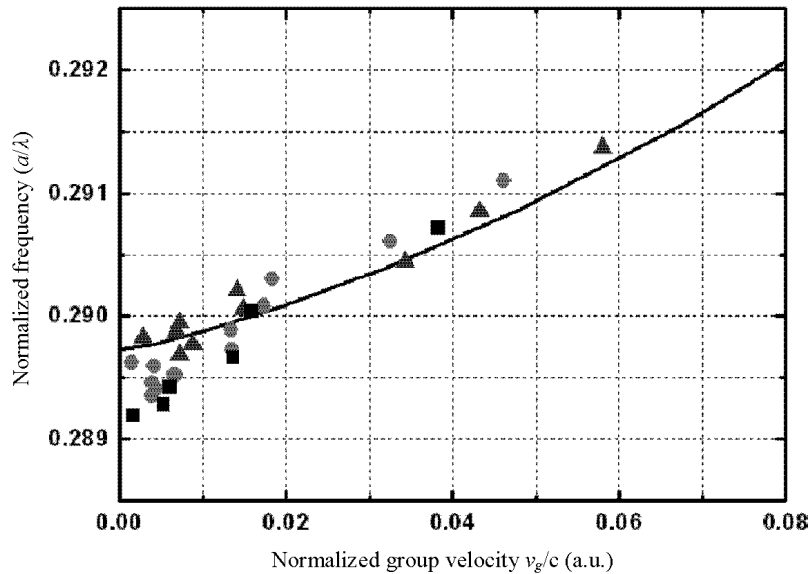

Fig. 5. Comparison of measured and calculated dispersive behavior for the fluid-filled PhCs. Cavity lengths of 8.2 µm (black squares), 16.8 µm (red circles) and 20.1 µm (blue triangles) are plotted against numerical data (black solid).

For each cavity length, the fringe spacing, $\Delta\lambda$, becomes smaller for increasing wavelength, which results from the dispersive nature of the PhC waveguide. The measured spectra are subsequently compared to the dispersion calculated for a W0.9 infiltrated waveguide using a three-dimensional plane-wave method with a supercell approach (RSoft's BandSOLVE) and the PhC parameters mentioned in Section 2. The result is shown in Fig. 5, which plots normalized frequency against group velocity and "maps" the dispersion. The calculated group velocity is

extracted from the gradient of the numerical dispersion relation, whereas the experimental group velocity is derived from the fringe spacing, $\Delta\lambda$, between the subsequent dips measured on the spectra of Fig. 4 and according to the equation $v_g = 2Lc\Delta\lambda/\lambda^2$. Note that the experimental dispersion curves derived for three different cavity lengths are reasonably superimposed, which is consistent with the fact that the FP modes all originate from the same dispersion relation, namely the one associated to the infiltrated W0.9 fundamental mode. In addition, this experimentally retrieved dispersion matches the calculated one within the bounds of fabrication tolerances.
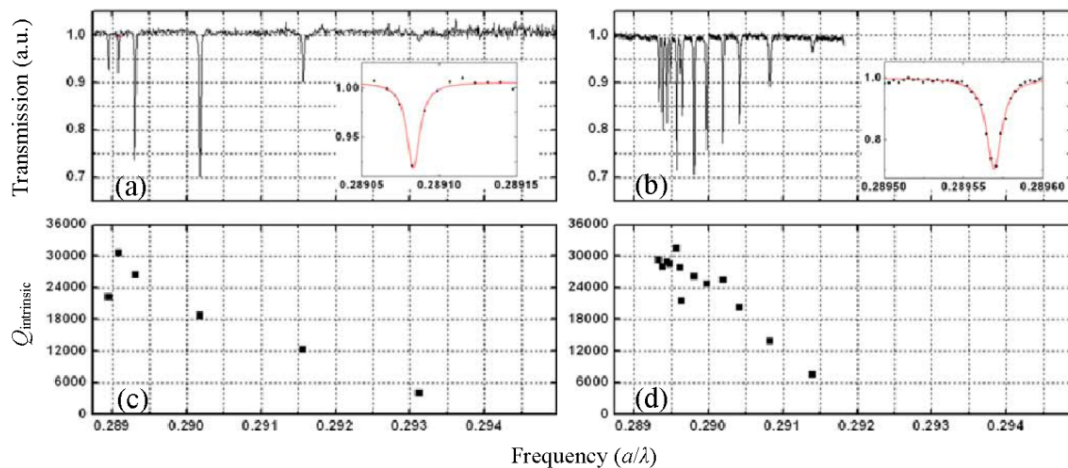
Fig. 6. Transmission and Q-factor versus frequency. (a) and (b) represent spectra from 5.3 µm and 16.8 µm cavity lengths with highest Q-factors shown inset. (c) and (d) are the corresponding Q-factors of the spectra to (a) and (b).

Next we consider the Q-factors associated to the modes of such optofluidic cavities. Figure 6 shows the trend of the mode Q-factor measured for two different cavity lengths (5.3 µm and 16.8 µm) as frequency increases. For each cavity, we have plotted their spectral signature (Fig. 6(a) and (b)) along with the corresponding Q-factors for each of the resonances revealed by the spectra (Fig. 6(c) and (d)). These two plots show the Q-factor increasing for a decreased frequency and this trend is representative of the whole set of cavity lengths. This is expected behavior [34], where the modes at lower frequency experience a higher effective index and thus better vertical confinement in the slab.

The Q-factors obtained in the experiments have values up to $Q = 3.5 \times 10^4$. The measurements are limited by the resolution of our OSA. More recent experiments have shown intrinsic Q-factors of $Q = 5.7 \times 10^4$ and these investigations will be reported elsewhere [35].
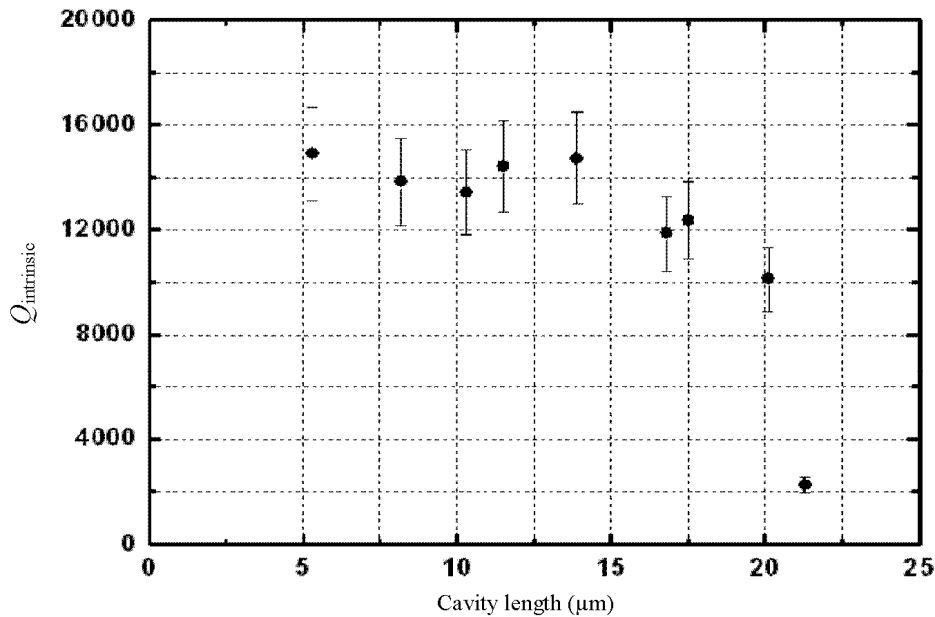
139

Fig. 7. Change of Q-factor against cavity length at an arbitrarily fixed frequency of 0.291 a/λ. The entire PhC structure is 25 μm.

We also investigate the Q-factor against cavity length at an arbitrarily fixed frequency of 0.291 a/λ, which is high enough for avoiding resolution limited Q-factor values. This is shown in Fig. 7. We apply a linear fit to obtain the data as the spectral dips typically occurred to either side of this point. The 2 μm cavity length resonances occur away from this point, so is not included in this comparison. The Q-factor remains quite constant between 5.3 μm and 13.8 μm. As the cavity lengths continue to increase from this point, the Q-factor drops as the in-plane confinement is reduced. This is due to the physically reduced uninfiltrated PhC section that provides the mode-gap. The trend continues through to the largest cavity length of 21.3 μm before the complete infiltration case. This suggests that 5 μm (12 holes in Γ-K direction) of uninfiltrated PhC section to each side of the microfluidic cavity is still large enough to maintain sufficient in-plane confinement. Note that the Q-factor remains larger than 10,000 for all cavity lengths excluding the 21.3 μm case, pointing out the large tolerances on the size of the infiltration region for generating reasonably high Q-factor modes with this approach.

4. Discussion

Our microfluidic approach to create flexible PhC cavities could feasibly be integrated within a chip-based microfluidic network in order to take full advantage of its reconfigurable characteristics. In this regard, there have been demonstrations of combining PhCs with microfluidics using a nanofluidic channel network to selectively address the intended PhC region [4, 7, 12]. These realizations rely on the challenging alignment between the PhC (linear or point) defect and the microfluidic delivery channel. By contrast, our approach is self-aligned: the structure forms *as a result* of the presence of fluid in the pores, which should make it less constraining to integrate within a microfluidic network. As opposed to the external method presented here that currently requires timescales on the order of minutes to reconfigure the device, a wholly integrated optofluidic platform should allow reconfigurable operation within seconds or milliseconds, as demonstrated in [12].

Liquid crystals (LCs) have been suggested in the past as a method to tune the static properties of PhC components [8]. LCs offer an index tuning range of $\Delta n \approx 0.05$ as achievable through electrical [10] or thermal [36] effects. This represents an order of magnitude less than what the available range of infiltration fluids could span: $n \approx 1.3 - 1.8$ ($\Delta n \approx 0.5$). Note that

140

because LCs offer a base index range of $n \approx 1.45 - 1.7$, they could be advantageously combined with our microfluidic double heterostructure scheme to provide both highly tunable (via electrical or thermal excitation) and reconfigurable (via fluid replacement) optical functionality.

5. Conclusion

We have reported a comprehensive study of microfluidic PhC DH cavities in silicon through the systematic comparison of the spectral properties of various cavity sizes created by this unique approach and supported by numerical simulations. Silicon is demonstrated to be well-suited to this approach. We have shown the spectral and spatial reconfigurability of the microfluidic cavities via flexible infiltration of selected holes. This technique offers a versatile solution for overcoming the many difficulties associated with integrating microfluidics with PhC cavities for sensing applications or tunable photonics. First, this approach is self-aligned in the sense that the optofluidic PhC cavities are created during the infiltration step, relaxing the constraint on alignment between the fluid and a pre-existing micro-scale cavity. Second, we have demonstrated that these cavities can be reconfigured in a flexible manner through control of the infiltrated region size combined with the possibility to "erase" the cavity by fully removing the fluid in toluene. Third, these cavities exhibit high Q-factors, which are here resolution limited, and this is achieved *because* of the presence of a fluid, rather than being degraded by it. Lastly, we show that the Q-factor of the generated modes remains high ($\approx 10,000$) over a large range of cavity lengths: 5 μm to 14 μm. In comparison with geometry perturbation schemes where precision is required to be nanometers, our approach extends this tolerance to the order of microns.

#98816 - $15.00 USD   Received 15 Jul 2008; revised 18 Sep 2008; accepted 18 Sep 2008; published 22 Sep 2008
(C) 2008 OSA   29 September 2008 / Vol. 16, No. 20 / OPTICS EXPRESS 15896

141

6.1   Epilogue

The discussion section of the third article mentions a comparison of the fluid infiltration technique to that of what liquid crystals may offer. If one considers a static geometry, where the fluid remains in the holes and the thermal or electrical tuning of the liquid crystal is the basis for tunability, device timescales would be on the order of 10's of μs. This is much faster than the complete infiltration or removal of fluid that can currently be achieved. However, this is still too slow for signal timescales, and if used for reconfigurability then perhaps it would be "overkill". In addition, liquid crystals offer an index contrast of $n \sim 0.05$ by thermal or electrical tuning, which is an order of magnitude less than what the available range of infiltration fluids could span, $n \sim 1.3 - 1.8$ ($n \sim 0.5$). Nevertheless, because liquid crystals offer a base refractive index range of $n \sim 1.45 - 1.7$, they could be advantageously combined with the microfluidic double heterostructure scheme to provide both highly tunable (via electrical or thermal excitation) and reconfigurable (via fluid replacement) optical functionality.

6.1.1   Propagation losses and reflectivity

A major result of the third article in this chapter is the demonstration of varying microfluidic cavity lengths. From this, the relevant information is available to use equation (49) of Chapter 2 to simultaneously solve the reflectivity at the end facets of the cavity and propagation losses along the waveguide. For cavity lengths 11.5 μm and 13.8 μm with Q-factors of 14434 and 14732 respectively at a wavelength $\lambda = 1409$ nm, and using a group refractive index of the modes $n_g = 20$ (±15%), equation (49) can be solved to reveal a reflectivity of:

$r = 0.9914 \pm 0.0013$,

and a propagation loss of:

$\alpha_{prop} = 54 \pm 8$ cm^{-1}.

These values are close to what one would expect considering the values presented in reference [136].

Summary

This work represents the investigations of introducing fluids to the air holes of planar photonic crystals to increase their functionality.

The paper reproduced from *Applied Physics Letters* Vol. 91, 121103, 2007, made the following advancements:

- First demonstration of microfluidically-defined photonic crystal cavities.

- Dispersion associated with the photonic crystal in good agreement with theory.

The paper reproduced from *Optics Letters* Vol. 33, 2008, made the following advancements:

- High Q-factors of up to 57,000 demonstrated in microfluidic photonic crystal cavities.

The paper reproduced from *Optics Express* Vol. 16, pp. 15887-15896, 2008, made the following advancements:

- Spectral and spatial configurability of photonic crystal cavities is achieved.

- High Q-factors for a broad range of cavity lengths are shown.

- Fluid can be removed by immersion in toluene, demonstrating reconfigurability.

Chapter 7

Comments and Outlook

The following section provides some author comments on the work that comprises this thesis and attempts to answer perhaps the most paramount question: where is it all going?

Firstly, some comments on the bow-, loop- and helical-shaped nanowire evanescent coupling technique. This scheme is capable of monitoring Fabry-Pérot resonances of a closed waveguide, enabling immediate access to the waveguide's dispersion and propagation losses in a quick, single spectral measurement [134]. This circumvents the need to use integrated access waveguides or internal light sources that may affect the spectral signature. As such, the strength of the nanowire coupling nanowire rests in its ability to accurately *characterise* photonic crystal structures non-invasively.

In terms of miniaturised components, it is, in its current stage, impractical to incorporate a suspended and finely shaped fibre above a planar photonic crystal device. This would be cumbersome in terms of both packaging and fabrication. However, device incorporation is not the anticipated path of nanowire evanescent coupling. As far as utilising it at a research level, it has been almost ideal to test a variety of novel structures. It is feasible to consider employing the technique to rapidly probe sample structure sets, although it may require dedicated closed waveguide sections. Nanowire evanescent coupling could also be beneficial to slow light dispersion engineering [34], where a measurement could be performed without the need for enhancing the coupling into the slow light regime.

Next, some comments on exploiting photosensitivity in chalcogenide glass photonic crystals. There are still challenges to overcome, for example obtaining a suitable material that would behave both stable and predictably. That being said, initial proof-of-concept results have been achieved, and future demonstrations could promote this as a flexible, elegant approach to optimising or writing photonic crystal structures after the fabrication stage.

There are several applications possible from utilising chalcogenide glass photosensitivity, for which some early predictions have since been demonstrated after the initial results in [93]. The photosensitive tunability available in chalcogenide glass has allowed the spectral alignment between a photonic crystal cavity resonance and quantum dot emission [96], offering a means to overcome a crucial challenge for single photon source quantum electrodynamics experiments. In the near future, the ability to write a photonic crystal cavity into a waveguide structure is particularly relevant. This could result in a post-processed double heterostructure cavity, potentially reaching Q-factors of 30,000 [118] – perhaps even beyond by a carefully written Gaussian refractive index profile.

Lastly, some comments on the microfluidic infiltration of select holes in a slab photonic crystal. There are still a number of challenges to overcome, including accurate knowledge of the penetration depth of the fluid in the holes, as well as highly selective infiltration – i.e. single-hole infiltration. That being said, the challenges that were presented initially during the investigation have been steadily overcome, such as removing the fluid from the holes and several-micron-selective infiltration. It seems reasonable to suggest that the outlook in terms of what will be achieved in the coming years is promising.

However, that does not answer the question of where the work is going. Professor Thomas Krauss made an insightful comment on this: "the fact that you can stick a blob of fluid onto the chip and get a high Q cavity is noteworthy". The key ingredient of the microfluidic approach is that fluids are inherently mobile, so it is natural to consider the scheme for not only creating a device, but a *reconfigurable* device. Currently, photonic crystal cavities are limited by the difficulty in altering their properties after fabrication, reducing diversity for applications in tunable photonics and adaptable sensing schemes. The potential to realise complex geometries and arbitrarily defined components in a photonic crystal via microfluidic infiltration paves the way toward sophisticated and flexible photonic crystal architectures.

The microfluidic infiltration may be a potentially reconfigurable approach, but it is also flexible in other promising ways. There are many interesting fluids and colloidal mixtures one could incorporate into the holes of a planar photonic crystal. Fluorescent dyes and cocktails containing quantum dots or nonlinear components offer a means to incorporate additional functionality. Liquid crystals promote further tunability by means of their thermal- or electro-tuning capability – this is on top of the reconfigurability aspect offered by the virtue of the solutions being a fluid. Recent work has taken an interest in ionic liquids – salts that are liquid at room temperature – due to their ability to dissolve practically anything. In addition to this trait, ionic liquids are currently recognised as solvents for green chemistry due to their non-volatile nature. However, the ions themselves would introduce a new source of damping due to their inability to conduct Ohmic currents.

The potential for analyte sensing offered by the microfluidic infiltration scheme was mentioned [144]. One of the major advantages here is that the holes of a slab photonic crystal occupy approximately 0.1 fL. That leads to the requirement of an incredibly small volume of fluid to be sensed. Reference [144] estimates a potential sensitivity $\Delta\lambda/\Delta n$ of 60 nm / RIU (refractive index units) and considers a minimum refractive index change detectable of $\delta n_{\text{fluid}} = 4.5\times10^{-4}$. This value is favourable to other photonic crystal cavity chemical sensing schemes ($\delta n_{\text{fluid}} = 0.002$ [86]), although the ratio of electromagnetic energy overlapping the holes where the analyte resides appears limited to ~6%. The field overlap and therefore the sensitivity could be improved by additional engineering of the cavity geometry.

As a final word, the glass micro-tip drawing scheme is amenable to robotics and actuators. By rigorously investigating the wetting properties of the fluid, the fluid manipulator and the sample surface, one could feasibly translate this approach to mass-production. There are also recent demonstrations of electrowetting capabilities that could be cleverly incorporated into the approach, decreasing reconfiguration times and possibly avoiding the necessity of a fluid manipulator tip altogether.

END OF THESIS

Appendix A

Acknowledgement of the author's contributions

The following forms acknowledge the contributions of the author of this thesis to the published journal articles discussed in Chapters 3, 4, 5 and 6. The forms are signed and acknowledged by each co-author of the articles.
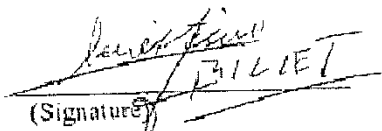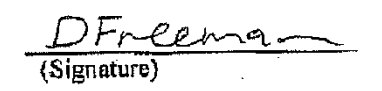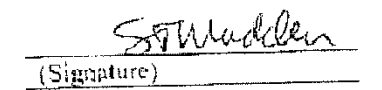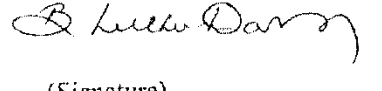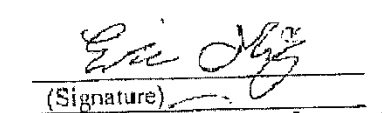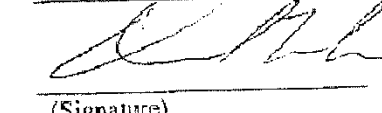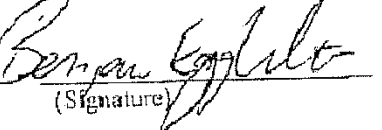
Acknowledgement of contribution to a published work

The following signed statement is to attest that the author of this thesis has made the indicated contributions to a published work contained in this thesis.

Title of published work:	Efficient coupling to chalcogenide glass photonic crystal waveguides via silica optical fiber nanowires
Journal and issue:	Optics Express, Vol. 14, No. 3, February 2006
Authors of published work:	Christian Grillet, Cameron Smith, Darren Freeman, Steve Madden, Barry Luther-Davis, Eric C. Mägi, David J. Moss, Benjamin J. Eggleton

We, the authors of the work entitled "Efficient coupling to chalcogenide glass photonic crystal waveguides via silica optical fiber nanowires", acknowledge that Cameron Smith has made the following contributions to the published work:

- Performed many of the experimental measurements and tapered fibre fabrication
- Provided some of the figures presented
- Contributed to the writing of the manuscript

_____ Christian Grillet   24/10/2008
(Signature)   (Name)   (Date)

DFreeman   Darren Freeman   3/11/2008
(Signature)   (Name)   (Date)

_____ Steve Madden   30/6/08
(Signature)   (Name)   (Date)

_____ Barry Luther-Davis   2-11-08
(Signature)   (Name)   (Date)

_____ Eric C. Mägi   3 Nov 2008
(Signature)   (Name)   (Date)

_____ David J. Moss   2-11/08
(Signature)   (Name)   (Date)

_____ Benjamin J. Eggleton   2-11-2008
(Signature)   (Name)   (Date)
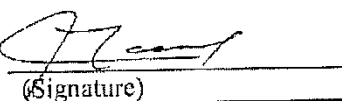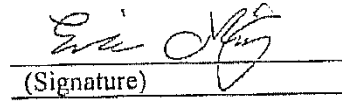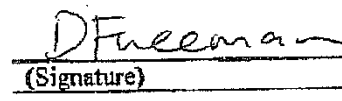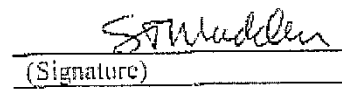
Acknowledgement of contribution to a published work

The following signed statement is to attest that the author of this thesis has made the indicated contributions to a published work contained in this thesis.

Title of published work:	Characterisation of chalcogenide 2D photonic crystal waveguides and nanocavities using silica fibre nanowires
Journal and issue:	Physica B – Condensed Matter, Vol. 394, No. 4, December 2006
Authors of published work:	C. Smith, C. Grillet, D. Freeman, S. Madden, S. Tomljenovic-Hanic, E. C. Mägi, D. Moss, B. Luther-Davis, B. J. Eggleton
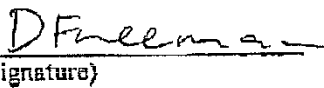
We, the authors of the work entitled **"Characterisation of chalcogenide 2D photonic crystal waveguides and nanocavities using silica fibre nanowires"**, acknowledge that Cameron Smith has made the following contributions to the published work:

- Performed the presented experimental measurements and tapered fibre fabrication
- Provided all of the figures presented
- Contributed significantly to the writing of the manuscript
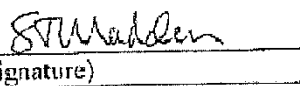
(Signature)   Christian Grillet _(Name)_   7 / / 7 0 / 2 0 0 8 _(Date)_
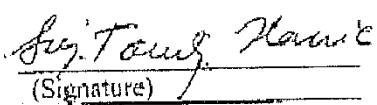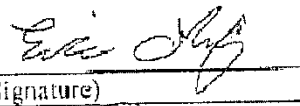
(Signature)   Darren Freeman _(Name)_   3 / 11 / 2008 _(Date)_

(Signature)   Steve Madden _(Name)_   30 / 6 / 08 _(Date)_
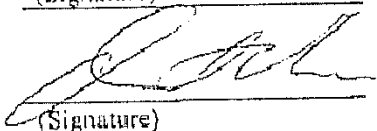
(Signature)   Snjezana Tomljenovic-Hanic _(Name)_   28 / 10 / 08 _(Date)_

(Signature)   Eric C. Mägi _(Name)_   3 Nov 2008 _(Date)_

(Signature)   David J. Moss _(Name)_   2 / 11 / 08 _(Date)_

_____

(Signature)

_____
Barry Luther-Davis
(Name)

2-11-08

(Date)

_____
(Signature)

Benjamin J. Eggleton
(Name)

2-11-2008

(Date)

151
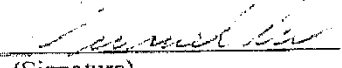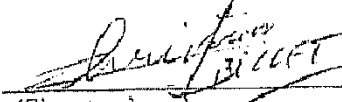
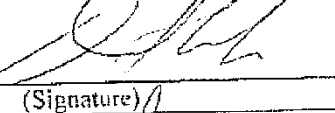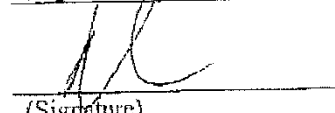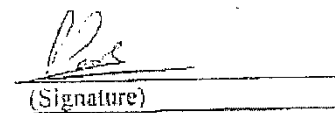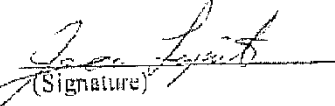# Acknowledgement of contribution to a published work

The following signed statement is to attest that the author of this thesis has made the indicated contributions to a published work contained in this thesis.

Title of published work:	Characterizing photonic crystal waveguides with an expanded k-space evanescent coupling technique
Journal and issue:	Optics Express, Vol. 16, 13800-13808 (2008)
Authors of published work:	Michael W. Lee, Christian Grillet, Christopher H. Poulton, Christelle Monat, Cameron L. C. Smith, Eric C. Magi, Darren Freeman, Steve Madden, Barry Luther-Davies, Benjamin J. Eggleton

We, the authors of the work entitled "**Characterizing photonic crystal waveguides with an expanded k-space evanescent coupling technique**", acknowledge that Cameron Smith has made the following contributions to the published work:

- Provided expertise for characterisation and tapered fibre fabrication
- Contributed to the writing of the manuscript

(Signature)	Michael W. Lee (Name)	2? /10/2008 (Date)
(Signature)	Christian Grillet (Name)	24 / 10 / 2008 (Date)
(Signature)	Christopher Poulton (Name)	27. 10.08 (Date)
(Signature)	Christelle Monat (Name)	24/10/2008 (Date)
(Signature)	Eric Magi (Name)	3 Nov 2008 (Date)
(Signature)	Darren Freeman (Name)	3/11/2008 (Date)
(Signature)	Steve Madden (Name)	30/6/08 (Date)

(Signature)

Barry Luther-Davies
(Name)

2-11-08
(Date)

(Signature)

Benjamin J. Eggleton
(Name)

2-10-2008
(Date)
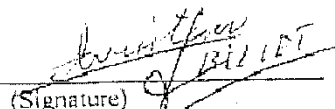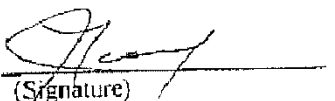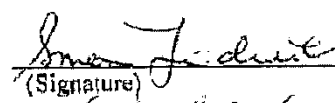
153

Acknowledgement of contribution to a published work

The following signed statement is to attest that the author of this thesis has made the indicated contributions to a published work contained in this thesis.

Title of published work:	Nanowire coupling to photonic crystal nanocavities for single photon sources
Journal and issue:	Optics Express, Vol. 15, No. 3, February 2007
Authors of published work:	Christian Grillet, Christelle Monat, Simon Frédérick, Cameron L. C. Smith, David J. Moss, Dan Dalacu, Philip J. Poole, Jean Lapointe, Geof Aers, Robin L. Williams, Benjamin J. Eggleton

We, the authors of the work entitled "**Nanowire coupling to photonic crystal nanocavities for single photon sources**", acknowledge that Cameron Smith has made the following contributions to the published work:

- Performed the presented experimental measurements
- Fabricated tapered fibre for experiment
- Contributed to the writing of the manuscript

(Signature)	Christian Grillet (Name)	2 4 / 10 / 2008 (Date)
(Signature)	Christelle Monat (Name)	24/10/2008 (Date)
(Signature)	Simon Frédérick (Name)	28/10/2008 (Date)
(Signature)	David J. Moss (Name)	2/11/2008 (Date)
(Signature)	Dan Dalacu (Name)	12-5-8 (Date)
(Signature)	Philip J. Poole (Name)	12/05/08 (Date)
(Signature)	Jean Lapointe (Name)	May 12, 2008 (Date)

(Signature)

Geof Aers

(Name)

May 12th 2008

(Date)

(Signature)

Robin L. Williams

(Name)

May 12th 2008

(Date)

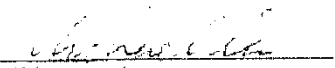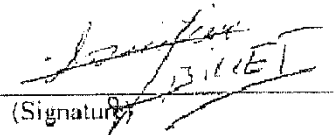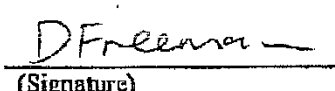_(Signature)_

Benjamin J. Eggleton

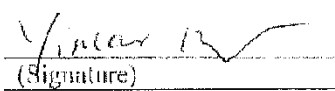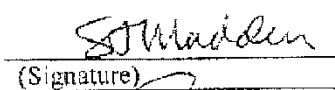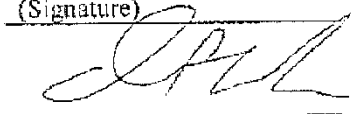(Name)

2-11-2008

(Date)

155

Acknowledgement of contribution to a published work

The following signed statement is to attest that the author of this thesis has made the indicated contributions to a published work contained in this thesis.

Title of published work:	Photosensitive post tuning of chalcogenide photonic crystal waveguides
Journal and issue:	Optics Express, Vol. 15, No. 3, February 2007
Authors of published work:	Michael W. Lee, Christian Grillet, Darren Freeman, Yinlan Ruan, Barry Luther-Davis, Cameron L. C. Smith, Steve Madden, David J. Moss, Andrei Rode, Yong-Hee Lee, Benjamin J. Eggleton

We, the authors of the work entitled **"Photosensitive post tuning of chalcogenide photonic crystal waveguides"**, acknowledge that Cameron Smith has made the following contributions to the published work:

- Provided expertise for characterisation and tapered fibre fabrication
- Involved in idea formation for experimental methods
- Contributed to the writing of the manuscript

(Signature)	(Name)	(Date)
	Michael W. Lee	28/10/08
	Christian Grillet	24/10/2008
	Darren Freeman	3/11/2008
	Yinlan Ruan	30 Oct 2008
	Barry Luther-Davis	2-11-08
	Steve Madden	30/6/08
	David J. Moss	2/11/08

(Signature)   Andrei Rode
                (Name)   30/06/2008
                                               (Date)

(Signature)   Yong-Hee Lee
                (Name)   7 May. 2008
                                               (Date)

(Signature)   Benjamin J. Eggleton
                (Name)   2-11-2008
                                               (Date)
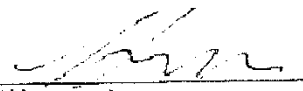
Acknowledgement of contribution to a published work

The following signed statement is to attest that the author of this thesis has made the indicated contributions to a published work contained in this thesis.
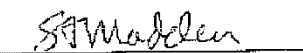
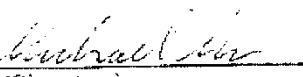|	
Title of published work:	Microfluidic photonic crystal double heterostructures
Journal and issue:	Applied Physics Letters, Vol. 91, No. 121103, September 2007
Authors of published work:	Cameron L. C. Smith, Darran K. C. Wu, Darren Freeman, Steve Madden, Michael W. Lee, Christelle Monat, Snjezana Tomljenovic-Hanic, Christian Grillet, Yinlan Ruan, Barry Luther-Davis, Harald Giessen, Yong-Hee Lee, Benjamin J. Eggleton

We, the authors of the work entitled "**Microfluidic photonic crystal double heterostructures**", acknowledge that Cameron Smith has made the following contributions to the published work:
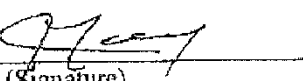
- Performed the microfluidic infiltration and characterisation measurements
- Performed calculations and provided the figures presented
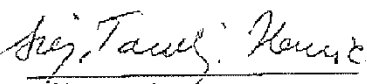- Contributed significantly to the writing of the manuscript

(Signature)	Darran K. C. Wu (Name)	28/10/08 (Date)
(Signature)	Darren Freeman (Name)	3/11/2008 (Date)
(Signature)	Steve Madden (Name)	30/6/08 (Date)
(Signature)	Michael W. Lee (Name)	28/10/08 (Date)
(Signature)	Christelle Monat (Name)	24/10/08 (Date)
(Signature)	Snjezana Tomljenovic-Hanic (Name)	28/13/08 (Date)
(Signature)	Christian Grillet (Name)	24/10/2008 (Date)

(Signature)

Yinlan Ruan
(Name)

30 Oct 2008
(Date)

(Signature)

Barry Luther-Davis
(Name)

2-11-08
(Date)

(Signature)

Harald Giessen
(Name)

6 May 08
(Date)

(Signature)

Yong-Hee Lee
(Name)

7 May 2008
(Date)
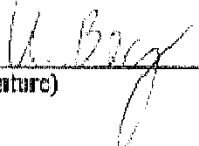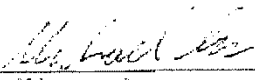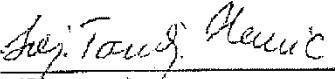
(Signature)

Benjamin J. Eggleton
(Name)

2-11-2008
(Date)

159

Acknowledgement of contribution to a published work

The following signed statement is to attest that the author of this thesis has made the indicated contributions to a published work contained in this thesis.

Title of published work:	High-Q microfluidic cavities in silicon-based 2D photonic crystal structures
Journal and issue:	Optics Letters, Vol. 33, 2206-2208 (2008)
Authors of published work:	Uwe Bog, Cameron L. C. Smith, Michael W. Lee, Snjezana Tomljenovic-Hanic, Christian Grillet, Christelle Monat, Liam O'Faolain, Christian Karnutsch, Thomas F. Krauss, Ross McPhedran, Benjamin J. Eggleton

We, the authors of the work entitled "**High-Q microfluidic cavities in silicon-based 2D photonic crystal structures**", acknowledge that Cameron Smith has made the following contributions to the published work:

- Performed the presented experimental measurements
- Fabricated tapered fibre for experiment
- Contributed to the writing of the manuscript

(Signature)	Uwe Bog (Name)	27/10/2008 (Date)
(Signature)	Michael Lee (Name)	28/10/08 (Date)
(Signature)	Snjezana Tomljenovic-Hanic (Name)	28/10/08 (Date)
(Signature)	Christian Grillet (Name)	24/10/2008 (Date)
(Signature)	Christelle Monat (Name)	24/10/2008 (Date)
(Signature)	Liam O'Faolain (Name)	28/10/08 (Date)
(Signature)	Christian Karnutsch (Name)	28/10/08 (Date)

(Signature)

Thomas Krauss
(Name)

27 October 2008
(Date)

(Signature)

Ross McPhedran
(Name)

3 — 11 — 2008
(Date)

(Signature)

Benjamin J. Eggleton
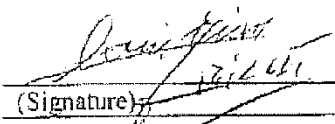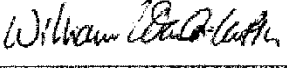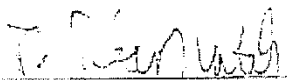(Name)

2 — 11 — 2008
(Date)
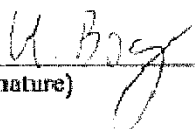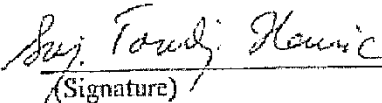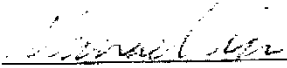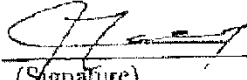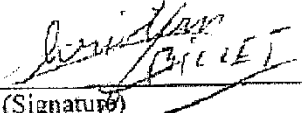
Acknowledgement of contribution to a published work
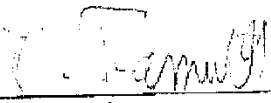
The following signed statement is to attest that the author of this thesis has made the indicated contributions to a published work contained in this thesis.

Title of published work:	Reconfigurable microfluidic photonic crystal slab cavities
Journal and issue:	Optics Express, Vol. 16, No. 3, 15887-15896, (2008)
Authors of published work:	Cameron L. C. Smith, Uwe Bog, Snjezana Tomljenovic-Hanic, Michael W. Lee, Liam O'Faolain, Christelle Monat, Christian Grillet, Thomas F. Krauss, Christian Karnutsch, Ross McPhedran, Benjamin J. Eggleton

We, the authors of the work entitled "**Reconfigurable microfluidic photonic crystal slab cavities**", acknowledge that Cameron Smith has made the following contributions to the published work:

- Performed the presented experimental measurements
- Fabricated tapered fibre for experiment
- Contributed the majority of writing for the manuscript

(Signature)	Uwe Bog _____ (Name)	27/10/2008 _____ (Date)
(Signature)	Snjezana Tomljenovic-Hanic (Name)	28/10/08 (Date)
(Signature)	Michael Lee (Name)	28/10/08 (Date)
(Signature)	Liam O'Faolain (Name)	28/10/08 (Date)
(Signature)	Christelle Monat (Name)	24/10/2008 (Date)
(Signature)	Christian Grillet (Name)	24/10/2008 (Date)
(Signature)	Thomas F. Krauss (Name)	28 October 2008 (Date)
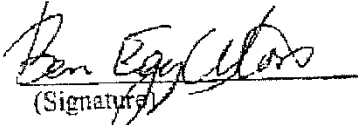
(Signature)

Christian Karnutsch
(Name)

_28/10/08_
(Date)
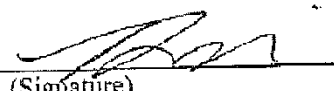
(Signature)

Ross McPhedran
(Name)

_3/11/08_
(Date)

(Signature)

Benjamin J. Eggleton
(Name)

_2-11-2008_
(Date)

(Signature)

Darran Wu
(Name)

_28/10/08_
(Date)

163

Appendix B

Complete list of the author's publications

Journal Articles – refereed

[1] <u>C. L. C. Smith</u>, U. Bog, S. Tomljenovic-Hanic, M. W. Lee, D. K. C. Wu, L. O'Faolain, C. Monat, C. Grillet, T. F. Krauss, C. Karnutsch, R. C. McPhedran, B. J. Eggleton "Reconfigurable microfluidic photonic crystal slab cavities," *Opt. Express* **16**, 15887-15896 (2008)

[2] U. Bog, <u>C. L. C. Smith</u>, M. W. Lee, S. Tomljenovic-Hanic, C. Grillet, C. Monat, L. O'Faolain, C. Karnutsch, T. F. Krauss, R. McPhedran, B. J. Eggleton, "High-*Q* microfluidic cavities in silicon-based 2D photonic crystal structures," *Opt. Lett.* **33** 2206-2208 (2008)

[3] M. W. Lee, C. Grillet, C. G. Poulton, C. Monat, <u>C. L. C. Smith</u>, E. C. Magi, D. Freeman, S. Madden, B. Luther-Davies, B. J. Eggleton, "Characterizing photonic crystal waveguides with an expanded *k*-space evanescent coupling technique," *Opt. Express* **16**, 13800-13808 (2008)

[4] D. Freeman, C. Grillet, M. W. Lee, <u>C. L. C. Smith</u>, Y. Ruan, A. Rode, M. Krolikowska, S. Tomljenovic-Hanic, M. de Sterke, M. J. Steel, B. Luher-Davies, S. Madden, D. J. Moss, Y.-H. Lee, B. J. Eggleton, "Chalcogenide glass photonic crystals," *Photonics and Nanostructures – Fundamentals and Applications* **6** 3-11 (2008).

[5] <u>C. L. C. Smith</u>, D. K. C. Wu, D. Freeman, Y. Ruan, S. J. Madden, and M. W. Lee, C. Monat, S. Tomljenovic-Hanic, C. Grillet, B. Luther-Davies, H. Giessen, Y.-H. Lee, and B. J. Eggleton, "Microfluidic Photonic Crystal Double Heterostructures," *Appl. Phys. Lett.* **91**, 121103 (2007).

[6]   M. W. Lee, C. Grillet, <u>C. L. C. Smith</u>, D. J. Moss, B. J. Eggleton, D. Freeman, B. Luther-Davies, S. Madden, A. Rode, Y. Ruan, and Y.-H. Lee, "Photosensitive post tuning of chalcogenide photonic crystal waveguides," *Opt. Express* **15**, 1277-1285 (2007).

[7]   C. Grillet, C. Monat, <u>C. L. C. Smith</u>, B. J. Eggleton, D. J. Moss, S. Frederick, D. Dalacu, P. J. Poole, J. Lapointe, G. Aers, and R. L. Williams, "Nanowire coupling to photonic crystal nanocavities for single photon sources," *Opt. Express* **15**, 1267-1276 (2007).

[8]   C. Monat, C. Grillet, R. Domachuk, <u>C. L. C. Smith</u>, E. Magi, D. J. Moss, H. C. Nguyen, S. Tomljenovic-Hanic, M. Cronin-Golomb, B. J. Eggleton, D. Freeman, S. Madden, B. Luther-Davies, S. Mutzenich, G. Rosengarten, and A. Mitchell, "Frontiers in microphotonics: tunability and all-optical control," *Laser Physics Letters* **4**, 177-186 (2007).

[9]   <u>C. L. C. Smith</u>, C. Grillet, S. Tomljenovic-Hanic, E.C. Mägi, D. Moss, D. Freeman, S. Madden and B. Luther-Davies, B.J. Eggleton, "Characterisation of chalcogenide 2D photonic crystal waveguides and cavities using evanescent coupling," *Physica B- Condensed Matter* **394**, 289-292 (2007).

[10] C. Grillet, <u>C. L. C. Smith</u>, D. Freeman, S. Madden, B. Luther-Davis, E. C. Mägi, D. J. Moss, and B. J. Eggleton, "Efficient coupling to chalcogenide glass photonic crystal waveguides via silica optical fiber nanowires," *Opt. Express* **14**, 1070-1078 (2006).

[11] H. C. Nguyen, B. T. Kuhlmey, M. J. Steel, <u>C. L. C. Smith</u>, E. C. Mägi, R. C. McPhedran, B. J. Eggleton, "Leakage of the fundamental mode in photonic crystal fiber tapers," *Opt. Lett.* **30**, 1123-1125 (2005).

[12] H. C. Nguyen, B. T. Kuhlmey, E. C. Mägi, M. J. Steel, P. Domachuk, <u>C. L. C. Smith</u>, B. J. Eggleton, "Tapered photonic crystal fibers: properties, characterizations and applications," *Appl. Phys. B* **81**, 377-387 (2005).

Conference Full Proceedings (presented by C. L. C. Smith)

[1]   <u>C. L. C. Smith</u>, U. Bog, S. tomljenovic-Hanic, M. W. Lee, D. K. C. Wu, L. O'Faolain, C. Monat, C. Grillet, T. F. Krauss, C. Karnutsch, R. C. McPhedran, B. J. Eggleton, "Reconfigurable microfluidic photonic crystal cavities," LEOS annual meeting, Newport Beach, California, USA (2008).

[2]   <u>C. L. C. Smith</u>, U. Bog, S. Tomljenovic-Hanic, L. O'Faolain, M. Spurney, C. Grillet, C. Monat, C. Karnutsch, R. C. McPhedran, T. F. Krauss, B. J.

Eggleton, "Comparison of microfluidic cavities based on chalcogenide and silicon photonic crystals," IUMRS-ICEM, Sydney, NSW, Australia (2008).

[3]   C. Karnutsch, <u>C. L. C. Smith</u>, U. Bog, D. Freeman, D. K. C. Wu, S. Tomljenovic-Hanic, S. Madden, M. W. Lee, C. Monat, C. Grillet, R. McPhedran, B. Luther-Davies, B.J. Eggleton, "Reconfigurable microfluidic photonic crystal cavities," CLEO meeting, San Jose, California, USA (2008).

[4]   <u>C. L. C. Smith</u>, D. K. C. Wu, M. W. Lee, C. Monat, S. Tomljenovic-Hanic, D. Freeman, S. Madden, C. Grillet, B. Luther-Davies, H. Giessen, B. J. Eggleton, "Microfluidic photonic crystal nanocavities," SPIE meeting, Canberra, ACT, Australia (2007).

[5]   <u>C. L. C. Smith</u>, D. K. C. Wu, M. W. Lee, C. Monat, S. Tomljenovic- Hanic, D. Freeman, C. Grillet, S. Madden, B. Luther-Davies, H. Giessen, B. J. Eggleton, "Microfluidic cavities in photonic crystal waveguides," LEOS annual meeting, Lake Buena Vista, Florida, USA (2007).

[6]   <u>C. L. C. Smith</u>, C. Grillet, E. C. Mägi, D. Moss, B. J. Eggleton, "Characterisation of Chalcogenide 2D photonic crystal waveguides using silica fibre nanowires," Australian Conference on Optical Fibre Technology, Melbourne (2006).

Bibliography

1. P. E. Barclay, K. Srinivasan, M. Borselli, and O. Painter, "Experimental demonstration of evanescent coupling from optical fibre tapers to photonic crystal waveguides," Electron. Lett. **39**, 842-844 (2003).

2. E. Yablonovitch, "Inhibited Spontaneous Emission in Solid-State Physics and Electronics," Phys. Rev. Lett. **58**, 2059-2062 (1987).

3. S. John, "Strong Localization of Photons in Certain Disordered Dielectric Superlattices," Phys. Rev. Lett. **58**, 2486-2489 (1987).

4. J. W. S. Rayleigh, "On the remarkable phenomenon of crystalline reflexion described by Prof. Stokes," Phil. Mag. **26**, 256-265 (1888).

5. T. F. Krauss, R. M. DeLaRue, and S. Brand, "Two-dimensional photonic-bandgap structures operating at near infrared wavelengths," Nature **383**, 699-702 (1996).

6. J. D. Joannopoulos, P. R. Villeneuve, and S. H. Fan, "Photonic crystals: Putting a new twist on light," Nature **386**, 143-149 (1997).

7. D. Freeman, S. Madden, and B. Luther-Davies, "Fabrication of planar photonic crystals in a chalcogenide glass using a focused ion beam," Opt. Express **13**, 3079-3086 (2005).

8. A. Mekis, J. C. Chen, I. Kurland, S. H. Fan, P. R. Villeneuve, and J. D. Joannopoulos, "High transmission through sharp bends in photonic crystal waveguides," Phys. Rev. Lett. **77**, 3787-3790 (1996).

9. C. Grillet, C. Smith, D. Freeman, S. Madden, B. Luther-Davis, E. C. Mägi, D. J. Moss, and B. J. Eggleton, "Efficient coupling to chalcogenide glass photonic crystal waveguides via silica optical fiber nanowires," Opt. Express **14**, 1070-1078 (2006).

10. J. M. Gerard, B. Sermage, B. Gayral, B. Legrand, E. Costard, and V. Thierry-Mieg, "Enhanced spontaneous emission by quantum boxes in a monolithic optical microcavity," Phys. Rev. Lett. **81**, 1110-1113 (1998).

11. G. S. Solomon, M. Pelton, and Y. Yamamoto, "Single-mode spontaneous emission from a single quantum dot in a three-dimensional microcavity," Phys. Rev. Lett. **86**, 3903-3906 (2001).

12. I. Fushman, D. Englund, A. Faraon, N. Stoltz, P. Petroff, and J. Vuckovic, "Controlled phase shifts with a single quantum dot," Science **320**, 769-772 (2008).

13. S. H. Fan, P. R. Villeneuve, and J. D. Joannopoulos, "Channel drop tunneling through localized states," Phys. Rev. Lett. **80**, 960-963 (1998).

14. B. S. Song, S. Noda, and T. Asano, "Photonic devices based on in-plane hetero photonic crystals," Science **300**, 1537-1537 (2003).

15. O. Painter, R. K. Lee, A. Scherer, A. Yariv, J. D. O'Brien, P. D. Dapkus, and I. Kim, "Two-dimensional photonic band-gap defect mode laser," Science **284**, 1819-1821 (1999).

16. H. G. Park, S. H. Kim, S. H. Kwon, Y. G. Ju, J. K. Yang, J. H. Baek, S. B. Kim, and Y. H. Lee, "Electrically driven single-cell photonic crystal laser," Science **305**, 1444-1447 (2004).

17. E. Centeno, and D. Felbacq, "Optical bistability in finite-size nonlinear bidimensional photonic crystals doped by a microcavity," Physical Review B **62**, R7683-R7686 (2000).

18. T. Tanabe, K. Nishiguchi, A. Shinya, E. Kuramochi, H. Inokawa, M. Notomi, K. Yamada, T. Tsuchizawa, T. Watanabe, H. Fukuda, H. Shinojima, and S. Itabashi, "Fast all-optical switching using ion-implanted silicon photonic crystal nanocavities," Appl. Phys. Lett. **90**, - (2007).

19. M. Soljacic, M. Ibanescu, S. G. Johnson, Y. Fink, and J. D. Joannopoulos, "Optimal bistable switching in nonlinear photonic crystals," Physical Review E **66**, - (2002).

20. M. F. Yanik, S. H. Fan, M. Soljacic, and J. D. Joannopoulos, "All-optical transistor action with bistable switching in a photonic crystal cross-waveguide geometry," Opt. Lett. **28**, 2506-2508 (2003).

21. B. S. Song, S. Noda, T. Asano, and Y. Akahane, "Ultra-high-Q photonic double-heterostructure nanocavity," Nat. Mater. **4**, 207-210 (2005).

22. T. Tanabe, M. Notomi, S. Mitsugi, A. Shinya, and E. Kuramochi, "Fast bistable all-optical switch and memory on a silicon photonic crystal on-chip," Opt. Lett. **30**, 2575-2577 (2005).

23. P. E. Barclay, K. Srinivasan, and O. Painter, "Nonlinear response of silicon photonic crystal microresonators excited via an integrated waveguide and fiber taper," Opt. Express **13**, 801-820 (2005).

24. F. Raineri, C. Cojocaru, P. Monnier, A. Levenson, R. Raj, C. Seassal, X. Letartre, and P. Viktorovitch, "Ultrafast dynamics of the third-order nonlinear response in a two-dimensional InP-based photonic crystal," Appl. Phys. Lett. **85**, 1880-1882 (2004).

25. T. Tanabe, M. Notomi, E. Kuramochi, A. Shinya, and H. Taniyama, "Trapping and delaying photons for one nanosecond in an ultrasmall high-Q photonic-crystal nanocavity," Nat. Photonics **1**, 49-52 (2007).

26. Y. Tanaka, J. Upham, T. Nagashima, T. Sugiya, T. Asano, and S. Noda, "Dynamic control of the Q factor in a photonic crystal nanocavity," Nat. Mater. **6**, 862-865 (2007).

27. M. Loncar, A. Scherer, and Y. M. Qiu, "Photonic crystal laser sources for chemical detection," Appl. Phys. Lett. **82**, 4648-4650 (2003).

28. S. Kita, K. Nozaki, and T. Baba, "Refractive index sensing utilizing a cw photonic crystal nanolaser and its array configuration," Opt. Express **16**, 8174-8180 (2008).

29. Y. Takahashi, H. Hagino, Y. Tanaka, B. S. Song, T. Asano, and S. Noda, "High-Q nanocavity with a 2-ns photon lifetime," Opt. Express **15**, 17206-17213 (2007).

30. K. J. Vahala, "Optical microcavities," Nature **424**, 839-846 (2003).

31. J. Vuckovic, D. Englund, D. Fattal, E. Waks, and Y. Yamamoto, "Generation and manipulation of nonclassical light using photonic crystals," Physica E-Low-Dimensional Systems & Nanostructures **32**, 466-470 (2006).

32. W. Bogaerts, P. Bienstman, D. Taillaert, R. Baets, and D. De Zutter, "Out-of-plane scattering in photonic crystal slabs," IEEE Phot. Tech. Lett. **13**, 565-567 (2001).

33. Y. Tanaka, T. Asano, Y. Akahane, B. S. Song, and S. Noda, "Theoretical investigation of a two-dimensional photonic crystal slab with truncated cone air holes," Appl. Phys. Lett. **82**, 1661-1663 (2003).

34. J. Li, T. P. White, L. O'Faolain, A. Gomez-Iglesias, and T. F. Krauss, "Systematic design of flat band slow light in photonic crystal waveguides," Opt. Express **16**, 6227-6232 (2008).

35. D. Dalacu, S. Frederick, A. Bogdanov, P. J. Poole, G. C. Aers, R. L. Williams, M. W. McCutcheon, and J. F. Young, "Fabrication and optical characterization of hexagonal photonic crystal microcavities in InP-based membranes containing InAs/InP quantum dots," J. Appl. Phys. **98**, - (2005).

36. D. Dalacu, S. Frederick, P. J. Poole, G. C. Aers, and R. L. Williams, "Postfabrication fine-tuning of photonic crystal microcavities in InAs/InP quantum dot membranes," Appl. Phys. Lett. **87**, - (2005).

37. D. J. Lockwood, and L. Pavesi, "Silicon fundamentals for photonics applications," Silicon Photonics **94**, 1-50 (2004).

38. E. B. Desurvire, "Capacity demand and technology challenges for lightwave systems in the next two decades," Journal of Lightwave Technology **24**, 4697-4710 (2006).

39. B. Jalali, and S. Fathpour, "Silicon photonics," Journal of Lightwave Technology **24**, 4600-4615 (2006).

40. E. Verpoorte, "Chip vision - optics for microchips," Lab on a Chip **3**, 42n-52n (2003).

41. S. Balslev, A. M. Jorgensen, B. Bilenberg, K. B. Mogensen, D. Snakenborg, O. Geschke, J. P. Kutter, and A. Kristensen, "Lab-on-a-chip with integrated optical transducers," Lab on a Chip **6**, 213-217 (2006).

42. N. A. Mortensen, S. S. Xiao, and J. Pedersen, "Liquid-infiltrated photonic crystals: enhanced light-matter interactions for lab-on-a-chip applications," Microfluidics and Nanofluidics **4**, 117-127 (2008).

43. K. Busch, and S. John, "Liquid-crystal photonic-band-gap materials: The tunable electromagnetic vacuum," Phys. Rev. Lett. **83**, 967-970 (1999).

44. C. Schuller, F. Klopf, J. P. Reithmaier, M. Kamp, and A. Forchel, "Tunable photonic crystals fabricated in III-V semiconductor slab waveguides using infiltrated liquid crystals," Appl. Phys. Lett. **82**, 2767-2769 (2003).

45. B. Maune, M. Loncar, J. Witzens, M. Hochberg, T. Baehr-Jones, D. Psaltis, A. Scherer, and Y. M. Qiu, "Liquid-crystal electric tuning of a photonic crystal laser," Appl. Phys. Lett. **85**, 360-362 (2004).

46. R. Ferrini, J. Martz, L. Zuppiroli, B. Wild, V. Zabelin, L. A. Dunbar, R. Houdre, M. Mulot, and S. Anand, "Planar photonic crystals infiltrated with liquid crystals: optical characterization of molecule orientation," Opt. Lett. **31**, 1238-1240 (2006).

47. W. Chen, and D. L. Mills, "Gap Solitons and the Nonlinear Optical-Response of Superlattices," Phys. Rev. Lett. **58**, 160-163 (1987).

48. B. J. Eggleton, R. E. Slusher, C. M. deSterke, P. A. Krug, and J. E. Sipe, "Bragg grating solitons," Phys. Rev. Lett. **76**, 1627-1630 (1996).

49. B. Xu, and N. B. Ming, "Experimental-Observations of Bistability and Instability in a 2-Dimensional Nonlinear-Optical Superlattice," Phys. Rev. Lett. **71**, 3959-3962 (1993).

50. H. G. Park, J. K. Hwang, J. Huh, H. Y. Ryu, Y. H. Lee, and J. S. Kim, "Nondegenerate monopole-mode two-dimensional photonic band gap laser," Appl. Phys. Lett. **79**, 3032-3034 (2001).

51. C. Monat, C. Seassal, X. Letartre, P. Viktorovitch, P. Regreny, M. Gendry, P. Rojo-Romeo, G. Hollinger, E. Jalaguier, S. Pocas, and B. Aspar, "InP 2D photonic crystal microlasers on silicon wafer: room temperature operation at 1.55 mu m," Electron. Lett. **37**, 764-766 (2001).

52. H. M. Gibbs, "Optical Bistability: Controlling Light with Light," Academic Press, Orlando, FL, USA (1985).

53. S. D. Smith, "Optical bistability, photonic logic, and optical computation," Applied Optics **25**, 1550-1564 (1986).

54. C. Monat, C. Grillet, R. Domachuk, C. Smith, E. Magi, D. J. Moss, H. C. Nguyen, S. Tomljenovic-Hanic, M. Cronin-Golomb, B. J. Eggleton, D. Freeman, S. Madden, B. Luther-Davies, S. Mutzenich, G. Rosengarten, and A. Mitchell, "Frontiers in microphotonics: tunability and all-optical control," Laser Physics Letters **4**, 177-186 (2007).

55. V. G. Ta'eed, N. J. Baker, L. B. Fu, K. Finsterbusch, M. R. E. Lamont, D. J. Moss, H. C. Nguyen, B. J. Eggleton, D. Y. Choi, S. Madden, and B. Luther-Davies, "Ultrafast all-optical chalcogenide glass photonic circuits," Opt. Express **15**, 9205-9221 (2007).

56. D. Freeman, C. Grillet, M. W. Lee, C. L. C. Smith, Y. Ruan, A. Rode, M. Krolikowska, S. Tomljenovic-Hanic, C. M. De Sterke, M. J. Steel, B. Luther-Davies, S. Madden, D. J. Moss, Y. H. Lee, and B. J. Eggleton, "Chalcogenide glass photonic crystals," Photonics and Nanostructures-Fundamentals and Applications **6**, 3-11 (2008).

57. C. Santori, M. Pelton, G. Solomon, Y. Dale, and E. Yamamoto, "Triggered single photons from a quantum dot," Phys. Rev. Lett. **86**, 1502-1505 (2001).

58. V. Zwiller, H. Blom, P. Jonsson, N. Panev, S. Jeppesen, T. Tsegaye, E. Goobar, M. E. Pistol, L. Samuelson, and G. Bjork, "Single quantum dots emit single photons at a time: Antibunching experiments," Appl. Phys. Lett. **78**, 2476-2478 (2001).

59. M. B. Ward, O. Z. Karimov, D. C. Unitt, Z. L. Yuan, P. See, D. G. Gevaux, A. J. Shields, P. Atkinson, and D. A. Ritchie, "On-demand single-photon source for 1.3 mu m telecom fiber," Appl. Phys. Lett. **86**, - (2005).

60. C. Zinoni, B. Alloing, C. Monat, V. Zwiller, L. H. Li, A. Fiore, L. Lunghi, A. Gerardino, H. de Riedmatten, H. Zbinden, and N. Gisin, "Time-resolved and antibunching experiments on single quantum dots at 1300 nm," Appl. Phys. Lett. **88**, - (2006).

61. E. Knill, R. Laflamme, and G. J. Milburn, "A scheme for efficient quantum computation with linear optics," Nature **409**, 46-52 (2001).

62. C. Grillet, C. Monat, C. L. C. Smith, B. J. Eggleton, D. J. Moss, S. Frederick, D. Dalacu, P. J. Poole, J. Lapointe, G. Aers, and R. L. Williams, "Nanowire coupling to photonic crystal nanocavities for single photon sources," Opt. Express **15**, 1267-1276 (2007).

63. S. J. McNab, N. Moll, and Y. A. Vlasov, "Ultra-low loss photonic integrated circuit with membrane-type photonic crystal waveguides," Opt. Express **11**, 2927-2939 (2003).

64. M. Notomi, A. Shinya, K. Yamada, J. Takahashi, C. Takahashi, and I. Yokohama, "Structural tuning of guiding modes of line-defect waveguides of silicon-on-insulator photonic crystal slabs," Ieee Journal of Quantum Electronics **38**, 736-742 (2002).

65. D. Taillaert, W. Bogaerts, P. Bienstman, T. F. Krauss, P. Van Daele, I. Moerman, S. Verstuyft, K. De Mesel, and R. Baets, "An out-of-plane grating coupler for efficient butt-coupling between compact planar waveguides and single-mode fibers," Ieee Journal of Quantum Electronics **38**, 949-955 (2002).

66. J. C. Knight, G. Cheung, F. Jacques, and T. A. Birks, "Phase-matched excitation of whispering-gallery-mode resonances by a fiber taper," Opt. Lett. **22**, 1129-1131 (1997).

67. K. Srinivasan, P. E. Barclay, M. Borselli, and O. Painter, "Optical-fiber-based measurement of an ultrasmall volume high-Q photonic crystal microcavity," Physical Review B **70**, - (2004).

68. K. Srinivasan, P. E. Barclay, M. Borselli, and O. J. Painter, "An optical-fiber-based probe for photonic crystal microcavities," Ieee Journal on Selected Areas in Communications **23**, 1321-1329 (2005).

69. I. K. Hwang, S. K. Kim, J. K. Yang, S. H. Kim, S. H. Lee, and Y. H. Lee, "Curved-microfiber photon coupling for photonic crystal light emitter," Appl. Phys. Lett. **87**, 131107 (2005).

70. W. Kuang, C. Kim, A. Stapleton, and J. D. O'Brien, "Grating-assisted coupling of optical fibers and photonic crystal waveguides," Opt. Lett. **27**, 1604-1606 (2002).

71. P. E. Barclay, K. Srinivasan, M. Borselli, and O. Painter, "Probing the dispersive and spatial properties of photonic crystal waveguides via highly efficient coupling from fiber tapers," Appl. Phys. Lett. **85**, 4-6 (2004).

72. P. E. Barclay, K. Srinivasan, and O. Painter, "Design of photonic crystal waveguides for evanescent coupling to optical fiber tapers and integration with

high-Q cavities," Journal of the Optical Society of America B-Optical Physics **20**, 2274-2284 (2003).

73.   P. E. Barclay, K. Srinivasan, M. Borselli, and O. Painter, "Efficient input and output fiber coupling to a photonic crystal waveguide," Opt. Lett. **29**, 697-699 (2004).

74.   L. M. Tong, R. R. Gattass, J. B. Ashcom, S. L. He, J. Y. Lou, M. Y. Shen, I. Maxwell, and E. Mazur, "Subwavelength-diameter silica wires for low-loss optical wave guiding," Nature **426**, 816-819 (2003).

75.   C. Monat, P. Domachuk, and B. J. Eggleton, "Integrated optofluidics: A new river of light," Nat Photon **1**, 106-114 (2007).

76.   D. Psaltis, S. R. Quake, and C. H. Yang, "Developing optofluidic technology through the fusion of microfluidics and optics," Nature **442**, 381-386 (2006).

77.   W. E. Haas, "Liquid-Crystal Display Research - the 1st 15 Years," Molecular Crystals and Liquid Crystals **94**, 1-31 (1983).

78.   R. W. Wood, "The mercury paraboloid as a reflecting telescope," Astrophysical Journal **29**, 164-176 (1909).

79.   S. Kuiper, and B. H. W. Hendriks, "Variable-focus liquid lens for miniature cameras," Appl. Phys. Lett. **85**, 1128-1130 (2004).

80.   U. Levy, K. Campbell, A. Groisman, S. Mookherjea, and Y. Fainman, "On-chip microfluidic tuning of an optical microring resonator," Appl. Phys. Lett. **88**, - (2006).

81.   T. M. Squires, and S. R. Quake, "Microfluidics: Fluid physics at the nanoliter scale," Rev. Mod. Phys. **77**, 977-1026 (2005).

82.   H. A. Stone, A. D. Stroock, and A. Ajdari, "Engineering flows in small devices: Microfluidics toward a lab-on-a-chip," Annual Review of Fluid Mechanics **36**, 381-411 (2004).

83.   J. Atencia, and D. J. Beebe, "Controlled microfluidic interfaces," Nature **437**, 648-655 (2005).

84.   M. Sumetsky, R. S. Windeler, Y. Dulashko, and X. Fan, "Optical liquid ring resonator sensor," Opt. Express **15**, 14376-14381 (2007).

85.   C. A. Barrios, K. B. Gylfason, B. Sanchez, A. Griol, H. Sohlstrom, M. Holgado, and R. Casquel, "Slot-waveguide biochemical sensor," Opt. Lett. **32**, 3080-3082 (2007).

86.   E. Chow, A. Grot, L. W. Mirkarimi, M. Sigalas, and G. Girolami, "Ultracompact biochemical sensor built with two-dimensional photonic crystal microcavity," Opt. Lett. **29**, 1093-1095 (2004).

87. M. L. Adams, M. Loncar, A. Scherer, and Y. M. Qiu, "Microfluidic integration of porous photonic crystal nanolasers for chemical sensing," Ieee Journal on Selected Areas in Communications **23**, 1348-1354 (2005).

88. P. S. Nunes, N. A. Mortensen, J. P. Kutter, and K. B. Mogensen, "Photonic crystal resonator integrated in a microfluidic system," Opt. Lett. **33**, 1623-1625 (2008).

89. D. Erickson, T. Rockwood, T. Emery, A. Scherer, and D. Psaltis, "Nanofluidic tuning of photonic crystal circuits," Opt. Lett. **31**, 59-61 (2006).

90. H. M. H. Chong, and R. M. De La Rue, "Tuning of photonic crystal waveguide microcavity by thermooptic effect," Ieee Photonics Technology Letters **16**, 1528-1530 (2004).

91. W. Park, and J. B. Lee, "Mechanically tunable photonic crystal structure," Appl. Phys. Lett. **85**, 4845-4847 (2004).

92. I. Marki, M. Salt, and H. P. Herzig, "Tuning the resonance of a photonic crystal microcavity with an AFM probe," Opt. Express **14**, 2969-2978 (2006).

93. M. W. Lee, C. Grillet, C. L. C. Smith, D. J. Moss, B. J. Eggleton, D. Freeman, B. Luther-Davies, S. Madden, A. Rode, Y. Ruan, and Y.-H. Lee, "Photosensitive post tuning of chalcogenide photonic crystal waveguides," Opt. Express **15**, 1277-1285 (2007).

94. F. B. Arango, M. B. Christiansen, M. Gersborg-Hansen, and A. Kristensen, "Optofluidic tuning of photonic crystal band edge lasers," Appl. Phys. Lett. **91**, 223503 (2007).

95. S. H. Kim, J. H. Choi, S. K. Lee, S. H. Kim, S. M. Yang, Y. H. Lee, C. Seassal, P. Regrency, and P. Viktorovitch, "Optofluidic integration of a photonic crystal nanolaser," Opt. Express **16**, 6515-6527 (2008).

96. A. Faraon, D. Englund, D. Bulla, B. Luther-Davies, B. J. Eggleton, N. Stoltz, P. Petroff, and J. Vuckovic, "Local tuning of photonic crystal cavities using chalcogenide glasses," Appl. Phys. Lett. **92**, - (2008).

97. R. van der Heijden, C. F. Carlstrom, J. A. P. Snijders, R. W. van der Heijden, F. Karouta, R. Notzel, H. W. M. Salemink, B. K. C. Kjellander, C. W. M. Bastiaansen, D. J. Broer, and E. van der Drift, "InP-based two-dimensional photonic crystals filled with polymers," Appl. Phys. Lett. **88**, - (2006).

98. S. Tay, J. Thomas, B. Momeni, M. Askari, A. Adibi, P. J. Hotchkiss, S. C. Jones, S. R. Marder, R. A. Norwood, and N. Peyghambarian, "Planar photonic crystals infiltrated with nanoparticle/polymer composites," Appl. Phys. Lett. **91**, - (2007).

99. M. Haurylau, S. P. Anderson, K. L. Marshall, and P. M. Fauchet, "Electrically tunable silicon 2-D photonic bandgap structures," Ieee Journal of Selected Topics in Quantum Electronics **12**, 1527-1533 (2006).

100. P. Barthelemy, M. Ghulinyan, Z. Gaburro, C. Toninelli, L. Pavesi, and D. S. Wiersma, "Optical switching by capillary condensation," Nat. Photonics **1**, 172-175 (2007).

101. P. El-Kallassi, S. Balog, R. Houdre, L. Balet, L. Li, M. Francardi, A. Gerardino, A. Fiore, R. Ferrini, and L. Zuppiroli, "Local infiltration of planar photonic crystals with UV-curable polymers," J. Opt. Soc. Am. B **25**, 1562-1567 (2008).

102. F. Intonti, S. Vignolini, V. Turck, M. Colocci, P. Bettotti, L. Pavesi, S. L. Schweizer, R. Wehrspohn, and D. Wiersma, "Rewritable photonic circuits," Appl. Phys. Lett. **89**, 211117 (2006).

103. C. L. C. Smith, D. K. C. Wu, M. W. Lee, C. Monat, S. Tomljenovic-Hanic, C. Grillet, B. J. Eggleton, D. Freeman, Y. Ruan, S. Madden, B. Luther-Davies, H. Giessen, and Y. H. Lee, "Microfluidic photonic crystal double heterostructures," Appl. Phys. Lett. **91**, 121103 (2007).

104. S. F. Mingaleev, M. Schillinger, D. Hermann, and K. Busch, "Tunable photonic crystal circuits: concepts and designs based on single-pore infiltration," Opt. Lett. **29**, 2858-2860 (2004).

105. H. Kurt, and D. S. Citrin, "Reconfigurable multimode photonic-crystal waveguides," Opt. Express **16**, 11995-11998 (2008).

106. S. Tomljenovic-Hanic, C. M. de Sterke, and M. J. Steel, "Design of high-Q cavities in photonic crystal slab heterostructures by air-holes infiltration," Opt. Express **14**, 12451-12456 (2006).

107. A. Zakery, and S. R. Elliot, "Optical properties and applications of chalcogenide glasses: a review," J. Non-Cryst. Solids **330**, 1-12 (2003).

108. S. Ramachandran, and S. G. Bishop, "Photoinduced integrated-optic devices in rapid thermally annealed chalcogenide glasses," Ieee Journal of Selected Topics in Quantum Electronics **11**, 260-270 (2005).

109. R. G. DeCorby, N. Ponnampalam, M. M. Pai, H. T. Nguyen, P. K. Dwivedi, T. J. Clement, C. J. Haugen, J. N. McMullin, and S. O. Kasap, "High index contrast waveguides in chalcogenide glass and polymer," Ieee Journal of Selected Topics in Quantum Electronics **11**, 539-546 (2005).

110. V. Lyubin, A. Klebanov, A. Feigel, and B. Sfez, "Films of chalcogenide glassy semiconductors: new phenomena and new applications," Thin Solid Films **459**, 183-186 (2004).

111. M. Shokooh-Saremi, V. G. Ta'eed, N. J. Baker, I. C. M. Littler, D. J. Moss, B. J. Eggleton, Y. L. Ruan, and B. Luther-Davies, "High-performance Bragg gratings in chalcogenide rib waveguides written with a modified Sagnac interferometer," Journal of the Optical Society of America B-Optical Physics **23**, 1323-1331 (2006).

112. T. K. Sudoh, Y. Nakano, and K. Tada, "Wavelength trimming technology for multiple-wavelength distributed-feedback laser arrays by photo-induced refractive index change," Electron. Lett. **33**, 216-217 (1997).

113. S. S. Song, S. S. Howard, Z. J. Liu, A. O. Dirisu, C. F. Gmachl, and C. B. Arnold, "Mode tuning of quantum cascade lasers through optical processing of chalcogenide glass claddings," Appl. Phys. Lett. **89**, - (2006).

114. A. Zakery, Y. Ruan, A. V. Rode, M. Samoc, and B. Luther-Davies, "Low-loss waveguides in ultrafast laser-deposited As2S3 chalcogenide films," Journal of the Optical Society of America B-Optical Physics **20**, 1844-1852 (2003).

115. T. T. Nang, M. Okuda, and T. Matsushita, "Photoinduced Absorption Change in Some Se-Based Glass Alloy Systems," Physical Review B **19**, 947-955 (1979).

116. K. Tanaka, "Reversible Photostructural Change - Mechanisms, Properties and Applications," J. Non-Cryst. Solids **35-6**, 1023-1034 (1980).

117. S. R. Elliott, "A Unified Model for Reversible Photostructural Effects in Chalcogenide Glasses," J. Non-Cryst. Solids **81**, 71-98 (1986).

118. S. Tomljenovic-Hanic, M. J. Steel, C. M. de Sterke, and D. J. Moss, "High-Q cavities in photosensitive photonic crystals," Opt. Lett. **32**, 542-544 (2007).

119. Y. Akahane, T. Asano, B. S. Song, and S. Noda, "High-Q photonic nanocavity in a two-dimensional photonic crystal," Nature **425**, 944-947 (2003).

120. P. Mach, M. Dolinski, K. W. Baldwin, J. A. Rogers, C. Kerbage, R. S. Windeler, and B. J. Eggleton, "Tunable microfluidic optical fiber," Appl. Phys. Lett. **80**, 4294-4296 (2002).

121. C. Kerbage, and B. J. Eggleton, "Tunable microfluidic optical fiber gratings," Appl. Phys. Lett. **82**, 1338-1340 (2003).

122. P. Domachuk, H. C. Nguyen, and B. J. Eggleton, "Transverse probed microfluidic switchable photonic crystal fiber devices," Ieee Photonics Technology Letters **16**, 1900-1902 (2004).

123. P. Domachuk, C. Grillet, V. Ta'eed, E. Magi, J. Bolger, B. J. Eggleton, L. E. Rodd, and J. Cooper-White, "Microfluidic interferometer," Appl. Phys. Lett. **86**, 024103 (2005).

124. J. C. Galas, J. Torres, M. Belotti, Q. Kou, and Y. Chen, "Microfluidic tunable dye laser with integrated mixer and ring resonator," Appl. Phys. Lett. **86**, 264101 (2005).

125. C. Monat, P. Domachuk, C. Grillet, M. Collins, B. J. Eggleton, M. Cronin-Golomb, S. Mutzenich, T. Mahmud, G. Rosengarten, and A. Mitchell, "Optofluidics: a novel generation of reconfigurable and adaptive compact architectures," Microfluidics and Nanofluidics **4**, 81-95 (2008).

126. S. S. Xiao, and N. A. Mortensen, "Proposal of highly sensitive optofluidic sensors based on dispersive photonic crystal waveguides," J. Opt. A: Pure Appl. Opt. **9**, S463-S467 (2007).

127. J. D. Joannapolous, R. D. Meade, and J. N. Winn, "Photonic Crystals - Molding the Flow of Light," Princeton University Press, Second edition (2007).

128. L. C. Andreani, G. Panzarini, and J. M. Gerard, "Strong-coupling regime for quantum boxes in pillar microcavities: Theory," Physical Review B **60**, 13276-13279 (1999).

129. C. Manolatou, M. J. Khan, S. H. Fan, P. R. Villeneuve, H. A. Haus, and J. D. Joannopoulos, "Coupling of modes analysis of resonant channel add-drop filters," Ieee Journal of Quantum Electronics **35**, 1322-1331 (1999).

130. D. Marcuse, "Theory of Dielectric Optical Waveguides," New York: Academic (1974).

131. H. Kogelnik, "Theory of Dielectric Waveguides," Integrated Optics, New York: Springer-Verlag (1975).

132. H. A. Haus, "Waves and Fields in Optoelectronics," Prentice-Hall Series in Solid State Physical Electronics, 59-71 (1984).

133. D. Marcuse, "Bandwidth of forward and backward coupling directional couplers," J. Lightwave Technol. **5**, 1773-1777 (1987).

134. M. W. Lee, C. Grillet, C. G. Poulton, C. Monat, C. L. C. Smith, E. Magi, D. Freeman, S. Madden, B. Luther-Davies, and B. J. Eggleton, "Characterizing photonic crystal waveguides with an expanded k-space evanescent coupling technique," Opt. Express **16**, 13800-13808 (2008).

135. M. Notomi, K. Yamada, A. Shinya, J. Takahashi, C. Takahashi, and I. Yokohama, "Extremely large group-velocity dispersion of line-defect waveguides in photonic crystal slabs," Phys. Rev. Lett. **87**, 253902 (2001).

136. X. Letartre, C. Seassal, C. Grillet, P. Rojo-Romeo, P. Viktorovitch, M. L. d'Yerville, D. Cassagne, and C. Jouanin, "Group velocity and propagation

losses measurement in a single-line photonic-crystal waveguide on InP membranes," Appl. Phys. Lett. **79**, 2312-2314 (2001).

137. T. A. Birks, and Y. W. Li, "The Shape of Fiber Tapers," Journal of Lightwave Technology **10**, 432-438 (1992).

138. W. J. Stewart, and J. D. Love, "Design limitation on tapers and couplers in single mode fibres," in Proc. ECOC (Venice), 559-562 (1985).

139. J. D. Love, and W. M. Henry, "Quantifying Loss Minimization in Single-Mode Fiber Tapers," Electron. Lett. **22**, 912-914 (1986).

140. L. F. Stokes, M. Chodorow, and H. J. Shaw, "All-single-mode fiber resonator," Opt. Lett. **7**, 288-290 (1982).

141. M. Sumetsky, "Optical fiber microcoil resonator," Opt. Express **12**, 2303-2316 (2004).

142. M. Sumetsky, Y. Dulashko, and A. Hale, "Fabrication and study of bent and coiled free silica nanowires: Self-coupling microloop optical interferometer," Opt. Express **12**, 3521-3531 (2004).

143. S. Frederick, D. Dalacu, J. Lapointe, P. J. Poole, G. C. Aers, and R. L. Williams, "Experimental demonstration of high quality factor, x-dipole modes in InAs/InP quantum dot photonic crystal microcavity membranes," Appl. Phys. Lett. **89**, 091115 (2006).

144. U. Bog, C. L. C. Smith, M. W. Lee, S. Tomljenovic-Hanic, C. Grillet, C. Monat, L. O'Faolain, C. Karnutsch, T. F. Krauss, R. McPhedran, and B. J. Eggleton, "High-Q microfluidic cavities in silicon-based 2D photonic crystal structures," Opt. Lett. **33**, 2206-2208 (2008).